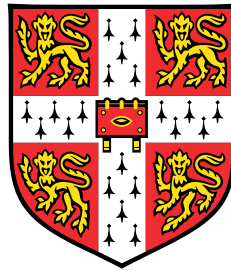


Well-Conditioned Heat Transfer Measurements on Engine Scale Gas Turbine Rigs



William Playford

Department of Engineering
University of Cambridge

This dissertation is submitted for the degree of
Doctor of Philosophy

Gonville and Caius College

April 2018

Declaration

I hereby declare that except where specific reference is made to the work of others, the contents of this dissertation are original and have not been submitted in whole or in part for consideration for any other degree or qualification in this, or any other university. This dissertation is my own work and contains nothing which is the outcome of work done in collaboration with others, except as specified in the text and Acknowledgements. This dissertation contains fewer than 65,000 words including appendices, bibliography, footnotes, tables and equations and has fewer than 150 figures.

William Playford
April 2018

Acknowledgements

Thanks first go to Nick Atkins, my supervisor, who has offered endless enthusiasm, support and guidance throughout the project. I have learned a great deal in the process, and I am very grateful indeed.

Thanks also go to the whole community at the Whittle laboratory - who have provided continuous support, advice, and motivation, as well as a lovely place to work and excellent friendships. Particular thanks go to John Saunders and Nick Hooper in the workshop, who have supported and encouraged my endeavours in labs. Thanks also go to Svilen, Antonio, Konstantinos and Tash, who have been excellent company.

Many thanks go to the FACTOR team, particularly Marc Stokes and Marc Tegeler, who it's been a pleasure to work with.

I would like to thank Simon Gallimore, Sam Beale and Rob Miller, who have opened many doors - and also Rolls-Royce for funding me.

Finally, I would like to thank my family who have been consistently supportive.

Abstract

High combustion temperatures are required in gas-turbine engines to achieve high cycle efficiencies. With increasing temperature, however, the life span of the turbine components are reduced. The ability to accurately predict engine component temperature as a function of combustion temperature is required to strike this balance correctly.

An experimental heat transfer measurement technique is developed in this thesis, which builds on a large body of existing literature. The technique enables a detailed quantification of turbine heat transfer on test rigs which closely represent gas-turbine engine configurations. Fundamental improvements are made to existing methods, in the definition of the ‘semi-infinite limit’ for transient measurement techniques, in Infra-red camera calibration, and in thermal effusivity measurement. The improvements were developed from first principles, verified experimentally, and have been used on a world leading heat transfer rig (the FACTOR combustor-turbine interaction rig, run on the NG-Turb facility at DLR Göttingen).

It was found that optimisation of a number of measurement parameters was required to minimise the measurement uncertainty. It is shown that the optimum measurement parameters are dependant, and sensitive to the specific configuration of the test rig. An experimental procedure was developed and tested, which has been ‘tuned’ for measurements on the FACTOR test rig. Despite the challenging measurement environment on the FACTOR rig, it was found that state-of-the-art heat transfer measurement uncertainties of approximately 5%, could nevertheless still be achieved, by using the new methods.

General principles and rules are established which can be used to guide the design of future heat transfer measurements, with the aim of minimising measurement uncertainty.

Table of contents

1	Introduction	1
1.1	Overview	1
1.2	Problem Definition	3
1.3	The Aims of the Current Research	4
1.4	Thesis Structure	5
2	Literature Review	7
2.1	Introduction	8
2.2	Review of Measurement Instrumentation	9
2.2.1	Thin-film resistance gauges	9
2.2.2	Thermo-chromic liquid crystals	16
2.2.3	Infra-red thermography	19
2.2.4	Summary of measurement instrumentation	26
2.3	Review of Steady State Measurement Techniques	27
2.4	Review of Transient Measurement Techniques	33
2.4.1	Direct fitting to analytical semi-infinite solutions	34
2.4.2	Heat flux reconstruction methods	36
2.4.3	Further methods reducing measurement uncertainty	42
2.5	Conclusions	46
3	Heat Transfer Measurement Theory	48
3.1	Choosing a Measurement Method	49
3.1.1	Measurement instrumentation	49
3.1.2	Measurement method	50
3.1.3	The selected approach	50
3.2	Sources of Uncertainty	51
3.3	Routes to a Well Conditioned Regression	53

3.4	One Dimensional Transient Conduction	57
3.5	Minimising Uncertainty in $\Theta_{\text{wall}}(t)$	58
3.5.1	Reducing uncertainty in $\Delta T_{\text{wall}}(t)$	59
3.5.2	Increasing the magnitude of ΔT_{aw}	61
3.6	Minimising Uncertainty in Q^*	62
3.6.1	Uncertainty in material properties	62
3.6.2	Uncertainty in initial conditions	65
3.6.3	Surface curvature induced errors	67
3.6.4	Boundary condition induced errors	73
3.7	Maximising the Regression Extent, Θ_{R}	75
3.7.1	Minimising $\tilde{\Theta}$	76
3.7.2	Maximising Θ_{limit}	78
3.7.3	Optimum substrate material properties	84
3.8	Conclusions	87
4	Uncertainty Analysis	90
4.1	Introduction	91
4.2	Uncertainty Modelling	92
4.2.1	The Monte-Carlo method	93
4.2.2	System modelling	94
4.2.3	Input uncertainty quantification	96
4.2.4	Un-modelled uncertainty sources	97
4.3	FACTOR NGV - Sensitivity Analysis	97
4.3.1	Base-line simulation parameters	97
4.3.2	Uncertainty as a function of h and $\Delta T_{0,\infty}$	98
4.3.3	Uncertainty as a function of h and τ_{∞}	100
4.3.4	Uncertainty as a function of h and δ	102
4.3.5	Key messages	103
4.4	FACTOR Uncertainty Analysis	103
4.4.1	Rotor conditions	104
4.4.2	LP vane conditions	105
4.5	Conclusions	107
5	FACTOR Turbine Rig: Design Features	109
5.1	The FACTOR Turbine Rig: A Brief Description	110
5.2	Blades and Vanes with Maximised Θ_{R}	111

5.2.1	Rotor blade finite element analysis	113
5.2.2	Rotor blade tensile testing	117
5.2.3	NGV and LP vane material specification	119
5.3	Achieving Full Optical Access	119
5.3.1	Design constraints	120
5.3.2	Design solution	122
5.3.3	Tip seal testing	130
5.4	Conclusions	134
6	Measurement Methods	135
6.1	Experimental Objectives	136
6.1.1	Objective 1: Verifying the theory from Chapter 3	136
6.1.2	Objective 2: Verifying the performance of the FACTOR measure- ment system	137
6.2	Experimental Facility	139
6.2.1	Flat plate rig	140
6.2.2	3D vane rig	147
6.3	Infra-Red Thermography	152
6.3.1	Camera selection	152
6.3.2	Lens selection	155
6.3.3	IR detector calibration	158
6.3.4	Optical path calibration	163
6.3.5	Emissivity calibration	171
6.4	Thermal Effusivity Calibration	174
6.4.1	Measurement requirements	174
6.4.2	Measurement method	175
6.5	Heat Flux Modelling	180
6.5.1	Numerical scheme	180
6.5.2	Structured mesh & boundary conditions	182
6.5.3	Model resolution	184
6.5.4	Model validation	185
7	Heat Transfer Measurement Results and Discussion	191
7.1	Flat Plate Rig Experiments - Baseline Measurement	192
7.1.1	Baseline measurement conditions	192
7.1.2	Results	194

7.2	Flat Plate Rig Experiments - Varying $U_{\Theta_{\text{wall}}}$	198
7.2.1	Varying the mainstream temperature step - un-cooled flat plate . . .	199
7.2.2	Varying the mainstream temperature step - film-cooled flat plate . .	200
7.2.3	In-situ IR calibration effect	203
7.2.4	Key observations	207
7.3	Flat Plate Rig Experiments - Varying U_{Q^*}	207
7.3.1	Spatial variation in boundary conditions	208
7.3.2	3D geometry effects	214
7.3.3	Key observations	215
7.4	Flat Plate Rig Experiments - Varying Θ_R	216
7.4.1	Experiments varying $\tilde{\Theta}$	216
7.4.2	Experiments varying Θ_{limit}	221
7.4.3	Key observations	226
7.5	3D Vane Rig Experiments: Without film-cooling	227
7.5.1	3D vane coordinate system mapping	228
7.5.2	Integration time specification for SNR levels matching FACTOR . .	230
7.5.3	Un-cooled vane measurement conditions	231
7.5.4	Valid data region	232
7.5.5	Preliminary result evaluation	233
7.5.6	Un-cooled vane results	238
7.5.7	Key observations	241
7.6	3D Vane Rig Experiments: With film-cooling	242
7.6.1	Cooled vane measurement conditions	242
7.6.2	Valid data region	244
7.6.3	Film-cooled vane results	246
7.6.4	Key observations	252
8	Conclusions & Future Work	253
8.1	Conclusions	253
8.2	Future Work	256
8.2.1	Transient radiance corrections on the FACTOR rig	256
8.2.2	Specular transient reflection errors on the FACTOR rig	258
8.2.3	FACTOR IR window lensing effects	260
8.2.4	Heat transfer measurements on vane and blade leading edges	261
	Nomenclature	262

Appendix A	FACTOR	272
A.1	Photographs of Vanes and Blades	272
A.2	Photographs of FACTOR Rig	274
A.3	Photographs of FACTOR IR Windows	276
A.4	FACTOR IR Window Drawings	277

Chapter 1

Introduction

1.1 Overview

An increase in the Turbine Entry Temperature (TET) of a gas-turbine engine operating on the Brayton cycle, will result in an increase in the specific power output. This results in a smaller, lighter engine, and a reduced Specific Fuel Consumption (SFC).

However, underestimates of the operating metal temperature of first stage turbine blades in aero-gas-turbine engines, of as little as 20 K, can lead to their in-service lifespan reducing to half the design intent [Plaut et al., 2007]. Correcting an excessive turbine metal temperature late in the development cycle of an engine can lead to large costs and project delays.

Consequently, gas-turbine engine designers need accurate means by which they can predict the operating temperature of the turbine components during the engine design process. This is needed in order to strike the right balance between, primarily, component life-span, and SFC.

The first turbine stage of modern aero-gas-turbine engines is supplied with cooling air, which maintains the metal temperature of the blades sufficiently below the temperature of the hot gasses flowing past them. Cooling is usually achieved by a combination of internal-cooling (within hollow cavities within the blade), and film-cooling (where cooling air is ejected onto the external surface of the blade). The cooling air is extracted from the outlet of the compressor of the engine.

Accurate predictions of the cooling performance of the cooling air-stream from Computational Fluid Dynamics (CFD) simulations, requires high-fidelity methods such as Direct Numerical Simulation (DNS) or Large Eddies Simulation (LES), which can be impractically expensive and time-consuming. As a result, lower cost, faster and less accurate computational modelling methods such as RANS and URANS are typically used. As described by Han

et al. [2012], these lower fidelity models often fail to accurately predict turbine heat transfer, due to their high sensitivity to the use and ‘tuning’ of appropriate turbulence models.

One method of performing this turbulence model ‘tuning’ is to calibrate the CFD model against a known and accurately measured test case. Turbulence model parameters can then be found which result in a close match between the CFD and the measurements. In order for this kind of calibration to translate most effectively to a CFD simulation of a gas-turbine engine, the test case should be closely representative of an engine. This means the inclusion of features such as film-cooled Nozzle Guide Vanes (NGVs), engine representative combustor hot-spots and swirl profiles, purged disk cavities, as well as high-speed rotating components with engine matched Mach and Reynolds numbers. The test case should permit the simultaneous measurement of both heat transfer and aerodynamic performance, such that the two can be related. We will call this type of test rig an ‘engine-scale’ turbine rig.

Currently there is limited detailed heat transfer measurement data from engine-scale turbine rigs. This is primarily due to the high complexity in taking heat transfer measurements on such rigs. There is however, a significant amount of empirical data from heat transfer measurements on less representative rigs, where features such as rotating components or combustor representative inlet profiles are often not present. On these less representative rigs, state of the art heat transfer measurements have an uncertainty of approximately 5%.

In this thesis, methods for taking low uncertainty heat transfer measurements on engine-scale turbine rigs are developed. A target is set of reaching, or surpassing, a measurement uncertainty of 5%. The methods are developed specifically for application to a new engine-scale turbine rig called ‘FACTOR’ - which is being commissioned by a European Commission FP7 consortium, and is operated run on the NG-Turb test facility at DLR. The FACTOR turbine rig is a world leading, full annulus, rotating 1.5 stage combustor-turbine interaction test rig, with engine representative Mach and Reynolds numbers, and combustor inlet profiles. A focus is made in this work, however, to determine general principles behind taking taking full field, low uncertainty heat transfer measurements on generic engine-scale turbine rigs.

1.2 Problem Definition

There are a number of features, or characteristics of an engine-scale turbine rig, which create challenges, or limit the use of many of the existing heat transfer measurement techniques from the literature. These are described below.

1. Small scale vanes and blades

It is often advantageous to increase the geometric scale of the test geometry, when undertaking heat transfer measurements, whilst matching the appropriate non-dimensional, such as Mach and Reynolds number. By increasing the geometric scale, instrument access can be made more easily, measurement resolution can be increased, and measurement uncertainty reduced. On engine-scale turbine rigs, with rotating disks, large increases in geometric scale are less practical, as overall rig size becomes prohibitively large, and there is greater difficulty in matching all of the appropriate non-dimensional values. Consequently, engine-scale turbine rigs typically have a geometric length scale similar to that of an engine, where for example, High Pressure (HP) turbine blade spans are in the region of 40mm. For reasons which will be described later in this thesis, this relatively small geometric scale can result in significantly increased measurement uncertainties, and reduced measurement resolution, when compared to measurements on a larger scaled up blade. The issue is amplified by the fact that high resolution measurements are required to resolve detailed film-cooling flows and hot-spot migration paths which will be present on engine-scale turbine rigs.

2. Non-adiabatic initial conditions

A common requirement for many heat transfer measurement techniques is that the blade surfaces are adiabatic (zero heat flux condition) prior to performing the measurement. This requirement is usually satisfied in short-duration facilities such as piston tube or blow-down facilities (types of wind tunnel configuration). However, engine-scale turbine rigs will typically be operated in a continuously operating steady state type facility in order to permit accurate aero-performance measurements. In this configuration, adiabatic initial conditions may not be achievable. This is particularly true on engine-scale turbine rigs with film-cooled blades.

3. High rotor tip speeds and high temperatures

The requirement for both engine-scale geometry and matched Mach and Reynolds numbers means that flow velocities and consequently both rotor tip speeds and rota-

tional speeds will be high in engine-scale turbine rigs. (The rotor tip speed on the FACTOR rig is ~ 220 m/s).

Additionally, multi-stage turbine rigs often require turbine inlet temperatures significantly greater than ambient temperature, to prevent condensation issues in downstream sections, or to provide adequate temperature ratios between mainstream and coolant flows. (The peak FACTOR TET is $\sim 280^\circ\text{C}$).

The high centrifugal stress and high TET in the FACTOR rig applies constraints to the range of materials and measurement instrumentation which can be used - preventing the application of many existing heat transfer measurement techniques.

1.3 The Aims of the Current Research

The objectives of the research are as follows:

1. To develop a high spatial resolution heat transfer measurement technique which is capable of taking low uncertainty measurements of heat transfer on engine-scale turbine rigs.
2. To determine the dominant sources of measurement uncertainty in the heat transfer measurement, and to establish measurement methods which reduce their magnitude.
3. To guide the design of the FACTOR turbine rig, so as to favourably condition the heat transfer measurements - with the aim of enabling full field, high resolution measurements on both the film-cooled NGVs and on the high speed rotating rotor blades.
4. To perform a series of experimental heat transfer measurements using the developed technique, with the following aims:
 - To verify the theories which will be developed as part of this work, with regards to the design of a well-conditioned heat transfer measurement.
 - To validate the measurement system which will be used on the FACTOR rig.

1.4 Thesis Structure

A brief description of each chapter is given below:

- **Chapter 2 - Literature Review** presents a review of the current state of the art in heat transfer measurement techniques.
- **Chapter 3 - Heat Transfer Measurement Theory** investigates the suitability of various heat transfer measurement techniques from the Literature Review, with application to engine-scale turbine rigs. A measurement approach is selected, and the relevant theoretical concepts are developed. The key factors which influence the uncertainty in the heat transfer measurements are described. The ideal rig design and experimental method is determined.
- **Chapter 4 - Uncertainty Analysis** presents the design and computational output of a predictive measurement uncertainty model. The model was used to evaluate the sensitivity of the heat transfer measurement uncertainty, as a function of a number of relevant variables. It was used to both validate the theory from Chapter 3, and to give a quantitative estimate of the measurement uncertainty for a variety of measurement conditions.
- **Chapter 5 - FACTOR Turbine Rig - Design Features** presents a series of examples of the means by which the theory developed in Chapter 3, and results from Chapter 4 were used to guide the design of FACTOR rig components. Some examples of engineered solutions to instrumentation integration are also given.
- **Chapter 6 - Measurement Methods** describes the experimental methods, tools, modelling approaches and calibration techniques which have been applied and/or developed. Two test rigs are also described, which were designed to mimic some of the features present in the FACTOR rig (and engine-scale rigs in general). The rigs enabled experimental heat transfer measurements to be taken, the results of which could be validated against the theory from Chapter 3.
- **Chapter 7 - Heat Transfer Measurement Results** presents the experimental results of the heat transfer measurements from the rigs described in Chapter 6. The sensitivity of the measurement result to a number of key variables are presented and discussed.

-
- **Chapter 8 - Conclusions & Future Work** summarises the key findings and conclusions from the research, and provides suggestions on how further developments can be made.

Chapter 2

Literature Review

In this chapter a review of the most commonly used heat transfer measurement techniques is provided. The capabilities and limitations of the various techniques are highlighted. All of the presented heat transfer measurement techniques primarily depend on instrumentation with which temperature measurements can be taken. A review of the most commonly used instrumentation is therefore also provided, along with their strengths and weaknesses.

2.1 Introduction

The dominant mechanism of heat transfer in gas-turbine engines, from the hot combustion gasses to the blades, is convection, and it is therefore the characterisation of heat transfer by convection which is of most interest. Heat transfer by convection can be linearised and quantified, approximately, in terms of a heat transfer coefficient, and adiabatic wall temperature. Heat flux through a solid-gas interface can then be given by equation 2.1, where h is the heat transfer coefficient (units: $[\text{Wm}^{-2}\text{K}^{-1}]$, which expresses a conductance value of the boundary layer), T_{aw} is the adiabatic wall temperature (being the temperature the wall would reach if the solid were a perfect insulator. It is also equal to the ‘recovery temperature’, from a fluid dynamic perspective), and T_{wall} is the actual wall temperature, where \dot{q} is the heat flux (units: $[\text{Wm}^{-1}\text{K}^{-1}]$).

$$\dot{q} = h(T_{\text{aw}} - T_{\text{wall}}) \quad (2.1)$$

By expressing the heat flux as a function of h , T_{aw} , and T_{wall} an engine designer is able to determine the heat flux which would result, under matched aerodynamic conditions, for any given wall temperature - which is an essential requirement enabling integration of the measurements into larger heat transfer system models. The measurement techniques reviewed in this chapter are capable of measuring heat transfer coefficients and/or adiabatic wall temperatures, thereby defining the convection characteristics, in a scalable way.

It is also common practice to nondimensionalise the heat transfer coefficient into a Nusselt number, an expression for which is given in equation 2.2, where x is a characteristic length scale, and κ is the thermal conductivity of the fluid. The Nusselt number characterises the convective heat transfer independently of the thermal conductivity of the fluid.

$$\text{Nu} = hx/\kappa \quad (2.2)$$

As a result of the developments in heat transfer measurement techniques, (as well as development in other areas such as turbine materials), gas turbine engine designers have been able to increase turbine entry temperatures from $\sim 800^\circ\text{C}$ in the 1960s, to $\sim 1900^\circ\text{C}$ at present - increasing cycle efficiency.

The objective of this literature review is to present the capabilities and limitations of the current state of the art in heat transfer measurement techniques, and associated instrumentation, on turbine rigs. The heat transfer measurement techniques can be categorised into two groups: steady-state, and transient techniques. These techniques are described in

section 2.3 and 2.4. All of the measurement techniques depend on temperature measurement instrumentation - the most commonly used instrumentation are described first, in section 2.2.

2.2 Review of Measurement Instrumentation

In the turbo machinery heat transfer measurement literature, from the last fifty years, there are three frequently recurring methods of determining steady-state and time-resolved surface temperatures: 1) The use of surface mounted thin-film resistance thermometers; 2) the use of thermo-chromic liquid crystals, and 3) infra-red thermography. Each of these instrumentation methods are reviewed in the following subsections.

There are also a number of less frequently occurring methods, such as the use of phase-change materials, and pressure sensitive paints, which are not included in this review.

2.2.1 Thin-film resistance gauges

Thin-film resistance gauges consist of an electrically conductive metallic film, whose electrical resistance is a function of its temperature. If a constant electrical current is passed through the film, a relationship between the film temperature, and the voltage-drop across the element can be determined. Monitoring the voltage drop consequently provides a means of monitoring the element temperature. Typically, thin-film gauges are mounted on the surface of a thermal and electrical insulator, where the film thickness is between 0.01 and 0.1 μm [Schultz and Jones, 1973]. Due to the low thickness of the film, the gauge measures a value close to the true surface temperature, and has a high temporal response.

Thin-film resistance gauges were initially developed for use in short-duration high Mach number wind tunnels, for the study of heat transfer in reentry vehicles. Flow duration in these wind tunnels is of the order of tens of microseconds, and as a result, high frequency response temperature measurement instruments were required.

Within the heat transfer measurement literature, there are three distinct instruments which make use of thin-film gauges; Single layer semi-infinite gauges, double layer semi-infinite gauges (also known as a 'two layer gauge'), and double layer non-semi-infinite gauges. These three gauge types are described in the following subsections.

Single layer semi-infinite gauge

The simplest gauge is the single layer semi-infinite gauge. This gauge consists of a thin-film applied to the surface of a semi-infinite body. The gauge measures time resolved

surface temperature. A diagram of a single layer semi-infinite gauge is shown in figure 2.1. This gauge type is used with transient measurement techniques: In transient measurement techniques, a step change in fluid temperature (or at least a rapid rise) over the gauge initiates a heat flux from the fluid, into the semi-infinite solid. Measurements of the resulting transient surface temperature, (from the gauge), combined with knowledge of the material properties of the semi-infinite solid, enable deduction of the time-resolved surface heat flux. With this information, it is then possible to determine the heat transfer coefficient and adiabatic wall temperature. (Transient measurement techniques are discussed in detail in section 2.4).

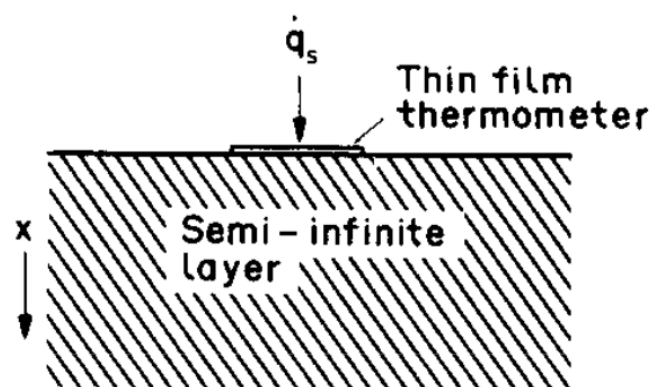


Fig. 2.1 Schematic of the single layer semi-infinite gauge [Doorly and Oldfield, 1986]

In order to deduce surface heat flux from a single layer gauge, the substrate must remain semi-infinite, over the measurement period. It consequently becomes desirable to produce the substrate from a low thermal conductivity material, with a large thickness (relative to the thermal length scale κ/h), so as to prolong the measurement duration, reducing measurement uncertainty.

Camci and Arts [1985] produced a film-cooled NGV from the machinable glass ceramic, 'Macor', with 45 platinum thin-films. (Macor having a low thermal conductivity). The platinum films were hand painted and fired in place, at high temperature. They used the gauges to measure the influence of film-cooling flows on the convective heat transfer coefficient at the leading edge of the NGV.

Didier et al. [2002] used a similar experimental technique to Camci and Arts [1985], where they mounted small Macor inserts into a rotor blade, with surface mounted thin film gauges. They were able to perform unsteady measurements, resolving individual wake passing events. In figure 2.2, one of the instrumented rotor blades is shown, where the discrete Macor inserts are visible at different measurement locations. In order to maintain

the mechanical integrity of the blades, only a small number of gauges could be fitted to each blade.

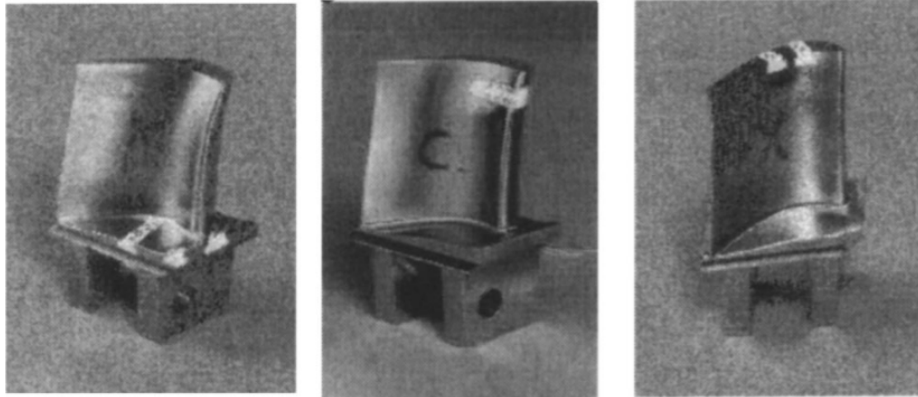


Fig. 2.2 Thin film gauges on Macor insert at rotor blade hub platform (left), 85% span (middle), and blade tip (right) Didier et al. [2002]

Double layer semi-infinite gauge

The double layer semi-infinite gauge, (usually called a ‘two layer gauge’) was developed to increase the ease of instrumentation, over single layer gauges, particularly with application to rotating blades in mind [Doorly and Oldfield, 1987]. The gauge construction also makes it easier to instrument existing metallic hardware in a cost effective and quick manor [Iliopoulou et al., 2004]. The gauge consists of a thin thermal and electrical insulating layer, which is fixed onto a semi-infinite substrate, which is usually the metal body of a vane or blade. Thin-films are positioned on the outside surface of the insulating layer. A schematic of the mechanical arrangement is shown in figure 2.3.

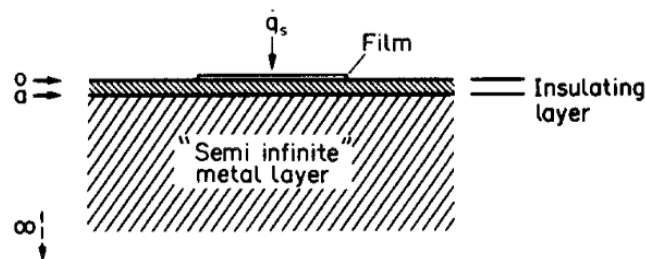


Fig. 2.3 Schematic of the double layer semi-infinite gauge [Doorly and Oldfield, 1986]

The thin layer of thermal insulation, (which is typically $\sim 0.1\text{mm}$ thick), allows the measurement surface to retain a high frequency response ($\sim 100\text{kHz}$ [Thorpe et al., 2005]), without the mechanical issues inherent in integrating relatively large Macor inserts, or other

materials, as with single layer semi-infinite gauges. During a measurement of heat transfer, employing a transient measurement technique, it is intended that the thin insulating layer does not remain semi-infinite, whereas the metallic substrate does. Doorly and Oldfield [1987] presented the theory of transient conduction within a one dimensional double layer semi-infinite gauge, as well as data reduction and calibration methods needed to determine transient heat flux from surface temperature measurement using this gauge type.

Iliopoulou et al. [2004] used double layer semi-infinite gauges to take time-averaged and time-resolved measurements of heat flux at the midspan on an NGV. The gauges consisted of a serpentine nickel thin-film, deposited on a $50\mu\text{m}$ thick Upilex-S polyamide sheet, that was bonded to the metallic blade with a $75\mu\text{m}$ thick double-sided adhesive sheet. The sensing element of the foil covered an area $1.9 \times 0.25\text{ mm}$, as shown in figure 2.4. Spatial measurement resolution with thin-film gauges is typically limited by the requirement to lead out the electrical connections to each gauge, the large size of which can also be seen in figure 2.4.

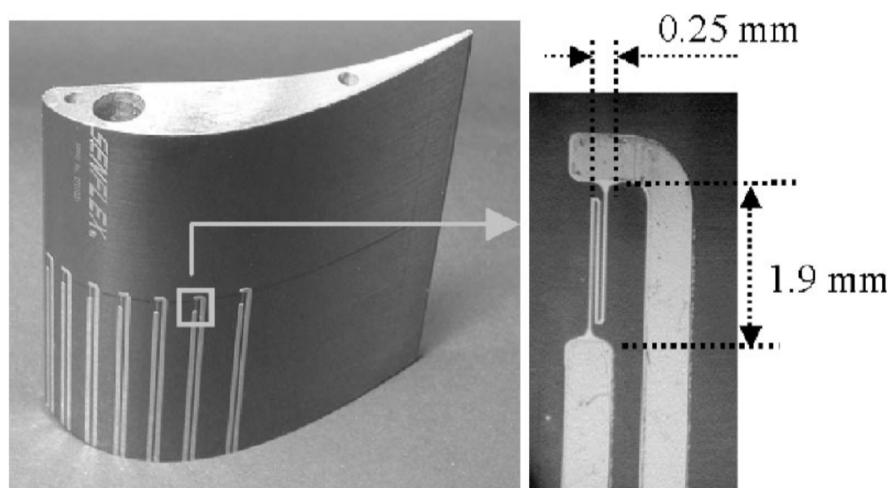


Fig. 2.4 Photograph of double layer semi-infinite gauge [Iliopoulou et al., 2004]

Iliopoulou et al. [2004] conducted their heat transfer measurements with both single-layer and double layer semi-infinite gauges, on the same test rig. They presented the Nusselt number (non-dimensional heat transfer coefficient), which was computed from each gauge type, at each measurement location around an NGV. Their measurements are shown in figure 2.5. The vertical error bars represent a measured precision uncertainty (random error). It can be seen that the vertical error bars for each gauge type, for the majority of their measurements, overlap - indicating a reasonable level of agreement between the measurements. A precision uncertainty in Nusselt number of $\pm 4.4\%$ was measured from the double layer gauge, and \pm

8.2 % for the single layer gauge. A bias uncertainty estimate was not provided, however it is evident from the fact that not all of the error bars are overlapping, that significant bias errors are present in at least one of the measurement techniques. (A definition of precision and bias uncertainty is given in section 4.2).

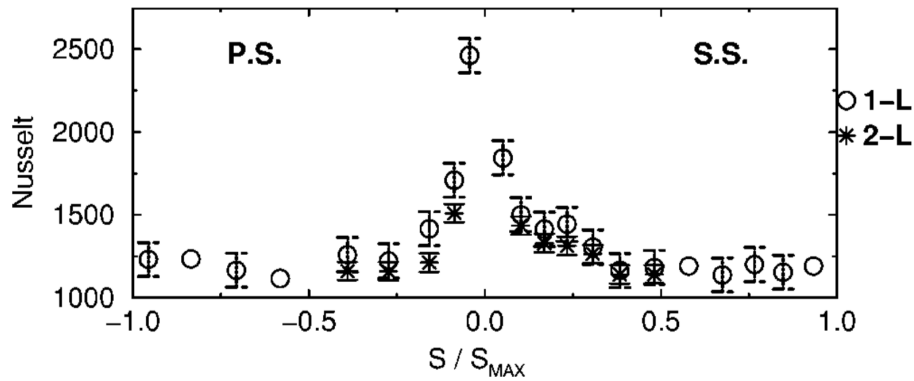
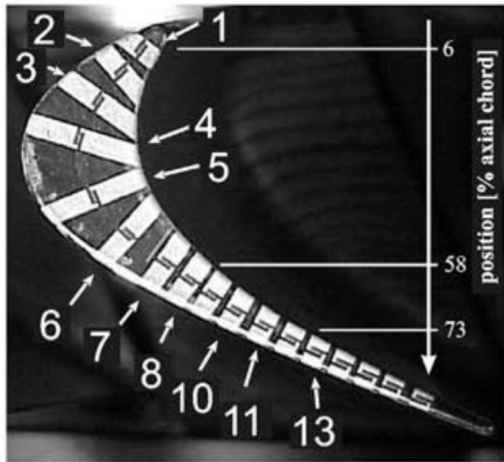
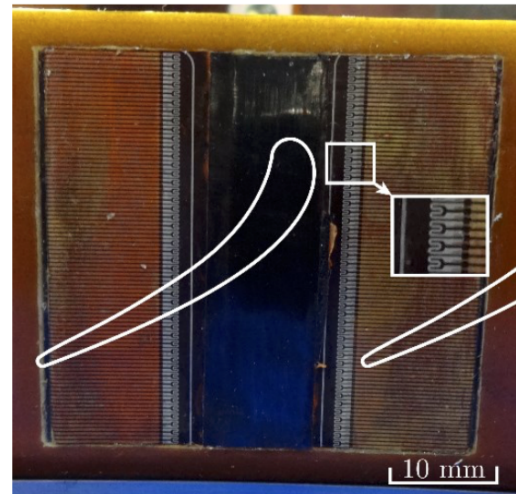


Fig. 2.5 Nusselt number measurements at midspan on a turbine stator blade, performed with single layer (1-L) and double layer (2-L) semi-infinite gauges [Iliopoulou et al., 2004]

Thorpe et al. [2005] performed similar measurements to Iliopoulou et al. [2004] on a rotating turbine blade tip (figure 2.6a), and Collins et al. [2015] on the over tip casing (figure 2.6b), all of which were performed on a short duration transonic turbine rig. They were both able to resolve periodic heat flux signals from either wake passing or rotor passing events, and time mean Nusselt numbers. Thorpe et al. [2005] quoted a measurement uncertainty on the heat flux of $\pm 5\%$, and Collins et al. [2015] quoted a Nusselt number measurement uncertainty between 10.25 and 13.25%.



(a) Double layer semi-infinite gauges distributed along the mean camber line of turbine blade tip [Thorpe et al., 2005]



(b) Two vertical arrays of double layer semi-infinite gauges on the over tip casing of a turbine rig [Collins et al., 2015]

Fig. 2.6

Collins et al. [2015] was able to produce an array of double-layer semi-infinite gauges with an increased spatial density in one direction, compared to others, by making use of a pre-laminated copper and polyimide substrate. They were able to achieve a lateral gauge width of 0.8mm, which defined the spatial resolution of the one-dimensional array of gauges.

These measurement techniques were able to provide high frequency heat flux measurements in both that stationary and rotating frame. The main drawback however, in the context of the present work, is their limited spatial measurement resolution, caused by limitations in the number of gauges which can be fitted to a given blade area.

Double layer non-semi-infinite gauge (a.k.a ‘Direct heat flux gauges’)

A variant on the double layer gauge is the double-layer non-semi-infinite gauge. As the name suggests, this gauge type does not depend on a semi-infinite analysis of a substrate to derive heat flux. Examples of this gauge type are found to be similar in construction to the double-layer semi-infinite gauge with the addition of time resolved temperature measurements at the interface between the thin layer of thermal insulation and the substrate. A diagram of a double layer non-semi-infinite gauge is shown in figure 2.7.

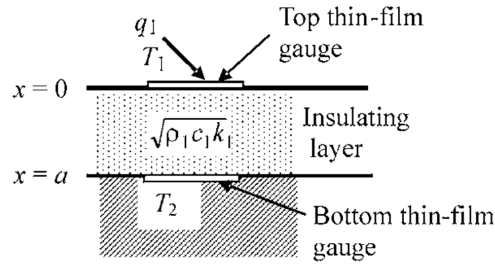


Fig. 2.7 Double layer non-semi-infinite gauge construction [Oldfield, 2008]

The double layer non-semi-infinite gauge enables DC and low frequency heat flux to be measured directly, using knowledge of the measured temperature gradient across the insulating layer, where heat flux is given by equation 2.3 and κ is the thermal conductivity of the insulating layer, and x is the thickness of the layer. Measurement of heat flux is independent of the material properties and topology of the metallic substrate.

$$\dot{q} = \kappa \frac{T_2 - T_1}{x} \quad (2.3)$$

High frequency components of the heat flux, can be determined using semi-analytical models, which use both of the temperature measurements as inputs, and models the thin layer of thermal insulation as homogeneous, with a known thickness and thermal properties. Data reduction methods for this type of gauge were presented by Epstein et al. [1986] and Piccini et al. [2000].

Epstein et al. [1986] used a thin polyimide insulating sheet, with thin-film nickel gauges sputtered on both sides. The sheet was then adhesively bonded onto a metallic NGV. They were able to resolve heat flux frequencies from DC up to 100kHz.

Piccini et al. [2000] used platinum gauges sputtered onto the outside of a polyimide sheet, which was adhesively bonded on to a metal NGV, which had a high thermal conductivity. They used a small number of thermocouples to record the temperature at the interface between the metal substrate and insulating layer. They explained that due to the high thermal conductivity of the substrate, a small number of thermocouples was sufficient to characterise the temperature distribution at the interface. They noted that the use of thermocouples to record the interface temperature, rather than sputtered thin films (as with Epstein et al. [1986]), greatly reduced the complexity of instrumentation. Although Piccini et al. [2000] do not quote a measurement uncertainty, they do provide a series of repeat measurement data, which has a repeatability of $\sim \pm 10\%$.

The double layer non-semi-infinite heat flux gauges provide a significant benefit over both the single and double layer semi-infinite gauges in that their output becomes independent from the substrate topology and material properties. Their spatial measurement resolution is low however, and would likely be insufficient to resolve the film-cooling flows on the FACTOR rig.

2.2.2 Thermo-chromic liquid crystals

Thermochromic liquid crystals (TLCs) are organic molecules which reflect different bands of the electromagnetic spectrum, as a function of their temperature. This can be seen as a dependence of the crystal colour with its temperature. Monitoring the spectral content of reflected radiation from a surface coated with TLCs, with a video camera, therefore provides a means on determining spatially resolved surface temperature. One of the principle advantages of using TLCs is that they enable high spatial resolution temperature measurements [Ireland and Jones, 2000]. A number of the important features of TLCs are now described.

Temperature range and colour play

Ireland and Jones [2000] explained that TLCs have a temperature range, over which they are optically active (the colour play range). While TLCs are at a temperature within their colour play range, it is possible to determine their temperature by spectral analysis of reflected light (within the visible band), which is related to temperature through a calibration. Outside of the colour play range, TLCs are transparent. The narrowest colour play range is approximately 1.0°C and the widest 20 °C. TLCs can be selected based on the absolute temperature at which they are active, which spans between -30°C and 115°C.

Yan and Owen [2002] explained that TLCs with narrower colour play ranges can be used to determine temperature with greater precision. Consequently, it is often desirable to use multiple TLC coatings, with narrow colour play ranges, where each TLC type is optically active at a different temperature. This can increase the range of measurable temperatures, whilst maintaining temperature measurement precision. In the transient measurement technique, at least two measurements of the temperature of a surface undergoing transient convective heating is required (because the underlying equation has two unknowns). The temperature measurements must be taken at different times, and at a time greater than zero (time zero being the start of the transient measurement). Two temperature measurements enables determination of the heat transfer coefficient and adiabatic wall temperature. Yan and Owen [2002] provided the output of an uncertainty model, which describes the optimum

choice of color play temperature range, which will yield the lowest measurement uncertainty in heat transfer coefficient and adiabatic wall temperature in a transient type measurement. In summary, their work concluded that one of the temperature measurements should be taken at the highest non-dimensional temperature rise possible, T_2 , and that the other measurement should be taken at $T_2/2$, for minimum precision uncertainty in h .

Maximum heat flux

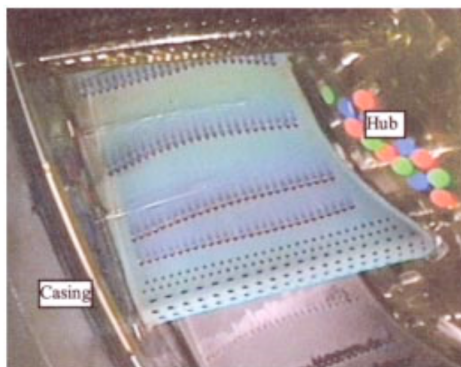
TLCs are usually acquired in an encapsulated form, where the TLCs are contained within a sealed polymeric spherical shell, with a diameter typically between 10 and 20 μm [Ireland and Jones, 1987]. The transparent polymeric shell provides mechanical protection for the crystals, which are otherwise easily damaged. TLC coatings consequently have a minimum thickness equal to the size of the encapsulating shell. According to Ireland and Jones [2000], the thermal conductivity of an encapsulated TLC layer is approximately $0.2 [\text{Wm}^{-1}\text{K}^{-1}]$. Where a steady state heat flux through the crystal layer of $2 \times 10^4 [\text{Wm}^{-2}]$ is present, a temperature drop across the layer of 2°C will exist. The difference between mean crystal temperature and true surface temperature therefore increases with increasing heat flux. Ireland and Jones [2000] recommends that a heat flux of $2 \times 10^4 \text{ Wm}^{-2}$ should not be exceeded, such that sufficient surface temperature measurement accuracy is maintained for accurate evaluation of h and T_{aw} .

Temporal delay

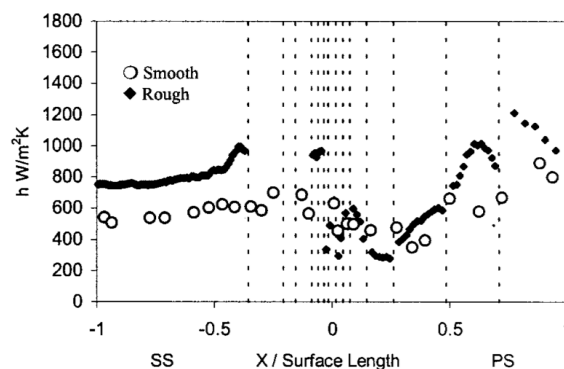
Ireland and Jones [1987] performed a series of experiments where a thin aluminium foil, coated with a $10\mu\text{m}$ thick layer of TLCs was rapidly heated with an electrical current. The time lag between the true foil temperature, and the recorded temperature from the TLCs was determined. Experiments were conducted over a range of linear rates of foil temperature increase, up to a rate of 2600°C/s . They found that there was a consistent temporal lag of $\sim 3\text{ms}$ between the true foil temperature and temperature reading from the TLCs, which was independent of the rate of temperature increase. They highlighted that at higher rates of temperature increase, the constant temporal lag leads to a larger temperature reading error. They also showed that increases in the rate of temperature rise led to a reduction in the intensity of the reflected radiation during the colour play, reducing signal to noise ratios on the image acquisition system.

Surface Roughness

As previously mentioned, the diameter of encapsulated TLCs are typically between 10 and 20 μm . Surfaces coated with encapsulated TLCs consequently have an appreciable surface roughness, of the order of 25 μm Ra [Guo et al., 2000], which can be sufficient to influence boundary layer flow. Guo et al. [2000] performed transient heat transfer measurements on a film-cooled NGV, using both TLCs and thin-film gauges as a means of surface temperature measurement. They found that measurements of heat transfer coefficient with TLCs were approximately 50% higher over large portions of the NGV, when compared to measurements from the thin-film gauges (which had a hydraulically smooth surface). A much smaller variation in the measurement of adiabatic wall temperature was seen. They attributed the larger values of heat transfer coefficient with the TLCs, to the larger roughness level. Their measurements of heat transfer coefficient, at mid-blade-span, are shown in figure 2.8b, where the larger heat transfer coefficients with the TLCs are clear visible. The film-cooled test section NGV, coated with TLCs, is shown in figure 2.8a, where a blue colour reflection is clearly visible.



(a) Film-cooled NGV, coated with TLCs



(b) Heat transfer coefficient measurements on the suction (SS) and pressure surface (PS) of the film-cooled NGV at mid-span. Measurements performed with TLCs (rough) and thin-film gauges (smooth) are shown.

Fig. 2.8 [Guo et al., 2000]

Damage

Ireland and Jones [2000] highlighted that TLCs are susceptible to permanent damage from contamination from organic compounds, and from exposure to UV light, which can destroy the colour play.

Calibration

TLCs can be calibrated by measuring the relationship between surface temperature, and the hue value (i.e. colour composition), of the measured reflected radiation. The reflected radiation is typically measured with a CCD video camera, and the true surface temperature with a series of surface mounted thermocouples.

In order to produce large radiation signals, surfaces coated with TLCs are often illuminated. Guo et al. [2000] explained that the recorded hue value was sensitive to both lighting and camera view angle. They explained that accurate calibration was only possible if done in-situ, under identical lighting and view angle conditions. Calibration was performed by heating the entire test section, to a uniform temperature, where no air flow was supplied from the wind tunnel. The test section was allowed to gradually cool, by natural convection, during which time the relationship between measured hue value and surface temperature was established. Surface temperature was measured with a small number of surface mounted thermocouples. As the hue value was sensitive to view angle, each pixel of the CCD camera was individually calibrated. Calibrations were performed periodically, to eliminate the effect of any degradation of the colour response of the crystals, due to age.

Summary

In summary, TLCs can provide a means of taking high spatial resolution temperature measurements. Their application is limited to temperatures below 120°C, which precludes their use on the FACTOR rig, which operates at significantly higher temperatures. TLCs also appear to need in-situ calibration in order to achieve good measurement accuracy, which may well be impractical on an engine-scale test rig such as FACTOR.

2.2.3 Infra-red thermography

The Basic Principles

Infra-red (IR) thermography is a method of using a measurement of the electro-magnetic radiation emitted from a body, in order to determine its temperature. An important concept in IR thermography is that of a black body: A black body is an hypothetical body which absorbs all incident radiation, at all frequencies. The electromagnetic radiative power of a black body is given by Plank's Law (equation 2.4).

$$L_{\text{bb}}(\lambda, T) = \frac{2h^*c^{*2}}{\lambda^5} \frac{1}{\exp\left(\frac{h^*c^*}{\lambda kT}\right) - 1} \quad (2.4)$$

Where;

- $L_{bb}(\lambda, T)$ is the electromagnetic power radiated per unit area of an emitting black body, in the normal direction, per unit solid angle per unit wavelength. [$\text{Wm}^{-2}\text{Sr}^{-1}$]
- h^* is Planck's constant [$\text{m}^2 \text{kg s}^{-1}$]
- c^* is the speed of light in a vacuum [m s^{-1}]
- k is the Boltzmann constant [$\text{m}^2 \text{kg s}^{-2} \text{K}^{-1}$]
- λ is the wavelength of the electromagnetic radiation [m]
- T is the absolute temperature of the black body [K].

A measurement of radiative power, $L_{bb}(\lambda, T)$, from a black body, over a known spectral range ($\lambda_{\min}, \lambda_{\max}$), can be directly related to the temperature of the body by Planck's law. At ambient temperature, the greatest intensity of radiation from a black-body is emitted in the IR band, hence IR sensitive cameras are commonly used in thermography applications. A series of solutions to equation 2.4 are shown in figure 2.9, at a number of different black body temperatures. It can be seen that between 300 and 500K, the peak radiance occurs between 2 and 15 μm . The approximate locations of the Medium Wave Infra-Red (MWIR) band and the Long Wave Infra-Red (LWIR) are shown.

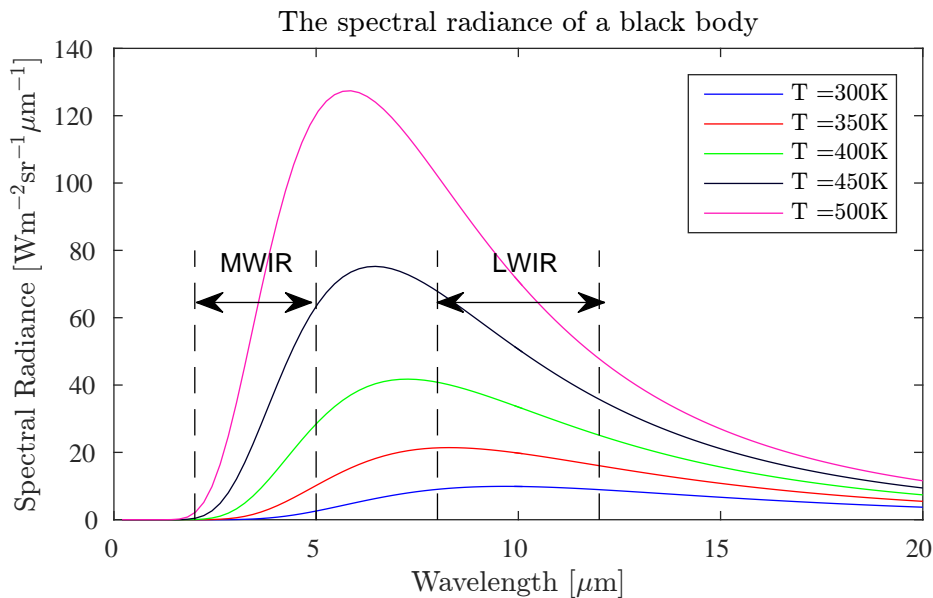


Fig. 2.9 The spectral radiance of a black body at a variety of temperatures

In practice, however, real materials do not behave as black bodies, and hence direct implementation of Planck's law to define the relationship between measured radiance and

body temperature yields errors. The radiative properties of real materials (known as gray bodies), are characterised by the emissivity, $\varepsilon(\lambda, T, \theta)$ (where λ is the wavelength, T is the temperature, and θ is the angle from surface normal). The emissivity specifies the radiance from a gray body, as a proportion of the radiance from a black body at the same temperature. The emissivity is a function of the wavelength of the radiation, the temperature of the body, and the angle of emission from the surface normal (although some materials exhibit low sensitivity of emissivity to these variables).

The absorptivity of a grey body is defined as the radiative power absorbed, as a proportion of that absorbed by a black body under the same conditions (a black body absorbing all radiation). Kirchoff's law of thermal radiation states that the emissivity of a body is equal to the absorptivity. This is necessarily true to satisfy conservation of energy. Consequently, if the emissivity of body is less than one (as with all real materials), then the absorptivity is also less than one, and a portion of incident radiation arriving at the surface of a gray body will be reflected.

An IR detector measuring the radiance from the surface of a gray body, will therefore be receiving both emitted and reflected radiation. If air, or some other transparent medium, with non-zero emissivity, is present between the surface and the detector, the radiation will be both attenuated and contributed to by the transparent medium. In practice, therefore, calibration procedures are needed to accurately determine the surface temperature of a gray body from measurements of surface radiance [Martiny et al., 1997].

Calibration methods

A number of different calibration approaches have been employed in the literature. All of the methods reviewed make use of a small number of surface mounted thermocouples to relate surface temperature to IR detector reading. Furthermore, all of the infra-red thermography methods reviewed make use a high emissivity black paint, applied to the test surface (where the emissivity is typically between ~ 0.93 and 0.97). The use of a high emissivity coating reduces the magnitude of reflected radiation terms, which can be challenging to quantify. In all of the reviewed heat transfer measurement articles, which employ IR thermography, an IR transparent window is used to gain optical access to the test section within the wind tunnel - the influence of which also requires calibration.

A common calibration method, which was used by O'Dowd et al. [2010], Ma et al. [2015] and Luque et al. [2015], is to directly determine the relationship between the IR detector reading, and the temperature from a surface mounted thermocouple. The calibration is performed in-situ, where the thermocouple is mounted on the test object surface, and the

IR camera takes a reading from a location on the surface close to the thermocouple, through the IR window. The temperature of the test object is then gradually changed, across the full temperature range relevant to the measurement, such that a full calibration function can be determined. The rig configuration during the calibration process is kept the same as the configuration during the heat transfer measurements - this ensures a number of parameters remain constant, such as the camera view angle and the distance between the IR camera and the test surface. An example of the calibration function determined by O'Dowd et al. [2010] is shown in figure 2.10. They observed an approximately linear relationship between object temperature and IR camera output value (most likely because their camera contained an internal linearising calibration function).

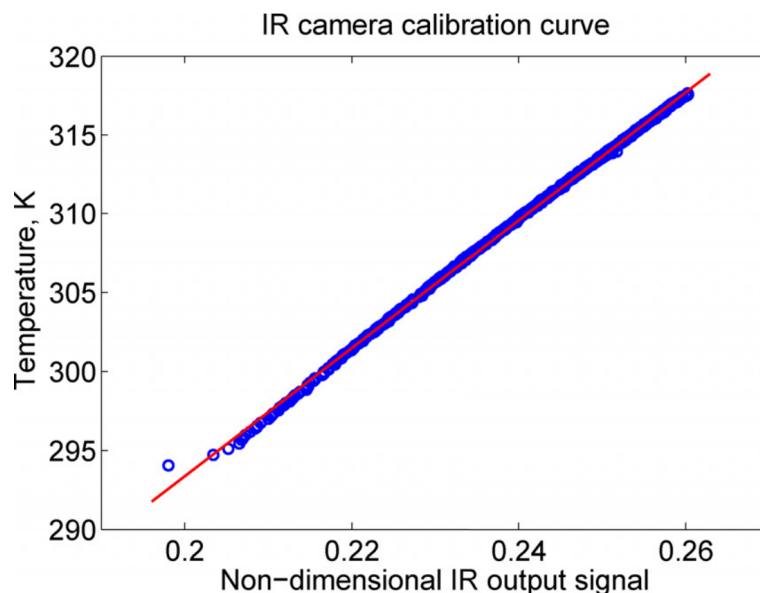


Fig. 2.10 Linear IR camera calibration function [O'Dowd et al., 2010]

O'Dowd et al. [2010]'s calibration was performed in pseudo-steady-state, where the test object was heated, and then allowed to gradually cool by natural convection. During the cool down, calibration points were taken at regular intervals. The low rate of cooling ensured that only small temperature gradients were present on the object surface. This ensured that the small number of surface thermocouples provided an accurate evaluation of the surface temperature. The calibration method assumes, however, that the transmissive properties of the air and optical access window do not change when the rig is operating with airflow, which may be at a substantially different temperature. It also does not account for the change in ambient or internal reflection intensity which will occur if nearby rig components operate at different temperatures.

Martiny et al. [1997] employed a semi-analytical calibration method, where a non-linear calibration function was defined, which modelled the dominant components of the underlying radiation physics. The function included three coefficients, which could be adjusted. An in-situ calibration was performed, between a surface mounted thermocouple and the IR camera detector. The calibration points were then used to determine the values of the three function coefficients, using a numerical error-minimisation approach. Because this method models the underlying radiation physics, an improved extrapolation accuracy may be achieved between calibration points. However, this improvement is dependant on the underlying physics being correctly modelled, and makes the assumption that the IR camera output is linearly proportional to radiance - which it may not be.

Ekkad et al. [2004] also employed a semi-analytical calibration method. They used measurements of the ambient relative humidity, background temperature and the distance between the test surface and the detector, to approximately quantify the radiation emission and absorption terms from the atmosphere. The analytical model used was not presented. Adjustments to the assumed surface emissivity were then made, in-situ, until the IR camera reading matched that of a surface mounted thermocouple. The method by which the influence of the optical access window is accounted for, is not described, (or not performed).

Ochs et al. [2009] presented a two part calibration process, which makes use of a semi-analytical calibration function, with four calibration parameters. Some of the calibration parameters are calibrated in-situ, and others are calibrated off-line. They describe that the necessary calibration procedure depends on the transmission characteristics of the transparent mediums (which are usually air and the optical access window) and the emissivity of the emitting surface. They highlighted three possible scenarios: 1) Where the transmissivity of the transparent medium, and/or the emissivity of the emitting surface, are not a function of temperature. 2) Where the transmissivity and/or emissivity are a function of temperature, but not a function of wavelength (over the sensitive spectral range of the IR detector). 3) Where the transmissivity and/or emissivity are a function of both medium temperature and wavelength. Depending on which scenario the optical set-up falls under, affects which parameters of their semi-analytical function need to be calibrated in-situ, and which can be calibrated off-line, (i.e. under better controlled conditions). They highlight that the most desirable case is the first scenario. In the first scenario the 'gain' of the optical path is independent of both the test surface and transparent medium temperature. Consequently, only offset terms, from ambient reflections need in-situ correction. The gain of the optical path can then be measured off-line, using, for instance, an accurate black-body radiation source. In the first scenario, only one of the four calibration function parameters need calibrating in-situ. In

the third scenario, all of their four calibration function parameters require calibration in-situ. It is apparent from the work of Ochs et al. [2009] that, if possible, the IR measurement set-up should be designed to fall under the first scenario for minimum temperature measurement uncertainty.

Optical access

A range of different materials have been used as IR transparent windows, providing optical access to wind tunnels. The windows are usually arranged such that they form part of the wind tunnel enclosure. Martiny et al. [1997], Martini et al. [2005] and Ochs et al. [2009] used a Sapphire window. Sapphire has a high transmissivity only in the short and medium-wave IR band (0.75 - 5 μm), and consequentially can only be used effectively with short and medium wave IR cameras (or wide band cameras combined with filters). The high hardness and durability of Sapphire is a significant attribute. Sapphire windows are usually supplied with anti-reflective coatings, however the authors above do not mention the use of coatings.

Ekkad et al. [2004] used a Calcium Fluoride window, which has good transmissivity in the short and medium-wave IR band, and extends to some degree into the long-wave IR band, where transmissivity drops off above $\sim 8 \mu\text{m}$. Due to its low index of refraction, it can be used without an anti-reflective coating.

O'Dowd et al. [2010], Luque et al. [2015] and Ma et al. [2015] all used a Zinc Selenide window, which has excellent transmissivity in the short, medium and long wave IR band, where the transmissivity drops off above 15 μm . Zinc Selenide windows require anti-reflective coatings to achieve their high transmissivity. It is also one of the softest commonly used IR windows, and so it damages easily.

Najafabadi et al. [2015] used a Silicone window with a high transmissivity in the short and medium-wave IR band, with high transmissivity up to $\sim 6 \mu\text{m}$. Silicone windows are hard, tough and have a low density. However, they do not transmit visible wavelength of light.

IR Cameras

In recent years commercial IR camera technology has advanced significantly, becoming both more affordable and more capable - this is likely the reason for the recent increase in their use in turbomachinery research. The main advantage of IR thermography, over other temperature measurement methods, is that it can be used to take measurements over a wide temperature range (-20 to +1500°C Ekkad et al. [2004]), can offer high spatial resolution

($\sim 3 \times 10^5$ pixels [Najafabadi et al., 2015]), whilst being non-intrusive. There are two main types of IR detector which are commonly used: Microbolometers and Photo-detectors.

Within a Microbolometer, infrared radiation arrives at the detector pixels, which causes a local increase in the detector temperature. This increase in temperature leads to a change in the electrical resistance of the detector material. The change in electrical resistance is then measured and related to incident radiation intensity (and subsequently temperature). The detector usually consists of a matrix of microbolometers, allowing a spatially resolved image to be formed.

- O'Dowd et al. [2010] used a FLIR A20 Microbolometer IR camera, with a sensitive spectral range of 7.5-12 μm , a resolution of 160x120 pixels, a full frame acquisition frequency of 30Hz, and NET¹ of 120mK.
- Ma et al. [2015] used a FLIR A325 Microbolometer IR camera, with a sensitive spectral range of 7.5-13 μm , a resolution of 320x340 pixels, a full frame acquisition frequency of 60Hz, and an NET of 50mK.

Photo-detector type IR cameras consist of a series of sensors within which low energy state electrons are contained. When an incident photon arrives, which has an appropriate energy, an electron within the sensor is excited to a higher energy state. When at the higher state, the electron is able to move, and there by conduct electricity, doing so under the influence of a driving voltage potential. The incident radiation thereby allows a current to flow, which can be measured and related to the incident radiation. Photo-detectors require cooling in order to function - which is often provided by an integrated Stirling heat pump. Operating detector temperature of $\sim 70\text{K}$ are common. Photo-detectors typically have a lower NET than microbolometers, but are more expensive.

- Ekkad et al. [2004] used a FLIR ThermaCAM SC3000 Photo-detector IR camera, with a sensitive spectral range of 8-9 μm , a resolution of 320x240 pixels, a full frame acquisition frequency of 60Hz and a thermal sensitivity of 20mK.
- Martini et al. [2005] used a THERMOVISION 900 by Agema Photo-detector IR camera, with a sensitive spectral range of 8-12 μm , a resolution of 136x270 pixels, a full frame acquisition frequency of 20Hz and a thermal sensitivity of 80mK.

¹NET (Noise equivalent temperature), is the value of a signal temperature variation which would match the noise of the camera - as some reference condition

-
- Najafabadi et al. [2015] used a FLIR Cedip Titanium 560M Photo-detector IR camera, with a sensitive spectral range of 3.5-5.1 μm , a resolution of 640x512 pixels and a full frame acquisition frequency of 5Hz.

2.2.4 Summary of measurement instrumentation

Three temperature measurement instruments and associated methods, used within the turbo machinery research community were reviewed: The use of thin-film resistance gauges, TLCs and IR cameras.

Thin-film resistance gauges offer the highest temporal resolution, with bandwidths up to 100kHz. This makes them particularly suitable for measurements on short duration wind tunnels, and where unsteady heat transfer measurement are of interest. Double layer gauges can be constructed, which enable a direct measurement of heat flux. This is particularly beneficial when instrumenting metallic blades, or thin-walled sections of blades, where the semi-infinite assumption cannot be made. The main drawback with thin-film gauges is the low gauge spatial density which is achieved, which is limited by the need to lead-out relatively large electrical connections. The large number of electrical connections also limits their use in rotating rigs, due to the limited number of channels on telemetry systems. Stick-on gauges can also only be apply with ease to surfaces with Gaussian curvature equal to zero - which is not the case for the FACTOR vanes and blades.

TLCs offer high spatial resolution. They can be used with ease on surfaces with non-zero Gaussian curvature. The temporal band width is limited by the temporal lag which TLCs exhibit ($\sim 3\text{ms}$ [Ireland and Jones, 1987]). The sample frequency may be limited by the video image acquisition system. The accuracy of TLCs is particularly sensitive to the calibration, where changes in view angle and illumination can affect accuracy significantly. Full in-situ calibrations are required, which may be impractical on an engine-scale turbine rig. TLCs have a limited active temperature range (between 1 and 20K), which can present problems on rigs with large temperature variations. An increase in the effective temperature range can be achieved by using multiple types of TLC which are active at different temperatures. TLC are also limited by a maximum working temperature of 115 $^{\circ}\text{C}$ and a maximum heat flux of $\sim 2 \times 10^4 \text{ Wm}^{-2}$ [Ireland et al., 1999], which can cause problems in high speed flow applications, with high heat transfer coefficients.

IR thermography also offers high spatial resolution (typically around 1×10^5 pixels). Temporal resolution for full frame images varies between different cameras, but typically lies between 5 and 200Hz. (With some IR cameras, an increase in the imaging frequency can

be achieved by reducing the spatial resolution). IR cameras can be used on surfaces with non-zero Gaussian curvature, and when appropriate substrate materials or surface coatings are used, exhibit a low sensitivity to view angle. Temperatures can be measured over a wide range (-30 to 1500° C). Calibration procedures with IR cameras can be complicated, and high performance IR cameras, along with IR transparent optical access windows can be costly.

The measurements on the FACTOR rig will require temperature measurement up to 230°C, and will also require high spatial measurement resolution, in order to resolve film-cooling flows and combustion hot-spot migration. It will be discussed in section 3.1 in detail why IR thermography was selected for the FACTOR temperature measurements.

2.3 Review of Steady State Measurement Techniques

Steady state heat transfer measurement techniques are measurements which are taken on rigs which are at steady-state operating conditions - where aerodynamic conditions and temperatures are constant in time (neglecting high frequency fluctuations). The most commonly used steady state measurement techniques are presented in this section.

Steady wall temperature measurements

The simplest form of steady state measurement is one which only provides measurements of steady wall temperature. Schultz [2000] performed steady state measurements of wall temperature, on an effusion cooled combustor liner section, using IR thermography. They assumed that the steady state wall temperature measurements were approximately equal to the adiabatic wall temperature, T_{aw} . A film-cooling effectiveness, η , was defined from the surface temperature measurements, which is a non-dimensional parameter commonly used to characterise the performance of film-cooling flows. The expression for film-cooling effectiveness is given in equation 2.5. Where a film-cooling effectiveness of one, indicates that the wall temperature is at the coolant temperature. An effectiveness of zero, indicates a complete absence of film-cooling, where the wall temperature is at the mainstream fluid temperature. The mainstream fluid temperature, far from the wall, is $T_{0,\infty}$. Similar measurements were performed by Sweeney and Rhodes [1999], where in both cases, measurements were performed on state-state wind tunnels, where steady state aerodynamic and thermal conditions were established prior to measurement.

$$\eta = \frac{T_{wall} - T_{0,\infty}}{T_{coolant} - T_{0,\infty}} \quad (2.5)$$

Luque and Povey [2010] performed steady state measurements of wall temperature on a film-cooled NGV, in a short-duration wind-tunnel. Short-duration wind tunnels are wind tunnels which can only operate for limited periods of time, due to their use of air stored in high pressure tanks, rather than continuously running pumps or fans to provide the air flow. Luque and Povey [2010] argued that state thermal conditions were established prior to the measurement, within the 30s run time of the facility. Measured wall temperature was assumed to be approximately adiabatic, from which adiabatic film-cooling effectiveness was defined - although justification for this assumption was not provided.

Baldauf et al. [1999] performed steady state measurements of wall temperature, on a film-cooled flat plate - using a steady state wind-tunnel. They performed a correction of the wall temperature measurements, in order to better estimate the true adiabatic wall temperature, particularly in close proximity to the cooling holes. They achieved this with the use of a finite-element numerical model, which was used to estimate the three-dimensional steady-state heat flux within the flat plate. The computed heat flux was used in conjunction with knowledge of the thermal conductivity of the plate material to determine the steady state temperature difference between the measured wall temperature and the adiabatic wall temperature - allowing the adiabatic temperature to be defined. A complete set of boundary conditions for the numerical model was determined by using flat plate forced convection correlations for the heat transfer coefficient on the external wall, and pipe flow convection correlations for the inside surface of the cooling holes. The correlation for the external flat plate flow did not account for the presence of the film-cooling flows. Boundary conditions on the back surface of the flat plate were provided by a small number of discrete thermocouples. Baldauf et al. [1999] argued that the use of heat transfer coefficient correlations, which provide an approximate solution, was sufficiently accurate, as the difference between the measured wall temperature and adiabatic wall temperature was small. An image of a section through the finite element computational domain is shown in figure 2.11, and an example of the adiabatic film-cooling effectiveness measurements, for a single cylindrical cooling hole, are shown in figure 2.11. The correction varied in magnitude, depending on the local magnitude of lateral heat flux values. Lateral heat flux values may be large in some regions on the FACTOR vanes and blades, due to their small geometric scale. Consequently, 3D heat flux modelling as shown here may be beneficial.

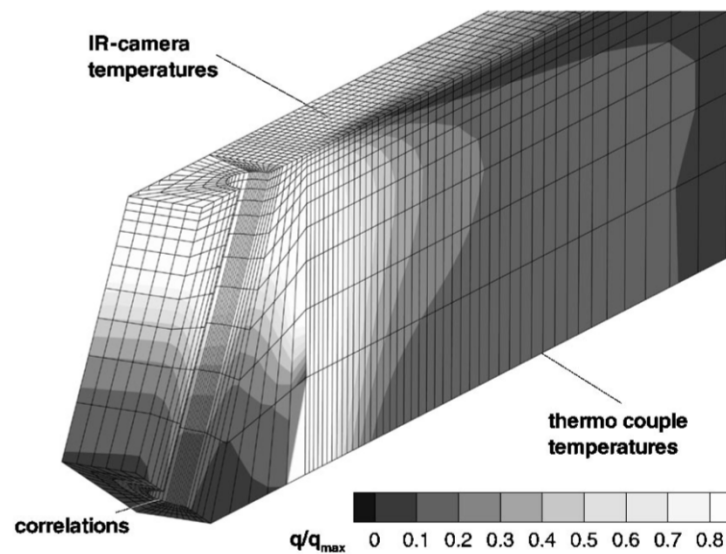


Fig. 2.11 Image of the computational domain around a single film-cooling hole [Baldauf et al., 1999]

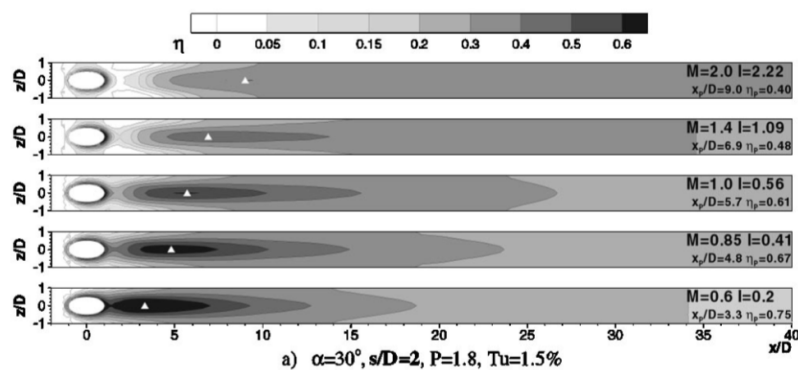


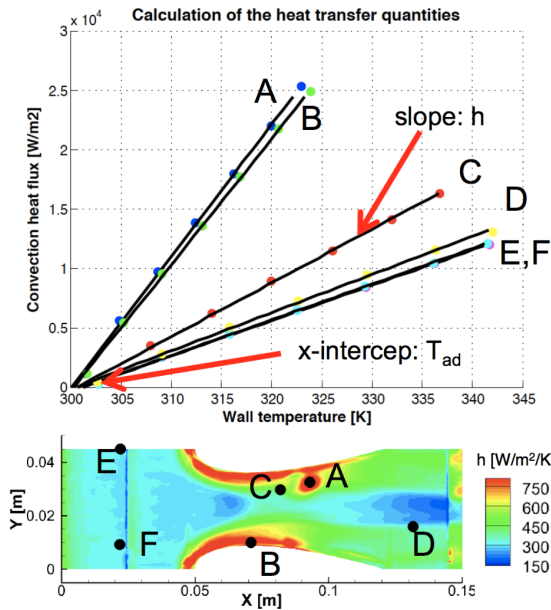
Fig. 2.12 High resolution measurements of film-cooling effectiveness, in regions of high lateral heat flux Baldauf et al. [1999]

Steady measurements of heat transfer coefficient and adiabatic temperature

Measurements of heat transfer coefficient *and* adiabatic wall temperature can be performed with steady state measurement techniques. Laveau et al. [2012] used an iso-thermal back-plate technique, with IR thermography. In this technique, a high thermal conductivity plate, made from copper, was covered with a thin thermally insulating polymer layer, 0.12mm thick. The insulating layer was attached to the copper back-plate with an adhesive sheet and the external surface of the insulating layer was painted with a black paint to increase the

surface emissivity - forming a three-layer substrate. The external surface of the three-layer substrate formed the gas-washed surface of a contoured NGV endwall. A free stream air flow, at a temperature higher than the thermally massive copper back-plate, supplied by a steady state wind tunnel, caused a heat flux from the air, into the three-layer substrate. A temperature difference was consequently established across the insulating layer. Due to the high thermal conductivity of the copper back-plate, its temperature was assumed uniform, and was measured with a thermocouple at one location. The temperature distribution on the external surface of the three-layer substrate was measured by means of IR thermography. With knowledge of the spatially resolved temperature difference across the three-layer coating, as well as the thickness and thermal conductivity of each of the layers in the coating, the spatial distribution of heat flux was evaluated using Fourier's law of conduction. The temperature of the copper back-plate was maintained at a steady state value with a PID controlled heating element.

A series of measurements were performed, where the temperature of the copper back-plate was established at a variety of different steady state temperatures. The heat transfer coefficient and adiabatic wall temperature, at each spatial location on the endwall, were evaluated by a linear regression of the heat-flux and wall temperature from each measurement, at each spatial location. The gradient of the regression function is equal to the heat transfer coefficient, and the value of the function, at a heat flux value of zero, is equal to the adiabatic temperature. An example of the linear regression and the computed values of heat transfer coefficient are shown in figure 2.13a, and a photograph of the rig is shown in figure 2.13b.



(a) Linear regression of heat flux and wall temperature to find h and T_{ad}



(b) Photograph of the insulating layer on the copper back plate (before the addition of black paint)

Fig. 2.13 [Laveau et al., 2012]

The technique is capable of providing high resolution measurements, which is limited, either by the thickness of the insulating layer (0.12mm), or the resolution of the IR camera. Laveau et al. [2012] estimated that the measurements of heat transfer coefficient had a relatively high uncertainty, of $\pm 13\%$ - with a 95% confidence level. The dominant source of measurement uncertainty was from uncertainty in the combined thermal conductance of the three-layer coating, caused by uncertainties in their thickness and thermal conductivities. They also observed problems with trapped air-pockets between the insulating layer and the copper plate - which created large local errors.

Laveau et al. [2015] used a similar measurement technique to Laveau et al. [2012], but used an in-situ calibration procedure, which measured the local thermal conductance of the three-layer coating - thereby reducing one of the dominant sources of measurement uncertainty. The calibration was performed using a laser mounted on a robotic arm, which focused a pulsed heat source at each measurement location. The surface temperature response was used to infer the thermal conductance. A lower measurement uncertainty of $\pm 9.5\%$ was calculated.

Giel et al. [2004] and Boyle et al. [2000] used an alternative steady state measurement technique, where a thin metallic foil was bonded onto the external surface of an NGV. The NGV was made from an electrical and thermal insulator. The NGV was assembled into a

steady state wind-tunnel, and an electrical current was passed through the metallic foil, such that heat was generated within the foil, as a result of its electrical resistance. Due to the low thermal conductivity of the NGV material, it was assumed that at thermal steady state, the heat generation rate at any given location on the foil, was equal to the rate of heat loss caused by a combination of convective cooling from the wind-tunnel air flow, and radiative heat loss. (i.e it was assumed that no heat was lost by conduction into the NGV.) Giel et al. [2004] performed measurements at low Reynolds numbers, leading to low convective heat transfer coefficients. Consequently the radiative heat loss constituted a relatively high proportion of the total heat loss (8.8 % at the lowest Reynolds number and 1.3% at the highest). By estimating the magnitude of the radiative heat loss, they were able to deduce the heat loss by convective cooling as the heat generation rate from the foil, minus the radiative heat loss. The total heat generation rate within the foil was calculated as the product of the voltage drop across, and the electrical current through the foil. The heat generation rate per unit area was assumed to be uniform, despite the dependence of local electrical resistance with local foil temperature. Temperature measurements of the NGV surface were taken with TLCs [Giel et al., 2004] and IR thermography [Boyle et al., 2000]. The heat transfer coefficient was then defined as the ratio of the local heat loss by convection, \dot{q}_{conv} and the difference between the measured wall temperature, T_{wall} , and the adiabatic wall temperature, T_{aw} - as indicated by equation 2.6. The adiabatic wall temperatures were derived from CFD calculations, and were not measured.

$$h = \frac{\dot{q}_{\text{conv}}}{T_{\text{wall}} - T_{\text{aw}}} \quad (2.6)$$

Giel et al. [2004] and Boyle et al. [2000] estimated somewhat different uncertainties in their measured values of heat transfer coefficient, of $\pm 8.2\%$ and $\pm 15\%$ respectively. Boyle et al. [2000] highlighted that a significant contribution to the uncertainty was caused by the low maximum service temperature of the thermally insulating substrate used from the NGV (+80 °C): The power delivered to the foil was set to a value such that the highest temperature of the foil was that of the maximum service temperature of the substrate - which occurred in a region with low heat transfer coefficient. The consequent limitations on the heating power resulted in poor sensitivity of the foil temperature, with heat transfer coefficient, in regions of high heat transfer coefficient - leading to large measurement uncertainties. Giel et al. [2004], on the other hand, explained that the dominant source of uncertainty in their measurements stemmed from uncertainty in the area average heat generation rate from the thin foil. This was caused by uncertainties in the area of the foil, and in the measurements of voltage and current. This measurement technique is unlikely to be suitable for the FACTOR

measurements, as T_{aw} will be an unknown, and the presence of film-cooling holes would make the uniform heat generate rate assumption with the foil invalid.

2.4 Review of Transient Measurement Techniques

Transient heat transfer measurement techniques are ones which derive heat transfer quantities from measurements of the dynamic response of a system to an input. In the measurement of convective heat transfer in turbomachinery applications, a transient system response is commonly achieved by generating a rapid change in the fluid temperature flowing past the object being measured. The increase in fluid temperature causes the object to also rise in temperature, where the transient response of the object temperature is a function of the convective heat transfer coefficient (among other things). Measurements of the transient temperature response of the object can then be used to derived either time averaged or time-resolved quantities of interest - such as the heat flux, heat transfer coefficient and adiabatic wall temperature. Typically, a time-resolved surface heat flux will first be calculated from the transient surface temperature measurement. Linear regression of the surface heat-flux and surface temperature can then yield time averaged values of h and T_{aw} . Phase averaging methods can also be used. (A more detailed explanation of the transient measurement technique is provided in section 3.3).

Transient measurement techniques are particularly well suited to short-duration wind tunnels, which typically have short maximum run times of the order of one second. In short duration facilities, steady state thermal conditions are often not reached within the run duration, thereby making steady state heat transfer measurement techniques inappropriate. Short duration wind tunnels also typically provide a step change in temperature, as an inherent aspect of their operation. The step change is caused by the sudden compression of the working fluid when the tunnel is activated. This step change initiates the transient measurement. In steady state wind tunnels, the step change in fluid temperature required for the transient measurement techniques has been achieved through two methods: By using fast switching valves, which can pass a heated air flow to, or away from the test section (Du et al. [1998]), and with DC powered electrical heater-meshes, which can rapidly heat upstream flows (Ireland et al. [1999] and Luque et al. [2015]).

2.4.1 Direct fitting to analytical semi-infinite solutions

A common method of determining the heat transfer coefficient and adiabatic wall temperature by transient measurement, is to make use of an analytical solution to the one dimensional heat equation. The heat equation describes transient conduction within a body.

An exact solution to the heat equation exists, for a semi-infinite one-dimensional body, under steady convective heating at its surface, where a step change in adiabatic wall temperature is applied. The solution describes the evolution of the temperature of the body, as a function of the material properties of the body, the constant heat transfer coefficient and the adiabatic wall temperature before (T_i) and after (T_{aw}) the step change. The analytical solution is shown in equation 2.7, and its derivation, from the heat equation, was presented by Schultz and Jones [1973]. (Note that a detailed description of one-dimensional semi-infinite conduction theory is described in Chapter 3)

$$\frac{T(t) - T_i}{T_{aw} - T_i} = 1 - \exp(\beta^2)\text{erfc}(\beta) \quad (2.7)$$

where;

$$\beta = \frac{h\sqrt{t}}{e} \quad (2.8)$$

Schultz and Jones [1973] explained that if the body material property, $e = \sqrt{\rho c \kappa}$, the transient wall temperature $T(t)$ and the initial wall temperature T_i are known. Then there remains only two unknowns in equation 2.7; h and T_{aw} - the heat transfer coefficient and the adiabatic wall temperature. A solution to h and T_{aw} can therefore be found by a solution of two simultaneous equations, where at least two values of surface temperature, $T(0, t)$ are required, where $t > 0$. Equally, if the adiabatic wall temperature is known, or estimated, then the heat transfer coefficient can be deduced from just one measurement of $T(0, t)$, where $t > 0$.

Note that on test rigs with film-cooling flows the adiabatic wall temperature will vary greatly over the surface of the blade/vane, and will likely be an unknown.

This method, of using one or two transient wall temperature measurements to determine h and T_{aw} is particularly appropriate where only low temporal resolution measurements of wall temperature are available, as only a small number of wall temperature measurements are required. [Clifford et al., 1980] employed this method, and used a surface coating with well defined phase transition temperature as a means of providing a single, spatially resolved measurement of wall temperature during the transient response. Najafabadi et al. [2015] used

the method in conjunction with IR thermography, to measure heat transfer coefficients and film-cooling effectiveness on a film-cooled NGV.

Schultz and Jones [1973] explained that the validity of this method depends on a number of conditions being satisfied, namely;

1. That the initial temperature and the medium is uniform
2. That the change in fluid temperature is a true step change
3. That the heat transfer coefficient and adiabatic temperature are time-independent, after the step change in temperature.
4. That the medium can be considered semi-infinite. This usually involves limiting the duration of the transient measurement, such that the heat penetration depth is less than the thickness of the substrate.

It is important to note that at least item 1 and 2 will likely not be satisfied on an engine-scale test rig.

In reality, the semi-infinite concept is a notional one, as a small temperature rise will occur through the entire medium, propagating almost instantaneously. Instead, a time limit is established, which limits the temperature rise on the back surface of the substrate to a negligible value. An expression for the time limit, t_{limit} , is given by equation 2.9, where δ is the thickness of the substrate, α is the thermal diffusivity ($\kappa/\rho c$) and Fo_{limit} is the non-dimensional Fourier number (representing a non-dimensional time).

$$t_{\text{limit}} = \text{Fo}_{\text{limit}} \frac{\delta^2}{\alpha} \quad (2.9)$$

Schultz and Jones [1973] defined the maximum value of Fo_{limit} to be 0.1, at which point the temperature of the back surface of the substrate will not have raised by more than 1% of the magnitude of the temperature step. They state that if the Fo_{limit} number does not exceed this value, then the substrate may adequately be considered semi-infinite. Iliopoulou et al. [2004] specified a more conservative value of 0.075, and Najafabadi et al. [2015] and Luque et al. [2015] specified yet more conservative values of 0.0625.

One of the main drawbacks with the data reduction approach described by Schultz and Jones [1973], is that its accuracy depends on the change in the fluid temperature being a step change - which is invariably an approximation of the truth. Metzger et al. [1991] accounted for the presence of non-instantaneous temperature rises in the mainstream flow, by expressing the surface temperature response, to a non-instantaneous temperature step,

as a summation of elemental true step responses. This mathematical method is known as Duhammel's supersposition integral, and is applicable, due to the heat equation being linear. Gillespie [1996] argued that mainstream temperature rise functions will be typically well represented by exponential functions with a negative exponent. An exact analytical solution to the one-dimensional heat equation, for a semi-infinite body, exposed to an exponential rise (with negative exponent) in fluid temperature was presented. Both of these methods were able to reduce measurement errors caused by non-instantaneous temperature steps, however they require the additional knowledge of the mainstream temperature rise time constant, which needs to be measured.

2.4.2 Heat flux reconstruction methods

More recently, it has become common to derive the time resolved wall heat flux from transient wall temperature measurements, as an intermediate step to determining the heat transfer coefficient and adiabatic wall temperature. In this method, transient wall temperatures are not directly fitted to an analytical solution. In order to derive the time resolved heat flux, **high temporal resolution** wall temperature measurements are required, which accurately resolve the wall temperature evolution through the whole transient measurement. This has become increasingly feasible with improvements in instrumentation technology, such as the use of high sample frequency thin-film temperature gauges, wide band TLCs and IR thermography. Calculation of time resolved heat-flux from high sample frequency wall temperature measurements requires significantly more computational power than the methods described in section 2.4.1, and hence have also been enabled by the reduction in the cost of computing power [Oldfield, 2008], and by advances in data reduction methods.

By directly deriving the time resolved heat flux, it becomes possible to determine unsteady heat transfer rates, and the influence of non-instantaneous mainstream temperature steps can easily be accounted for, without necessarily measuring the mainstream temperature rise time constant.

Deriving heat flux with the impulse response method

Oldfield [2008] developed a computationally efficient method of deriving time resolved heat flux from transient wall temperature measurements, using a convolution integral method. The heat flux is first described as a convolution of the wall temperature, $T(t)$, and an impulse response function $h(t)$.

$$\dot{q}(t) = h(t) * T(t) = \int_{-\infty}^{\infty} h(\tau) T(t - \tau) d\tau \quad (2.10)$$

The convolution integral is then replaced by a discrete convolution sum - which enables manipulation of discrete measurement data. The summation is also limited to the range $n > 0$, as all signals are zero prior to the start of the measurement.

$$\dot{q}[n] = h[n] * T[n] = \sum_{k=0}^{N-1} h[k] T[n-k] = \sum_{k=0}^{N-1} h[n-k] T[k] \quad (2.11)$$

$$\text{for } k = 0, 1, 2, \dots, N-1$$

If the impulse response function, $h[n]$ can be found, then the discrete heat flux values, $\dot{q}[n]$, can be found by convolution of the wall temperature measurements, $T[n]$ with the impulse response function.

Oldfield [2008] describes a method by which $h[n]$ can be found. The method uses a pair of analytical solutions to the heat equation, of wall temperature and heat flux, which are termed the basis functions. Commonly, an appropriate pair of basis functions is the parabolic response of a one-dimensional semi-infinite body to a step in heat flux imposed at its surface. With knowledge of a matching pair of wall temperature and heat flux values, for the given one-dimensional semi-infinite system, the impulse response function $h[n]$ can be found using Z-transforms - the full details of which are described in the article.

The method enables computationally efficient evaluation of the heat flux from large data sets of wall temperature measurements. The numerical accuracy of the method is high, quoted better than $\pm 1 \times 10^{-14}$ normalised error [Oldfield, 2008]. It is important to note that this method is only possible when a pair of basis functions exists for the system under analysis - this tends not to be the case when complications, such as temperature dependant material properties, and three-dimensional geometry affects are included - which may preclude its use in the FACTOR rig.

The impulse response data reduction method has been used numerous times, in the analysis of thin-film gauge and IR thermography measurements, by, for example Collins et al. [2015] and Luque et al. [2015].

Deriving heat flux with numerical methods

Numerical approaches to determining heat flux, which make use of finite-difference or finite-element methods have also been popular. Iliopoulou et al. [2004] used a one-dimensional finite difference model, based on a semi-implicit Crank-Nicolson scheme to numerically

evaluate transient heat flux from transient wall temperature measurements. Clustering of the discretisation grid close to wall surface was used in order to efficiently resolve regions with high second derivatives of temperature in space. The semi-infinite assumption was also assumed far from the surface to limit the extent of the domain.

Bertolazzi et al. [2012] investigated the performance of two finite element numerical schemes in determining transient heat flux from artificially generated transient wall temperature measurements; one explicit in time and one semi-implicit in time. They found that both finite element techniques, particularly the implicit scheme were significantly more capable in accurately resolving time varying heat flux values than the early numerical transform methods described by Cook and Felderman [1966]. They highlighted additional potential benefits that finite element methods can provide over some other data reduction techniques; that temperature dependant material properties and multi-layer substrates can be easily be modelled, and that modelling non-semi-infinite substrates is enabled. These benefits are particularly beneficial for engine-scale test rigs

O'Dowd et al. [2010] compared a number of different transient heat transfer measurement techniques and data reduction methods: A direct fitting approach, to the one-dimensional semi-infinite analytical solution to a step (described in section 2.4.1), as well as two data reduction methods where the heat transfer was determined by linear regression of transient heat flux and wall temperature were investigated. Identical transient wall temperature measurements were used for each data reduction method. Transient heat flux was determined by both the impulse response method and a one-dimensional finite difference numerical method. They found that data reduction methods by linear regression of transient heat flux and wall temperature, yielded a lower measurement uncertainty than a direct fitting to the analytical solution. The finite difference model used, being one-dimensional and semi-infinite, yielded no benefit over the impulse response method. The impulse response method being computationally more efficient, was consequently deemed superior.

Evaluating the heat transfer coefficient and adiabatic wall temperature

With measurements of transient wall temperature, and derived values of transient heat flux, the heat transfer coefficient and adiabatic wall temperature can be determined. Several methods have been employed to achieve this.

Didier et al. [2002] and Iliopoulou et al. [2004] made the assumption that the free-stream gas total temperature was appropriately equal to the adiabatic wall temperature of the test object. They defined an expression for the time varying heat transfer coefficient, given in equation 2.12. This assumption fails to account for the difference in free stream

total temperature and adiabatic wall temperature which exists, characterised by the thermal recovery factor, described by Schlichting [1979]. This method, however, is well suited when only a comparison of relative heat transfer coefficients is required, between, for example, measurement at different spatial locations. It should also be noted that this method will lead to significant errors where film-cooling, high Mach number flows, or combustion hot-spots are present, as $T_{0,\infty}$ no longer becomes representative of T_{aw}

$$h(t) = \frac{\dot{q}_{wall}(t)}{T_{0,\infty} - T_{wall}(t)} \quad (2.12)$$

O'Dowd et al. [2010] and Luque et al. [2015] used a linear regression method to determine both the heat transfer coefficient and the adiabatic wall temperature. A linear function was fitted to corresponding values of heat flux and wall temperature, where the gradient of the regression function represents the time averaged heat transfer coefficient. The linear regression function is then extrapolated to a heat flux value of zero, representing the adiabatic case, and the corresponding temperature was given as the adiabatic temperature. An example of the linear regression function from Luque et al. [2015] is shown in figure 2.14a, and their measurements of Nusselt number (non-dimensional heat transfer coefficient) from an un-cooled NGV are shown in figure 2.14b.

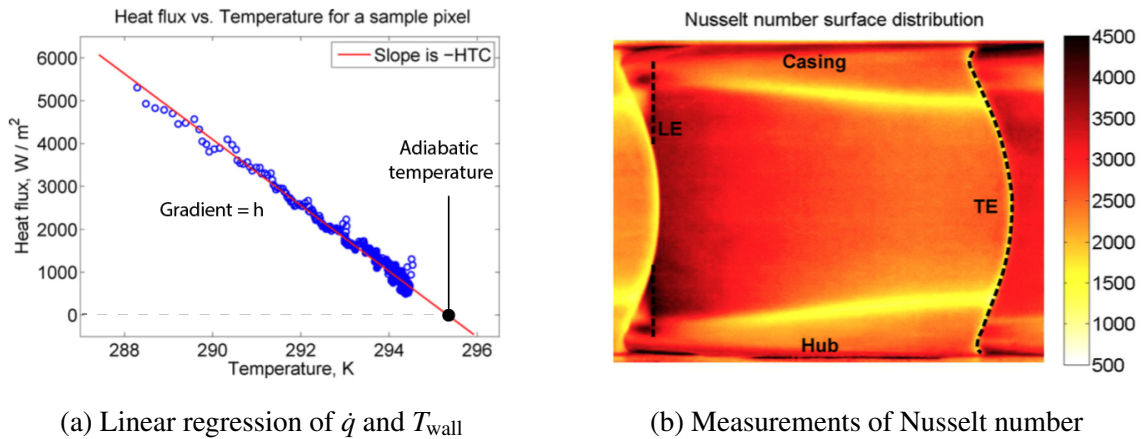


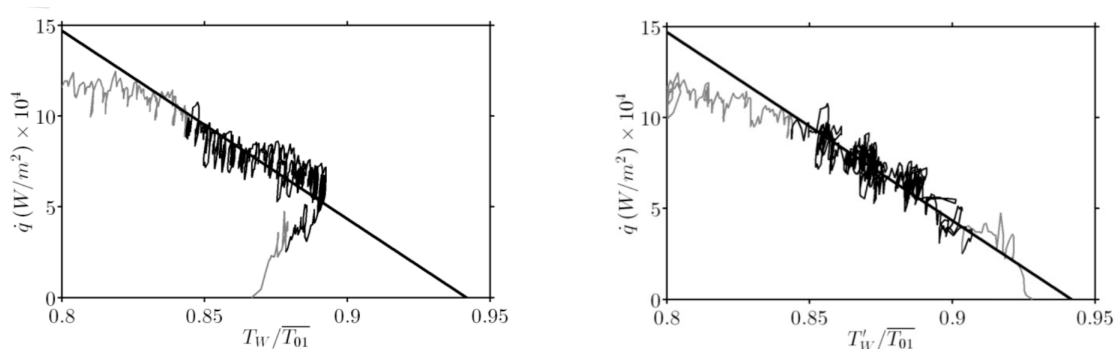
Fig. 2.14 [Luque et al., 2015]

An important assumption with the linear regression methods used by O'Dowd et al. [2010] and Luque et al. [2015] (amongst others), to determine adiabatic wall temperature, is that the method depends on the initial condition of the substrate being adiabatic. They were both able to make this assumption on the basis that the thermal conductivity of the NGV material (Luque et al. [2015]) and stationary turbine blade tip material (O'Dowd et al. [2010])

), was low, and that there was no film-cooling. This ensured low steady-state heat flux values at the steady state condition prior to the transient measurement.

Another important limitation with the linear regression method described above, is that it assumes that both the heat transfer coefficient and adiabatic wall temperature remain constant during the period over which the linear regression is performed. Collins et al. [2015] performed unsteady heat transfer measurements on the over-tip casing of a short duration transonic turbine rig, with a run time of approximately 0.4s. Within the short duration of the transient measurement, they observed significant fluctuations in the mainstream total temperature, which caused the adiabatic wall temperature to vary significantly during the transient measurement. In order to account for this variation, they proposed a floating regression method, where the heat flux was regressed against a corrected wall temperature. The corrected wall temperature was determined by an iterative process, which made use of time-resolved measurements of the free-stream total temperature, and relied on isentropic assumptions about the flow conditions within the rig. No quantification was provided of the influence of the floating regression method on the measurement uncertainty.

An example of the experimental data from Collins et al. [2015] is shown in figure 2.15a and 2.15b, which also shows the fitted linear function. The floating regression method leads to a more linear relationship, suggesting the uncertainty in the regression is reduced. Only a middle portion of the data was used for the regression, where initial and final measurement data is excluded. The basis on which the data cut-off limits were applied were not described.



(a) Linear regression with uncorrected wall temperature

(b) Linear regression with corrected wall temperature

Fig. 2.15 A comparison of standard linear regression and floating linear regression data reduction methods. Excluded experimental data is shown in grey. [Collins et al., 2015]

The time average Nusselt number and adiabatic wall temperature on the over tip casing measurements from Collins et al. [2015] are shown in figure 2.16a and 2.16b - the location of

the rotor tip is illustrated on the figures. A phase locking method was used to retrieve the low frequency transient response signal in relation to the rotor blade location, the principles of which are illustrated in figure 2.17. The phase locking method isolated wall temperature and heat flux readings which corresponded to consistent rotor blade positions - these readings were then used for the linear regression. It is unclear what the source of the circumferential streaks are in figure 2.16a and 2.16b, but they do not appear to be aerodynamic.

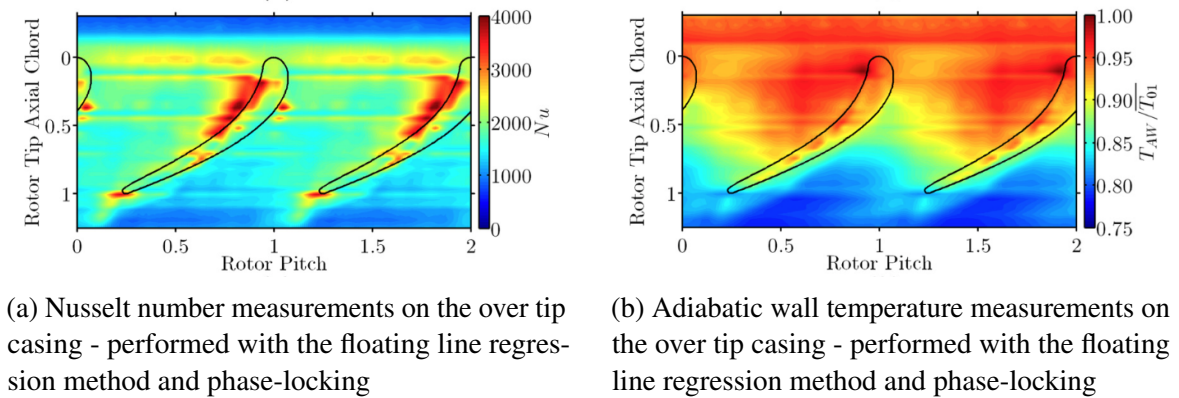


Fig. 2.16 [Collins et al., 2015]

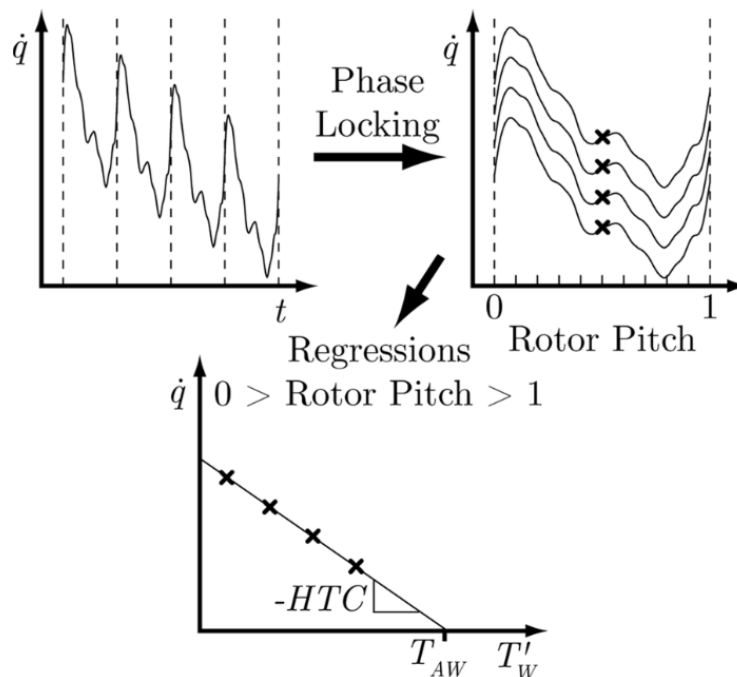


Fig. 2.17 Illustration of the phase locking method used by Collins et al. [2015], to determine time mean heat transfer in the rotating frame

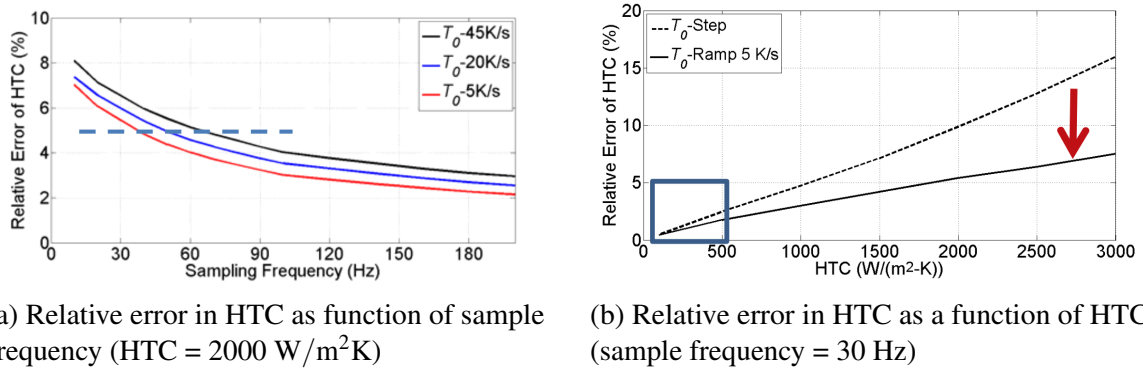
2.4.3 Further methods reducing measurement uncertainty

A number of rig operation and data processing techniques have been proposed, which can reduce measurement uncertainties in transient heat transfer measurements. Three methods from the literature are described below.

Ramp heating method

Ma et al. [2015] provided a one-dimensional simulation, and corresponding heat transfer measurement results, which indicated that under certain circumstances, a ramped change in the mainstream fluid temperature, rather than a step change can lead to reduced measurement uncertainties in heat transfer coefficient and adiabatic wall temperature. In situations with high heat transfer coefficients ($\sim 2000[\text{W m}^{-2}\text{K}^{-1}]$), and low wall temperature measurement acquisition frequency ($\sim 30[\text{samples/s}]$), they showed that a significant rise in measurement uncertainty can occur, due to the wall temperature response being under-resolved in time. By initiating the transient measurement with a ramp increase in fluid temperature, over a period of between 1 and 4 seconds, they showed that the rate of wall temperature increase, during the transient response, was greatly reduced. This enabled sufficient temporal resolution of the wall temperature rise, with relatively low acquisition frequency instrumentation.

Ma et al. [2015] performed one-dimensional heat transfer measurement simulations were performed for three different rates of mainstream fluid temperature increase, and the precision uncertainties in the heat transfer coefficient for each case, were determined with a Monte-Carlo type analysis. The results indicated that lower rates of mainstream temperature rise lead to reduced measurement uncertainties. However, the simulations with slower rates of temperature increase, were also run for longer periods of time, and hence a component of the reduction in measurement uncertainty will be caused by the increased number of data points. The method also depends on the additional measurement of the *time-resolved* mainstream fluid temperature. It is apparent that care must be taken to ensure that there is no significant phase-lag in the mainstream temperature measurements, which are invariably present, to some degree, with thermocouple measurements [Terzis et al., 2012]. Sufficient phase-lag will introduce a greater measurement uncertainty that the ramp method removes. The relative precision uncertainty in the heat transfer coefficient, as a function of sample frequency, is shown in figure 2.18a, and as a function of heat transfer coefficient, in figure 2.18a. Solutions are shown for three different rates of mainstream temperature increase.



(a) Relative error in HTC as function of sample frequency (HTC = 2000 W/m^2K)

(b) Relative error in HTC as a function of HTC (sample frequency = 30 Hz)

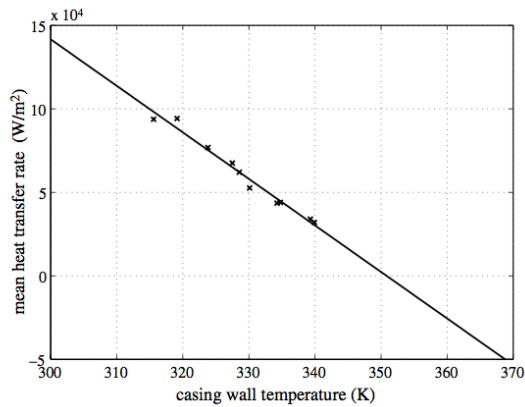
Fig. 2.18 Monte-Carlo simulation results illustrating the reduced uncertainty with the ramp heating method[Ma et al., 2015]

It can be seen from figure 2.18a, that the relative error diminishes as the sampling frequency is increased.

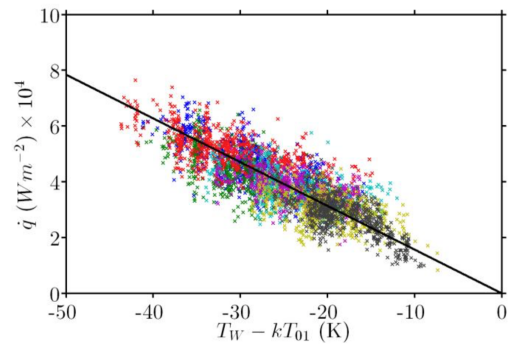
Multiple initial wall temperature method

Thorpe et al. [2004a], Thorpe et al. [2004b] performed a series of transient heat transfer measurements, where the initial temperature of the test surface was set to a range of different values, prior to measurement. The test surface was either pre-heated or pre-cooled with an embedded Peltier heat pump. By either pre-heating or pre-cooling the test surface, different levels of heat flux resulted during the transient measurement. The heat flux and wall temperature measurements from all of the measurements were regressed together, where the increased range of values in wall temperature and heat flux led to a reduced uncertainty in the fit of regression function. A similar experimental procedure was also employed by Collins et al. [2015].

An example of the experimental data from Thorpe et al. [2004a] and Collins et al. [2015], with multiple initial wall temperatures is shown in figure 2.19a and 2.19b. In figure 2.19a, each data point represents a measurement from an individual run of the test facility, where a different initial wall temperature was set. In figure 2.19b data from each measurement is highlighted by a different colour. The increased span of data values can be seen. Quantification of the reduction in measurement uncertainty as a result of using multiple initial wall temperatures was not provided.



(a) Thorpe et al. [2004a]



(b) Colours indicate different initial wall temperatures. [Collins et al., 2015]

Fig. 2.19

The short duration experimental rig used by Collins et al. [2015] (0.4s run duration), was evacuated to a near total vacuum prior the transient measurement. This enabled the turbine disk to be spun at design speed, prior to aerodynamic operation, with a low power consumption. Consequently, heat transfer through the test surface, prior to the transient measurement was limited to heat transfer by radiation only (which was considered negligible). This enabled Collins et al. [2015] to pre-heat or pre-cool the test surface, while being able to confidently assume a zero surface heat flux initial condition - which is a necessary assumption in the measurement technique. This assumption may not hold sufficiently true in a test facility which does not evacuate the rig at the initial condition.

Corner correction method

Chen et al. [2014] presented an analytical method for accounting for the influence of three-dimensional conduction effects at corner locations. The method enables one-dimensional analytical data reduction approaches to produce more accurate evaluations of heat transfer coefficient in the corner region - which is highly effected by lateral heat conduction. They highlighted the corner, present at the perimeter of a two-dimensional turbine blade tip, as a suitable topology on which the correction method can be applied. An illustration of the two-dimensional conduction problem is illustrated in figure 2.20.

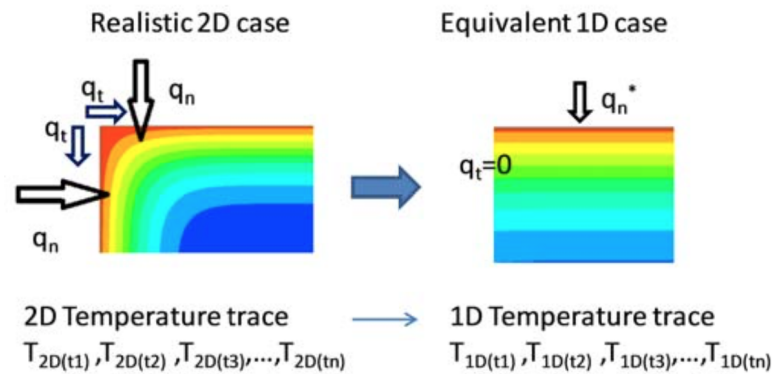


Fig. 2.20 Illustration of the corner correction method [Chen et al., 2014]

The principle of the correction method, is that the transient surface temperature response near a 90 degree corner, can be modelled as the product of two one-dimensional semi-infinite solutions, representing each side of the corner. If a set of boundary conditions on one side of the corner is known, or assumed, then the hypothetical one-dimensional solution for the other side of the corner can be derived from the true solution of the two dimensional case.

In the case of heat transfer measurements on a turbine blade tip, transient temperature measurements will typically only be taken on the tip surface, and not the side walls. If an appropriate heat transfer coefficient is assumed for the side walls, then a significant improvement in the evaluation of the heat transfer coefficient on the tip surface, can be achieved, with one-dimensional analytical models. In figure 2.21a, an example of the error in the evaluated heat transfer coefficient on a turbine blade tip is shown, where a one-dimensional semi-infinite modelling assumption is made, and no corner correction method is applied. In figure 2.21b, the same experimental data is shown, where a data reduction method including the corner correction method is used. At the center of the blade, far from the corner, both methods result in small errors, as the one-dimensional semi-infinite assumption holds true. Close to the corner, a lower measurement error can be seen with in figure 2.21b. It is unclear however, how the assumed 'true' value was acquired.

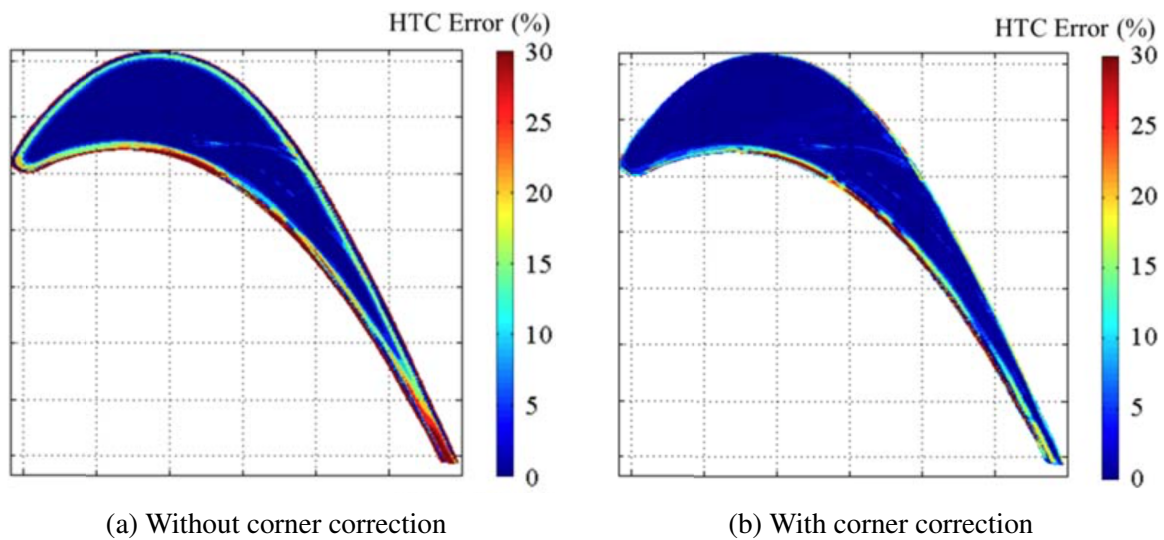


Fig. 2.21 Errors in in heat transfer coefficient on a turbine blade tip[Chen et al., 2014]

It is not apparent from the work presented by Chen et al. [2014] whether the their corner correction method can be applied to corners with non-perpendicular faces. It is also unclear on what basis the assumed value of the heat transfer coefficient on the side wall should be made. The method they present, however, provides a computationally efficient means of reducing errors in heat transfer coefficient for the topologies they present.

2.5 Conclusions

This chapter has described the state of the art in heat transfer measurement techniques for turbomachinery applications. Both experimental instrumentation and measurement methods were reviewed. The turbine rigs, from which the measurements were taken were also described.

A large body of research has been undertaken on transonic turbine rigs, using thin-film gauges, which are able to resolve both the time mean and time resolved heat transfer. Measurements have been successfully taken on stationary and rotating components. However, limited experimental work has been found for film-cooled NGVs or rotor blades using thin-film gauges. The low spatial resolution with thin-film gauges suggests that they would be unable to resolve film-cooling flows in sufficient detail to gain substantial insight into the influence of film-cooling flows on turbine heat transfer.

High spatial resolution measurement techniques, employing IR thermography and TLCs, have been successfully used to resolve film-cooling flows in detail. However, these exper-

perimental techniques have been predominately confined to relatively simple linear cascade turbine rigs, without rotating components and without a variety of other engine-representative features, such as engine representative combustor inlet conditions. These simplifications are significant, as many of the experimental techniques which have been described depend on assumptions which may no longer be valid in engine-scale turbine rigs.

There is evidently an absence of high spatial resolution experimental heat transfer data from engine-scale turbine rigs, with film-cooling, rotating components and combustion hot-spots. Experimental methods needed to address the additional measurement challenges in engine-scale turbine rigs are also lacking in the literature. The development of experimental methods presented in this thesis will contribute to an improved understanding in this area.

Chapter 3

Heat Transfer Measurement Theory

This chapter begins by determining the most suitable heat transfer measurement technique from the literature, for application to engine-scale turbine rigs, and more specifically, for application to the FACTOR turbine rig. A transient type measurement technique is selected, employing IR thermography.

Theoretical concepts are then established, which are used to determine the most significant sources of heat transfer measurement uncertainty.

Turbine rig design features, and measurement methods which can minimise measurement uncertainty are determined. These principles are used in subsequent chapters as a guide in both the design of FACTOR rig components (Chapter 5), and in the experimental methods (Chapter 6).

3.1 Choosing a Measurement Method

As has been shown in Chapter 2, there are a number of ways in which to perform heat transfer measurements, yielding both heat transfer coefficient, and adiabatic wall temperature. The measurement approach which is capable of yielding the best results depends on the specific objectives of the measurements, and on the constraints applied by the rig.

The objective of this work is to develop a heat transfer measurement technique which is capable of taking high spatial resolution and low uncertainty measurements of time mean h and T_{aw} , on an engine scale turbine rig. In Section 1.2 some of the attributes common to engine scale turbine rigs were highlighted. All of these attributes apply constraints to the selection of an appropriate measurement method.

The capabilities of the instrumentation techniques and measurement methods from the literature review with application to engine-scale turbine rigs are summarised below.

3.1.1 Measurement instrumentation

Techniques using thin-film gauges offer high temporal resolution, but require a large footprint area on the measurement surface for the electrical leads for each sensing element. Since the geometric scale of the FACTOR blades is relatively low ($\sim 40\text{mm}$ blade spans), thin-film gauges would offer poor spatial measurement resolution. Measurements taken from thin-film gauges mounted on the rotor, would need to be coupled with a telemetry system to transfer the data from the rotating to the stationary frame of reference - possibly further limiting resolution.

Techniques using TLCs are limited to a maximum service temperature of 115°C [Ireland and Jones, 2000], which is lower than the turbine entry temperature of the FACTOR rig. Consequently, they cannot be used.

Techniques using IR thermography can offer high spatial resolution, can take measurements on surfaces with non-zero Gaussian curvature, do not require significant surface mounted instrumentation, and can measure on surfaces with temperatures up to 1500°C . IR thermography is consequently particularly appealing for temperature measurements on engine-scale turbine rigs. IR measurements on rotating blades are likely to be significantly more challenging than on stationary vanes: Low noise and fast response IR detectors will be required to avoid motion blur in acquired images, and to achieve sufficient signal to noise ratios. Elevated operating temperatures which may be present in engine-scale turbine rigs provide an increased IR radiation intensity over ambient temperature rigs, providing an increased measurement signal.

3.1.2 Measurement method

Steady state measurement techniques from the literature are unappealing with application to engine scale turbine rigs. Iso-thermal back-plate techniques require a uniform thickness insulating layer to be applied to the blade surface, which will be challenging on non-zero Gaussian curvature surfaces. Film-coolant delivery networks within the NGV will present significant challenges in establishing iso-thermal conditions on the back plate, and will leave little room for back plate temperature control systems. Steady state foil heating techniques will require the application of a uniform thickness metallic foil to a small surface with non-zero Gaussian curvature, which is likely to be challenging. The assumption of uniform heat generation rates within the foil would also not be possible, due to both the non-zero Gaussian curvature and the presence of film-cooling holes perforating the film.

Transient measurement techniques making use of semi-infinite modelling assumptions require a sufficiently high Biot number (hx/κ), in order to achieve a well conditioned experimental arrangement (as is described in more detail in section 3.4). A Biot number of approximately 0.8 or greater is required for the transient experimental technique to be well conditioned.

On the FACTOR rig it will be possible to achieve Biot numbers in the range of 1 to 11 (depending on the local heat transfer coefficient) if low thermal conductivity polymers are used for the vanes and blades. This suggests a transient measurement technique will be able to yield a well conditioned measurement.

3.1.3 The selected approach

A transient measurement technique, making use of IR thermography as a time-resolved surface temperature measurement instrument, and a mainstream temperature step to initiate the transient, was selected as the most suitable heat transfer measurement approach for the FACTOR rig, for the following reasons:

1. A well conditioned transient measurement can be achieved, provided the vanes and blades of the FACTOR rig are made from a material with a thermal conductivity of approximately $0.4 \text{ [Wm}^{-1}\text{K}^{-1}\text{]}$, or less. Certain high grade engineering polymers have been identified, which have both a sufficiently low thermal conductivity, and adequate mechanical properties to withstand the thermal and mechanical loading within the rig.

-
2. High spatial resolution temperature measurements can be obtained with IR cameras, which will be able to resolve film-cooling flows in detail, and will enable full field measurements on the whole blade surface.
 3. As is shown later in section 6.3.1, IR cameras with sufficiently high temporal resolution exist, which can adequately resolve the transient surface temperature responses found in the transient measurement technique.
 4. Black body radiation levels from the FACTOR blade and vane surfaces will be high, due to their high temperature. This will result in significantly greater signal levels when compared to a rig run at ambient temperature (by a factor of ~ 5).
 5. Modern high performance IR cameras, can achieve high signal to noise levels with integration times (shutter speeds) down to $\sim 5 \mu\text{s}$. This permits IR measurements on high speed rotating turbine blades, with minimal motion blur. Consequently, full field, high spatial resolution heat transfer measurements on the rotor should be possible.

The following sections of the chapter will address the optimisation of a transient type measurement technique, which makes use of semi-infinite modelling assumptions, and time resolved surface temperature measurements.

3.2 Sources of Uncertainty

Unavoidable uncertainties in measured quantities and uncertainties introduced by imperfect modelling simplifications both contribute to the inevitable presence of uncertainties in heat transfer measurements. Reducing the magnitude of the measurand uncertainty (i.e. the actual quantity being measured, such as radiation intensity), choosing appropriate modelling simplifications and favourably conditioning the experimental approach is essential to achieving low uncertainty heat transfer measurements.

The most important sources of uncertainty in transient heat transfer measurement techniques are described below:

1. Uncertainty in the transient surface temperature response

Uncertainties in the transient surface response arise from three sources; uncertainties in the value of the temperature measurements, finite measurement resolution in time, and finite measurement resolution in space.

2. Uncertainty in substrate thermal conductivity and heat capacity

The derived value of the heat transfer coefficient from transient surface temperature measurements depends on an assumed value of the thermal conductivity, κ , and the heat capacity per unit volume, ρc , of the substrate.

3. 3D conduction

Derivation of heat flux from a transient surface temperature response, is usually performed under the assumption that the transient conduction within the substrate is one-dimensional. Under almost all circumstances, the heat flux within the substrate will be three-dimensional. Errors introduced into the derived value of heat flux caused by this assumption, can be negligible, or significant. Specifically, a one-dimensional modelling assumption fails to capture the following features:

(a) Boundary condition induced lateral heat diffusion

In the case where heat transfer measurements are being taken on a flat semi-infinite substrate, where h and/or T_{aw} vary spatially over the surface; then the transient response of the substrate will also vary in space. Temperature gradients within the substrate, on a plane parallel to the substrate surface, will be generated. These gradients will vary in time. Consequently, there will be time-varying lateral heat-flux terms within the substrate. If these terms are left un-modelled - as is the case with a 1D modelling assumptions - errors will be introduced in the solutions heat flux, and consequently into h and T_{aw} .

(b) 3D Geometry effects

In the case where heat transfer measurements are being taken on a curved surface, or near a corner, a 1D modelling assumption does not hold true. If the heat penetration depth is comparable to the radius of curvature of the surface, or distance from a corner, then 2D or 3D (in the case of non-zero Gaussian curvature) substrate modelling is required to accurately evaluate heat flux from transient surface temperature response.

4. Unsteady aerodynamic conditions

The heat transfer coefficient and adiabatic wall temperature are evaluated by performing a linear regression on a series of data pairs of wall temperature and heat-flux. The regression function is extrapolated beyond the range of measured data, to determine T_{aw} . If the mainstream aerodynamic conditions vary during the period over which the

linear regression is performed, errors in the value of h and T_{aw} can be introduced. These errors can only be removed if additional measurements of the mainstream aerodynamic conditions are available.

5. Steady state heat flux

Transient heat transfer measurements are usually performed under the assumption that adiabatic conditions exist prior to the measurement, with the heat flux at the wall equal to zero. If this assumption is true, then extrapolation of the linear regression function from the transient measurement, to a heat flux level matching the initial conditions will result in a true evaluation of adiabatic wall temperature. However, if prior to a transient measurement, there is significant steady-state wall heat flux, then extrapolation of the linear regression function to an adiabatic condition is not possible, unless the initial heat flux levels are known. Failure to quantify this steady state heat-flux will result in an error in the evaluation of adiabatic wall temperature, but not h . It is important to note, that steady state turbine rigs with film-cooling, such as the FACTOR rig, do not have adiabatic initial conditions.

3.3 Routes to a Well Conditioned Regression

Many of the root sources of uncertainty described in section 3.2 cannot, practically, be reduced to zero. The process of designing a well-conditioned transient heat transfer measurement technique is then; to firstly minimise the source uncertainty terms, and secondly, to minimise the sensitivity of the heat transfer coefficient and adiabatic wall temperature solution to these uncertainty terms.

To understand the means by which measurement uncertainty sensitivity can be reduced, an explanation of the basic transient measurement principle is provided first. Figure 3.1 illustrates an idealised set of transient measurement data - axis values are excluded for simplicity. A step change in the mainstream fluid temperature, ΔT_{∞} , initiates the transient measurement - we will assume that this step change is actually represented by an exponential function with a negative exponent, as shown in figure 3.1 (left). The surface on which heat transfer measurements are being taken will increase in temperature over time in response to the step change in mainstream temperature. The response of a one-dimensional semi-infinite substrate is shown in figure 3.1 (middle), as ΔT_{wall} . From the transient surface temperature response (which would be measured experimentally) the transient heat flux at the surface of the substrate, \dot{q} , can be calculated, and is shown in 3.1 (right).

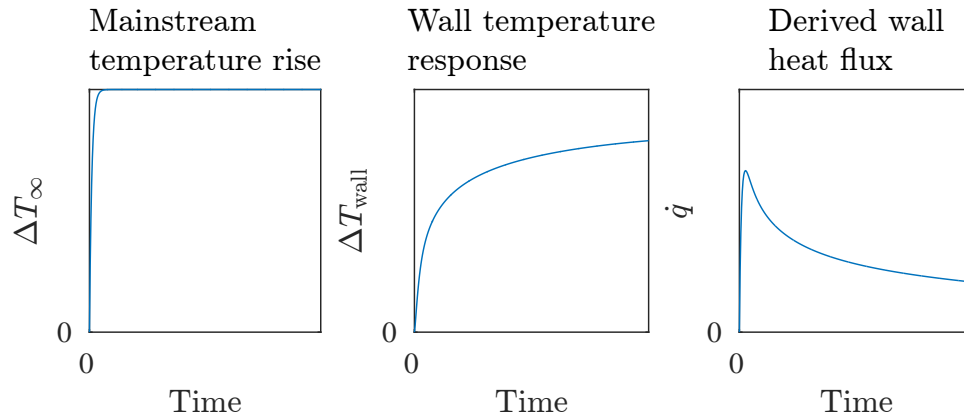


Fig. 3.1 The transient surface temperature and heat flux response to a mainstream temperature rise

The heat transfer coefficient and adiabatic wall temperature are then found by linear regression of $\dot{q}(t)$ and $T_{\text{wall}}(t)$, as illustrated in figure 3.2. (Note that this makes the inherent assumption that T_{aw} and h are constant in time). The ‘Regression start’ point corresponds to the point in time at which mainstream temperature step has fully risen and a stable mainstream temperature is established. The ‘Regression end’ point corresponds to the point in time at which the substrate is no longer semi-infinite, due to its finite thickness. The data points between the two limits are the valid data points, to which a linear regression function is fitted. The gradient of the linear function is equal to the negative magnitude of the heat transfer coefficient. Extrapolation of the linear function to a \dot{q} value of zero defines the adiabatic wall temperature.

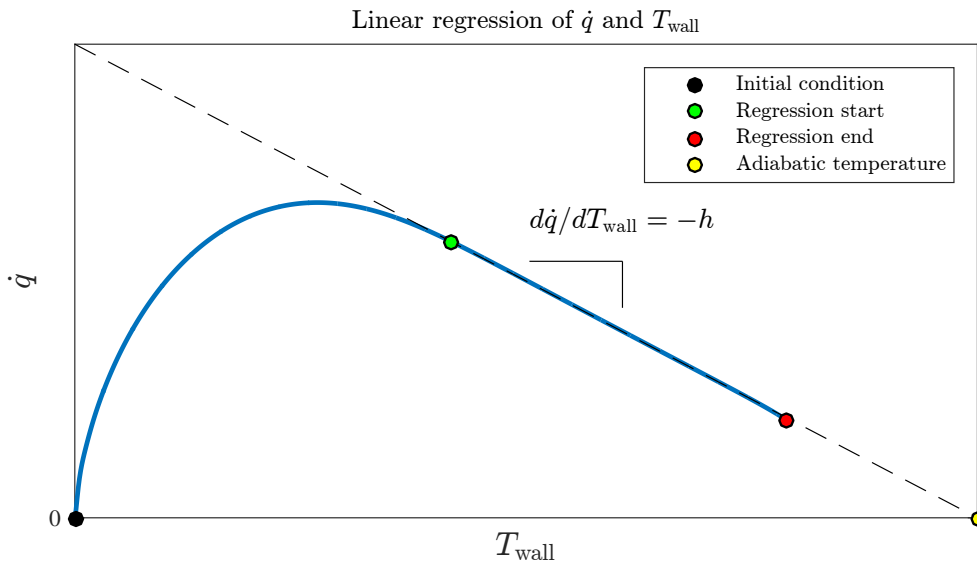


Fig. 3.2 An illustration of the linear regression of \dot{q} and T_{wall} , to find h and T_{aw}

The linear regression of $\dot{q}(t)$ and $T_{\text{wall}}(t)$ can also be represented in a non-dimensional form, as shown in figure 3.3. (Representation in a non-dimensional form will prove useful later - as it will allow more effective comparisons to be drawn between different data sets)

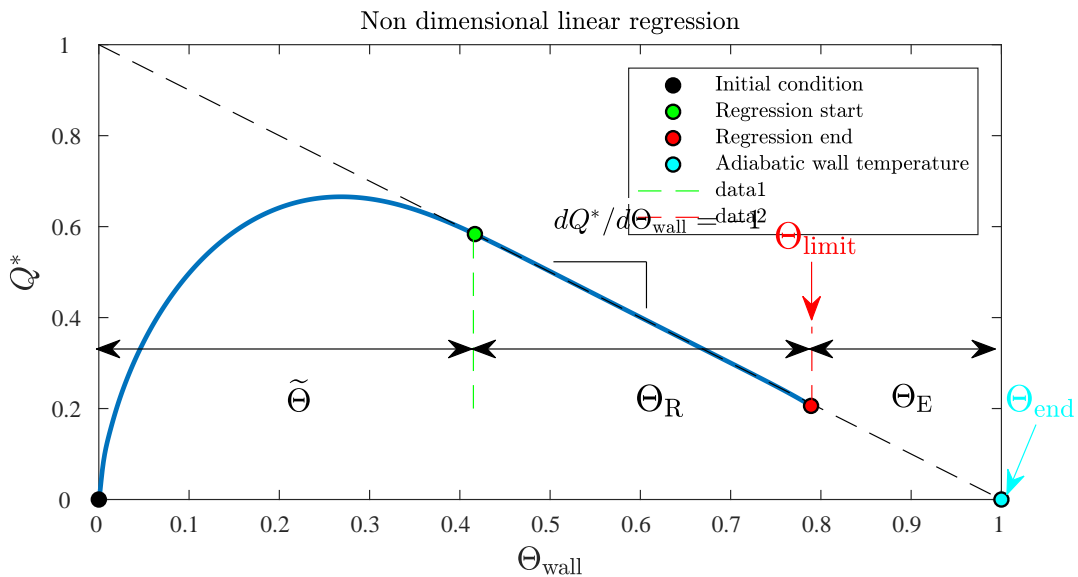


Fig. 3.3 Non-dimensional form of a hypothetical linear regression

Where;

$$\Theta_{\text{wall}} = \frac{\Delta T_{\text{wall}}(t)}{\Delta T_{\text{aw}}} \quad (3.1)$$

$$Q^* = \frac{\dot{q}}{h\Delta T_{aw}} \quad (3.2)$$

From figure 3.3, five new variables are defined. $\tilde{\Theta}$ is the non-dimensional wall temperature change which occurs during the initial unsteady period, where the mainstream fluid temperature has not yet stabilised. Θ_R is the non-dimensional wall temperature change over which the linear regression is performed. Θ_E is the non-dimensional wall temperature change over which extrapolation is performed in order to define T_{aw} , Θ_{end} is the value of Θ_{wall} when at adiabatic conditions (i.e. 1), Θ_{limit} is the non-dimensional wall temperature at which point the semi-infinite assumption becomes invalid.

Under real measurement circumstances, the values of $\dot{q}(t)$ and $T_{wall}(t)$ will be corrupted with errors due imperfect measurement. The linear function is then fitted to the data with a least squares regression method. It is apparent that under these conditions the following will lead to a reduction in the uncertainty of the fit of the linear function:

1. A reduction in the uncertainty of $\Theta_{wall}(t)$ (which is now termed $U_{\Theta_{wall}}$ (see equation 3.3))
2. A reduction in the uncertainty of $Q^*(t)$ (which is now termed U_{Q^*} (see equation 3.4))
3. An increase in the extent of valid regression region, Θ_R , achieved through either:
 - (a) A reduction of $\tilde{\Theta}$
 - (b) A reduction in Θ_E

In section 3.4, the heat equation is presented, and important non-dimensional values introduced. Methods of reducing $U_{\Theta_{wall}}$, reducing U_{Q^*} and increasing Θ_R are then addressed in the subsequent sections.

$$U_{\Theta_{wall}} = \frac{U_{T_{wall}}}{\Delta T_{aw}} = \frac{\sqrt{P_{T_{wall}}^2 + B_{T_{wall}}^2}}{\Delta T_{wall}} \quad (3.3)$$

$$U_{Q^*} = \frac{U_{\dot{q}}}{h\Delta T_{aw}} = \frac{\sqrt{P_{\dot{q}}^2 + B_{\dot{q}}^2}}{h\Delta T_{aw}} \quad (3.4)$$

(Where P and B denote the precision and bias uncertainty in the measured quantity. A more detailed explanation of precision and bias uncertainties are provided in section 4.2.)

3.4 One Dimensional Transient Conduction

Transient heat conduction problems are described by the heat equation, which is a linear partial differential equation. The one-dimensional form of the heat equation is shown in equation 3.5, where α is the thermal diffusivity of the substrate, equal to $\kappa/\rho c$. The heat equation describes the temperature of a body, in time and space, as a function of the initial and boundary conditions. A solution to the one-dimensional heat equation exists, if an initial condition, and two boundary conditions are known, known as an initial-boundary-value-problem.

$$\frac{\partial T(x,t)}{\partial t} = \alpha \frac{\partial^2 T(x,t)}{\partial x^2} \quad (3.5)$$

If we make the assumption, for the time being, that the transient conduction which occurs beneath the surface of the substrate in the heat transfer measurement technique is one-dimensional and semi-infinite, then we can establish the following initial condition and two boundary conditions necessary to solve the heat equation.

Initial condition:

$$T(x,0) = T_i \quad (3.6)$$

First boundary condition:

$$\left. \frac{\partial T}{\partial x} \right|_{x=0} = -\frac{h}{\kappa} [T(0,t) - T_{aw}] \quad (3.7)$$

Second boundary condition:

$$\left. \frac{\partial T}{\partial x} \right|_{x=\infty} = 0 \quad (3.8)$$

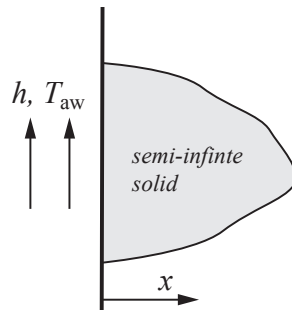


Fig. 3.4 A semi-infinite solid - with one spatial dimension

The initial condition (Equation 3.6) defines the initial temperature throughout the one-dimensional region to be uniform at a value T_i . Equation 3.7 defines a constant convection boundary, with heat transfer coefficient h and adiabatic temperature T_{aw} . Equation 3.8 defines the solid as semi-infinite in the $+x$ direction, where at $x = \infty$, the spatial temperature gradient is zero for all time. For these boundary conditions, an exact analytical solution to the partial differential equation exists, and is given by equation 3.9 [Incropera et al., 2006], where erfc is the complimentary error function.

$$\Theta(x,t) = \frac{T(x,t) - T_i}{T_{\text{aw}} - T_i} = \text{erfc}\left(\frac{x}{2\sqrt{\alpha t}}\right) - \left[\exp\left(\frac{hx}{\kappa} + \frac{h^2\alpha t}{\kappa^2}\right)\right] \left[\text{erfc}\left(\frac{x}{2\sqrt{\alpha t}} + \frac{h\sqrt{\alpha t}}{\kappa}\right)\right] \quad (3.9)$$

Equation 3.9 can be expressed as a function of two non-dimensional values; the Biot number, Bi , and the Fourier number, Fo , as shown in equation 3.11

$$\text{Bi} = \frac{hx}{\kappa}, \quad \text{Fo} = \frac{\alpha t}{x^2}, \quad \text{Bi}\sqrt{\text{Fo}} = \frac{h\sqrt{\alpha t}}{\kappa} \quad (3.10)$$

$$\Theta(x,t) = \text{erfc}\left(\frac{1}{2\sqrt{\text{Fo}}}\right) - \left[\exp\left(\text{Bi} + \text{Bi}^2\text{Fo}\right)\right] \left[\text{erfc}\left(\frac{1}{2\sqrt{\text{Fo}}} + \text{Bi}\sqrt{\text{Fo}}\right)\right] \quad (3.11)$$

Evaluating equation 3.11 at $x = 0$, we obtain an expression for the transient response of the surface (or wall) temperature, $\Theta_{\text{wall}}(t)$.

$$\Theta(0,t) = 1 - \exp(\text{Bi}^2\text{Fo})\text{erfc}(\text{Bi}\sqrt{\text{Fo}}) \quad (3.12)$$

From equation 3.12, it can be seen that the transient wall temperature response is only a function of the non-dimensional value $\text{Bi}\sqrt{\text{Fo}}$.

3.5 Minimising Uncertainty in $\Theta_{\text{wall}}(t)$

The analytical expression for the transient wall temperature described by equation 3.9 is defined under the assumption that the initial conditions are adiabatic. In order to consider a more general case, where initial conditions may not be adiabatic, the non-dimensional transient wall-temperature is now defined as a function of the initial **adiabatic** wall temperature, $T_{\text{aw},i}$, rather than the initial temperature T_i .

$$\Theta_{\text{wall}} = \frac{\Delta T_{\text{wall}}(t)}{\Delta T_{\text{aw}}} = \frac{T_{\text{wall}}(t) - T_{\text{wall}}(t(0))}{T_{\text{aw}} - T_{\text{aw},i}} \quad (3.13)$$

It can be seen from the form of equation 3.13 that uncertainty in the value of Θ_{wall} can be reduced by either;

1. Reducing the absolute measurement uncertainty in the transient wall temperature change measurements, $\Delta T_{\text{wall}}(t)$
2. Increasing the magnitude of ΔT_{aw} , which leads to an increase in the magnitude of $\Delta T_{\text{wall}}(t)$, and a consequent reduction in its measurement uncertainty.

These two methods are described in more detail in the following two subsections.

3.5.1 Reducing uncertainty in $\Delta T_{\text{wall}}(t)$

A low uncertainty in $\Delta T_{\text{wall}}(t)$ can be achieved by; 1) using a measurement instrument with a low single point measurement uncertainty, and 2) by acquiring temperature measurements at a high sample rate, such that $\Delta T_{\text{wall}}(t)$ is well resolved in time and precision uncertainties are reduced by statistical effects.

Assuming the most capable temperature measurement method available has been selected, in terms of single point measurement uncertainty and sample rate, there remains an additional means by which temporal resolution can effectively be increased. By selecting a substrate material for the test surface with a high thermal effusivity, the frequency response of the surface will be reduced. This reduces the rate of surface temperature change in response to a given surface heat flux. In doing so, the transient response is effectively ‘slowed down’, allowing the transient wall temperature to be better resolved in time. The thermal effusivity of a material, is defined in equation 3.14, where ρ is the mass density [kg m^{-3}], c is the specific heat capacity [$\text{J kg}^{-1}\text{K}^{-1}$], and κ is the thermal conductivity [$\text{Wm}^{-1}\text{K}^{-1}$].

$$e = \sqrt{\rho c \kappa} \quad (3.14)$$

The thermal effusivity is the material property which governs the transient surface temperature response. Taking equation 3.11, expressed in terms of the thermal effusivity, we have:

$$\Theta(0,t) = 1 - \exp\left(\frac{h^2 t}{e^2}\right) \text{erfc}\left(\frac{h\sqrt{t}}{e}\right) \quad (3.15)$$

Differentiating with respect to time, making use of the identity given in equation 3.17, equation 3.15 becomes;

$$\frac{d}{dt}\Theta(0,t) = \frac{h}{e\sqrt{t\pi}} - \frac{h^2}{e^2}\exp\left(\frac{h^2t}{e^2}\right)\text{erfc}\left(\frac{h\sqrt{t}}{e}\right) \quad (3.16)$$

$$\frac{d}{dt}\text{erfc}(t) = -\frac{2\exp(-t^2)}{\sqrt{\pi}} \quad (3.17)$$

From equation 3.16 it can be seen that the only variables which affect the rate of surface temperature change is the ratio h/e .

Three solutions to equation 3.16 are plotted in figure 3.5. It can be seen that increasing the value of e leads to a lower peak in the rate of surface temperature change at the beginning of the transient. This results in a wall temperature response which would be better resolved in time by a discrete sampling instrument at the beginning of the transient. Consequently, a reduced uncertainty in $\Delta T_{\text{wall}}(t)$ is achieved.

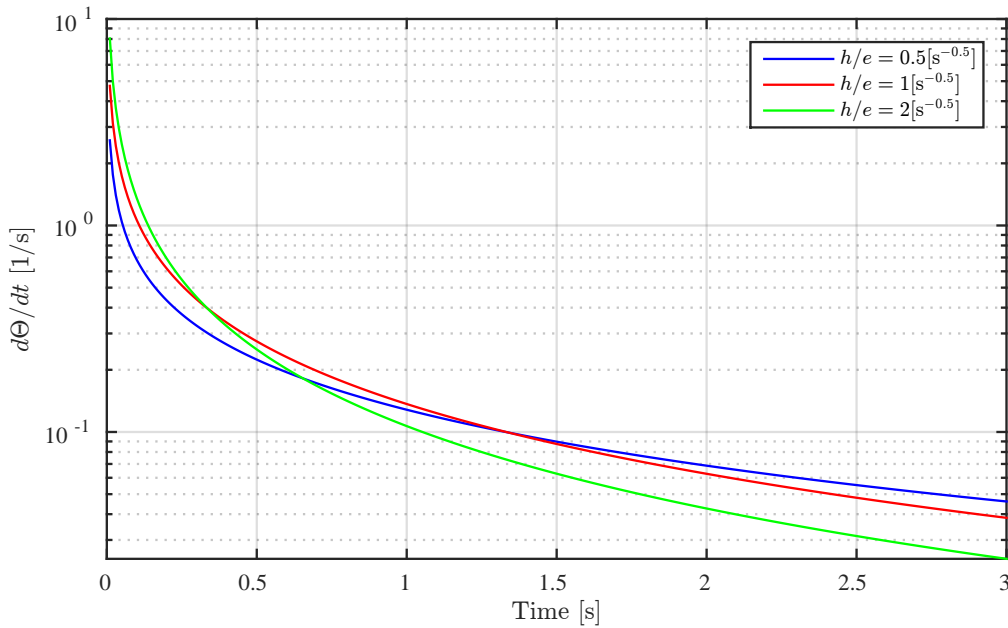


Fig. 3.5 The rate of non-dimensional wall temperature change in an idealised transient measurement, as a function of t and h/e

3.5.2 Increasing the magnitude of ΔT_{aw}

Yet another way of reducing $U_{\Theta_{wall}}$ is to increase ΔT_{aw} : By increasing the magnitude of ΔT_{aw} , the magnitude of the wall temperature response will be increased by an equal proportion. Recalling equation 3.3, (shown below for convenience), it is apparent that the value of $U_{\Theta_{wall}}$ is reduced.

$$U_{\Theta_{wall}} = \frac{U_{T_{wall}}}{\Delta T_{aw}} = \frac{\sqrt{P_{T_{wall}}^2 + B_{T_{wall}}^2}}{\Delta T_{wall}} \quad (3.18)$$

The adiabatic wall temperature is related to the near wall fluid total temperature by the relation given in equation 3.19, where \hat{r} is the recover factor, γ is the heat capacity ratio of the fluid, and Ma_{∞} is the Mach number in the adjacent mainstream. The recovery factor for a turbulent boundary layer, where the fluid is air, is ~ 0.89 [Schlichting, 1979], which is approximately equal to $Pr^{1/3}$.

$$T_{aw} = T_{\infty} \left(1 + \hat{r} \frac{\gamma - 1}{2} Ma_{\infty}^2 \right) \quad (3.19)$$

Assuming that the step change in fluid temperature in the transient measurement is sufficiently small that γ and Ma remain approximately constant, then the adiabatic wall temperature will be approximately proportional to the local fluid temperature. An increase in the magnitude of ΔT_{∞} therefore leads to an approximately proportional increase in ΔT_{aw} .

$$\Delta T_{aw} \propto C \cdot \Delta T_{\infty} \quad (3.20)$$

An important consideration when performing measurements on film-cooled components, is that changes in the free stream total temperature will have a reduced effect on the local fluid temperature downstream of a film-cooling hole. In this case, the change in local adiabatic wall temperature would be given by equation 3.21, where η is the film-cooling effectiveness. Turbine rigs with film-cooled vanes and blades would therefore require greater free stream fluid temperature steps in order to achieve the same value of ΔT_{aw} .

$$\Delta T_{aw} \approx C \cdot \Delta T_{\infty} \cdot \eta \quad (3.21)$$

Increasing the magnitude of ΔT_{aw} is therefore simply achieved by increasing the magnitude of ΔT_{∞} .

3.6 Minimising Uncertainty in Q^*

The non-dimensional wall heat-flux was defined in equation 3.2, as follows:

$$Q^*(t) = \frac{\dot{q}(t)}{h(T_{aw} - T_{aw,i})} \quad (3.22)$$

The uncertainty in Q^* , U_{Q^*} was defined in equation 3.4, shown again below for convenience:

$$U_{Q^*} = \frac{U_{\dot{q}}}{h\Delta T_{aw}} = \frac{\sqrt{P_{\dot{q}}^2 + B_{\dot{q}}}}{h\Delta T_{aw}} \quad (3.23)$$

In the proposed heat transfer measurement technique, heat flux is derived from the transient surface temperature response. Uncertainties in the derived value of heat flux will originate from uncertainties in the original wall temperature measurements, and from the methods used and assumptions made in calculating the heat flux.

It can be seen from equation 3.23 that U_{Q^*} can be reduced by either reducing uncertainty in \dot{q} , or increasing the magnitude of $h\Delta T_{aw}$. (The methods by which ΔT_{aw} can be increased were discussed in section 3.5.2). The heat transfer coefficient is the quantity we wish to measure, and therefore cannot be used as a control variable. Consequently, only the methods of reducing uncertainty in \dot{q} are discussed in this section.

Uncertainty in \dot{q} , from an assumed perfect set of wall temperature measurements can originate from three sources, which are addressed in the following subsections:

1. From uncertainty in the substrate conductivity, κ and heat capacity, ρc .
2. From uncertainty in the initial conditions of the substrate.
3. From invalid modelling assumptions (e.g semi-infinite and 1D assumption)

All of these error sources act primary to introduce systematic Bias¹ uncertainties into the derived value of \dot{q} . The underlying equations which govern the impact of these three sources of uncertainty are now explored.

3.6.1 Uncertainty in material properties

An inaccurate measurement (or assumed value) of the substrate material properties will lead to a bias error in the heat flux derived from transient wall temperature measurements.

¹For a definition of Bias uncertainty - see section 4.2

The material property which wholly governs the transient surface temperature response of a one-dimensional semi-infinite body is the thermal effusivity, as given in equation 3.16. The following calculations are used to show the relationship between assumed thermal effusivity and derived heat flux.

Taking the partial differential of equation 3.9 with respect to x , an expression for the spatial temperature gradient within the semi-infinite body can be found:

$$\frac{\partial T(x,t)}{\partial x} \frac{1}{\Delta T_{aw}} = \frac{-1}{\sqrt{\alpha t \pi}} \exp\left(-\left(\frac{x}{2\sqrt{\alpha t}}\right)^2\right) - \exp\left(\frac{h^2 \alpha t}{\kappa^2} + \frac{hx}{\kappa}\right) \left[\frac{h}{\kappa} \operatorname{erfc}\left(\frac{h\sqrt{\alpha t}}{\kappa} + \frac{x}{2\sqrt{\alpha t}}\right) - \frac{1}{\sqrt{\alpha t \pi}} \exp\left(-\left(\frac{h\sqrt{\alpha t}}{\kappa} + \frac{x}{2\sqrt{\alpha t}}\right)^2\right) \right] \quad (3.24)$$

Fourier law of conduction is given as;

$$\dot{q} = -\kappa \frac{\partial T}{\partial x} \quad (3.25)$$

Substituting equation 3.25 into equation 3.22, we have;

$$Q^*(t) = -\frac{\partial T(0,t)}{\partial x} \frac{\kappa}{h\Delta T_{aw}} \quad (3.26)$$

An expression for the transient non-dimensional wall heat flux can then be found by substitution of equation 3.26 into equation 3.24, and evaluating at $x = 0$.

$$Q^*(t) = -\frac{-\kappa}{h\sqrt{\alpha t\pi}} + \exp\left(\frac{h^2\alpha t}{\kappa^2}\right) \left[\operatorname{erfc}\left(\frac{h\sqrt{\alpha t}}{\kappa}\right) - \frac{1}{\sqrt{\pi}} \frac{\kappa}{h\sqrt{\alpha t}} \exp\left(-\left(\frac{h\sqrt{\alpha t}}{\kappa}\right)^2\right) \right] \quad (3.27)$$

Simplifying, this yields;

$$Q^*(t) = \exp\left(\frac{h^2\alpha t}{\kappa^2}\right) \operatorname{erfc}\left(\frac{h\sqrt{\alpha t}}{\kappa}\right) \quad (3.28)$$

Recognising the dimensionless quantities;

$$\frac{h\sqrt{\alpha t}}{\kappa} = \frac{h\sqrt{t}}{e} = \operatorname{Bi}\sqrt{\operatorname{Fo}} \quad (3.29)$$

Equation 3.27 can be expressed as follows;

$$Q^*(t) = \frac{\dot{q}}{h\Delta T_{aw}} = \exp(\operatorname{Bi}^2\operatorname{Fo}) \operatorname{erfc}(\operatorname{Bi}\sqrt{\operatorname{Fo}}) \quad (3.30)$$

or more simply as;

$$Q^*(t) = 1 - \Theta_{\text{wall}}(t) \quad (3.31)$$

From equation 3.30 we can see that non-dimensional heat flux is only a function of $\operatorname{Bi}\sqrt{\operatorname{Fo}}$ ($h\sqrt{t}/e$). It follows that an uncertainty in either e or \sqrt{t} will lead to a linearly proportional uncertainty in the the heat flux. Since the heat transfer coefficient is derived by linear regression of \dot{q} , it also follows that uncertainty in the heat transfer coefficient will be linearly proportional to uncertainty in \sqrt{t}/e . Consequently, it is important that the substrate thermal effusivity is known or measured accurately.

$$\frac{U_h}{h} \propto \frac{U_{\sqrt{t}}}{\sqrt{t}} \cdot \frac{U_e}{e} \quad (3.32)$$

It is important to note, however, that this holds true only for one-dimensional semi-infinite case, where the boundary conditions defined in equations 3.6, 3.7 and 3.8 are met.

3.6.2 Uncertainty in initial conditions

In section 3.4 it was described that a uniform initial temperature condition is required in order to derive transient heat flux from transient wall temperature measurements, using the analytical solution to the heat equation presented in section 3.4. If the uniform initial temperature condition is not met, then there exists an initial heat flux within the substrate, which cannot be quantified with wall temperature measurements alone. A transient heat transfer measurement, evaluated under the assumption of uniform initial conditions, will result in an error in the derived heat flux if this condition is not satisfied. In an engine-scale turbine rig with small scale film-cooled components, this initial condition may well not be satisfied.

The heat equation is a linear differential equation. Consequently, the superposition principle can be applied to it, wherein a solution to the heat equation can be expressed as a linear summation of multiple individual solutions. If we assume a transient heat transfer measurement is performed on a substrate with a steady initial heat flux, then the heat flux at the wall can be expressed as the summation of a steady and transient component. (NB: non-adiabatic steady state initial conditions can be easily achieved on engine-scale turbine rigs, by allowing steady state conditions to be reached).

$$\dot{q}_{\text{wall}}(t) = \dot{q}_{\text{transient}}(t) + \dot{q}_{\text{steady}} \quad (3.33)$$

The transient wall heat flux and wall temperature from a hypothetical measurement, performed on a substrate with an initial steady state heat flux is shown in figure 3.6. The initial condition is not adiabatic, and hence the initial wall temperature (prior to the mainstream temperature step), differs from the initial adiabatic wall temperature, $T_{\text{aw},i}$.

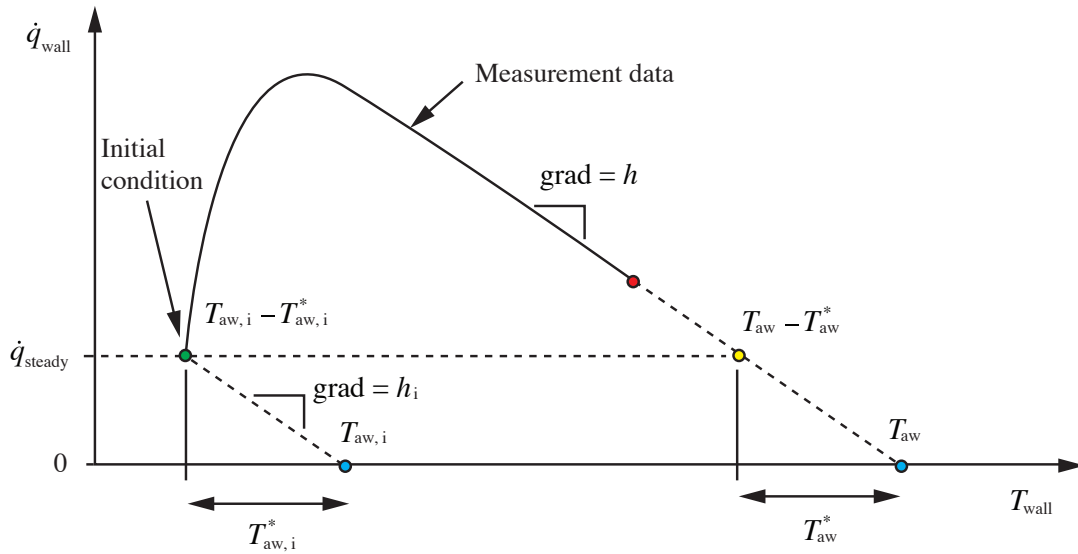


Fig. 3.6 The idealised transient wall heat flux and wall temperature for a substrate with non-adiabatic initial conditions

The linear regression methods described in section 2.4.2 determines T_{aw} by extrapolation of the regression function to the initial heat flux value. When the initial condition is adiabatic, this results in a true evaluation of T_{aw} . In the case with initial steady state heat flux, an error in the evaluation of T_{aw} , equal to T_{aw}^* will arise, where the value of T_{aw}^* is given by equation 3.34. The evaluation of h , however, is unaffected by the presence of an initial steady state heat flux, since its value is not dependant on the absolute value of wall heat flux (neglecting second order effects).

$$T_{aw}^* = h\dot{q}_{steady} \quad (3.34)$$

The consequence of this, is that in order to determine the true value of T_{aw} , the value of \dot{q}_{steady} would need to be quantified. It is therefore highly desirable to design a turbine rig in such a way that adiabatic initial conditions can be achieved, so as to avoid the need to measure \dot{q}_{steady} .

In the case where adiabatic initial conditions cannot be achieved, and where \dot{q}_{steady} cannot be quantified, it is nevertheless possible to approximate the adiabatic ‘non-dimensional recovery temperature’: Assuming that h_i is approximately equal to h , which is reasonable if the mainstream temperature step is relatively small, then it follows that;

$$T_{aw,i}^* \approx T_{aw}^* \quad (3.35)$$

Therefore;

$$(T_{aw} - T_{aw}^*) - (T_{aw,i} - T_{aw,i}^*) \approx T_{aw} - T_{aw,i} = \Delta T_{aw} \quad (3.36)$$

A non-dimensional recovery temperature, Θ_{rec} , can then be defined as shown in equation 3.37, which by logical deduction, is equal to one minus the film-cooling effectiveness (equation 2.5).

$$\Theta_{rec} = \frac{\Delta T_{aw}}{\Delta T_{0,\infty}} = 1 - \eta \quad (3.37)$$

Note that this quantity can be defined in the presence of an unquantified steady state heat flux! Note however, that the mainstream total temperature change $\Delta T_{0,\infty}$ now needs to be measured - this is however significantly easier than measuring a spatially resolved \dot{q}_{steady} .

Given that steady state heat-flux is expected to be present in the FACTOR rig, Θ_{rec} will be used, rather than T_{aw} throughout this thesis.

3.6.3 Surface curvature induced errors

Derivation of the wall heat flux from transient surface temperature measurements, is often made under the assumption that the substrate is semi-infinite and one-dimensional. If the substrate surface is in fact curved, this assumption will introduce errors in the derived heat flux. If the radius of curvature is large, the errors introduced will be small. The question arises; what is the lowest radius of curvature which yields acceptably small errors?

Figure 3.7 illustrates a section through an infinite cylinder, with radius r_0 . The cylinder, at an initial temperature T_i is exposed to a constant convection boundary condition at $t = 0$, with heat transfer coefficient h and adiabatic temperature T_{aw} . Over time, heat propagates in the radial direction, and we can consider a heat penetration depth $\Delta r(t)$. As $r_0/\Delta r(t) \rightarrow \infty$, the local heat affected region behaves in an increasingly one-dimensional manner.

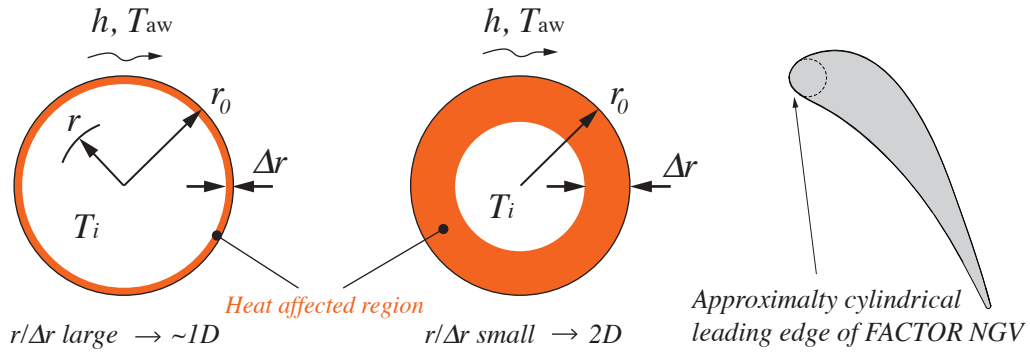


Fig. 3.7 Transient conduction within an infinite cylinder is initially approximately one-dimensional

The conduction within the curved leading edge of an NGV or turbine blade, during a transient heat transfer measurement, will behave in a similar fashion to the cylinder in figure 3.7. If the heat flux within the blade is modelled with a one-dimensional semi-infinite model, then it becomes important to know at what point in time the measurement should end, such that significant errors are not introduced by the inaccurate modelling assumption.

Transient conduction within the infinite cylinder represented in figure 3.7, is described by the Bessel functions in equation 3.38, as documented by Incropera et al. [2006].

$$\Theta(t, r) = \frac{T(t, r) - T_i}{T_{aw} - T_i} = \sum_{n=1}^{\infty} C_n \exp\left(-\zeta_n^2 \frac{\alpha t}{r_0^2}\right) J_0\left(\zeta_n \frac{r}{r_0}\right) \quad (3.38)$$

where,

$$C_n = \frac{2 J_1(\zeta_n)}{\zeta_n J_0^2(\zeta_n) + J_1^2(\zeta_n)} \quad (3.39)$$

the discrete values of ζ_n are the positive roots of,

$$\zeta_n \frac{J_1(\zeta_n)}{J_0(\zeta_n)} = \text{Bi}_r \quad (3.40)$$

where,

$$J_0(\zeta) = \sqrt{\frac{2}{\pi \zeta}} \cos\left(\zeta - \frac{\pi}{4}\right) \quad (3.41)$$

$$J_1(\zeta) = \sqrt{\frac{2}{\pi \zeta}} \cos\left(\zeta - \frac{3\pi}{4}\right) \quad (3.42)$$

and,

$$\text{Bi}_r = \frac{hr_0}{\kappa} \quad (3.43)$$

A solution to equation 3.38 requires an infinite summation, and calculation of the implicit roots ζ_n . A large finite summation was used to numerically estimate a solution, which is shown in figure 3.8, at the radial location $r = r_0$, and $\text{Bi}_r = 10$. Time is represented in its non-dimensional form on the horizontal axis. A one-dimensional semi-infinite body solution, is also shown, where the characteristic length scale used matches that of the cylinder, r_0 . The deviation of the infinite cylinder solution from the semi-infinite body solution can be seen to grow over time, and then reduce back to zero at infinite time.

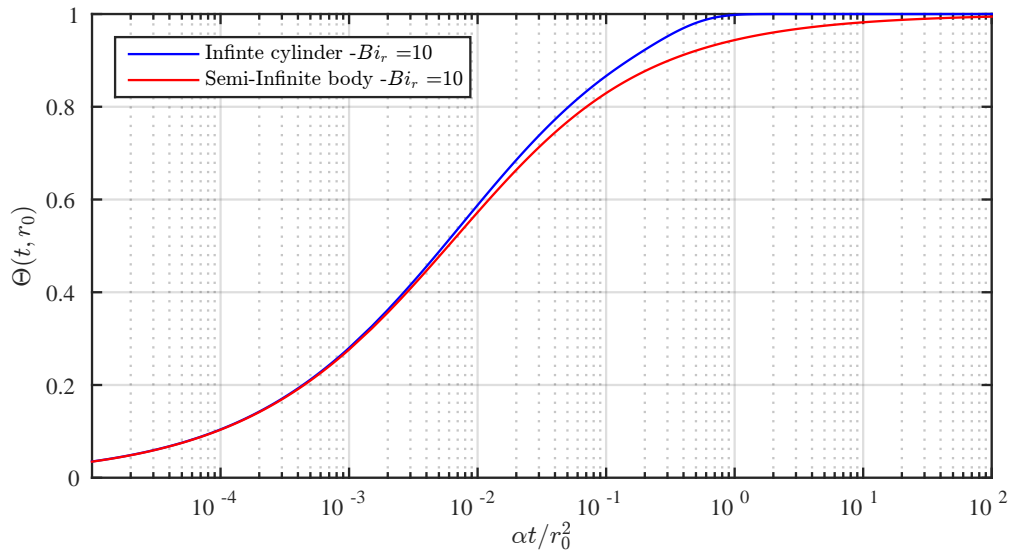


Fig. 3.8 Comparison of the transient response of an infinite cylinder and semi-infinite body

A series of solutions were generated for a range of Bi_r numbers. The deviation of the infinite cylinder solutions, from the semi-infinite body solution are shown as a function of non-dimensional time in figure 3.9.

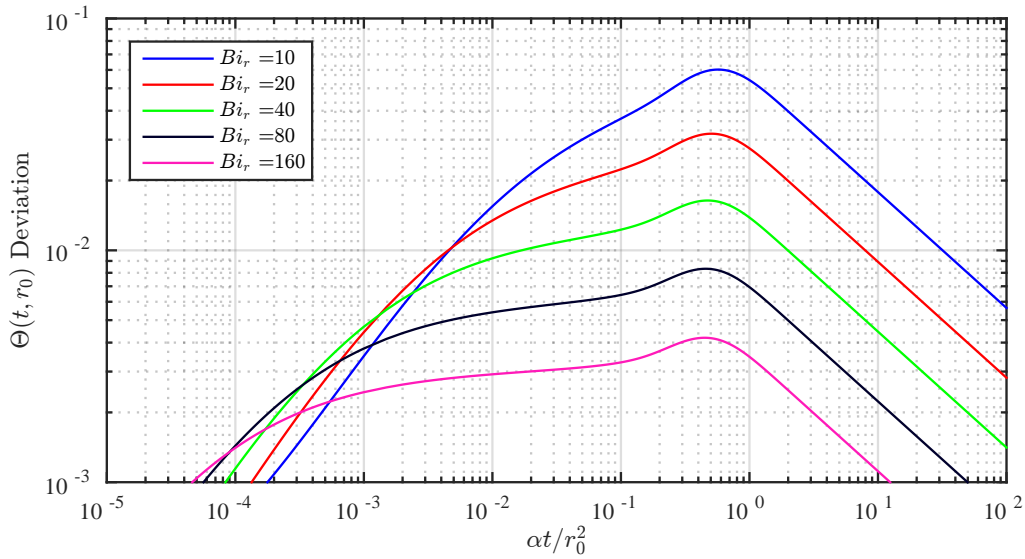


Fig. 3.9 Deviation of infinite cylinder solution to semi-infinite body solution over time, for a range of Bi_r numbers

The solution in figure 3.9 shows that for Bi_r numbers greater than 40, the non-dimensional transient surface temperature of an infinite cylinder deviates from a semi-infinite solution by no more than $\sim 1.8\%$. The non-dimensional heat flux is equal to one minus $\Theta(t, 0)$ (equation 3.30) - It can therefore be said that if the Bi_r number is greater than 40, then one dimensional semi-infinite heat flux modelling assumptions will introduce a maximum heat flux error of 1.8%, as a result of neglecting to model the surface curvature alone.

The question which follows, is what is the impact of these modelling errors on derived values of h and Θ_{rec} . In order to quantify the impact, the transient wall heat flux was calculated from the transient temperatures presented in figure 3.9. A one-dimensional semi-infinite implementation of the Impulse Response heat flux modelling method was used [Oldfield, 2008] (section 2.4.2). The calculated non-dimensional heat flux for each Bi_r number is plotted against non-dimensional temperature in figure 3.10. The solution for a semi-infinite body is also shown. It can be seen that as the Bi_r number reduces the cylinder solution deviates increasingly from the semi-infinite solution. The gradient of the relationship between $Q^*(t)$ and $\Theta(t, r_0)$ reduces in magnitude, which would lead to an underestimate in the heat transfer coefficient, and overestimate in the adiabatic wall temperature. (NB: The large deviation from the semi-infinite solution at $\Theta(t, r_0) \approx 0.05$ is caused by numerical errors in the implementation of Impulse Response model, which is caused by finite temporal resolution of $\Theta(t, r_0)$)

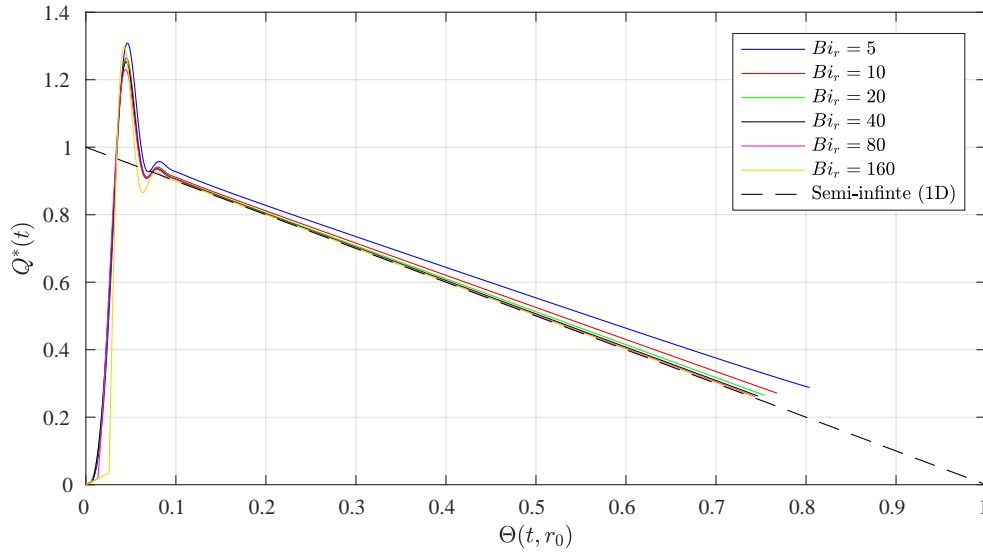
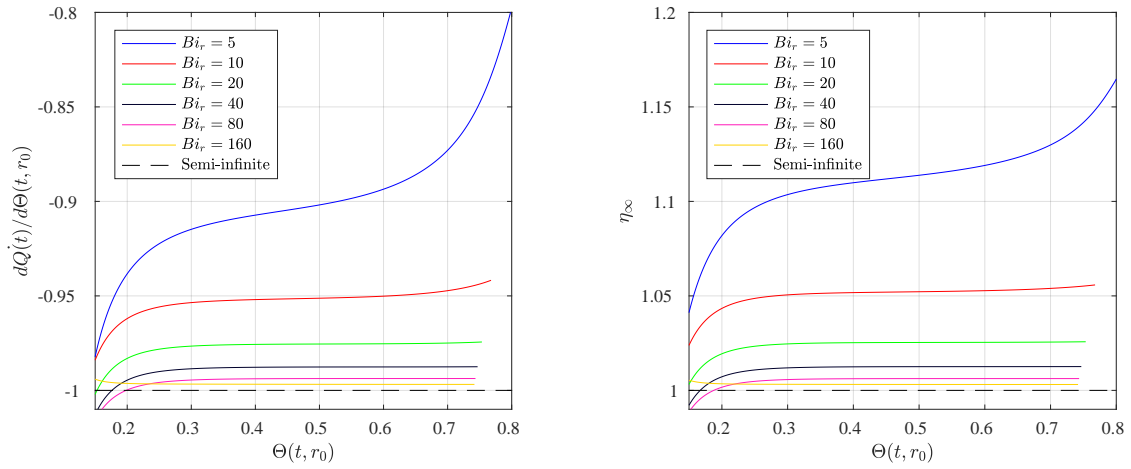


Fig. 3.10 Low Bi_r numbers lead to errors in derived heat flux

In figure 3.11a the derivative of $Q^*(t)$ with respect to $\Theta(t, r_0)$ is shown as a function of $\Theta(t, r_0)$. Since $dQ^*(t)/d\Theta(t, r_0)$ is equal to minus one in the semi-infinite case, the deviation from minus one provides an evaluation of the error in h as a function of Bi_r and $\Theta(t, r_0)$. As the Bi_r number reduces, the magnitude of $dQ^*(t)/d\Theta(t, r_0)$ also reduces. An important observation is that the value of $dQ^*(t)/d\Theta(t, r_0)$ is largely independent of $\Theta(t, r_0)$, where $\infty > Bi_r > 10$. The consequence of this is that the error in h will be largely independent of the duration of the transient measurement, and therefore reducing the duration of the transient measurement will have little impact on reducing error in h .

In figure 3.11b the evaluation of the non-dimensional adiabatic wall temperature is shown, as a function of $\Theta(t, r_0)$, where the true value is equal to one. The deviation from unity provides an evaluation of the error in Θ_{rec} . A similar trend in errors in Θ_{rec} can be seen as with errors in h . In summary, for Bi_r numbers greater than 40, the errors in both h and Θ_{rec} do not exceed 1.8%. Above a Bi_r number of 40, significant errors will arise which cannot practically be removed by reducing the duration of the transient measurement.



(a) Gradient of regression function, as a function of $\Theta(t, r_0)$ (b) Adiabatic wall temperature (by extrapolation of regression function) as a function of $\Theta(t, r_0)$

Fig. 3.11

FACTOR NGV - Example Analysis

Figure 3.12 shows the midspan vane section of the FACTOR NGV. An approximate mean surface radius is illustrated on the section, in four regions.

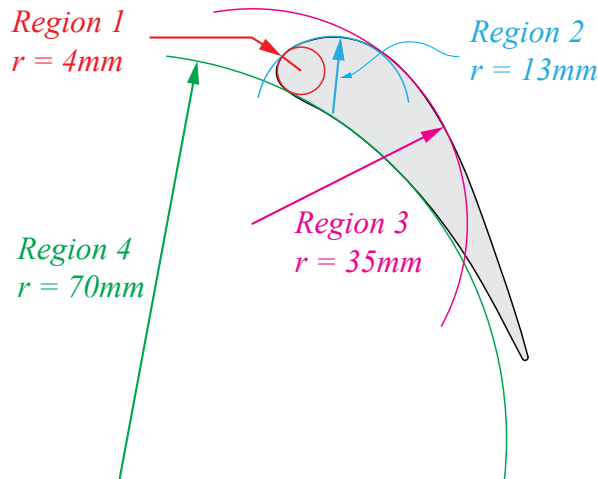


Fig. 3.12 Approximation of surface curvatures of the FACTOR NGV

The FACTOR NGV will be produced from a substrate with a thermal conductivity of $0.36 \text{ [Wm}^{-2}\text{K}^{-1}]$ (The reasons for which are described in section 5.2). An estimate of the

heat transfer coefficient which will exist in each region was made, and has been tabulated in table 3.1. From this information, the value of the Bi_r number can be estimated, and is also shown in table 3.1.

Note that ‘*Region 4*’ is a concave surface, and that the curvature induced error model just described, is based on conduction through a cylinder, with a convex surface. It will be assumed that for small values of $\Delta r/r_0$, errors introduced by convex curvature will be similar in magnitude to errors introduced by concave curvature.

Table 3.1 Approximate Bi_r on the FACTOR NGV in four regions

Region	Radius [mm]	h [Wm ⁻² K ⁻¹]	Bi_r
Region 1	~ 4	1000	11
Region 2	~ 13	1000	36
Region 3	~ 35	600	58
Region 4	~ 70	600	116

The Bi_r number in Region 3 and 4 is greater than 40, and hence the surface can be modelled as if it were a flat semi-infinite surface, without introducing significant errors in either \dot{q} , h or T_{aw} . The Bi_r number in Region 1 and 2 is less than 40, and hence, leaves us with the following options;

1. Use a substrate with a lower thermal conductivity, increasing Bi_r
2. Use a heat flux processing method which can account for surface curvature, reducing errors in $\dot{q}(t)$. (Such as the analytical curvature correction methods proposed by Buttsworth and Jones [1997]).
3. Accept the larger errors ($\sim 5\%$ error in ‘*Region 1*’ and $\sim 2\%$ in ‘*Region 2*’).

3.6.4 Boundary condition induced errors

It was described in section 3.2 that derivation of wall heat flux using one-dimensional semi-infinite models makes the assumption that the convective boundary conditions (h and T_{aw}) on the wall surface are uniform in space. If the boundary conditions are not uniform, errors in the derived heat flux will arise. Consider the portion of a semi-infinite body illustrated in

figure 3.13, where the body extends to infinity in the $\pm x$, $\pm y$ and $+z$ direction. Considering the case where the body is at uniform initial temperature of zero, at $t = 0$, and at $t > 0$, the adiabatic wall temperature on half the body is raised to unity. The convective heat transfer coefficient on the surface, at $z = 0$, is h .

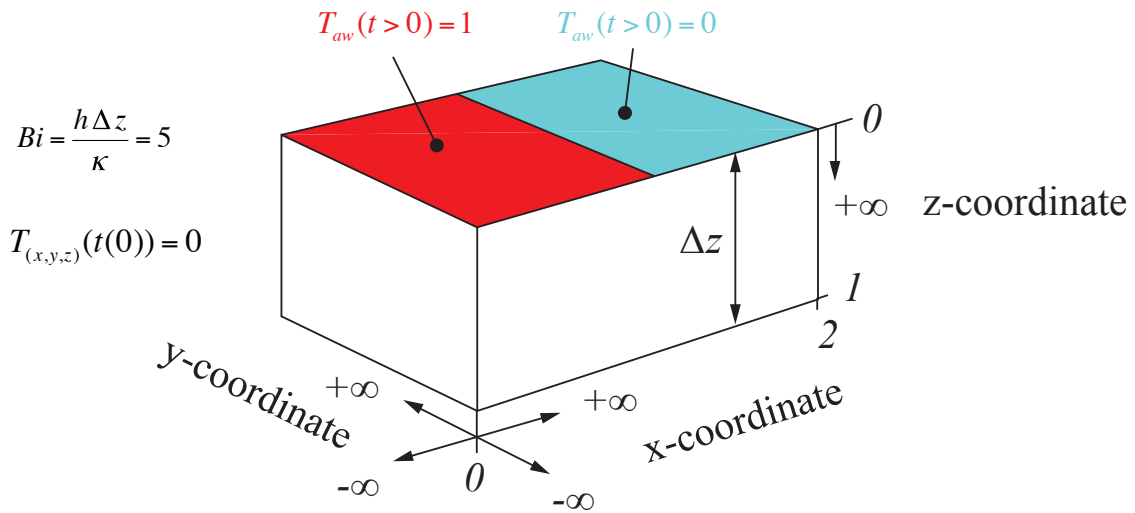


Fig. 3.13 A three dimensional semi-infinite body, with non-uniform convective boundary conditions

Due to the different heat transfer rates which occur in the two regions (red and blue surface), a non-symmetric temperature field about the $z - y$ plane, at $x = 1$, will be established over time. The resulting temperature gradients in the x direction will cause a lateral heat flux in the $+x$ direction, which will affect the surface temperature of the body over time.

A numerical simulation of the transient problem described above is shown in figure 3.14, at $t = Fo\Delta z^2/\alpha$, where Fo equals 0.11 (A Fo number of 0.11 ensures the numerical solution is semi-infinite in the z direction - since a finite domain extent in the z -direction was used - see section for further explanation 3.7.2). The left hand plot shows the non-dimensional temperature distribution in the $x - z$ plane, at an arbitrary location in y . The middle plot shows the partial derivative of the temperature distribution, with respect to z , and represents a heat flux term in the z direction. The right hand plot shows the partial derivative with respect to x , and represents a heat flux term in the x direction. It can be seen that in the region around the interface between the two surface boundary conditions, a lateral heat flux is induced. This heat flux distributes heat from left to right, altering the surface temperature, locally, near the boundary condition interface. The region significantly affected by this lateral heat flux,

has a length scale approximately equal to the heat penetration depth, δ , where δ is given by equation 3.44 (a re-arrangement of equation 2.9)

$$\delta = \sqrt{\frac{\alpha t}{Fo}} \quad (3.44)$$

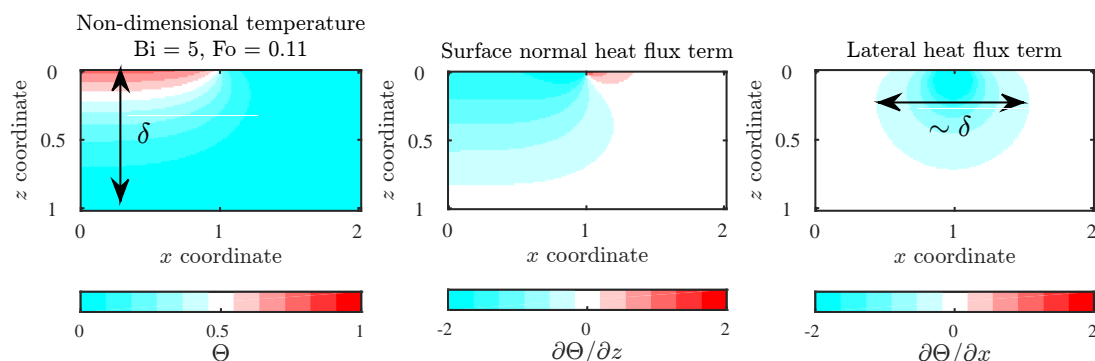


Fig. 3.14 Lateral heat flux terms are induced by the non-uniform convective boundary conditions

One-dimensional heat flux models are not capable of resolving this lateral heat flux term, and would consequently produce an inaccurate value of heat flux. In regions close to the BC interface - this would lead to an inaccurate local evaluation of h and T_{aw} . A two-dimensional, or three-dimensional heat flux modelling approach is required to accurately resolve the heat flux. In conclusion, if heat transfer measurements are made on a body with boundary condition variations which have a length scale approximately equal to, or less than the heat penetration depth, then 2D or 3D heat flux modelling methods will enable reduced local measurement error.

3.7 Maximising the Regression Extent, Θ_R

In Section 3.3, it was briefly described how there are two significant effects which limit the span of non-dimensional surface temperature rise measurement data which can be used for the linear regression. A reduction in the span of data for the linear regression leads to an increase in the uncertainty in the linear regression fit.

The first effect, is caused by non-instantaneous mainstream fluid temperature rises. During the temperature rise, the adiabatic wall temperature is varying, and hence measure-

ment data from this period is excluded from the regression. The non-dimensional surface temperature rise over this period was denoted $\tilde{\Theta}$.

The second effect, is caused by the finite thickness of the semi-infinite substrate. Complete non-dimensional surface temperature rise cannot be achieved in a substrate with finite thickness during a period of semi-infinite behaviour. The maximum surface temperature which can be achieved whilst remaining semi-infinite was denoted Θ_{limit} (where $\Theta_{\text{limit}} = \tilde{\Theta} + \Theta_R$). (See figure 3.3)

The theoretical approaches by which $\tilde{\Theta}$ can be minimised and Θ_{limit} maximised are explored in the following subsections.

3.7.1 Minimising $\tilde{\Theta}$

If we assume that a likely mainstream temperature rise can be approximately modelled as an exponential function (with a negative exponent), of the form given in equation 3.45, with time constant τ_∞ , then the non-dimensional surface temperature rise $\tilde{\Theta}$ which occurs during the initial unsteady period can be approximated by equation 3.46. (NB: An exact formula for determining $\tilde{\Theta}$ is provided by Ireland et al. [1999], but is unnecessarily complicated for the present purposes)

$$\frac{T_\infty(t) - T_{\infty,i}}{\Delta T_\infty(t \rightarrow \infty)} = 1 - \exp(-t/\tau_\infty) \quad (3.45)$$

$$\tilde{\Theta} \approx 1 - \exp\left(\frac{6h^2\tau_\infty}{e^2}\right) \operatorname{erfc}\left(\frac{h\sqrt{6\tau_\infty}}{e}\right) \quad (3.46)$$

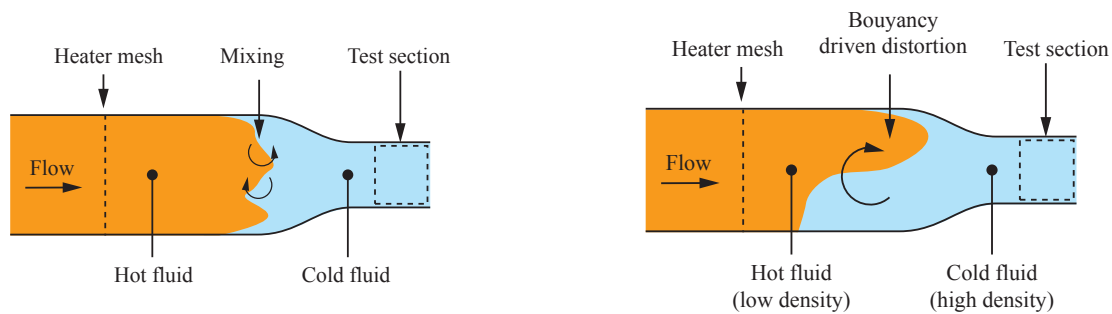
The multiplier 6, in equation 3.46 defines the mainstream temperature to be considered steady after 6 time constants have passed (i.e. the mainstream temperature has reached 99.8% of the total temperature rise). We can see from equation 3.46 that there are two variables with which $\tilde{\Theta}$ can be modified; τ_∞ and e . The magnitude of $\tilde{\Theta}$ can be reduced by the following:

1. Reducing the temperature rise time constant, τ_∞

In the case where a mainstream heater-mesh is being used to generate the mainstream temperature rise, as is the case on the FACTOR rig, reduction in the time constant can be made by:

- Reducing the thermal mass of the heater mesh - allowing the mesh to rise in temperature quickly.

- Reducing the period of time it takes the fluid to travel from the heater-mesh to the test section. This will have two effects: Firstly, it will reduce the amount of mixing at the interface between the cold and hot air stream as it advects to the test section (figure 3.15a). Secondly, by reducing the advection time, distortions in the interface between cold and hot air streams, caused by buoyancy, are reduced. (figure 3.15b).



(a) Mainstream mixing will increase τ_∞

(b) Buoyancy effects will increase τ_∞

Fig. 3.15

- Reducing the heat transfer from the mainstream fluid to the wind tunnels walls, between the heater-mesh and the test section. This can be achieved by using thermal insulation, with low thermal mass, on the wind tunnels walls, and will reduce heat transfer from the mainstream fluid, maintaining a low τ_∞ .

2. Increasing substrate thermal effusivity

Increasing the thermal effusivity of the measurement substrate will reduce the rate at which the surface temperature changes in response to the temperature step. The surface temperature rise will then be smaller over the unsteady period, resulting in a smaller $\tilde{\Theta}$. This concept has already been introduced in terms of effectively increasing the temporal resolution of wall temperature measurements, in section 3.5.1.

Yet another approach to effectively reduce $\tilde{\Theta}$, is to *measure* the mainstream temperature rise function. If this can be measured sufficiently accurately, then a *floating linear regression* method can be used, as Collins et al. [2015] showed. (The *floating linear regression* method was described in section 2.4.2 of the Literature Review).

One implementation of this approach, would be to define the non-dimensional surface temperature rise as a function of the time-varying mainstream temperature, as shown in

equation 3.47. In theory, this method will permit $\tilde{\Theta}$ to be reduced to zero, provided sufficiently well resolved and accurate measurements of $\Delta T_\infty(t)$ can be obtained.

$$\Theta(t) = \frac{T_{\text{wall}}(t) - T_{\text{wall},i}}{\Delta T_\infty(t)} \quad (3.47)$$

It is important to note however, that small temporal lags in the measurement of $\Delta T_\infty(t)$ can introduce substantial errors by this method, due to the high rate of mainstream temperature rise. If $\Delta T_\infty(t)$ were measured with a thermocouple, temporal lags will be present.

The consequence of this is that practically speaking, not all of $\tilde{\Theta}$ can be recovered, without introducing new larger errors than those being removed. Care must be taken to determine from what point in time the measurements of $\Delta T_\infty(t)$ are accurate, and only perform the *floating linear regression* from that point in time onwards.

3.7.2 Maximising Θ_{limit}

The second means by which Θ_R can be increased, is to increase Θ_{limit} - which is the maximum value the wall temperature reaches - as it approaches the semi-infinite limit (see figure 3.3).

The equations governing the value of Θ_{limit} are now explored. Recalling equation 3.11, which describes the one-dimensional heat propagation through a semi-infinite body, in response to a step change in mainstream temperature, we have;

$$\Theta(x,t) = \text{erfc}\left(\frac{1}{2\sqrt{\text{Fo}}}\right) - \left[\exp\left(\text{Bi} + \text{Bi}^2\text{Fo}\right)\right] \left[\text{erfc}\left(\frac{1}{2\sqrt{\text{Fo}}} + \text{Bi}\sqrt{\text{Fo}}\right)\right] \quad (3.48)$$

We can see from equation 3.48 that the temperature at any given point in space and time is only a function of the two non-dimensional values Bi and Fo. A series of solutions to equation 3.48 are shown in figure 3.16. The value $1/\sqrt{\text{Fo}}$ represents a non-dimensional depth into the semi-infinite body, and $\text{Bi}\sqrt{\text{Fo}}$ represents a non-dimensional time.

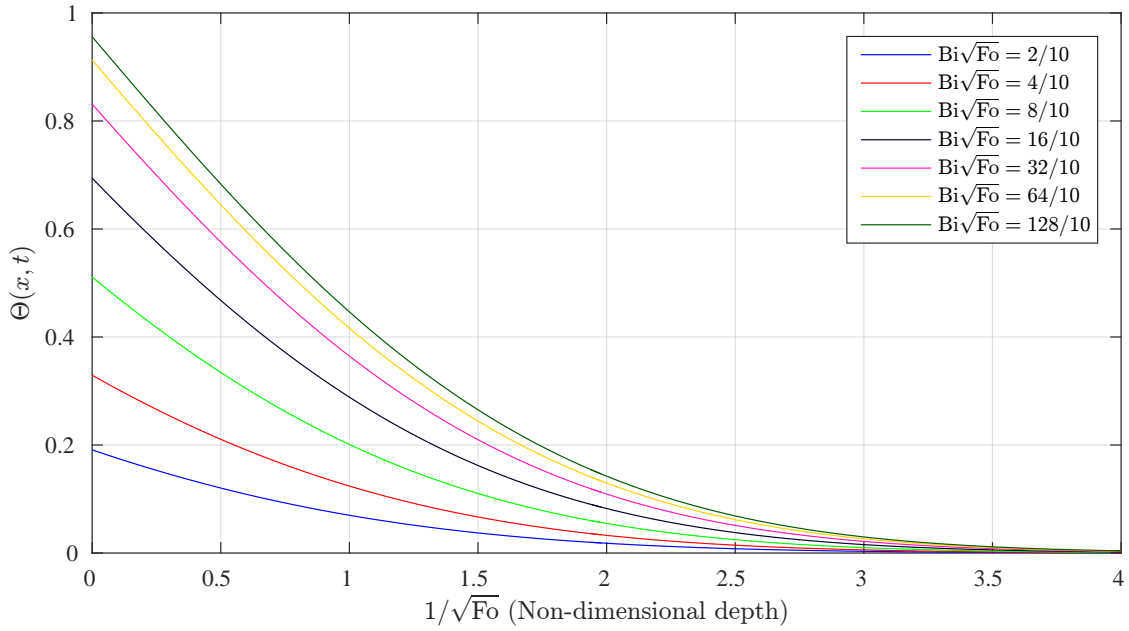


Fig. 3.16 Non-dimensional transient conduction solutions (equation 3.48)

It can be seen from figure 3.16, that the value of $\Theta(x, t)$ is approximately zero, where $1/\sqrt{Fo}$ is greater than ~ 4 , for all $Bi\sqrt{Fo}$. This, in essence, is the semi-infinite assumption: If $1/\sqrt{Fo}$ is kept above ~ 4 , the substrate can be considered to be infinitely thick.

As discussed in the Literature Review (section 2.4.1), different authors have adopted different limiting values of $1/\sqrt{Fo}$. Schultz and Jones [1973] specified a minimum value of 3.16, Iliopoulou et al. [2004] of 3.65, and Najafabadi et al. [2015] and Luque et al. [2015] of 4. It is desirable to have this value as low as possible, so as to prolong the measurement duration and maximise Θ_R . We can now consider a maximum Fourier number, Fo_{limit} , at which value a finite thickness substrate will be at the limit of the semi-infinite assumption, such that;

$$\Theta_{\text{limit}}(0, t) = 1 - \exp(Bi^2 Fo_{\text{limit}}) \text{erfc}(Bi\sqrt{Fo_{\text{limit}}}) \quad (3.49)$$

From equation 3.49, we now see that in order to maximise Θ_{limit} , the value of $Bi\sqrt{Fo_{\text{limit}}}$ must be maximised.

For a given heat transfer coefficient, the Biot number can readily be maximised by maximising the thickness of the substrate, x , and minimising the thermal conductivity, κ . This point emphasises the value in having large scale test rig components, where large substrate thickness can be achieved, leading to large Biot numbers and consequently large

values of Θ_{limit} . In the FACTOR turbine rig, large Biot numbers are not easily achieved, due to the low geometric scale of the vanes and blades, and due to the inability to use ideal substrate materials, due to high operating temperatures and stresses.

It thus becomes particularly important to determine the optimum value of Fo_{limit} , which, on the one hand maximises Θ_{limit} , and on the other hand minimises errors introduced by non-semi-infinite effects. An optimum Fo_{limit} number will exist, which minimises the overall uncertainty of the measurement. The value of this optimum Fo_{limit} will not be fixed, and is a function of other measurement parameters.

Optimum Fourier Number

In figure 3.17 the transient non-dimensional temperature in a semi-infinite body, at a distance x from the surface is shown, as a function of Biot and Fourier number. It can be seen that while $1/\sqrt{\text{Fo}}$ is greater than ~ 3.5 , the temperature rise at distance x does not exceed ~ 0.01 (i.e 1%), for all Biot numbers. For lower values of $1/\sqrt{\text{Fo}}$, the temperature rise becomes increasingly significant. It is on this basis that Schultz and Jones [1973] defined a minimum $1/\sqrt{\text{Fo}}$ number of 3.16, to ensure a sufficiently semi-infinite condition.

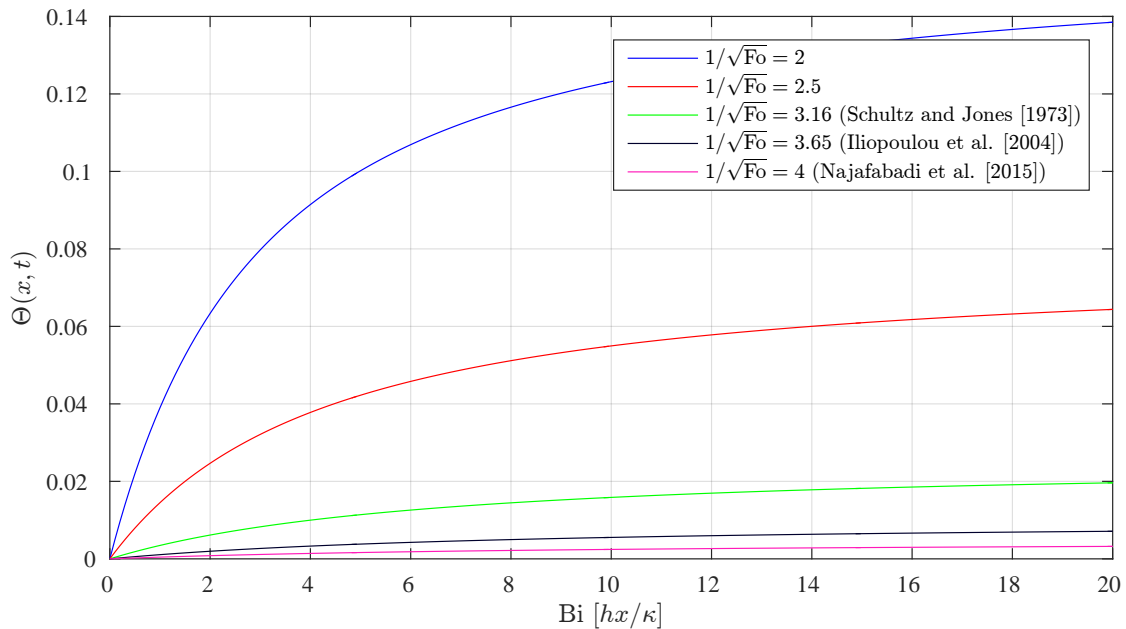


Fig. 3.17 Back surface temperature rise as a function of Biot and Fourier number

An alternative logic is as follows: We wish to find the maximum value of Fo_{limit} which leads to a negligible contribution to the uncertainty in h and T_{aw} , caused by non semi-infinite

effects. h and T_{aw} are derived from the transient **surface** temperature response $T(0,t)$. Therefore, if Fo_{limit} is set to a value which leads to a maximum deviation in $T(0,t)$ (or equally $\Theta(0,t)$), from the true semi-infinite solution of no more than, say, 1%, then we can expect the uncertainty contribution in h and T_{aw} to be less than 1%. (Since the maximum deviation in $\Theta(0,t)$ will only occur for the last data point - all other data points will have a lower error - hence the linear regression function will be dominated by data points with lower errors).

Two cases are considered, and illustrated in figure 3.18, where a one-dimensional slab of thickness Δx is exposed to a constant convection boundary condition on its top surface. The slab is initially at uniform temperature T_i . In *Case 1*, the bottom surface boundary condition is a Dirichlet condition, with fixed temperature $T(\Delta x)(t) = T_i$. In *Case 2*, the bottom surface boundary condition is an adiabatic Neumann condition, with temperature gradient $dT_{(\Delta x)}(t)/dx = 0$.

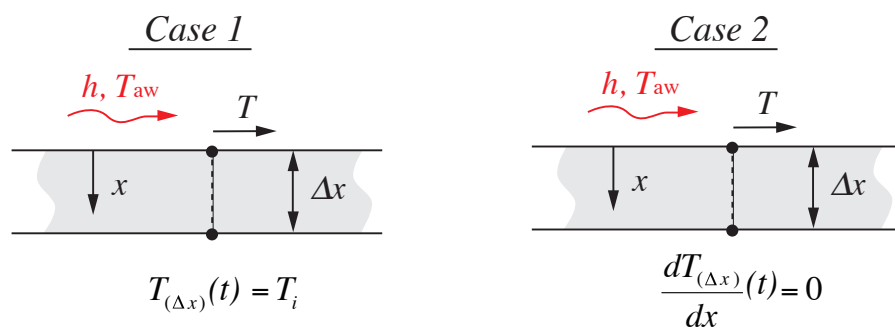


Fig. 3.18 Back surface boundary conditions for Case 1 and 2

These two cases represent the worst case, (maximum and minimum), deviations from a true semi-infinite body response which can be expected to occur in a turbine rig (assuming the slab is flat). *Case 1* is representative of a scenario with maximum back surface heat loss, where the back surface of the slab is aggressively cooled by an internal cooling flow (with infinite heat transfer coefficient). *Case 2* is representative of a scenario with zero back surface heat loss, which will approximately be the case on an NGV trailing edge, where an adiabatic mid-plane can be imagined. These concepts are illustrated in figure 3.19.

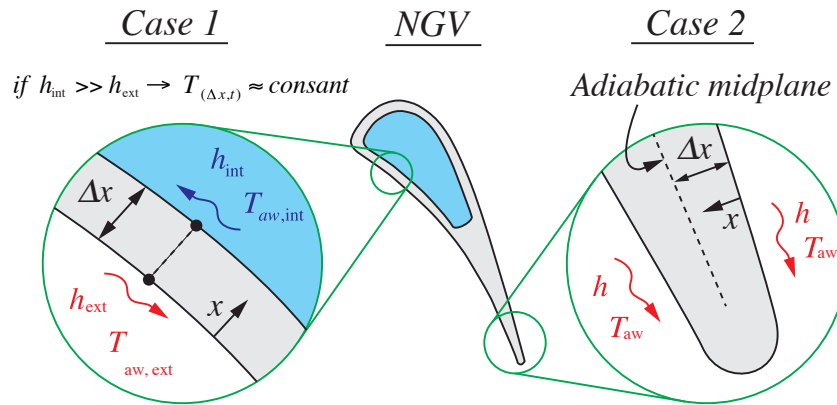
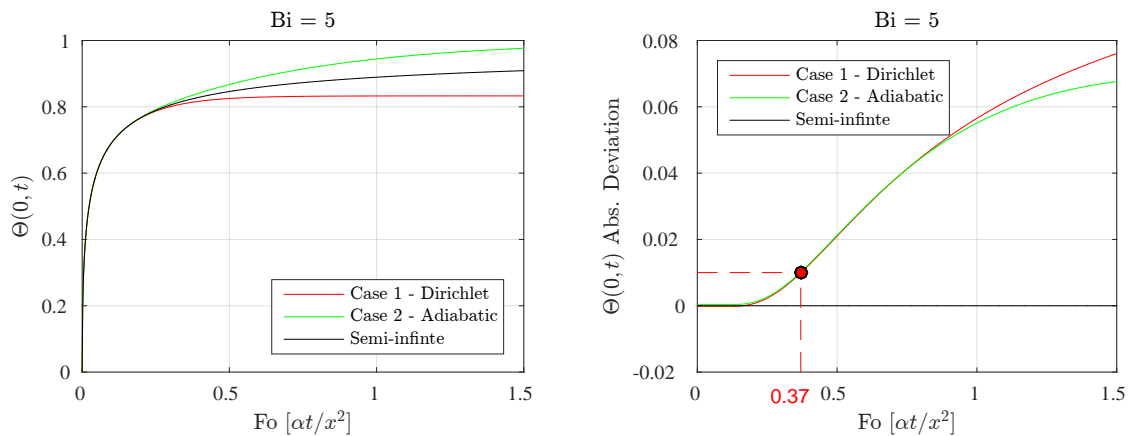


Fig. 3.19 Expected location of worst case back surface boundary conditions on an NGV

The transient surface temperature response of these two slabs, and a semi-infinite body, in response to a step change in T_{aw} , where the Biot number equals 5, is shown in figure 3.20a. (A Biot number of 5 was chosen as this is similar to the Biot numbers expected on the FACTOR rig). The absolute value of the deviation of the surface temperature from the semi-infinite response is shown over time in figure 3.20b, for both *Case 1* and *Case 2*. The solutions were generated by means of a one-dimensional finite-difference model.



(a) Transient response for *Case 1*, *Case 2*, and the semi-infinite case (b) Absolute deviation of *Case 1* and *Case 2* from the semi-infinite case

Fig. 3.20

From figure 3.20b it can be seen that an error in $\Theta(0, t)$ greater than 1% occurs only when the Fo number is greater than ~ 0.37 (or $1/\sqrt{Fo} < 1.64$). This is in contrast with Schultz and Jones [1973], who determined the maximum Fo number to be 0.1, at which value the error in $\Theta(0, t)$ is approximately zero. The consequence of this analysis, is that it suggests that

by allowing a slight increase in the semi-infinite modelling uncertainties, of order 1%, the duration of the transient measurement can be extended in time by a factor of ~ 3.7 . Under certain circumstances, this will greatly reduce measurement uncertainties which originate from other sources, outweighing the $\sim 1\%$ modelling error.

The Fourier number at which a 0.5, 1 and 2% deviation in $\Theta(0,t)$ occurs, was assessed for a range of relevant Biot numbers, using the numerical model. The assessment was made for both Case 1 and Case 2 boundary conditions. The case with the greatest Fourier number was recorded, and is shown as a function of Biot number in figure 3.21.

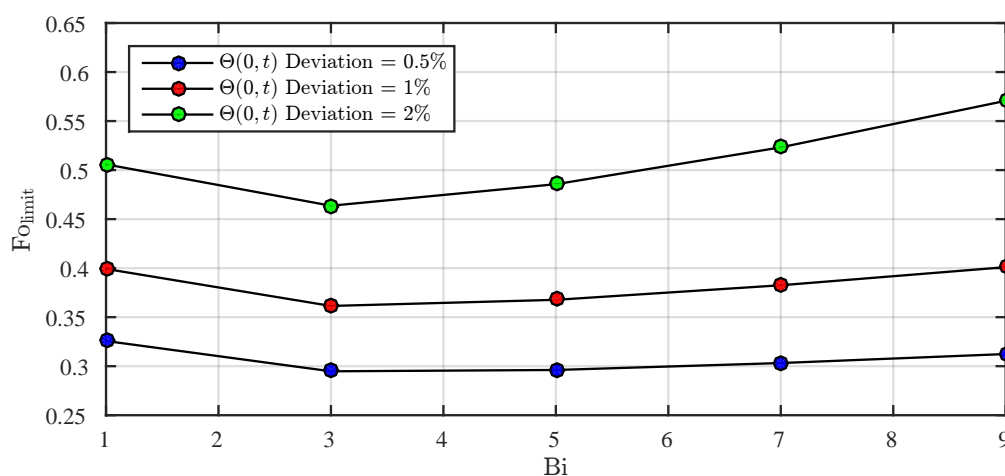


Fig. 3.21 Fo_{limit} as a function of maximum $\Theta(0,t)$ deviation from semi-finite case and Biot number

The case (*Case 1* or *Case 2*), with the greater deviation from the semi-infinite case, changes as a function of Biot number, which is the reason for the inflection point in figure 3.21 at $Bi \approx 3$. Overall, however, the Fo_{limit} number remains relatively constant for a given prescribed deviation in $\Theta(0,t)$, over the range of evaluated Biot numbers.

Figure 3.22 shows the value of Θ_{limit} as a function of Biot number and Fo_{limit} . (In the FACTOR rig, the Biot numbers on the vanes and blades will be between ~ 0.5 and 10 - hence only this range of Biot numbers are shown).

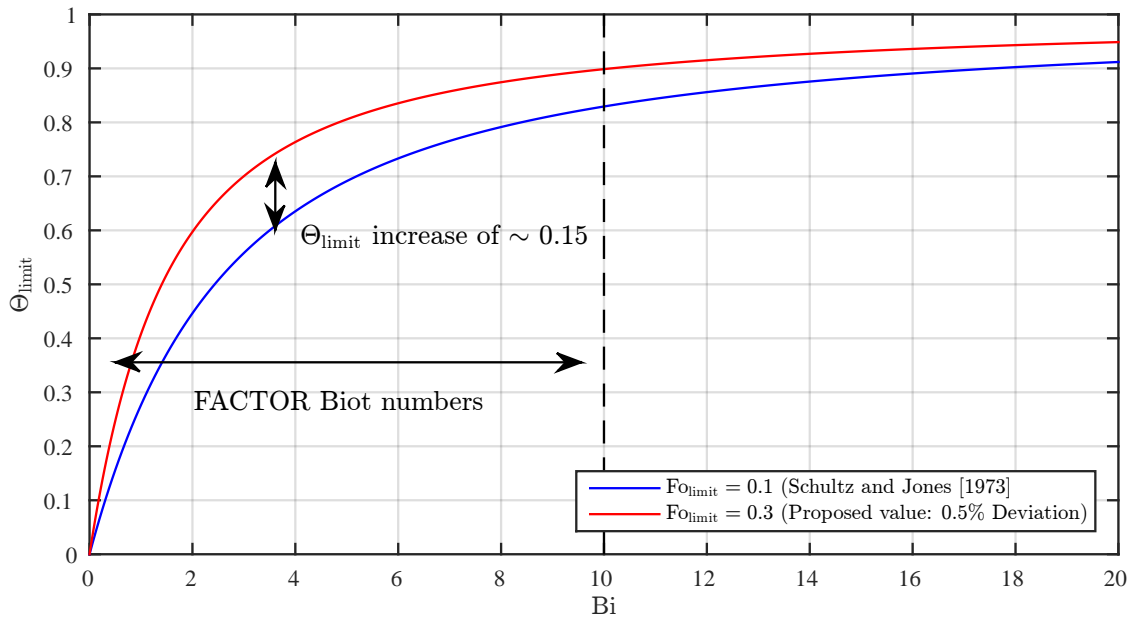


Fig. 3.22 Increasing the Fo_{limit} number from 0.1 to 0.3 provides a significant increase in Θ_{limit} at FACTOR Biot numbers

It can be seen from figure 3.22 that an increase in the Fo_{limit} number from 0.1, (as proposed by [Schultz and Jones, 1973]), to 0.3, (as currently proposed), provides a significant increase, (up to +0.15), in the value of Θ_{limit} at FACTOR Biot numbers.

If we assume a typical value of $\tilde{\Theta}$ to be 0.3 (as has been found to be the case, in section 7.4), then this increase in Θ_{limit} represents a $\sim 50\%$ increase in Θ_R , and is therefore likely to lead to a significant reduction in the uncertainty of both h and T_{aw} .

It is apparent from this analysis that an optimum Fo_{limit} number will exist, which balances the uncertainty contributions from inaccuracies in the semi-infinite assumption, and from the linear regression over the transient surface temperature Θ_R . Calculation of the true optimum is beyond the scope of this analytical work, as its value is dependant on a large number of complex variables (such as the characteristics of the noise of the wall temperature measurements). A value of 0.25 was adopted, and used in the uncertainty analysis in Chapter 4, and the experimental measurements in Chapter 7.

3.7.3 Optimum substrate material properties

In Section 3.3 it was identified that in order to increase Θ_R , to gain a reduction in measurement uncertainty, $\tilde{\Theta}$ must be reduced, or Θ_{limit} must be increased. In this section, (Section 3.7), it

has been identified that $\rho c, \kappa, x, \tau_\infty$ and Fo_{limit} are the control variables which can be used to maximise Θ_R . In summary;

1. $\tilde{\Theta} \rightarrow$ minimise by: maximising e ($e = \sqrt{\rho c \kappa}$), or by minimising τ_∞
2. $\Theta_{\text{limit}} \rightarrow$ maximise by maximising Bi (i.e. maximise x/κ)
3. $Fo_{\text{limit}} \rightarrow$ maximise by maximising t (errors $\sim 0.5\%$ are introduced if $Fo_{\text{limit}} > 0.3$).

Increasing κ leads to a reduction in $\tilde{\Theta}$, but also a reduction in Θ_{limit} . The question arises; which substrate material, with material properties κ and ρc , maximises Θ_R ?

The non-dimensional wall temperature rise of a semi-infinite body, at uniform initial temperature, in response to an exponential increase in adiabatic wall temperature (with a negative exponent), and constant heat transfer coefficient, is given by equation 3.50 [Ireland et al., 1999].

$$\Theta(t) = 1 - \frac{\rho c \kappa / h^2 \tau_\infty}{(1 - \rho c \kappa / h^2 \tau_\infty)} \exp\left(\frac{h^2 t}{\rho c \kappa}\right) \operatorname{erfc}\left(\frac{h \sqrt{t}}{\sqrt{\rho c \kappa}}\right) - \exp\left(\frac{t}{\tau_\infty}\right) \left(\frac{1}{(1 + \rho c \kappa / h^2 \tau_\infty)}\right) \left(1 + \frac{\sqrt{\rho c \kappa}}{h \sqrt{\tau_\infty}} \left(\frac{1}{\pi} \sqrt{\frac{t}{\tau_\infty}} + \frac{2}{\pi} \sum_{n=1}^{\infty} \frac{1}{n} \exp\left(-\frac{n^2}{4} \sinh n \sqrt{\frac{t}{\tau_\infty}}\right)\right)\right) \quad (3.50)$$

An expression for $\tilde{\Theta}$ can then be found by substituting $t = 5.5 \tau_\infty$ into equation 3.50. The value of 5.5 time constants specifies the temperature rise to have reached 99.5% of its final value - the temperature after this point being considered to be stable. (Note that a value of 5.5 time constants was specified so as to approximately match the error contribution from the optimum Fourier number analysis discussed in the previous section).

Equally, an expression for Θ_{limit} can be found by substituting equation 3.51 into equation 3.50.

(Note that equation 3.50 is an exact solution, whereas the the equation used previously, (equation 3.46), was an approximation. An exact solution is required for the current analysis, whereas as the approximation used previously was more suitable for the purposes of the analysis).

$$t_{\text{limit}} = \frac{x^2 Fo_{\text{limit}}}{\alpha} \quad (3.51)$$

The value of Θ_R is then given as;

$$\Theta_R = \Theta_{\text{limit}} - \tilde{\Theta} = f(h, \rho c, \kappa, \tau_\infty, x, \text{Fo}_{\text{limit}}) \quad (3.52)$$

A series of solutions to equation 3.52 were calculated numerically. In figure 3.23a - 3.23c the calculated value of Θ_R is shown as a function of ρc and κ , representing a matrix of conceivable substrate materials. The solutions were calculated assuming a substrate thickness of 2mm (justification for which is provided in section 4.5) and a mainstream temperature rise time constant of 0.1s - which are representative of the FACTOR rig. A Fo_{limit} number of 0.25 was specified. Three solutions are shown for three different heat transfer coefficients - again, representative of the range of values expected in the FACTOR rig. It is evident from figures 3.23a - 3.23c that an optimum value of κ exists, which maximises Θ_R , where the optimum value varies with h .

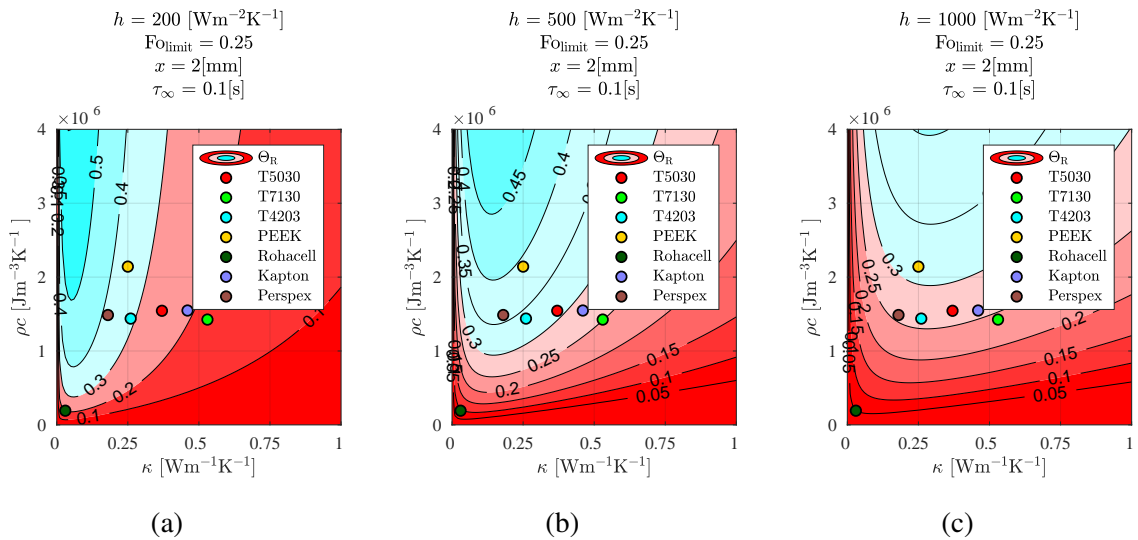


Fig. 3.23 Analytical expression of Θ_R as a function of h , κ and ρc

In figure 3.24a - 3.24c a further set of solutions to equation 3.52 are shown, where the substrate thickness has been increased from 2 to 5mm. The values of Θ_R are significantly increased, which illustrates the impact of small scale geometry on measurement uncertainty. The change in substrate thickness has also altered the value of the optimum thermal conductivity.

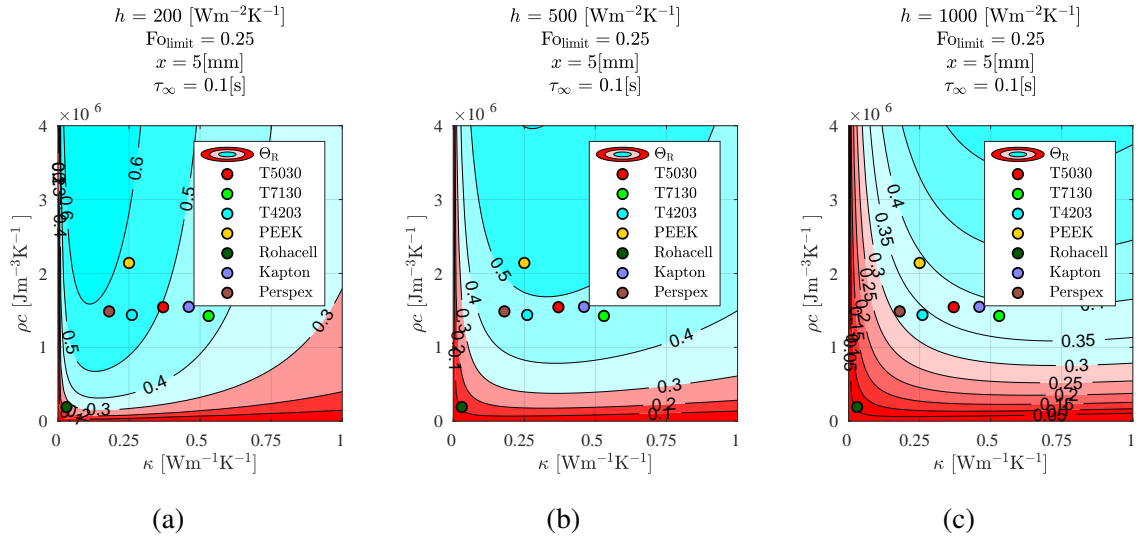


Fig. 3.24

A range of candidate substrates for the FACTOR rig have been plotted in figure 3.23a - 3.24c, including Torlon 5030 (T5030), Torlon 7130 (T7130), Torlon 4203 (T4203) and Polyether-ether-keytone (PEEK). (Metals, with their comparatively high thermal conductivities, are evidently not suitable candidate substrates). It can be seen that the material which achieves the greatest value of Θ_R varies with h and x as illustrated in the figures, but also with τ_∞ and Fo_{limit} . Given the large set of variables which governs the optimum value of κ , a full set of solutions to equation 3.52 cannot be shown here. Rather, the author suggests evaluation of equation 3.52 around the expected measurement conductions as an analysis tool. (Note the dependence of the uncertainty in h and Θ_{rec} as a function of all of these variables are explored in the uncertainty modelling chapter - section 4).

In summary, then, the optimum substrate material properties are dependant on variables which are likely to be governed by the features of the specific rig in question. Substrate materials should be ‘tuned’ to the rig, in order to minimise measurement uncertainty. This tuning is performed for the FACTOR rig in Chapter 4.

3.8 Conclusions

The most important results from this chapter are summarised below:

- The heat transfer measurement technique which will yield the lowest measurement uncertainties is significantly influenced by the constraints of the test facility. The measurement technique needs to be matched to the test facility.

- For the FACTOR turbine test rig, a transient measurement technique, making use of IR thermography was selected as the most capable measurement method.
- Uncertainty in transient heat transfer measurements can be significantly influenced by:
 - **Substrate thermal conductivity:** It was shown that an optimum substrate thermal conductivity will exist, which leads to a maximum range of non-dimensional surface temperatures over which a linear regression is performed - leading to a well conditioned evaluation of h and T_{aw} . It was shown that the optimum value of the thermal conductivity depends on the geometric scale of the rig, the magnitude of the heat transfer coefficients, the time-constant of the mainstream temperature-step, and the heat capacity of the substrate - most of which are highly rig-specific.
 - **Substrate heat capacity:** Increasing the heat capacity of the substrate (alone), will result in measurements with lower uncertainty.
 - **Geometric scale:** Large rigs can permit greater heat penetration depths before 3D conduction errors begin to escalate. This leads to longer transient measurement periods, with greater non-dimensional surface temperature rise, resulting in reduced measurement uncertainty. Alternatively, for a given heat penetration depth, large rigs will allow greater spatial measurement resolution, due to reduced lateral conduction induced errors.
 - **Uncertainty in non-dimensional surface temperature:** It was shown that the transient surface temperature changes must be large in relation to surface temperature measurement uncertainty. Sufficiently large mainstream temperature steps, or sufficiently low uncertainty measurement instruments must be used.
 - **Uncertainty in the substrate thermal effusivity:** Errors in the measured heat transfer coefficient will be scaled linearly by errors in the assumed substrate thermal effusivity. Errors in the adiabatic wall temperature, however, are unaffected.
 - **Uncertainty in substrate steady initial conditions:** Uncertainty in the adiabatic wall temperature measurement was found to be linearly proportional to uncertainty in the initial steady state heat-flux at the surface of the substrate. Uncertainty in the heat transfer coefficient, however, is unaffected (neglecting small second order effects). A new parameter, Θ_{rec} , was defined as a means of expressing a meaningful non-dimensional adiabatic wall temperature, in the presence of an unknown steady state initial heat-flux.

-
- One-dimensional semi-infinite models can be used to accurately determine transient heat-flux, provided the Biot number, based on the radius of curvature, is above 40.
 - When using one-dimensional semi-infinite heat flux modelling, the ability to resolve aerodynamic features (in h or T_{aw}), with length scales less than the heat penetration depth is significantly limited by lateral conduction effects. (i.e. resolution is limited by the heat penetration depth). Three-dimensional heat-flux modelling is required to gain increased resolution beyond this limit.

Chapter 4

Uncertainty Analysis

In this chapter an uncertainty and a sensitivity analysis is performed with a Monte-Carlo simulation. The simulation outputs provide an estimate of the measurement uncertainty in h and Θ_{rec} as a function of h , ρc , κ , τ_{∞} , $\Delta T_{0,\infty}$ and δ . Calculations are performed at FACTOR rig conditions, and an expected FACTOR rig measurement uncertainty is provided for each measurement location.

4.1 Introduction

In Chapter 3 analytical and numerical models were used to determine which parameters are most influential in affecting uncertainty in transient measurements of heat transfer. Many of these parameters have a non-linear influence on measurement uncertainty, as evident from the form of equation 3.50. It was shown that there is a requirement to balance the uncertainty contributions from competing mechanisms, in order to minimise the overall measurement uncertainty. It is therefore important to understand the sensitivity of the heat transfer measurement uncertainty to these parameters, such that an optimal balance can be achieved - minimising overall measurement uncertainty.

In this chapter, an uncertainty model is described, in section 4.2, and the output presented in section 4.3 and 4.4 . The model estimates measurement uncertainty as a function of the dominant variables. Due to the large number of variables (dominant terms) which govern the uncertainty, a full solution cannot be presented graphically. Instead, the following are provided:

1. A **Sensitivity Analysis** is performed at conditions matching those of the FACTOR NGV, in section 4.3. In this analysis, the affect of varying h , $\Delta T_{0,\infty}$, τ_∞ , δ (heat penetration depth) and κ , on the predicted heat transfer measurement uncertainty is examined. These parameters directly affect the four conditioning parameters, U_Θ , U_{Q^*} , $\tilde{\Theta}$ and Θ_{limit} which were introduced in section 3.3. This analysis is provided to give greater insight into the influence of each of the conditioning parameters, and develop an understanding of what absolute values of these parameters are required to yield low uncertainty measurements. The output from the sensitivity analysis was used to guide rig design decisions in the FACTOR project.
2. An **Uncertainty Analysis** of the FACTOR rig heat transfer measurements, for the NGV, rotor and LP vane, based on the final design specification of the rig, is provided in section 4.4. Uncertainty is estimated as a function of h and $\Delta T_{0,\infty}$, representing a matrix of probable boundary conditions which will be present at various spatial locations on the blades and vanes. The solutions therefore provide an initial estimate of the measurement uncertainty which is expected on the FACTOR rig.

4.2 Uncertainty Modelling

To begin with, a definition of two categories of measurement uncertainty are provided; Precision, and Bias uncertainty.

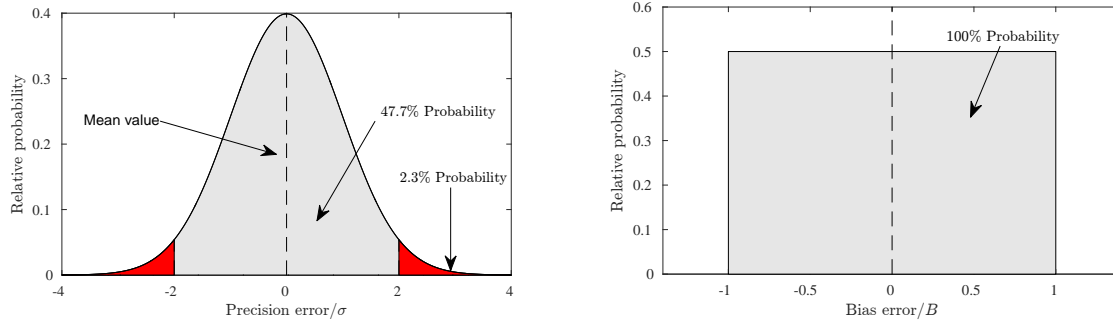
Precision uncertainties

Precision uncertainties are an expression of the magnitude of random variation in a quantity, which occurs within a relevant time scale. A ‘relevant time scale’, in this instance, is the duration of the transient measurement. The high frequency noise component in, for instance, IR radiance measurements from a constant temperature target, is an example of a precision error. It is convenient to express this range of potential measurement errors in terms of a precision uncertainty in the measured value.

Precision uncertainties in measurement systems are often well characterised by a Normal distribution (figure 4.1a), where the probability of obtaining a measurement with a given error, decreases with the magnitude of the error, according to the Normal distribution function. The precision uncertainty can be quantified as a multiple of the Standard Deviation, (σ), of the measurement, from the mean value. If the errors in a measured quantity are normally distributed, then there is a 95.4% probability that any one measurement will lie within $\pm 2\sigma$ of the time mean value. Precision uncertainties will be expressed as $\pm 2\sigma$, from here onwards. Precision uncertainty terms will be denoted P .

Bias uncertainties

Bias uncertainty, in contrast, is an expression of the magnitude of the uncertainty in a quantity, which remains constant over the relevant time scale. In our case, an uncertainty in the thermal conductivity of the substrate would represent a bias uncertainty, as the error between the assumed value and the true value is unlikely to change significantly over the relevant time scale. Bias uncertainties are often better characterised by square probability distribution functions (figure 4.1b). Bias uncertainty will be denoted B .



(a) Normal probability distribution function - Used to characterise precision errors (b) Square probability distribution function - Used to characterise bias errors

Fig. 4.1 The probability distribution functions used for Precision and Bias error terms

4.2.1 The Monte-Carlo method

As previously stated - measurement uncertainty in h and Θ_{rec} is a non-linear function of a large number of parameters. From Chapter 3, the following parameters were identified as highly influential on the measurement uncertainties. (Where $f_{T_{\text{wall}}}$ is the wall temperature sampling frequency, and $U_{\Delta T_{\infty,t}}$ is the uncertainty in the mainstream total temperature)

$$U_h, U_{\Theta_{\text{rec}}} = f(h, \rho c, \kappa, \tau_{\infty}, \text{FO}_{\text{limit}}, x, U_{\Delta T_{\infty,t}}, U_{\Delta T_{\text{wall},t}}, f_{T_{\text{wall}}}) \quad (4.1)$$

Analytical methods of evaluating the overall measurement uncertainty, as a function of all of the above parameters, are likely to be inadequate, as indicated by GUM [2008]. This is due to the non-linearity of the system we wish to model, and the requirement to model potentially large uncertainties. A statistical Monte-Carlo (MC) approach was identified as a suitable means of uncertainty quantification, as this method is able to model non-linear systems, with potentially large measurement uncertainties. Successful examples of MC model implementation for similar applications were presented by Yan and Owen [2002] and Ma et al. [2015].

In the MC method, a system of functions is defined, which transforms a number of inputs into a number of outputs. In our case, the system is one that represents the measurement system that transforms time resolved wall temperature measurements into time mean values of h and Θ_{rec} . The system of functions is then executed, numerically, a statistically large number of times, where the inputs to the system are perturbed in each iteration, so as to represent either a precision or bias uncertainty in the measured values. The range of output

values from the system of functions can then be examined with statistical tools, to determine the magnitude of bias and precision errors which result, as a function the input uncertainties.

4.2.2 System modelling

We wish to characterise the precision and bias uncertainties in the output values of h and Θ_{rec} , as a function of a number of system variables, and of the source measurement precision and bias uncertainty terms. In order to achieve this, three parallel MC numerical simulations were performed:

1. Bias error variation only

In this implementation of the MC model, bias errors were introduced into the relevant model inputs. In each iteration of the MC model, the magnitude of each bias error was randomly sampled from a continuous uniform type distribution, with upper and lower limits. From this distribution, there is an equal probability of a bias error term having any value between the upper and lower limit. Errors from precision uncertainty terms were not introduced.

The range of output values from the MC model, thereby represent the range of probable bias uncertainties in h and Θ_{rec} .

The bias uncertainty was calculated from the root mean square sum of the standard deviation and the mean output value error, $\bar{h}_{MC} - h$, as shown in equation 4.2. (Where \bar{h}_{MC} is the mean predicted heat transfer coefficient, and h is the true heat transfer coefficient - as defined from the source wall temperature transient signal). The subscript 'MC', indicates an output value from the MC model. (Substitution of h for Θ_{rec} , in equation 4.2 provides the expression for bias uncertainty in Θ_{rec}).

$$B_h = \sqrt{(2\sigma_{h_{MC}})^2 + (\bar{h}_{MC} - h)^2} \quad (4.2)$$

2. Precision error variation only

In a second implementation of the model, precision errors were introduced into the relevant model inputs. The magnitude of the precision errors were randomly sampled from a Normal probability distribution. Different randomised precision errors were added to the relevant terms at each instant in time, throughout the system simulation. Errors from bias uncertainty terms were not introduced. The variation of the output of the model, thereby represents the precision uncertainty in h and Θ_{rec} .

The precision uncertainty was defined as two times the standard deviation of the output value.

$$P_h = 2\sigma_{h_{MC}} \quad (4.3)$$

3. Bias and precision error variation

In the two model implementations described above, an assumption is made; that the influence of the bias and precision error terms are independent. In reality, this is not the case - the presence of a bias error can influence the magnitude of the precision uncertainty in the output. It is expected however, that under most conditions, this interaction is weak, and that significant interaction only occurs under extreme poor conditioning of the transient measurement, where uncertainties are large. The solutions to the two models described above, therefore provide an approximate evaluation of the bias and precision uncertainties in the output.

A third MC model implementation was executed, where both bias *and* precision errors were introduced - such that the interaction between the two types of uncertainty would be present. However, with this model, it is not possible to distinguish the constituent components of bias and precision error in the output values, rather an overall uncertainty term is given, the expression for which, is given in equation 4.4.

$$U_h = \sqrt{(2\sigma_{h_{MC}})^2 + (\bar{h}_{MC} - h)^2} \quad (4.4)$$

A description of the Monte-Carlo algorithm used is given briefly below - provided in sequential order of events:

1. An idealised transient surface temperature response is generated from a given set of system variables - making use of the analytical expression given in equation 3.50. The solution is generated at discrete points in time, representing the finite sample frequency of an IR camera, $f_{T_{\text{wall}}}$.
2. Representative errors are introduced into the transient surface temperature response signal. In the *Bias error variation only* model - only bias errors are introduced. In the *Precision error only* model - only precision errors are introduced. In the *Bias and Precision error variation* model - both errors are introduced. The magnitude of the errors are randomly sampled from their probability distribution functions (Note that the limits of these functions are provided in table 4.1)

3. A time varying heat flux is then computed from the error corrupted wall temperature ‘virtual measurements’, making use of one-dimensional semi-infinite modelling assumptions. (Note that as a result, this model does not include measurement uncertainty contributions from errors in heat flux caused by non-semi-infinite and non-1D conduction effects. These error contributions are highly circumstantial and are not appropriate for a general uncertainty model).
4. Additional Bias errors are then introduced into the derived heat flux values, as a result of Bias errors in substrate material properties.
5. A linear regression of the corrupted heat flux and corrupted wall temperature is performed, over the temporal regression limits.
6. Bias and precision errors are introduced into the non-dimensional expression of the recovery wall temperature, Θ_{rec} , which originate from Bias and Precision errors in the free-stream temperature step measurement, ΔT_{∞} .
7. The outputs, h_{MC} and $\Theta_{\text{rec,MC}}$ are given.
8. Steps 2 to 7 are then re-executed multiple times, to produce a probability distribution of h_{MC} and $\Theta_{\text{rec,MC}}$, from which the bias, precision and total uncertainty terms are calculated. The loop is iterated until the solutions to σ had converged (approximately 400 loops).
9. The models are then re-run, with altered system variables in step 1, in order to determine the sensitivity of the output uncertainty to the system variables.

4.2.3 Input uncertainty quantification

The measured quantities, which are subject to measurement uncertainties, are provided in table 4.1. The magnitude of the precision and/or bias uncertainty for each quantity is indicated. These quantities were used as inputs to the MC model. The precision uncertainty in the IR temperature measurements, T_{IR} , and thermocouple temperature measurements, T_{TC} were evaluated directly from the instrumentation which is to be used on the FACTOR rig. Note that the precision uncertainty in T_{IR} , at the FACTOR rotor conditions is significantly higher than at the NGV conditions. This is due to the short ($5\mu\text{s}$) imaging period required for imaging moving objects.

The bias uncertainties in IR window transmissivity, τ_{win} , the surface emissivity, ε and substrate effusivity, e , were estimated.

The bias uncertainty in the IR window transmissivity, τ_{win} , was determined from the window specifications provided by the window manufacturer. The bias uncertainty in ε is calculated in section 6.3.5, and the bias uncertainty in e is estimated in section 6.4.

Table 4.1 Uncertainties in measured quantities, used as inputs from the Monte-Carlo simulations

Parameter	Precision Uncertainty	Bias Uncertainty
T_{IR} (FACTOR NGV/LP)	0.068 K (measured)	$f(B_{\text{TC}}, B_{\tau_{\text{win}}}, B_{\varepsilon}, \lambda_{\text{max}}, \lambda_{\text{min}}, T_{\text{wall}(t)})$
T_{IR} (FACTOR Rotor)	0.30 K (measured)	$f(B_{\text{TC}}, B_{\tau_{\text{win}}}, B_{\varepsilon}, \lambda_{\text{max}}, \lambda_{\text{min}}, T_{\text{wall}(t)})$
T_{TC} (thermocouple)	0.15 K	± 0.5 K
τ_{win} (transmissivity)	0	$\pm 2\%$
ε (emissivity)	0	$\pm 2\%$
e (effusivity)	0	$\pm 5\%$

4.2.4 Un-modelled uncertainty sources

There are several sources of uncertainty which are not introduced into the MC model. The model will consequently under-predict the measurement uncertainty. The most significant sources which are not included are identified below:

- Errors in the derived heat flux, caused by three-dimensional conduction and non-semi-infinite effects.
- Errors introduced by fluctuations in the heat transfer coefficient or adiabatic wall temperature, during the transient measurement. If the fluctuations are low frequency with respect to the duration of the transient measurement (i.e. drift), this can cause a bias error. If the fluctuations are high frequency, the error will be negligible.

4.3 FACTOR NGV - Sensitivity Analysis

4.3.1 Base-line simulation parameters

Due to the large number of system variables which govern the measurement uncertainty, an attempt to graphically present a full solution is inappropriate. Rather, a set of base-line system variables were defined, and the affect of varying two system variables - h and one

other - on the model output was examined. The base-line system variables are provided in table 4.2, which approximately match those of the FACTOR NGV measurement conditions.

Table 4.2 Baseline variables for the FACTOR NGV uncertainty sensitivity analysis

System variable	Value
ρc	$1.59 \times 10^6 \text{ J.m}^{-3}\text{K}^{-1}$ (Torlon 5030)
κ	$0.37 \text{ W.m}^{-1}\text{K}^{-1}$ (Torlon 5030)
$\Delta T_{0,\infty}$	35 K
Approximate substrate temperature	485 K
τ_∞	0.1 s
Regression start time	$5.5\tau_\infty$
δ	2 mm
FO_{limit}	0.25

4.3.2 Uncertainty as a function of h and $\Delta T_{0,\infty}$

In this MC simulation, the measurement uncertainty was evaluated as a function of h and $\Delta T_{0,\infty}$. The simulation results provide useful guidance on what approximate magnitude of mainstream temperature step is required to achieve a given measurement uncertainty.

In figure 4.2a - 4.2c, the output from the three MC models are shown, where the Bias, Precision and total uncertainty terms are non-dimensionalised by the true value.

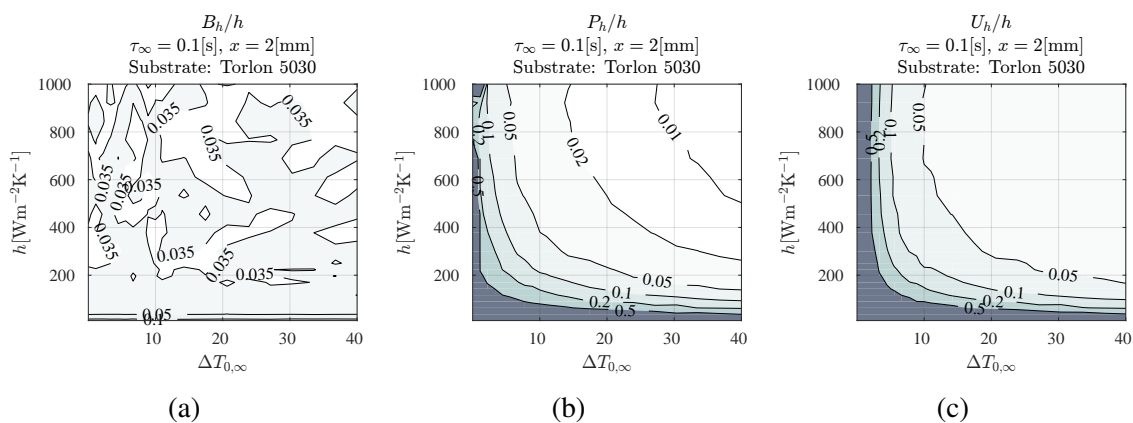


Fig. 4.2 Uncertainty in h measurements on the FACTOR NGV, as a function of h and $\Delta T_{0,\infty}$, non-dimensionalised by h

The following observations and analysis are made from figure 4.2a - 4.2c:

- The bias uncertainty in h , (fig. 4.2a), is largely independent of h and $\Delta T_{0,\infty}$. Its value is predominantly governed by the bias uncertainty in thermal effusivity of the substrate, B_e . At very low values of h and $\Delta T_{0,\infty}$, the bias uncertainty increases.
- The precision uncertainty in h , (fig. 4.2b), is strongly influenced by both h and $\Delta T_{0,\infty}$, in a non-linear fashion. Both a low value of h and a low value of $\Delta T_{0,\infty}$ lead to a small surface temperature rise during the transient measurement. As the magnitude of the surface temperature rise is reduced, and approaches the precision uncertainty in the wall temperature measurements, the overall measurement uncertainty increases sharply.
- The total uncertainty in h , (fig. 4.2c), is approximately equal to the root mean square (RMS) summation of the bias and precision uncertainties, at most values of h and $\Delta T_{0,\infty}$. This indicates that the mechanisms causing bias and precision errors are largely independent from one another. However, it can be seen that at values of $\Delta T_{0,\infty}$ of ~ 2 [K] or less, the total uncertainty appears larger than the RMS summation of the bias and precision uncertainties - indicating a significant interaction of bias and precision uncertainty mechanisms.
- It can be seen that beyond a certain threshold value of h and $\Delta T_{0,\infty}$, further increase in either h or $\Delta T_{0,\infty}$ leads to little reduction in the total uncertainty. This is due to bias errors dominating the measurement uncertainty in these regions, which are not significantly influenced by h or $\Delta T_{0,\infty}$.

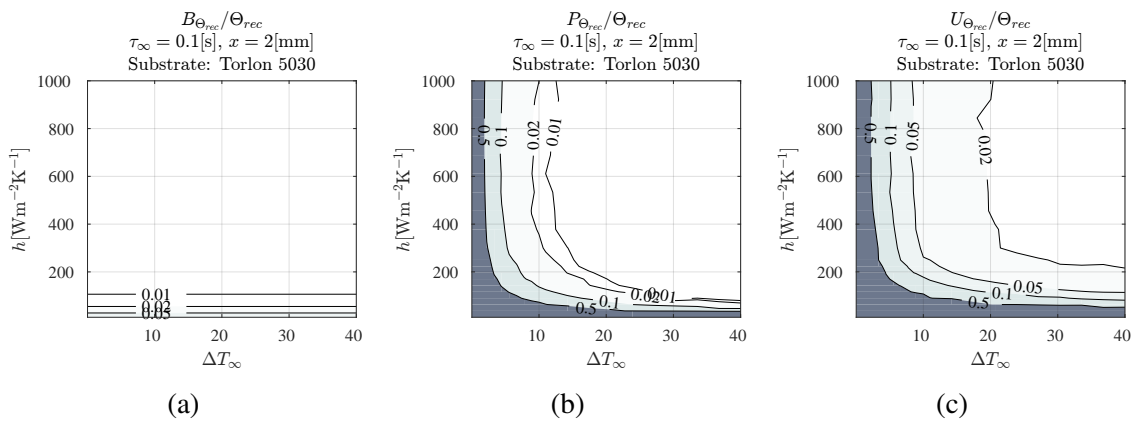


Fig. 4.3 Uncertainty in Θ_{rec} measurements on the FACTOR NGV, as a function of h and $\Delta T_{0,\infty}$, non-dimensionalised by Θ_{rec}

In figure 4.3a - 4.3c, solutions are shown for Θ_{rec} . The following observations are made:

- The bias uncertainty in Θ_{rec} (fig 4.3a), is as a weak function of h , and not a function of $\Delta T_{0,\infty}$. Bias errors introduced into Θ_{rec} , from bias errors in τ_{win} and ϵ , are approximately proportional to the surface temperature change - hence as $\Delta T_{0,\infty}$ approaches zero, these bias error terms also approach zero. Θ_{rec} is given as the *change* in adiabatic wall temperature, divided by the *change* in mainstream total temperature, and is consequently insensitive to time constant bias errors in either the numerator or denominator.
- The trends, and also the causes of precision uncertainties in Θ_{rec} closely follow that of the precision uncertainties in h , which were given in the analysis of figure 4.2b.
- Uncertainty in Θ_{rec} is dominated by precision uncertainties.

4.3.3 Uncertainty as a function of h and τ_{∞}

In this MC simulation, the measurement uncertainty was evaluated as a function of h and τ_{∞} . The simulation results provide useful guidance on what maximum value of τ_{∞} can be accepted. This information was subsequently used to guide decisions in the design of the electrical heater-mesh in the FACTOR rig, which will provide the temperature step.

In figure 4.4a - 4.4c and 4.5a - 4.5c, the output from the three MC models are shown.

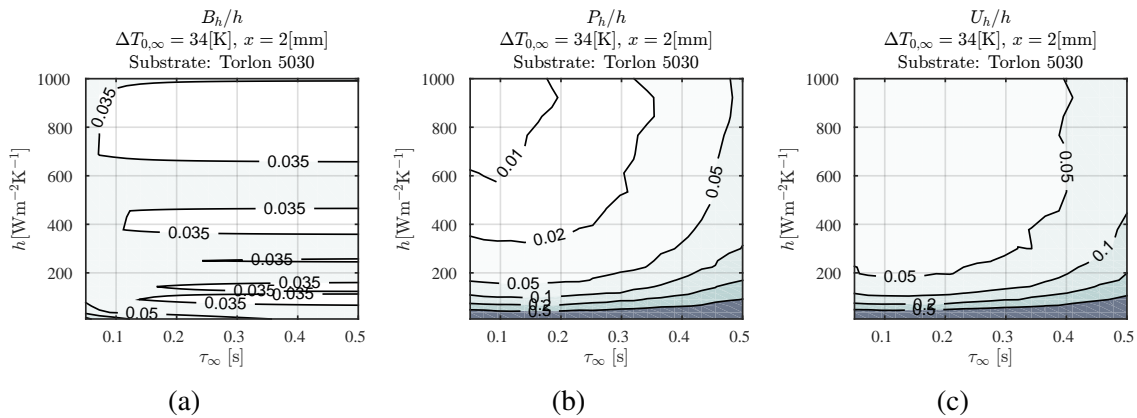


Fig. 4.4 Uncertainty in h measurements on the FACTOR NGV, as a function of h and τ_{∞} , non-dimensionalised by h

The following observations and analysis are made from figure 4.4a - 4.4c;

- The bias uncertainty in h (fig. 4.4a), is predominately governed by the bias uncertainty in the substrate thermal effusivity, which is not a function of h or τ_{∞} .

- As the value of τ_∞ increases, the sensitivity and magnitude of the precision uncertainty in h also increases (fig. 4.4b). At low values of τ_∞ (0.05 - 0.3s), this sensitivity is weak. The increase in uncertainty with τ_∞ is caused by an increase in the magnitude of $\tilde{\Theta}$.
- Increases in h cause a reduction in the precision uncertainty for the evaluated values of τ_∞ . An increase in h has two effects: Firstly, it leads to an increase in $\tilde{\Theta}$, which will contribute to an *increase* in the precision uncertainty. Secondly, however, it also leads to an increase in Θ_R , causing a reduction in the precision uncertainty in h . The solution indicates that the second effect has a greater impact on the uncertainty than the first, for all evaluated values of τ_∞ .

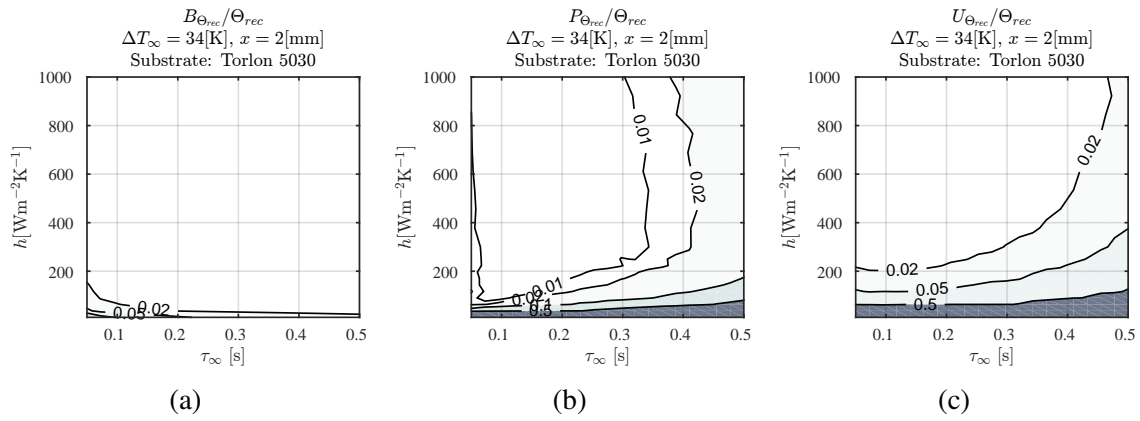


Fig. 4.5 Uncertainty in Θ_{rec} measurements on the FACTOR NGV, as a function of h and τ_∞ , non-dimensionalised by Θ_{rec}

The following observations and analysis are made from figure 4.5a - 4.5c;

- The bias uncertainties in Θ_{rec} are low for all evaluated values of τ_∞ and h , the reasons for which were provided in the analysis of figure 4.4a - 4.4c. As τ_∞ is increased beyond the nominal value, however, a slight reduction in the bias uncertainty can be seen, at low values of h . At low values of h , and with a low discrete sampling frequency, the 1D impulse response heat flux processing method can generate small bias errors in the initial heat flux values. As τ_∞ is increased, this initial biased heat flux data is excluded from the linear regression, slightly lowering errors.
- The total uncertainty in Θ_{rec} is dominated by the precision uncertainty, which follows a similar trend, and is governed by the same mechanism as the precision uncertainties in h .

4.3.4 Uncertainty as a function of h and δ

In this MC simulation, the measurement uncertainty was evaluated as a function of h and the heat penetration depth, δ (equivalent to substrate thickness x). The simulation results provide useful guidance on what minimum value of x can be accepted. This information was subsequently used to guide decisions in the design of the FACTOR NGV rotor blade and LP vane, ensuring a substrate with a sufficient x/κ value was achieved. (The value of x/κ is the control quantity which sets the Biot number, and therefore sets Θ_{limit})

In figure 4.6a - 4.6c and 4.7a - 4.7c, the output from the three MC models are shown.

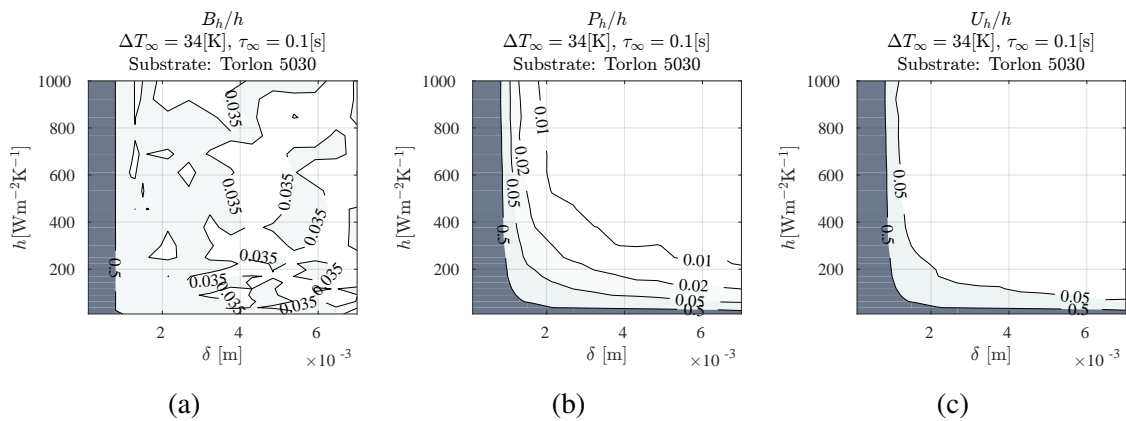


Fig. 4.6 Uncertainty in h measurements on the FACTOR NGV, as a function of h and δ , non-dimensionalised by h

The following observations and analysis are made from figure 4.6a - 4.6c and 4.7a - 4.7c:

- A highly non-linear relationship is observed between the uncertainty in h and δ . At low values of δ , between zero and ~ 1 [mm], the semi-infinite limit of the substrate is reached before the mainstream temperature rise has stabilised, resulting in zero valid data for the linear regression, and an undefined solution.
- As δ is increased beyond a value of ~ 1 [mm] the bias uncertainty in h becomes governed, primarily, by uncertainty in the thermal effusivity, and is no longer a function of δ . The precision uncertainty in h decreases significantly as δ is increased from ~ 1 to ~ 3 [mm]. An increase in δ beyond ~ 3 [mm] leads to a relatively minor decrease in precision uncertainties in h .
- Similar trends are observed in the bias and precision uncertainties in Θ_{rec} .

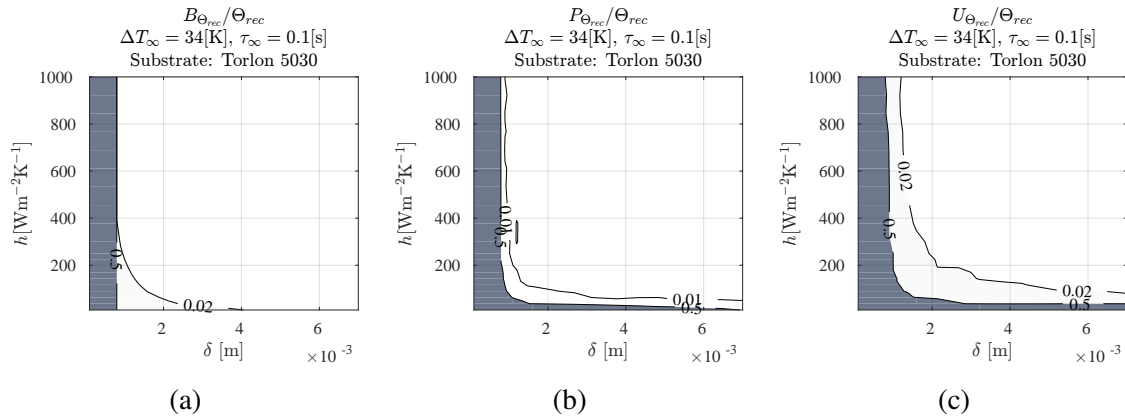


Fig. 4.7 Uncertainty in Θ_{rec} measurements on the FACTOR NGV, as a function of h and δ , non-dimensionalised by Θ_{rec}

4.3.5 Key messages

This sensitivity analysis has investigated the effects of varying three measurement variables: ΔT_{∞} , τ_{∞} and δ , on the predicted measurement uncertainty of h and Θ_{rec} , at and around the FACTOR NGV conditions. All solutions were also shown as a function of h . These three variables directly affect the four key measurement conditioning parameters, established in Chapter 3 - namely; U_{Θ} , U_{Q^*} , $\tilde{\Theta}$ and Θ_{limit} .

The trends observed in the sensitivity analysis agree, qualitatively, with the trend predictions made in Chapter 3. Most significantly, some non-linear relationships were observed, where minor changes in some of the measurement variables can lead to large variations in measurement uncertainty.

It should be noted that the solutions provided are not general solutions, and are highly dependant on the base-line measurement conditions given in section 4.3.1.

4.4 FACTOR Uncertainty Analysis

In this section the heat transfer measurement uncertainty predictions for the FACTOR rig are presented. Detailed measurement uncertainty predictions have already been presented for the NGV in the previous section, and are consequently not repeated here. Solutions for measurements on the FACTOR Rotor and LP vane are provided.

4.4.1 Rotor conditions

In table 4.3 the key system variables which are expected for the FACTOR rig rotor measurements are provided. The input uncertainty values were provided in table 4.1 - (Note the significantly higher precision uncertainty value in T_{IR} at the rotor conditions - due to the moving target).

Due to the need to meet more stringent mechanical performance requirements on the rotor, a material with a higher specific strength, but importantly, a higher thermal conductivity was specified for the rotor - namely Torlon 7130. The higher thermal conductivity serves to further ill-condition the measurements, in addition to increased precision uncertainties in T_{IR} . Uncertainties are consequently significantly higher than with the NGV. It is also worth noting, however, that these measurement which are planned for the FACTOR rotor may be the first of their kind - offering high spatial resolution measurements on high speed rotating components.

Table 4.3 FACTOR rotor vane measurement variables

System variable	Value
ρc	$1.47 \times 10^6 \text{ Jm}^{-3}\text{K}^{-1}$ (Torlon 7130)
κ	$0.53 \text{ Wm}^{-1}\text{K}^{-1}$ (Torlon 7130)
ΔT_∞	33 K
Approximate substrate temperature	460 K
τ_∞	0.1 s
Regression start time	$5.5\tau_\infty$
δ	2 mm
Fo_{limit}	0.25

In figure 4.8a - 4.8c and 4.9a - 4.9c , the output from the three MC models are shown, where the bias, precision and total uncertainty terms are non-dimensionalised by the true value. Solutions are shown for uncertainty in h and Θ_{rec} , as function of h and ΔT_∞ , representing a matrix of possible boundary conditions.

The solutions show a similar trend to those from the NGV, described in section 4.3. However, significantly higher levels of uncertainty are predicted for a given value of h and ΔT_∞ . This is caused by the higher thermal conductivity of the substrate, and the higher precision uncertainty in T_{IR} .

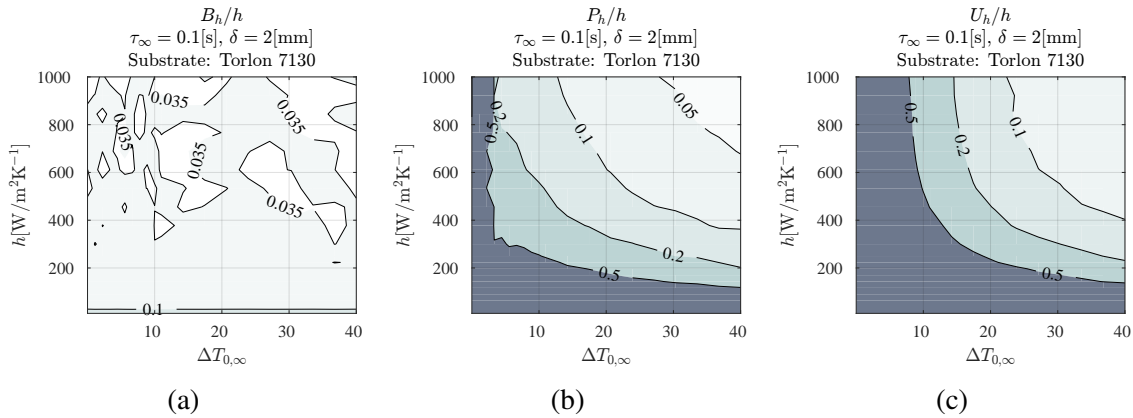


Fig. 4.8 Uncertainty in h measurements on the FACTOR rotor, as a function of h and ΔT_{∞} , non-dimensionalised by h

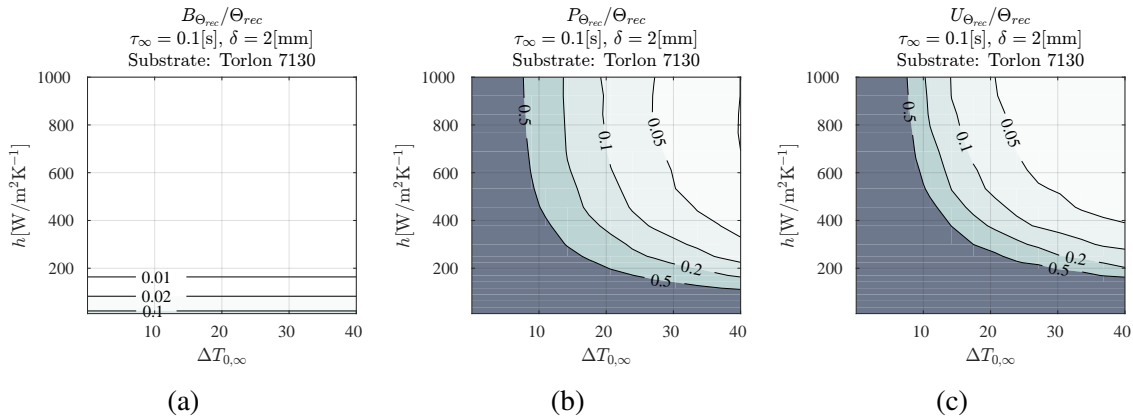


Fig. 4.9 Uncertainty in Θ_{rec} measurements on the FACTOR rotor, as a function of h and ΔT_{∞} , non-dimensionalised by Θ_{rec}

4.4.2 LP vane conditions

In table 4.4 the key system variables which are expected for the FACTOR rig LP vane measurements are provided. The input uncertainty values were provided in table 4.1.

Due to the larger geometric scale of the LP vane, in comparison to the NGV, a greater value of δ can be achieved (3 [mm]) over the majority of the vane surface, reducing uncertainty in the measurement. Work extraction from the rotor, however, leads a reduction in the mainstream temperature step, increasing measurement uncertainty.

Table 4.4 FACTOR LP vane measurement variables

System variable	Value
ρc	$1.59 \times 10^6 \text{ J/m}^3\text{K}$ (Torlon 5030)
κ	$0.36 \text{ Wm}^{-1}\text{K}^{-1}$ (Torlon 5030)
ΔT_∞	26 K
Approximate substrate temperature	359 K
τ_∞	0.1 s
Regression start time	$5.5\tau_\infty$
δ	3 mm
Fo_{limit}	2

In figure 4.10a - 4.10c and 4.11a - 4.11c, the output from the three MC models are shown, where the bias, precision and total uncertainty terms are non-dimensionalised by the true value. Solutions are shown for uncertainty in h and Θ_{rec} , as a function of h and ΔT_∞ , representing a matrix of possible boundary conditions.

The solutions are almost identical to those of the NGV, described in section 4.3, and therefore are not discussed further.

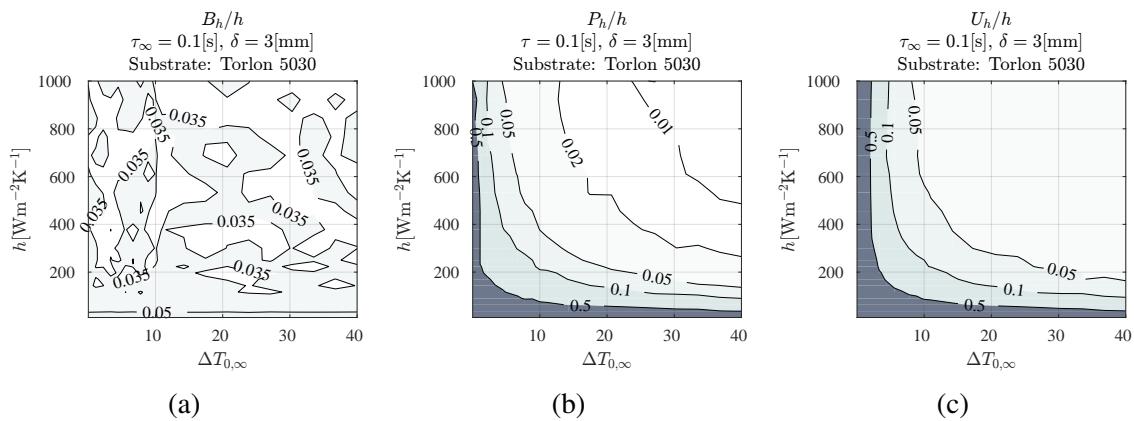


Fig. 4.10 Uncertainty in h measurements on the FACTOR LP vane, as a function of h and ΔT_∞ , non-dimensionalised by h

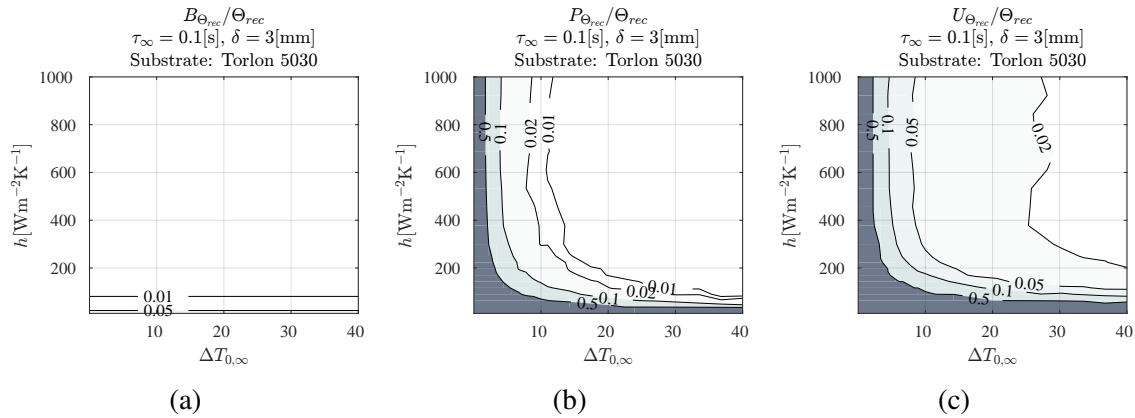


Fig. 4.11 Uncertainty in Θ_{rec} measurements on the FACTOR LP vane, as a function of h and ΔT_{∞} , non-dimensionalised by Θ_{rec}

4.5 Conclusions

The following conclusions are made:

- The MC method provides a powerful means of evaluating the measurement uncertainty in a non-linear measurement system, as a function of the parameters of interest.
- The trends in the uncertainty predictions align well with the theoretical principles and mechanism that affect measurement uncertainty, which were established in Chapter 3. With the MC analysis, however, a greater level of understanding of the combined affect of competing or supporting mechanisms can be gained. This enables the ‘design-space’ of the measurement to be explored, and optimum, or appropriate, system parameters to be defined, aiding rig and measurement method design.
- For the FACTOR rig design, the following targets are established:

1. Minimum $\Delta T_{\infty} = 25K$

The FACTOR rotor blade exhibits the highest measurement uncertainties - and hence the mainstream temperature step magnitude target is based on the rotor simulation outputs. From figure 4.9b and 4.9c it can be seen that with a 25K mainstream temperature step the uncertainty in h and Θ_{wall} is approximately 15% with an h of $300 \text{ Wm}^{-2}\text{K}$, and approximately 5% with an h of $1000 \text{ Wm}^{-2}\text{K}$. The uncertainties on both the NGV and LP vane are considerably lower with the same temperature step. It should also be noted that there are practical limitations

to the magnitude of the temperature step - as a 25K temperature step will require a ~ 100 kW power supply to the heater-mesh.

2. Maximum $\tau_{\infty} = 0.3s$

From figure 4.4c it can be seen that there is a negligible benefit in reducing the mainstream temperature rise time constant below 0.3s for the NGV. The rotor blade, however, being less well conditioned benefits more from the increase in the value of Θ_R . A minimum target value of 0.3s was specified.

3. Minimum $\delta = 2mm$

From figure 4.6c it can be seen that at the FACTOR NGV conditions, the measurement uncertainty begins to rise sharply as the substrate thickness is reduced below 2mm - and hence this value was defined as a minimum.

(As is shown later in section 5.2, the geometric scale of the FACTOR NGV and rotor blades limits the *maximum* substrate thickness, also to a value of 2mm! This shows that there is a narrow design space ‘window’ within which low uncertainty measurements can be taken).

(Note that these targets are valid only for the substrate materials specified: Torlon 5030 and Torlon 7130, justification for which is provided in Chapter 5).

- The predictions for the measurement uncertainties in h and Θ_{rec} on the FACTOR rotor are relatively high - greater than 50% in regions with an h below $200Wm^{-2}K$, and $\sim 5-10\%$ in regions with an h equal to $1000Wm^{-2}K$. Although these values are high, it should be noted that the high spatial resolution measurements planned for the high speed rotating turbine, are likely to be the first of their kind.

Chapter 5

FACTOR Turbine Rig: Design Features

In Chapter 3 , an understanding of the most important rig design features which influence the uncertainty of transient heat transfer measurements was developed. In Chapter 4 the results from an uncertainty model were presented. The model provided estimates of the measurement uncertainty on the FACTOR rig as a function of these influential rig features. Specifications were established for these rig features, which will enable low uncertainty measurements to be taken on the FACTOR rig. A variety of systems and component designs within the FACTOR rig have been produced based on these specifications.

In this chapter, two of the design solutions are described: The first solution addresses the requirement to maximise the value of Θ_R (the non-dimensional transient temperature change over which the heat transfer measurement is performed) for the blades and vanes. The second solution addresses the requirement to obtain full optical access to the turbine stage for optical IR measurements.

The design solutions shown are specific to the FACTOR turbine rig. However, the solutions address problems which can be expected to exist on engine-scale turbine rigs in general, and hence the principles behind the solutions may be extended to future rig designs.

5.1 The FACTOR Turbine Rig: A Brief Description

The 'FACTOR rig' is a reference to a Technology Readiness Level (TRL) 4 engine-scale turbine test section, which has been designed and built under an EU Framework 7 project called FACTOR. The test section has been installed and operated at the NG-Turb test facility at DLR Göttingen, in Germany.

The FACTOR rig consists of a full annular lean-burn combustor 'simulator', and a 1.5 stage turbine (i.e NGV, Rotor and Low Pressure (LP) vane). The lean-burn combustor 'simulator' has been designed to produce a swirl and hot-spot turbine inlet profile, which is representative of a real lean-burn combustion chamber.

The combustor 'simulator' has been designed to mimic the hot spot and swirl profile of a lean burn combustor. To achieve this, it is supplied with a hot air stream, at 550K, delivered through swirler nozzles into the chamber and also with full annular effusion cooling (at 300K) on the hub and casing walls. A meridional section view of the FACTOR rig is shown in figure 5.1.

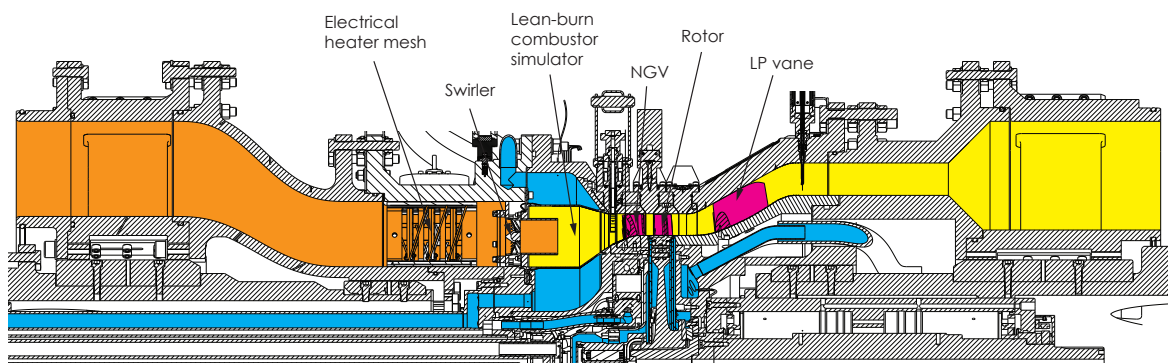


Fig. 5.1 Working section of the FACTOR turbine rig - CAD model (*Reference: Personal email communication with project team members at DLR*)



Fig. 5.2 Working section of the FACTOR turbine rig - During commissioning (Aug 2017) (Reference: Personal email communication with project team members at DLR)

The NGV is film-cooled, with an array of shower head film-cooling holes, and two rows of late pressure side film-cooling holes. A disk cavity purge cooling flow is also supplied on both sides of the rotor disk. The rotor has a diameter of 0.56m and a design point rotational speed of 8500 RPM. The span of the NGV and rotor blade is 40mm, which is comparable to that of an aero-gas-turbine engine.

The objective of the FACTOR project is to provide experimental and computational data on the aerodynamics and heat transfer of high swirl lean burn combustors-turbine systems - furthering their development.

5.2 Blades and Vanes with Maximised Θ_R

In this section, the method by which the substrate materials for the FACTOR rig vanes and blade were chosen is described. A composite construction of the rotor blade was required, which is also described.

In the FACTOR turbine rig, heat transfer coefficients within the range of approximately $200 - 1000 [\text{Wm}^{-2}\text{K}^{-1}]$ can be expected (estimates were provided by CFD calculations from the FACTOR group). Due to the small absolute geometric length scale of the blades and vanes, a heat penetration depth of no less than $\sim 2\text{mm}$ can be accepted (see section 4.5) whilst keeping the surface approximately semi-infinite and one-dimensional. An image of the mid-span section through the three vanes and blades is shown in figure 5.3, where a 2mm skin depth is illustrated. It can be seen from figure 5.3 that the 2mm skin depth just avoids the coolant cavities in the NGV, maintaining a semi-infinite substrate.

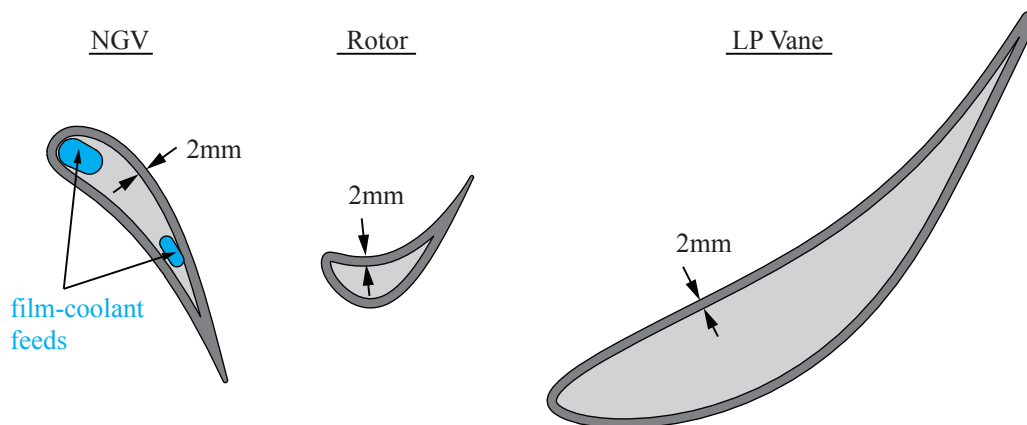


Fig. 5.3 Illustration of 2mm heat penetration depth limit

Referring back to figure 3.23a - 3.23c, the value of Θ_R was shown as a function of h , κ and ρc , for substrate thickness of 2mm. Over the range of expected FACTOR heat transfer coefficients, it was shown that the optimum value of κ was between ~ 0.1 and 0.3 [$\text{Wm}^{-1}\text{K}^{-1}$], and that the value of ρc should be maximised, in order to maximise Θ_R .

There are a number of constraints which limit the selection of suitable substrate materials. The NGV will operate with a mean inlet temperature of 485K. The maximum temperature the rotor blades will need to withstand is given by the relative total temperature, which is approximately 450K. The rotor blade will also be under stress, due to the rotation at 8500 RPM. In addition to this, decisions about the construction, geometry and material selection had to be made early in the project, in accordance with the design freeze deadlines of the FACTOR project.

In figure 5.4 a range of candidate materials are shown on a graph of specific strength (Tensile strength/density) against thermal conductivity. (The materials and their properties were extracted from the material database program 'CES Selector' [CES, 2017], and directly from material supplier data sheets). All materials shown have a maximum service temperature greater than 485K. The specific strength of a material is a good indication of its ability to withstand centrifugal loading on the rotor. The specific stiffness of the material is also an important consideration.

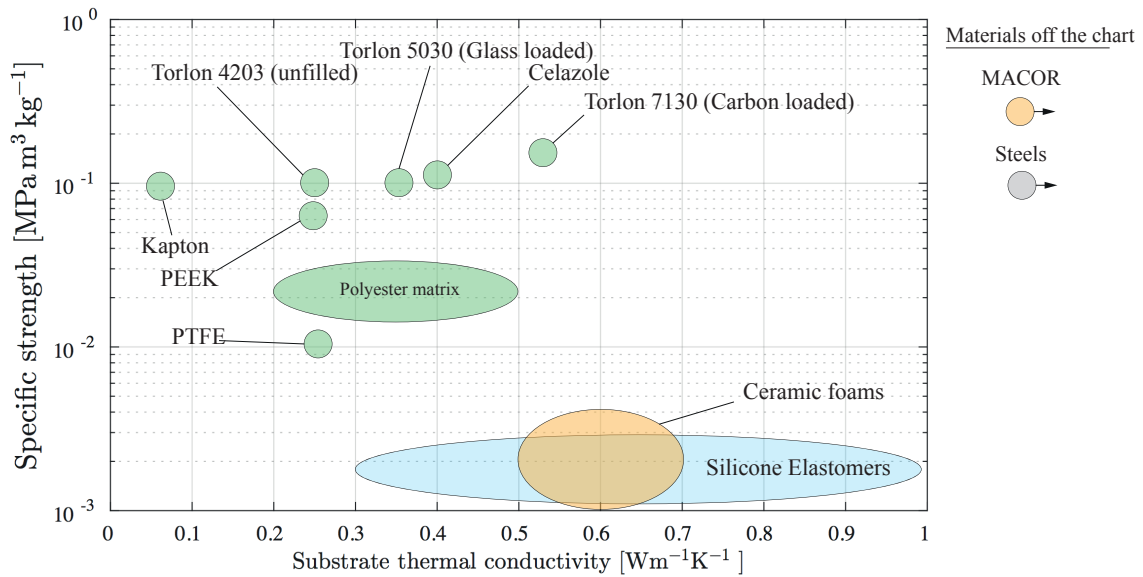


Fig. 5.4 Candidate materials for the FACTOR vanes and blades

From figure 5.4, it can be seen that the only classes of material which satisfy the constraints are; certain polymers, silicone elastomers, and ceramics. The high specific strength of the polymers, in comparison to the ceramics and silicone elastomers make them more suitable for application to the rotor.

The FACTOR rotor blade and NGVs/LP vane have differing mechanical constraints, and are therefore considered separately in the following subsections.

5.2.1 Rotor blade finite element analysis

From figure 5.4, Torlon 4203, a polyamide-imide, appeared to give the most suitable material properties for the FACTOR rotor blade, with both a low thermal conductivity ($0.25 \text{ W}\cdot\text{m}^{-1}\cdot\text{K}^{-1}$) and a high specific strength ($0.1 \text{ MPa}\cdot\text{m}^3\cdot\text{kg}^{-1}$). Finite element analysis (FEA) was used to determine the mechanical stresses in the rotor blade, when made from this material, to see if a sufficient factor of safety was achieved. The entire blade, including aerofoil hub and root section was specified as Torlon 4203. In figure 5.5 the boundary conditions applied to the FEA model are illustrated. (The CAD and FEA program ‘SolidWorks’ [Solidworks, 2017] was used to perform the calculation).

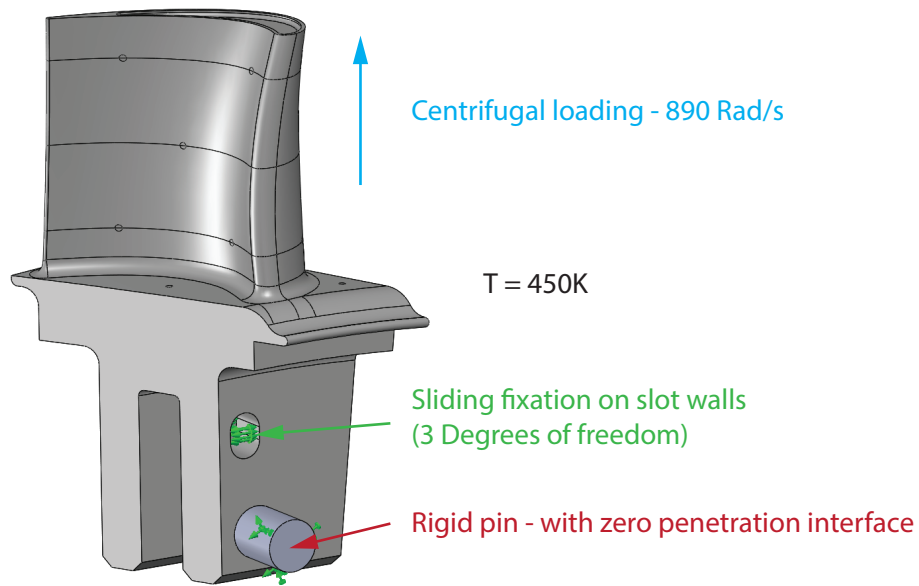


Fig. 5.5 FEA Boundary conditions applied to the Torlon 4203 rotor blade model

The solution to the FEA is shown in figure 5.6a (radial displacement) and figure 5.6b (factor of safety). Under the centrifugal loading, a large amount of elastic radial deformation of the rotor blade occurs, with the tip of the rotor blade extending by 2.2mm (5 times the radial tip gap). The elastic deformation is not localised, and occurs relatively uniformly throughout the blade span and root. The Factor of Safety (FOS) plot also indicates that plastic yielding of the material will occur in the high stress regions around the pin connection, indicated by the regions with $FOS < 1$. This indicated that a material with a higher specific strength and a higher specific stiffness was required.

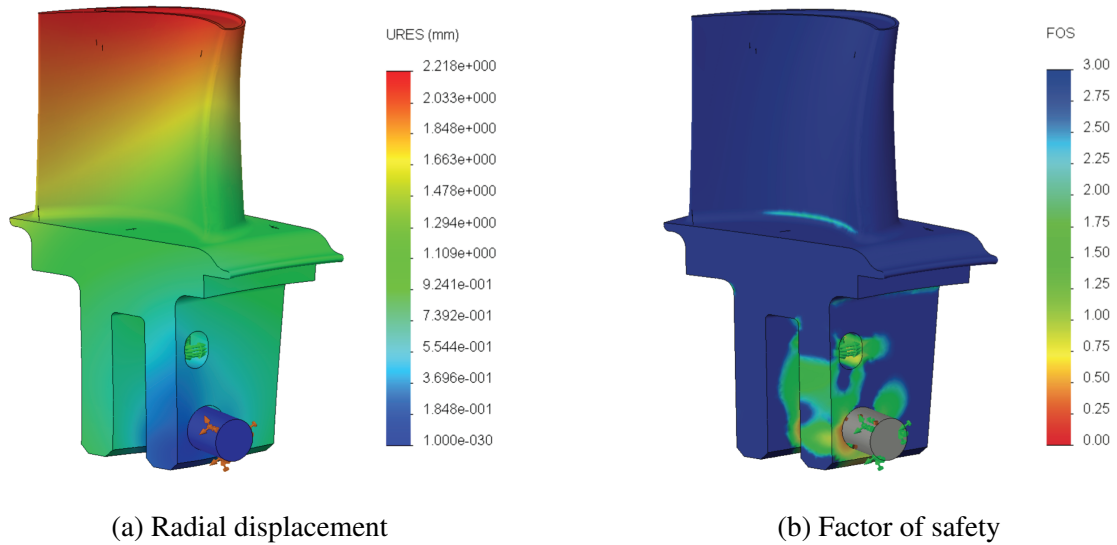


Fig. 5.6 FE simulation of solid Torlon 4203 FACTOR rotor blade

Since no suitable materials could be found which provided a higher specific strength, whilst meeting the other constraints, a composite solution was adopted. The solution was to construct the turbine blade out of two materials: Where the aero-surfaces of the blade are formed from a low thermal conductivity polymer, whilst the root section, and core of the blade are made from a material with a higher specific strength and specific stiffness. The strong core section provides high stiffness, preventing elastic stretching of the blade. The increased specific strength of the core section leads to a higher FOS at the pin interface. The polymer ‘coating’ was specified to be 2mm thick, in order to provide sufficient substrate depth to achieve the desired value of Θ_R during the heat transfer measurement. This composite construction approach is the a logical extension of the ceramic inserts used on rotor blades at the Von Karman Institute [Didier et al., 2002].

In order for this solution to work, the design must have distributed intimate mechanical linkages between the two materials, to prevent relative elastic deformation between the two. The final design solution is shown in figure 5.7. The design ensures a high degree of mechanical linkage between the two materials, enabling a uniform distribution of the load path.

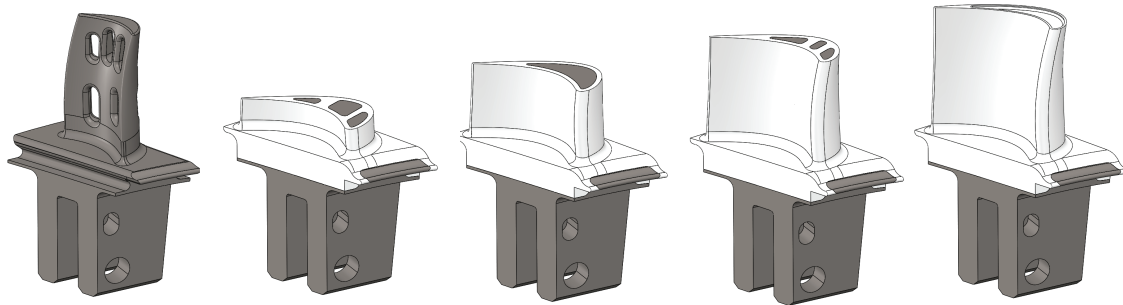
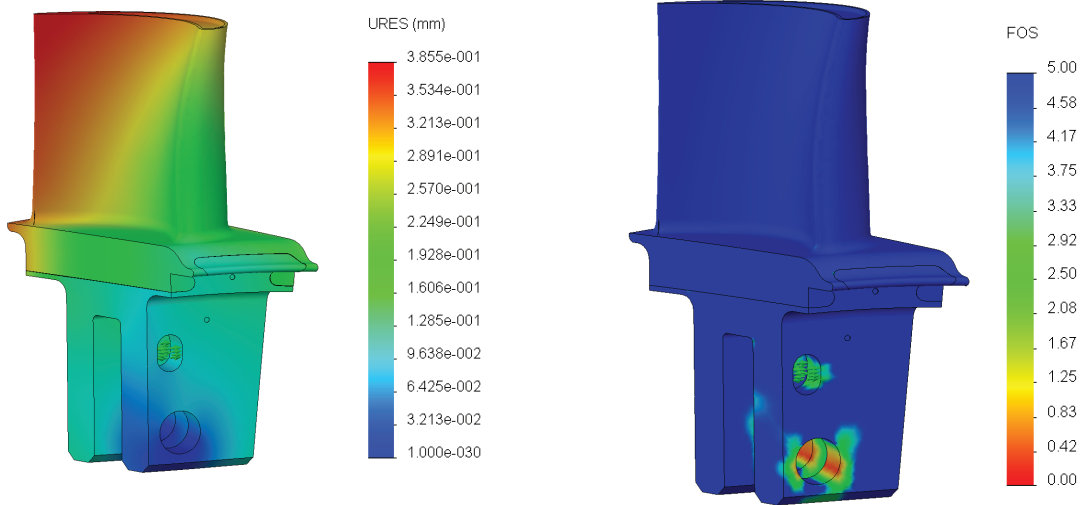


Fig. 5.7 A series of sections through the composite rotor blade design (Titanium 6,4 (gray), Torlon 7130 (white))

The root of the blade is Titanium 6,4; which has a specific strength ~ 4.5 times greater than Torlon 4203 and a specific stiffness ~ 8 times greater. A carbon fibre filled grade of Torlon, Torlon 7130 was chosen for the polymer substrate. Torlon 7130 has a higher specific strength than Torlon 4203, and critically, it has a similar Coefficient of Linear Thermal Expansion (CLTE) to Titanium 6,4: The Torlon 7130 must be injection moulded over the titanium root at high temperature, and subsequently allowed to cool. If there is a large difference in the CLTE between the two materials, significant stresses would be introduced during the cooling after injection moulding, which may run the risk of causing fractures within the Torlon. The relative differential thermal expansion between Titanium 6,4 and Torlon 7130 would be ~ 60 times smaller than with a Titanium 6,4 and Torlon 4203 combination.

The FEA solution to the composite blade is shown in figure 5.8a and 5.8b. The majority of the turbine blades in the FACTOR rig will be made from solid Titanium 6,4, and only a small number of composite blades are required for the heat transfer measurements. The solid Titanium blades undergo an elastic deformation of $\sim 0.15\text{mm}$ under the centrifugal loading. The composite blade deforms by 0.35mm ; 0.2mm greater. The FOS on the composite blade is higher than on the solid Titanium blade, due to the lower mass, and consequently lower centrifugal loading at the pin interface. On the solid Titanium blades, it is expected that an acceptably small amount of plastic deformation will occur around the pin interface.



(a) Composite rotor blade displacement under load

(b) Composite rotor blade factor of safety

Fig. 5.8 FE simulation of composite Torlon 5030/Titanium 6/4 FACTOR rotor blade

5.2.2 Rotor blade tensile testing

Fabrication of the Titanium 6,4/Torlon 7130 composite blade requires a specialist injection moulding procedure and post-curing processes. Due to the uncertainty in the material properties of injection moulded Torlon 7130, tensile testing of injection moulded samples was considered necessary to validate the process.

In figure 5.9a an image of the CAD model of the tensile test sample is shown. The tensile sample was designed to have a similar mechanical interface between the Torlon and Titanium, as exists in the rotor blade design. Three samples were tensile tested, at a temperature of 453K (figure 5.9b). Loading was increased gradually, until brittle fracture of the Torlon 7130 occurred. One of the samples, after fracture is shown in figure 5.9c.

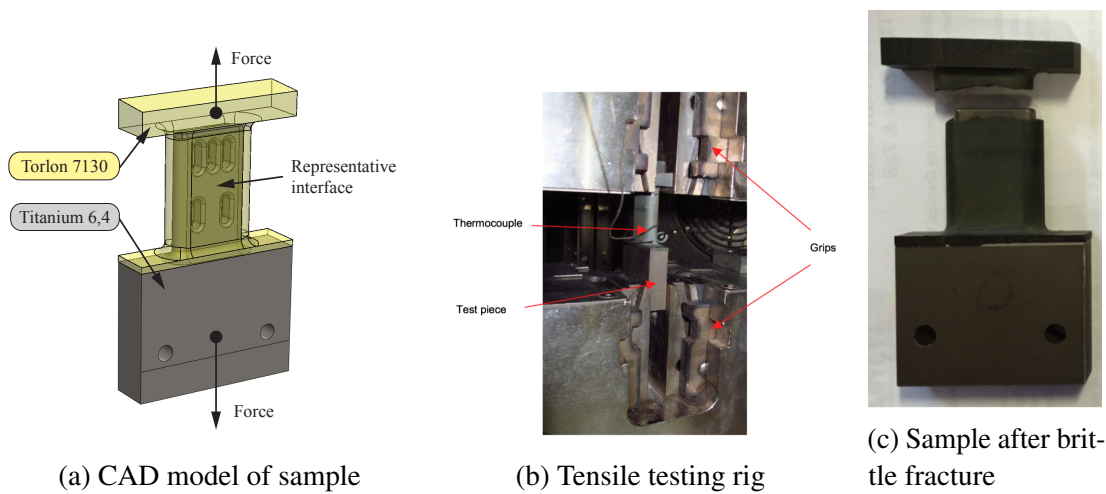


Fig. 5.9

The failure load of the three samples was 7.6, 10.1 and 10.7kN. An FEA simulation of the test sample geometry was also performed under a tensile loading of 8kN, which yielded a minimum FOS of 0.32. This indicated that the FEA significantly under-predicts the FOS, which is likely caused by uncertainty in the injection moulded Torlon material properties at elevated temperatures (for which there is limited available data), and also due to the inherent difficulty in predicting brittle fracture loading with FEA models. The FEA model was therefore not considered to be validated, however, the results of the tensile testing provided a high degree of confidence that the FEA solutions under-predict the FOS, which was considered sufficient to verify the mechanical integrity of the manufacturing process.

A photograph of the final injection moulded composite rotor blades is provided in figure 5.10. The blades were manufactured by the FACTOR project manufacturing partner Progesa (Brescia, Italy). The blades were instrumented with thermocouples by The Von Karman Institute (VKI).



Fig. 5.10 Finished injection moulded FACTOR rotor blade (the embedded thermocouples installed by VKI can be seen)

5.2.3 NGV and LP vane material specification

The NGVs and LP vanes on the FACTOR rig are not under such significant mechanical loading as the rotor blade, and thus there is greater freedom in the selection of substrate materials. The tips of NGVs and LP vanes must be sealed against an optical access window, which is assembled in the casing of the rig. Due to the relatively low toughness of the optical access window, it is important that significant stresses are not introduced into the window as a result of relative thermal expansion of the vanes and the rig casing. It is therefore desirable to match the CLTEs of the FACTOR casing materials and the material of the vanes as closely as possible.

The majority of the large components in the FACTOR rig, most significantly the casings, are produced from a 400 series stainless steel, with a CLTE of $\sim 11 \mu\text{m.m}^{-1}\text{K}^{-1}$. Torlon 5030 has a CLTE of $\sim 16 \mu\text{m.m}^{-1}\text{K}^{-1}$ which is relatively similar. The thermal conductivity of Torlon 5030 is $0.36 \text{ Wm}^{-1}\text{K}^{-1}$, which is close to the target value of $0.1 - 0.3 \text{ Wm}^{-1}\text{K}^{-1}$. Torlon 5030 was therefore selected as a suitable material. (Note that using Torlon 4203 would result in ~ 4 times the relative thermal expansion)

5.3 Achieving Full Optical Access

Within the FACTOR turbine rig, there are 20 circumferentially distributed combustor swirlers, 40 NGVs, 60 rotor blades and 20 LP vanes. Therefore, in order to obtain full optical coverage

of a periodic section of the aero-surfaces, a 1/20th segment of vane rings must have optical access enabling IR measurement. The optical access must also extend over a large axial distance - from the leading edge of the NGVs to the trailing edge of the LP vanes. This presents two significant challenges: Firstly, the large circumferential extent of the optical access requirements means that flat windows cannot be used - increasingly the complexity of the fabrication process of the window. Secondly, because optical access is required to span across two neighbouring NGVs (to achieve a periodic data set), the window will need to create a seal against the tip of at least one NGV. Due to relative thermal expansion between the NGVs and the turbine casing, and due to the low fracture toughness of optical access window material, careful design of an NGV tip seal is required to ensure large mechanical loads are not imparted into the window - which may lead to its fracture in use.

5.3.1 Design constraints

The main constraints in the design of the FACTOR optical access windows are summarised below:

- Circumferential and axial span

As mentioned above, in order to obtain a periodic measurement data set, a 1/20th segment (18°) of the vane rings must be optically accessible.

- Operating temperature

The mean mainstream fluid temperature through the NGV passage will be 450K. Peak temperatures, within the hot-spot from the swirllers may be up to 550K. The window must be able to withstand this temperature, and maintain adequate optical performance in terms of optical transmissivity.

- Pressure loading

The FACTOR rig will operate within a closed-loop continuously operating wind tunnel. In order to remove moisture from the air within the wind-tunnel, and reduce start-up loads on the compressor, the closed loop will initially be evacuated to a near total vacuum, and subsequently re-filled with dry air prior to operation. At operating conditions, the static pressure at the NGV inlet will be ~ 1.5 bar (absolute pressure). As a result, the optical windows will need to form part of a pressure vessel, withstanding loads from both the vacuum condition and the operating condition.

- Vane tip sealing and contact force

During the start-up procedure of the FACTOR rig, relative radial movement between the NGV tips and turbine casing will occur, due to thermal expansion. An aerodynamic seal must exist between the vane tips and window, in order to prevent over-tip leakage. The seal must have both a sufficiently large radial working range to cope with the radial movements, whilst not introducing significant mechanical loads into the window, which may cause brittle fracture. A target maximum vane-tip contact force was specified not to exceed 15% - so as not to contribute significantly to the window stresses.

-
- Optical transmissivity

As discussed in section 2.2.3 it is beneficial to produce the optical window from a material with both a high optical transmissivity, and also a low dependence of transmissivity with temperature and incident radiation wavelength. One implication of this requirement is that a thin window is desirable, in order to maximise transmissivity.

5.3.2 Design solution

General arrangement

In order to achieve a relatively simple window shape, for manufacturing reasons, the casing profile was defined to be cylindrical over the NGVs and rotor blades, and conical over the LP vane tips (see fig 5.1). Two windows were then designed - one which covers the NGVs and rotor blades (HP window), and one which covers the LP vane (LP window). The general arrangement of the two windows is illustrated in figure 5.11. The perimeter shape of the windows were defined such that each vane tip (either NGV or LP vane), was either in full contact with the window, or in full contact with the metal casing. This was done to reduce the possibility of over-tip leakage through the casing-window interface.

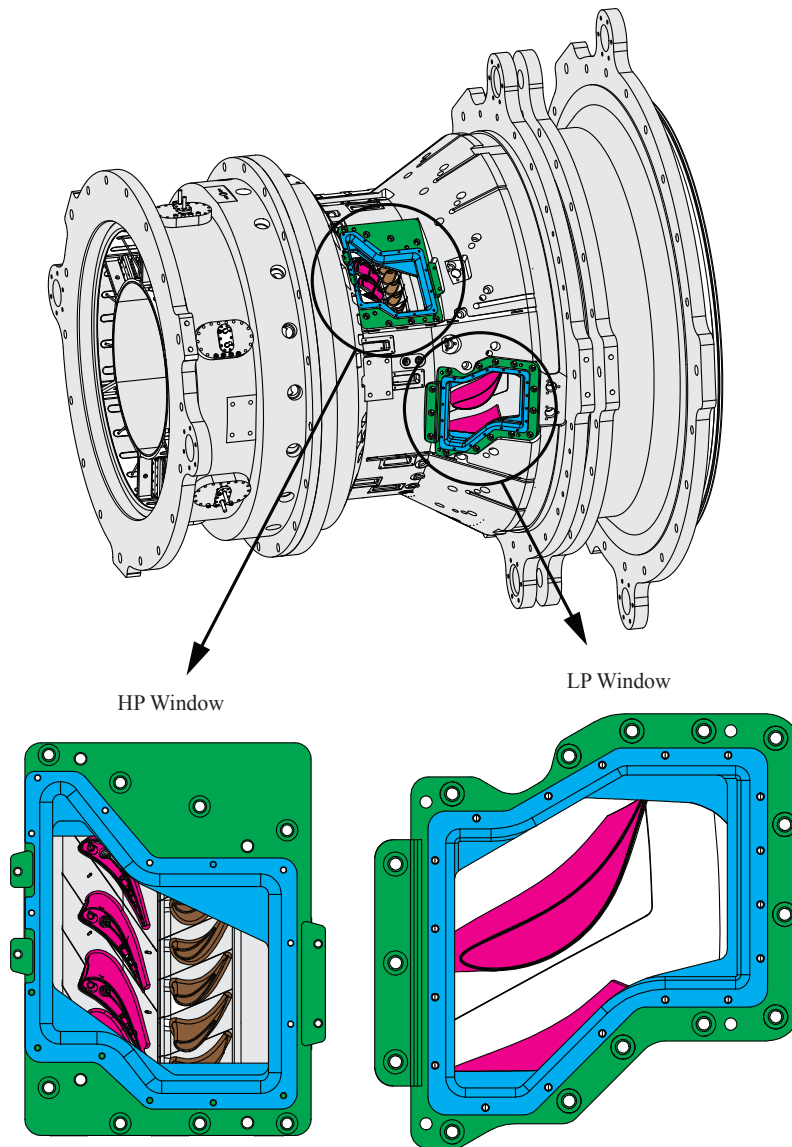


Fig. 5.11 FACTOR optical access window general arrangement

In figure 5.12 the HP window is shown. Three NGV tips are in full contact with the inside surface of the window, ensuring that two passages have full optical access. The NGV tip seals can be seen in orange, which are described in a later section. A model of the IR camera selected for the FACTOR measurements is also shown in two different orientations. The ‘light capture cones’ have been illustrated, representing the optical paths from vane surface to camera lens. An ‘optical clash study’ was performed, which determined the necessary camera orientations and locations relative the blades, required to achieve unobstructed optical access. (NB: details on the camera selection are provided in section 6.3.3)

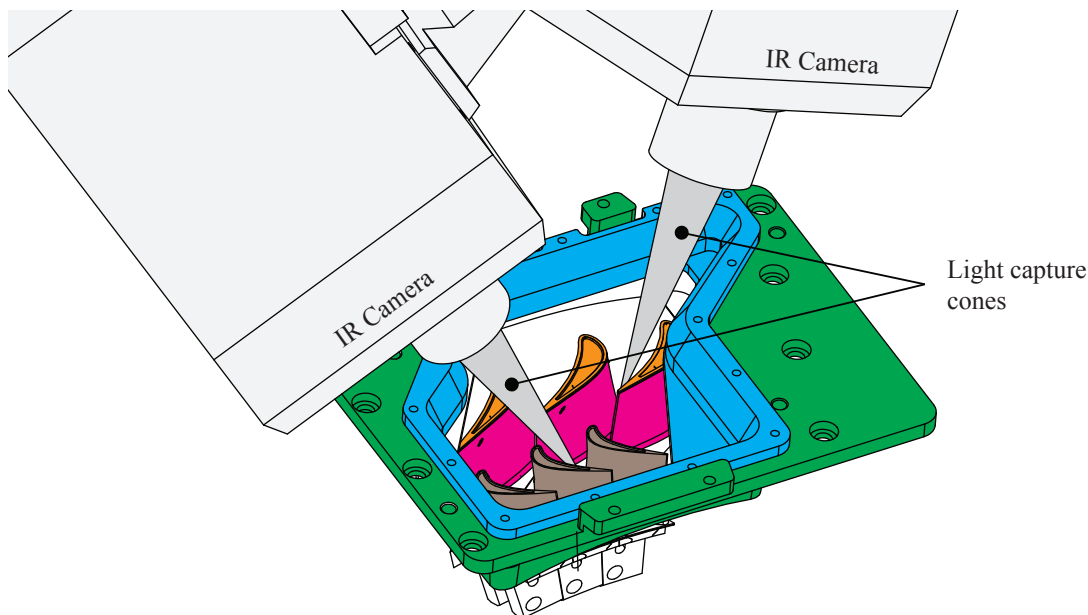


Fig. 5.12 Three NGV tips are interfaced with the HP window, enabling measurements within two passages

Window material and anti-reflection coating

The window material was specified as Zinc-Sulphide - with an anti-reflective coating in the $7.7\mu\text{m}$ to $9.3\mu\text{m}$ wavelength band. Justification for the window material choice is provided in section 6.3.4.

The optical windows were manufactured by a vapour deposition process - followed by a precision machining and polishing process. The work was carried out by the company *II-VI Infrared*.

Window fixation

In figure 5.13 an axial section through the HP window is shown, just upstream of the NGV leading edge. The mechanical containment of the window can be seen, where the window is held captive between a frame and a frame lip, forming a sub-assembly which can be attached and removed from the rig as a complete unit. The frame lip provides a mechanical support to the window around the full perimeter, which braces the pressure loading under operating conditions. Two captive lips are present (only one is visible in figure 5.13) which provides mechanical support for the window under the vacuum condition. Silicone gaskets

provide a compliant interface between the frame, frame lip and window, to reduce local stress concentrations in the window.

The window was designed with a flat external surface and concave internal surface (plano-concave). As a result the window can behave as a weak lens, resulting in slight spatial distortions in the IR images. Although a window with a constant thickness (convex-concave) would result in lower optical distortions, the plano-concave design greatly reduced the cost of fabrication. The optical distortions introduced by lensing from the window will be removed by post-processing methods.

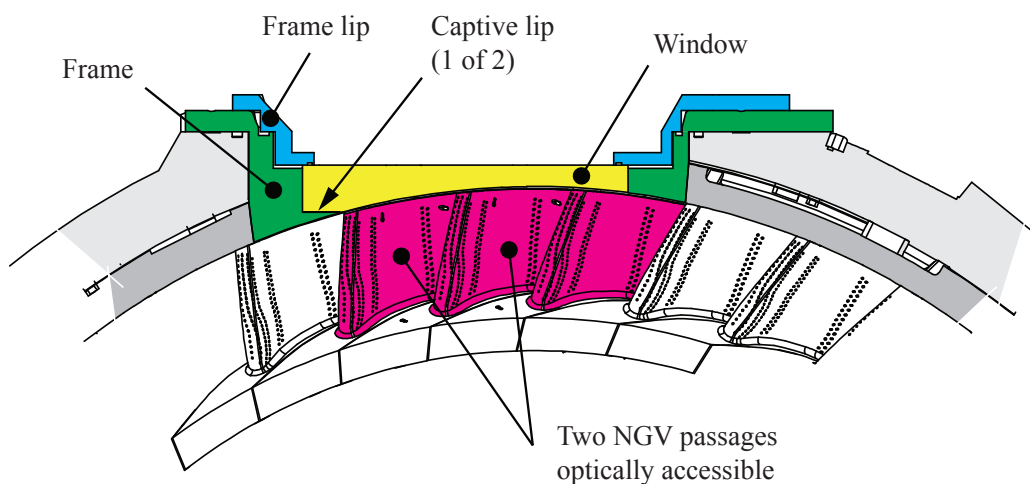


Fig. 5.13 Section through HP window (section plane normal to rig axis)

It is desirable to maximise the transmissivity of the IR window, (the reasons for which are described in section 6.3.4). It was therefore important to find the minimum thickness of the window which could safely support the pressure loading. Finite element (FE) analysis was performed in conjunction with empirical brittle fracture analysis, to determine the optimal window thickness. An iterative design process was used to arrive at the final window design. The design process is summarised below:

1. A mechanical design is generated.
2. Finite element stress analysis is performed under both operating and vacuum conditions loading.
3. A loading Factor of Safety (FOS) is defined, using the Mohr's-Coulomb stress criterion, which is appropriate for brittle material analysis. If the minimum FOS is lower than 4, then the process returns to step 1.

-
4. The peak Von-Mises stress is recorded from the FE analysis, and used to determine the maximum safe pre-existing crack size within the window, using empirical brittle fracture correlations. The maximum safe crack size is then used as a measure to determine the safety of small cracks which will inevitably be present in the fabricated window.

In figure 5.14 a set of FE solutions are presented from the vacuum loading condition, for the final HP window design. Stresses are higher in the vacuum loading condition compared to the operating condition. The results therefore represent a worst case loading. It can be seen that the minimum FOS does not fall below 4, and was therefore considered satisfactory. (NB: a minimum FOS of 4 was recommended by specialist optics suppliers).

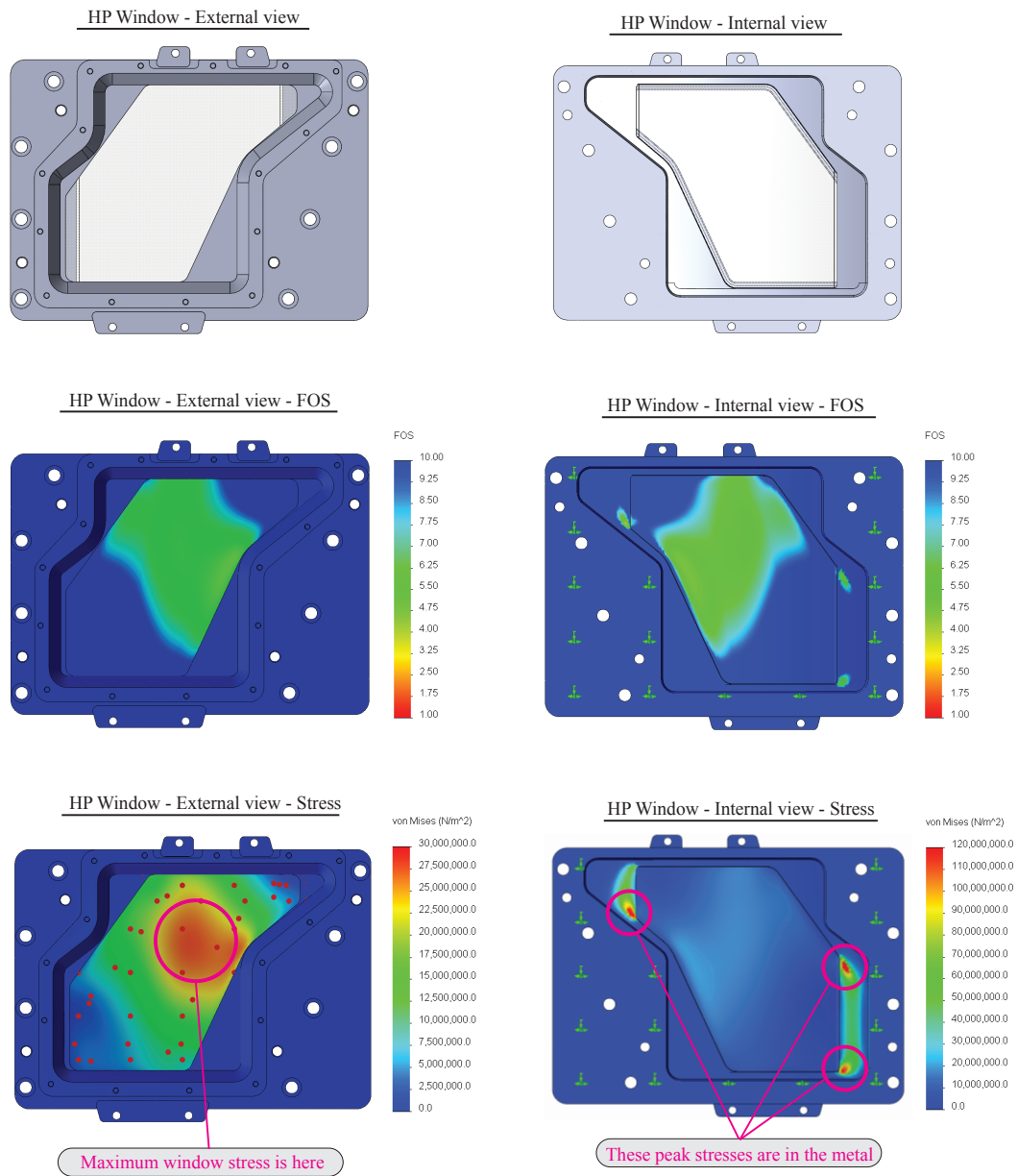


Fig. 5.14 HP window FE stress analysis results - Vacuum condition

Similar calculations were also performed for the LP window, but are not provided here.

Tip seal design

A tip seal is required between the NGV tips and the optical window, to prevent over-tip leakage. Due to relative thermal expansion between the NGV tips and the casing, careful

design of the seal is required to ensure excessive contact loads are not imparted to the window. The design process of the tip seal is summarised here.

A model of the steady state thermal expansion of the FACTOR rig was performed by members of the FACTOR project. Models were performed separately for the NGV ring and the external casing, from which the radial displacement of the NGV tips and HP IR window could be determined. The solutions are shown in figure 5.15, where a steady state casing radial displacement (at the location of the HP window) of $\sim 0.27\text{mm}$ and NGV tip displacement of $\sim 0.294\text{mm}$ were evaluated. A steady state tip gap closure between the HP IR window and the NGV tips of 0.024mm was therefore predicted. As a result of closely matching the CLTE of the plastic and metal blades, a small relative movement between the NGV tips and the casing is seen.

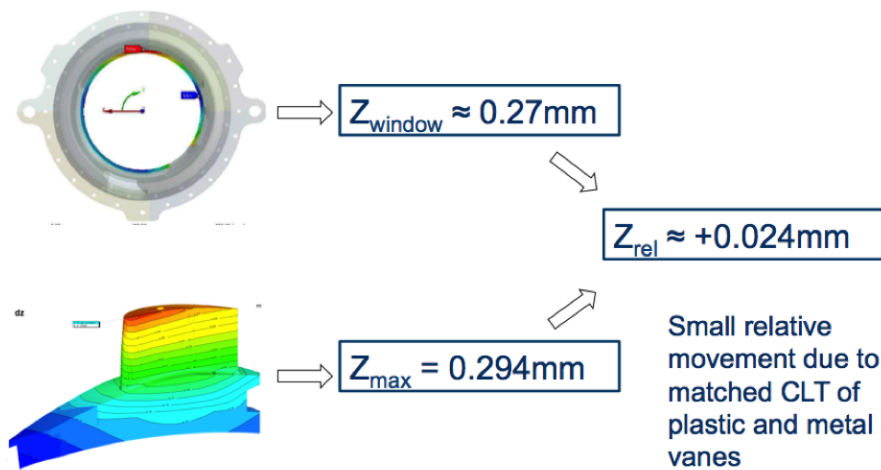


Fig. 5.15 Relative displacement of casing and NGV tips from ambient to operating point temperature (source: FACTOR project consortium partners)

The steady state closure may not be the worst case closure, however - during the heating-up phase of the rig operation, the casing and the NGVs may rise in temperature at different rates. If the NGV increases in temperature at a greater rate than the casing, then a larger transient closure will occur. A transient thermal model of the casing and NGVs was not performed, as the solution is highly sensitive to the local heat transfer coefficients, which are unknown. The planned FACTOR rig heating-up phase is gradual, where operating fluid temperature is reached, approximation linearly, over a one hour period, from ambient temperature. It is assumed that the heating-up time constant of both the casing and the NGVs is considerably lower than one hour, and therefore that transient closure will be significantly less than the theoretical maximum (i.e. the maximum being full NGV expansion, and zero

casing expansion: 0.293mm). An assumption was made, that no more than 33% of this maximum transient closure would occur. A peak closure of 0.1mm was therefore assumed for the design.

An NGV tip seal was then required which could achieve both of the following:

- An aerodynamic seal across the whole face of the NGV tip, under a closure of 0.024mm
- A combined window contact force (for three vane tips) of no more than 450 N (i.e 15% of the operating condition pressure loading on the HP window), under a closure of 0.1mm.

In figure 5.16 and 5.17, the design solution adopted is illustrated. The seal is made from an injection moulded silicone elastomer (Loctite 5920), with a low hardness and high temperature stability. Contact between the seal and the window only occurs on the raised lip around the perimeter. The design enables the following:

- A high contact pressure between the seal lip and the window, but a low contact force, due to the low contact area.
- An aerodynamic seal around the full perimeter of the NGV, preventing leakage flows.
- A relatively low radial seal stiffness (compared to a seal without a lip), where a given radial displacement results in a low change in contact force.

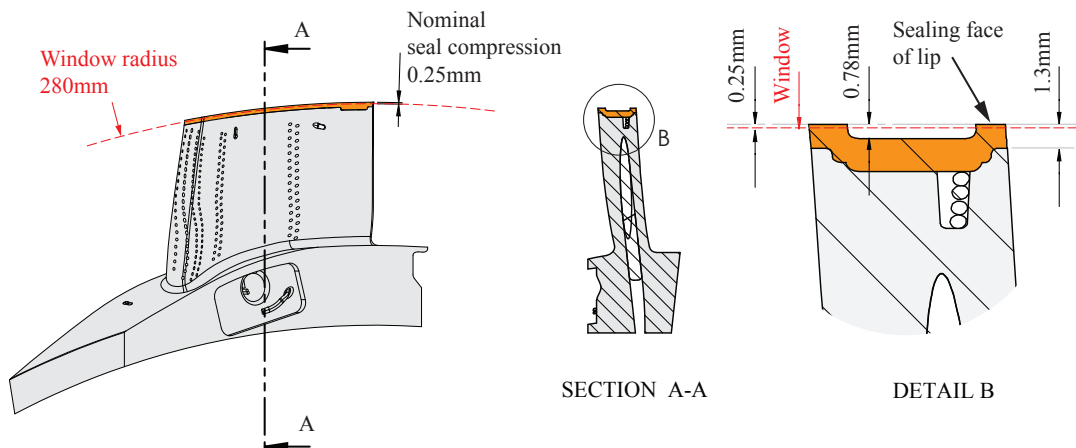


Fig. 5.16 NGV tip seal design (1 of 2)

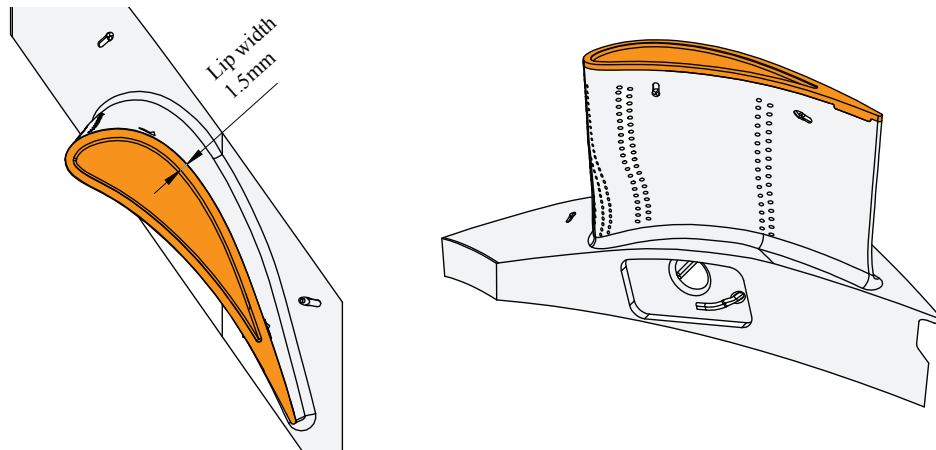


Fig. 5.17 NGV tip seal design (2 of 2)

The geometry of the seal was determined iteratively, making use of a one-dimensional analytical computer model. The model estimated the radial stiffness of the tip seal, as a function of the seal compression. A constant Young's modulus of the tip seal was assumed, along with a Poisson's ratio of 0.33.

The geometry of the seal lip was altered in the model until the model predicted an appropriate stiffness and maximum contact force with the window.

5.3.3 Tip seal testing

Considering the significant impact to the FACTOR project, should the IR window crack under unexpected excessive loading, a prototype NGV tip seal was tested. Finite element methods of design validation were not considered appropriate, due to the high levels of strain the seal lip is expected to undergo, and due to uncertainty in the behaviour of the tip seal material at high temperatures. A 1:1 scale tip seal was injection moulded, and is shown in figure 5.18a - 5.18b.

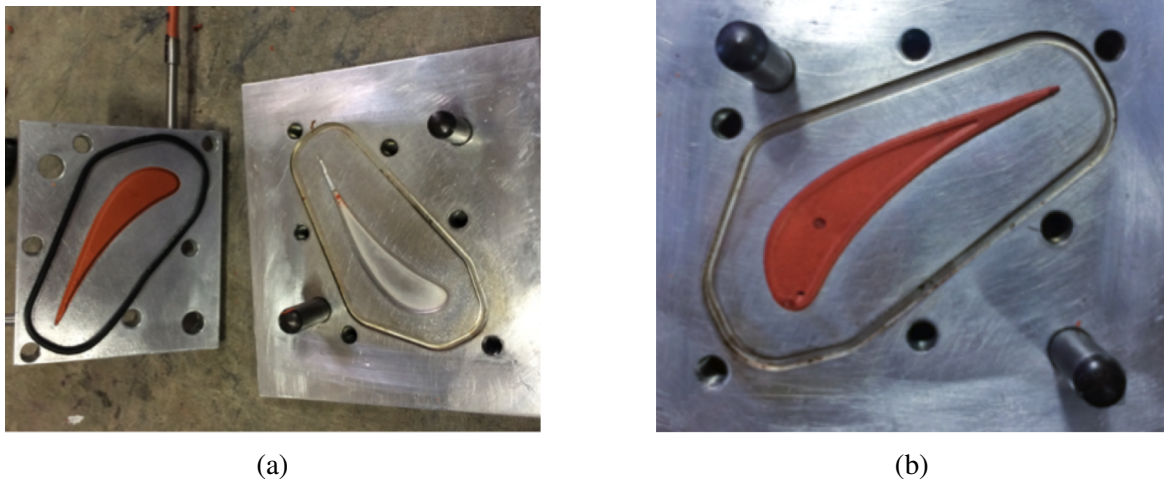


Fig. 5.18 Injection moulded prototype NGV tip seal. The raised lip around the perimeter can be seen in image (b)

The stiffness of the seal was then measured using a custom configuration compression test rig: The spindle of a CNC milling machine was used to compress the tip seal against a flat disk, representing the IR window. The CNC milling machine provided a high resolution displacement reading of $1\mu\text{m}$, whilst being able to deliver sufficient compression force. The seal was seated in a support structure, which had identical geometry to the tip of the NGV. Three load cells provided a reading of the total compression force. The test assembly is shown in figure 5.19.

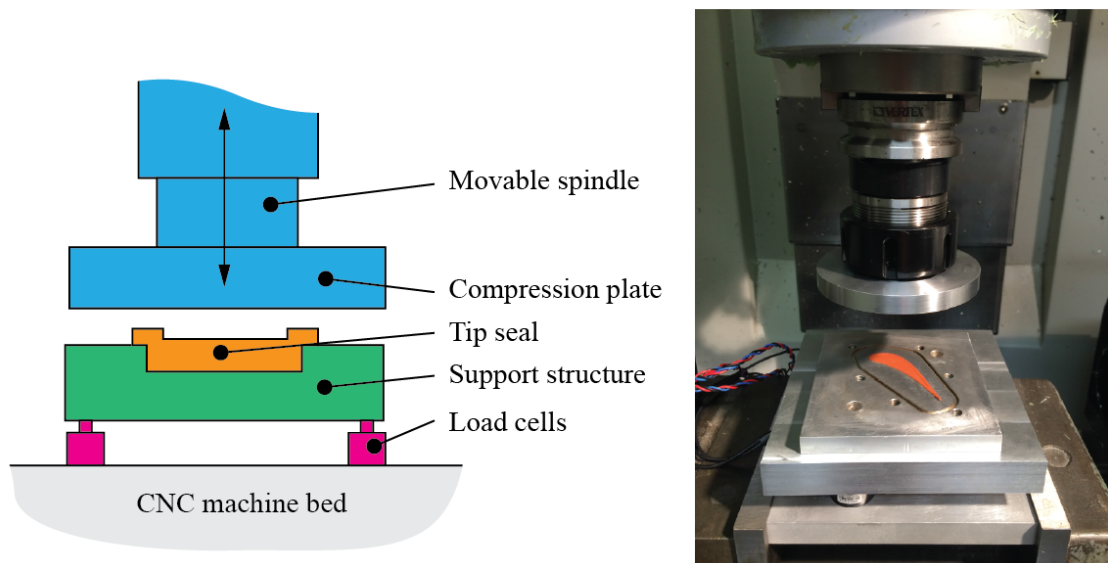


Fig. 5.19 Seal compression test rig

Four consecutive force-displacement measurements were made on the seal. The state of the seal in each test is described below:

- **As Cast 1** - Seven days after injection moulding, and subsequent exposure to ambient levels of relative humidity (necessary to cure the silicone compound), the force displacement characteristics of the seal were measured.
- **As Cast 2** - After letting the seal settle in an unloaded state after the 'As Cast 1' test, the force-displacement characteristics were measured for a second time. This was to establish if there was any significant plastic deformation during the first compression test.
- **Post Heat 1** - After letting the seal settle from the 'As Cast 2' test, the seal was loaded to 60N with a static weight, and placed in an oven, at 450K for two hours (equating to FACTOR operating temperatures). The weight was then subsequently removed and the seal was allowed to cool. After cooling, the force displacement characteristics of the seal were re-measured. This was necessary to establish if prolonging strain at high temperatures resulted in plastic deformation of the seal.

- **Post Heat 2** - After the 'Post Heat 1' test, the seal was allowed to settle, and was then returned to the oven, again under a static loading of 60N and at a temperature of 450K for two hours. The force-displacement characteristics of the seal were then re-measured. This was necessary to establish if there was further plastic deformation from the 'Post Heat 1' test.

The results of the force-displacement measurements are shown in figure 5.20, where the following can be observed:

- The 'As Cast 1' and 'As Cast 2' results are almost identical. This shows that compression of the seal at room temperature does not lead to plastic deformation.
- The 'Post Heat 1' test and the 'As Cast' tests differ. With the 'Post Heat 1' test, no compression force is registered until a displacement of $\sim 0.1\text{mm}$ has occurred. This suggests that the seal was plastically deformed during the high temperature loading.
- The 'Post Heat 1' and 'Post Heat 2' tests yield almost identical force-displacement plots. This shows that the seal had reached the limit of plastic deformation under the high temperature loading.
- The 'Post Heat' results show that a working range of more than 0.1mm is provided by the seal, where the maximum safe compression load is not exceeded - validating the seal performance.

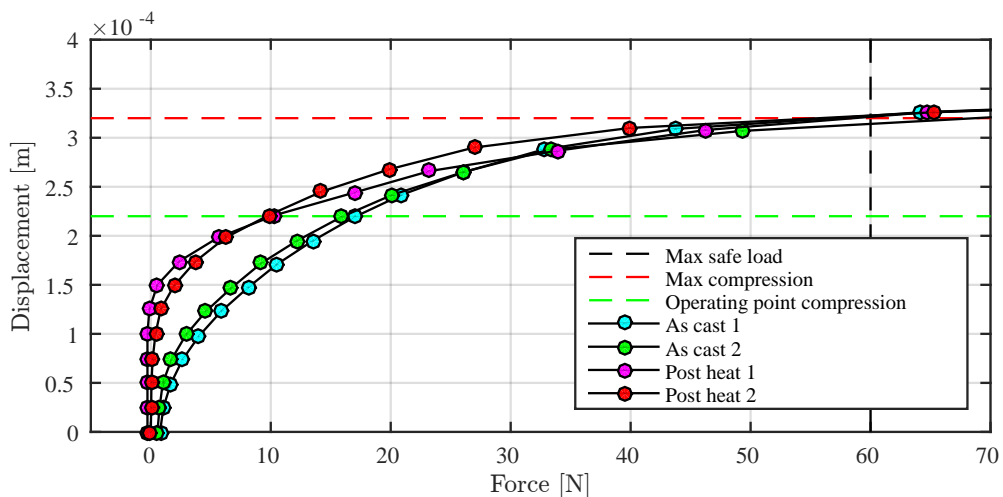


Fig. 5.20 NGV tip seal compression force test results

At the ‘maximum compression’ level (figure 5.20), corresponding to the maximum compression during rig heat up, the stiffness of the seal is high. Consequently, a small error in the clearance between the NGV tip and window location, could cause excessive seal compression and therefore excessive window loading. This clearance error could be caused by the tolerance stack-up of the components which govern the clearance. The true clearance between the window and NGV tip will be unknown, until the rig is assembled. As a result, an adjustable NGV seal mould was designed and made, which enables seals of a variable thickness to be injection moulded, such that the seal thickness can be tailored to the true clearance, which will be measured during rig commissioning.

5.4 Conclusions

In this chapter, two examples of FACTOR rig component designs were provided. All of these components are required to enable low uncertainty and full field heat transfer measurements on the rig. The design solutions address problems which are likely to be present in future engine-scale heat transfer rigs. The solutions adopted will therefore be of benefit to future projects.

Photographs of the manufactured IR windows, Torlon vanes and blades, and the FACTOR rig itself can be found in Appendix A.

Chapter 6

Measurement Methods

In Chapter 3 the theoretical principles behind performing well conditioned transient heat transfer measurements were established. It is necessary to test these principles experimentally, for validation purposes. In this chapter, two experimental facilities will be introduced, which were used to perform heat transfer measurements under a variety of measurement conditions, and were used to validate the theory from Chapter 3. The results of the measurements are provided in Chapter 7.

Experimental equipment, as well as calibration methods and heat flux modelling tools will be described. The influence of the means by which this equipment, methods and tools are used, on the uncertainty of the heat transfer measurements, will also be described.

In Chapter 5, some of the specific technical features of the FACTOR rig were described. These features are fundamental to enabling the heat transfer measurements. The experimental facilities described in this Chapter were designed to mimic features of the FACTOR rig, and thereby served as a means of validating the technical solutions used in FACTOR.

6.1 Experimental Objectives

The objectives of the measurements presented in this thesis fell into two categories: The first, was to verify the theories which were established in Chapter 3, with regards to the design of a well-conditioned heat transfer measurement, within the constraints of an engine scale turbine rig. The second, was to develop, test and validate the measurement system which will be used on the FACTOR turbine rig. These two groups of objectives are described in more detail in the following subsections.

6.1.1 Objective 1: Verifying the theory from Chapter 3

In Chapter 3 it was established that uncertainty in the heat transfer measurements can be considered to be a function of four parameters: 1) the uncertainty in the non-dimensional transient wall temperature, $U_{\Theta_{\text{wall}}}$; 2) the uncertainty in the non-dimensional wall heat flux, U_{Q^*} ; 3) the magnitude of the non-dimensional wall temperature rise during the unsteady mainstream temperature rise period $\tilde{\Theta}$, 4) the magnitude of the non-dimensional wall temperature rise at the semi-infinite limit, Θ_{limit} .

In order to test the influence of each of these parameters on the measured heat transfer, a series of experiments were performed. In these experiments, the effect of varying one parameter on the measured heat transfer was determined. The experimental rigs described in this chapter were designed to provide the ability of make these variations, and were achieved by the methods described below:

Varying $U_{\Theta_{\text{wall}}}$

The value of $U_{\Theta_{\text{wall}}}$ was altered by varying both the magnitude of the mainstream temperature step and by varying the single point measurement uncertainty of the IR camera (achieved by altering the integration time of the IR detector).

Varying U_{Q^*}

The value of U_{Q^*} was altered by;

1. Introducing non-semi-infinite geometry, by means of surface curvature and insufficient substrate thickness;
2. Introducing large lateral temperature gradients, resulting in three-dimensional heat flux;

3. Introducing steady state heat flux, prior to the transient measurement
4. Using different heat flux modelling approaches (1D and 3D), resulting in different values of U_{Q^*} .

Varying $\tilde{\Theta}$

The value of $\tilde{\Theta}$ was varied by altering the time-constant of the mainstream temperature step, to simulate large time-constants which may arise from large inlets, and generally poor heat-mesh response times.

Varying Θ_{limit}

The value of Θ_{limit} was varied by altering both the Biot number and Fo_{limit} number, achieved by altering the substrate material thermal conductivity, and by altering the duration of the transient experiment (i.e. altering the heat penetration depth, δ).

6.1.2 Objective 2: Verifying the performance of the FACTOR measurement system

Heat transfer measurements on the FACTOR rig will be taken on the NGV, the rotor, and the LP vane. The measurement conditions in each case will be different, leading to a different measurement uncertainty. The experimental rigs described in this Chapter were used to perform heat transfer measurements at conditions similar to those which will be found in each measurement location in the factor rig FACTOR.

There are several features of the FACTOR rig measurement system whose performance requires experimental validations. They are listed below.

IR camera temperature measurement uncertainty

The non-dimensional wall temperature measurement uncertainty, $U_{\Theta_{\text{wall}}}$, has a strong influence of the heat transfer measurement uncertainty. In the FACTOR rig, there are two regions where $U_{\Theta_{\text{wall}}}$ is expected to be relatively large: In regions of high film-cooling effectiveness on the NGV, and on the rotor blade, as a result of short integration times.

In regions of high film-cooling effectiveness, on the NGV, the blade surface temperature will be dominated by the film-coolant temperature. Variations in the mainstream temperature, introduced by the mainstream temperature step, will have a reduced impact on the wall

temperature, (as was described in section 3.5.2). As a result, a smaller surface temperature change will occur in these regions, during the transient measurement, increasing the local value of $U_{\Theta_{\text{wall}}}$. An experimental study was undertaken to understand at what value of film-cooling effectiveness does the measurement become ill-conditioned. These tests were performed with a mainstream temperature step magnitude, and IR camera measurement uncertainty matching those at the FACTOR rig NGV conditions.

On the rotor, radiance measurements with the IR camera must be taken with a reduced integration time (exposure time), to avoid motion blur. The HP rotor blades will have a tip speed of ~ 220 [m/s]. If motion blur is to be limited to, say 3% of the rotor blade pitch, then IR camera exposure time will need to be $\sim 3.5 \mu\text{s}$. This is approximately 10 times lower than the ideal integration time for the IR camera, at those radiance levels, and will result in a significantly decreased SNR. Experimental measurements were performed, at FACTOR rotor conditions, to understand the trade-off between SNR and motion blur.

Additionally, the conversion of IR radiance measurements, to accurate surface temperature measurements, requires a series of calibration steps. The IR transparent windows used in the FACTOR rig add a significant degree of complexity to the calibration process. Validation of the calibration process, which is described in this chapter was required.

Film-coolant trace measurement resolution

The film-cooling holes in the FACTOR NGV shower-head and late pressure side, have a diameter of 0.8 and 1.0mm respectively. The aerodynamic features caused by the film-cooling flow can be expected to have a length scale approximately equal to the hole diameter. The heat transfer measurement technique will need to be able to resolve feature of this scale.

The heat penetration depth on the FACTOR vanes and blades will be 2mm - which is larger than the length scale of the film-cooling holes. Consequently it can be expected that 3D heat flux terms will be significant in close proximity to the film-cooling flows. The use of one-dimensional heat flux models, in this instance, may generate significant errors in the measurements, as indicated in section 3.7.

If the duration of the transient heat transfer measurement is reduced, then the length scale of the lateral conduction will also be reduced, allowing smaller aerodynamic features to be resolved accurately. However, a reduced transient measurement duration will also decrease the non-dimensional surface temperature rise, increasing measurement uncertainty in all regions. An optimum measurement duration will exist, which strikes the right balance of spatial measurement resolution and measurement uncertainty. The location of this optimum will be influenced by the heat flux modelling method used, be it one-dimensional or three-

dimensional. A series of experiments were performed on geometry with film-cooling holes matching the FACTOR size, in order to establish the optimum.

Heater-mesh performance

It was described in Chapter 3 and 4 that the mainstream fluid temperature step, which initiates the transient conduction in the vanes and blades, should approach a step change to minimise the heat transfer measurement uncertainty. The mainstream temperature rise will be characterised, approximately, by an exponential function with a negative exponent, and time constant τ_{HM} .

An electrical heater-mesh, similar in construction to the one which will be used in the FACTOR rig, was used in the experimental rigs described in this chapter. The heater-mesh was supplied with DC electrical current, providing heat to the mainstream flow. The power supply was able to introduce artificially slow temperature rises, by means of supplying power following an exponential function. An experimental study was performed to understand how fast the step change in temperature needs to be to ensure low uncertainty heat transfer measurements, confirming the results from Chapter 3 and 4.

6.2 Experimental Facility

In this section, the experimental rigs which were used to conduct the heat transfer measurements are introduced. Two rigs were constructed: A Flat Plate rig, and a 3D Vane rig. The rigs used the same open-loop wind-tunnel, but had different working sections.

The Flat Plate rig provided a geometrically simple arrangement, where heat transfer can be measured on a flat surface, which has developed a new turbulent boundary layer at its leading edge. The mainstream flow is parallel to the flat plate. Well established correlations exist for convective heat transfer under this geometric arrangement, which were used as a means of measurement validation.

The 3D Vane rig provided a more geometrically complex arrangement, intended to closely represent the measurement arrangement in the FACTOR rig. Established heat transfer correlations for this geometric arrangement do not exist.

These two rigs are described in more detail in the following subsections.

6.2.1 Flat plate rig

General Arrangement

The general arrangement of the flat plate rig is shown in figure 6.1. The rig is on an open-loop wind-tunnel, which draws from atmosphere. A downstream sub-atmospheric vacuum pump draws air through the rig. A large cross-sectional area inlet section houses the electrical heater-mesh. The cross-section of the channel then reduces, accelerating the flow to Mach 0.38 through the test section. (The rig was an existing facility at the Whittle laboratory, and was not designed or built as part of this work - excluding the test section).

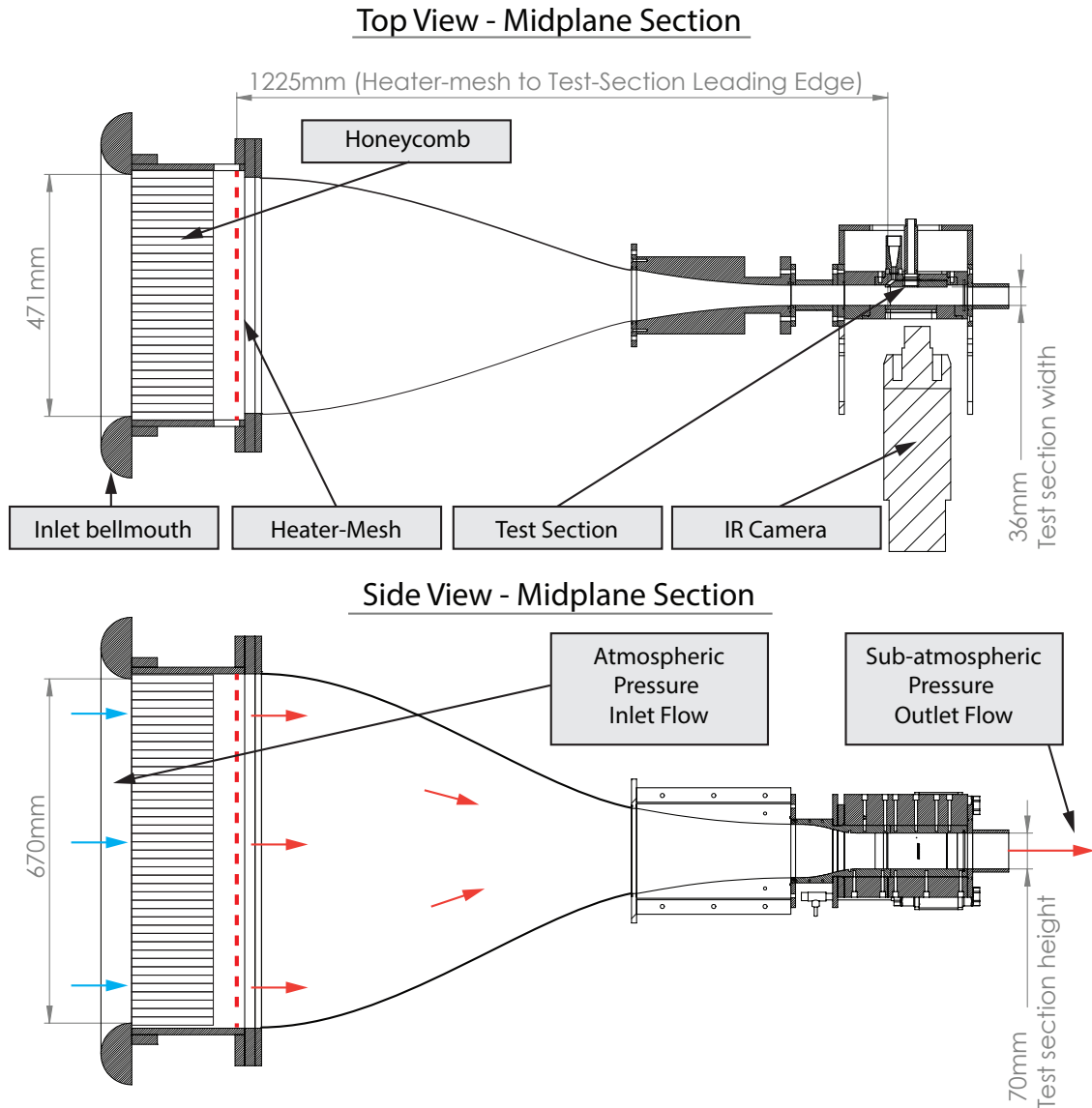


Fig. 6.1 Flat plate rig general arrangement

A detailed view of the test-section is shown in figure 6.2. A boundary layer bleed draws fluid from one side of the channel in the test section, extracting the low momentum fluid in the boundary layer. In doing so, the mainstream flow presented to the leading edge of the test-section-plate has a uniform velocity field, which has well known heat transfer correlations. A new boundary layer then forms from the leading edge of the test-section-plate. The test-section-plate can be removed and replaced with an alternative plate; made from a different material, or with/without film-cooling holes. A film-coolant feed flow provides air to the film-cooling holes. On the opposite side of the channel from the test-section-plate is

an IR transparent window. This permits the IR camera to take IR radiance measurements from the gas-washed surface of the test-section-plate.

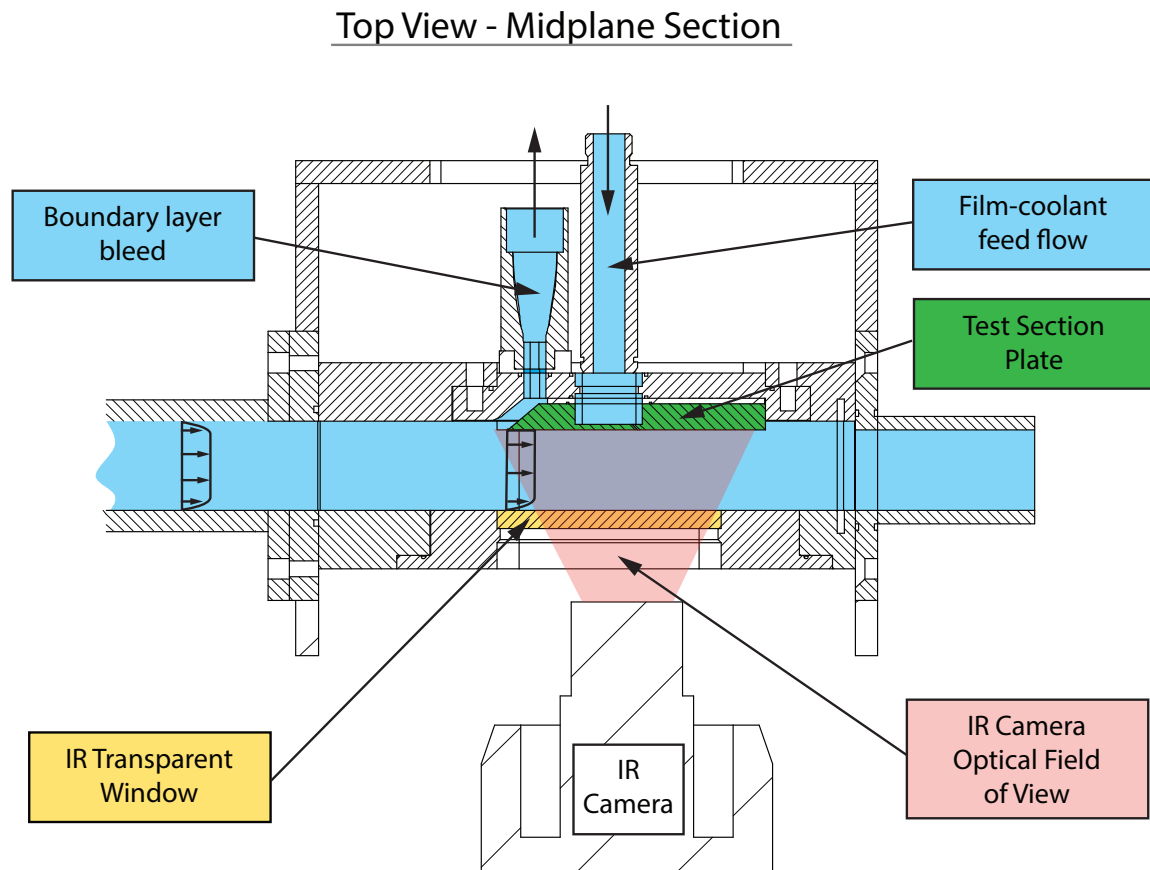


Fig. 6.2 Flat plate rig test section

Test Section Plates

Three test-section-plates were produced for use in the Flat Plate rig. Each plate is briefly described below.

- Torlon 5030 (glass filled grade) - **without** film-cooling holes

This plate was constructed from the same material (Torlon 5030) which has been used to construct the FACTOR NGV and LP vane. Heat transfer measurements on this plate were compared with establish forced convection heat transfer correlations, for measurement validation purposes. This plate was also used for the baseline measurements.

- Torlon 5030 - **with** film-cooling holes

The addition of a double row of cylindrical film-cooling holes produced a more representative aerodynamic arrangement of the FACTOR NGV measurement conditions. The diameter of the holes matched those of the FACTOR NGV. This was used to assess the ability of the measurement system to resolve and quantify heat transfer in a film-cooled configuration.

- Torlon 7130 (carbon fibre filled grade) - **without** film-cooling holes

This plate was constructed from the same material (Torlon 7130) which has been used to construct the FACTOR rotor blade. Heat transfer measurements on this plate were compared with established forced convection heat transfer correlations, for measurement validation purposes.

Each plate had its gas washed surface coated with a thin layer of black-paint (Electrolube PNM400), which was applied with a spray-can. The paint has a maximum service temperature of 923K, which makes it suitable for FACTOR operating temperatures. This was done to maximise the emissivity of the surface (to a value of ~ 0.94). The importance of maximising the surface emissivity is discussed in section 6.3. The un-cooled and film-cooled test plate geometry is shown in figure 6.3.

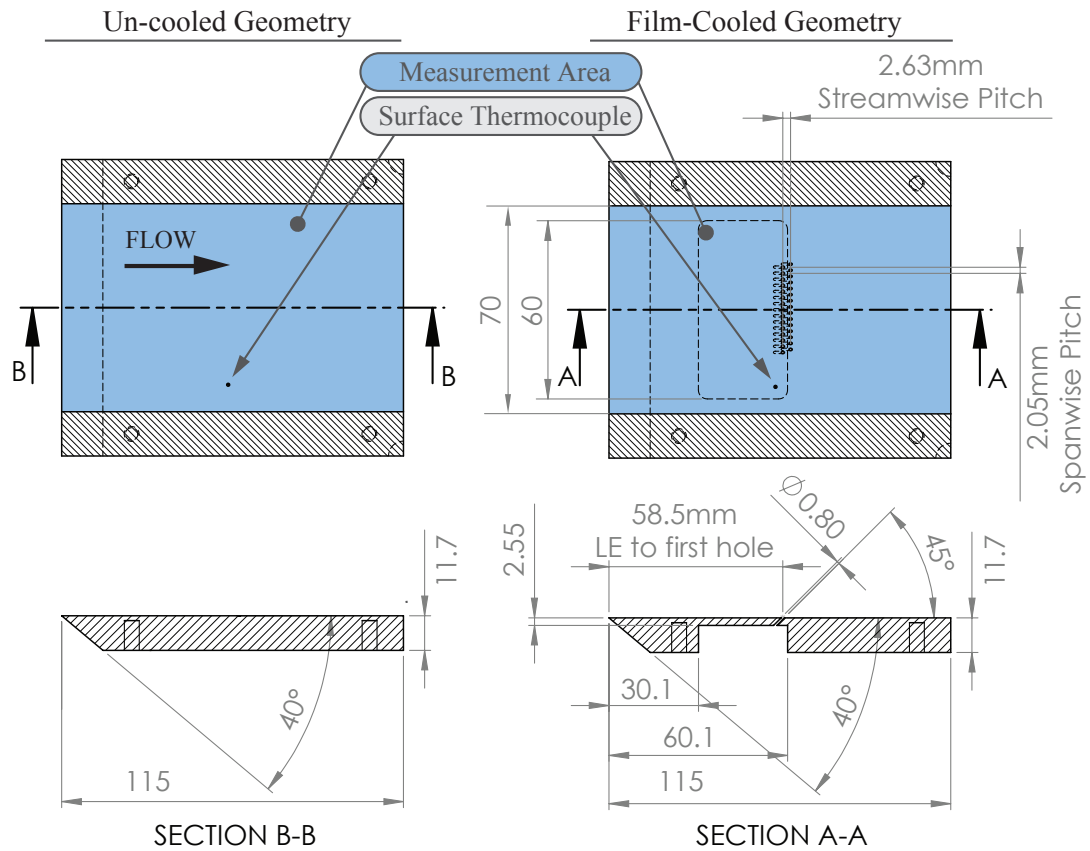


Fig. 6.3 Un-cooled and film-cooled flat plate geometry (dimensions in mm)

The film-cooled geometry has a double row of cylindrical cooling holes, with a diameter of 0.8mm, a streamwise pitch of 2.63mm and a spanwise pitch of 2.05mm. There are 30 holes in total (two rows of 15). The substrate thickness just upstream of the holes is 2.55mm, giving the film-cooling holes a length/diameter ratio of 2.25. Downstream of the film-cooling holes, the substrate thickness is 11.7mm, providing a large heat penetration depth. The location of a surface mounted thermocouple is indicated, which is used for IR camera calibration purposes.

Instrumentation Locations

A list is given below of all measurement instrumentation, and the location on the rig:

- Mainstream conditions
 - **Total pressure** was measured with a pitot tube in the centre of the mainstream channel, at the streamwise location of the leading edge of the test section plate.
 - **Static pressure** was measured with eight pressure tapings, located on the top wall of the channel, at the same streamwise location as the leading edge of the test section plate. The tapings are spaced equally across the width of channel. The mass flow rate through the boundary layer bleed port was adjusted until a uniform static pressure reading was achieved across the width of the channel. This ensured the mainstream flow at the leading edge of the test section plate was parallel to the test section plate gas washed surface.
 - **Mainstream temperature** was measured with a bare K-type thermocouple, located in the centre of the channel, 100mm downstream of the test section plate leading edge. The total temperature was inferred from this reading using isentropic Mach number relationships and an experimentally measured recovery factor for the thermocouple bead. The thermocouple bead was 0.14mm in diameter, which insured a measurement frequency response of greater than $\sim 40\text{Hz}$ could be achieved, required to resolve the mainstream temperature step characteristics.
- Substrate surface temperature
 - **IR Thermography** was used to measure the time resolved surface temperature of the test section plate. The IR camera had an acquisition rate of 200 frames/second, and a resolution of 320x256 pixels. The optics of the camera were arranged such that a single pixel represented a 0.3mm x 0.3mm square area on the test section plate. More details on the IR camera and the calibration process will follow in later sections.
 - A **thermocouple** was located on the surface of the test section plate. The bead was located just beneath the gas washed surface. The test plate surface above the thermocouple was hand finished using an epoxy filler, followed by fine sand-paper dressing, such that a flat gas washed surface remained, which did not disturb the

local boundary layer. This thermocouple was required for in-situ calibration of the IR camera.

- Film-coolant conditions
 - Film-coolant **mass flow** was measured with a sonic nozzle. The total temperature and total pressure upstream of a choked nozzle were measured, which enabled calculation of the mass flow through the nozzle. The value of the area and discharge coefficient of the nozzle were provided by the nozzle manufacturer.
 - **Total temperature** was measured with a thermocouple in the film-coolant delivery plenum, within the test section plate, a short distance from the film-cooling holes, in a low velocity region.

Aerodynamic Conditions

Table 6.1 summarises the aerodynamic conditions at the leading edge of the test section plate, at the nominal flat plate rig operating conditions. The conditions for the case with zero mainstream heating power and maximum mainstream heating power from the heater-mesh are shown. (The turbulence measurements were provided by D’Ammaro [2016]).

Table 6.1 Baseline flat plate rig operating conditions

	Heater-mesh Power	
	0 [kW]	15 [kW]
Mach number [-]	0.38	0.38
Mainstream velocity [ms^{-1}]	129.6	137.3
Mainstream total temperature [K]	298	334
Mainstream static temperature [K]	289.6	324.6
Density [$\text{kg}\cdot\text{m}^{-3}$]	1.10	0.98
Dynamic viscosity [Nsm^{-2}]	1.80×10^{-5}	1.96×10^{-5}
Mass flow [$\text{kg}\cdot\text{s}^{-1}$]	0.36	0.34
Re (based on plate length - 115mm) [-]	900,000	790,000
Turbulence intensity [%] (Approximate)	1.3	-
Turbulence length scale [mm] (Approximate)	17	-

6.2.2 3D vane rig

General Arrangement

The 3D Vane rig uses the same open loop wind tunnel described in section 6.2.1, with a different test section installed. The general arrangement of the 3D vane rig test section is shown in figure 6.4.

The test section has a single film-cooled vane installed slightly below the mid-height of the mainstream channel. The vane spans the full width of the channel, and seals against the IR transparent window, with a tip seal. (The geometry of the tip seal is based on the geometry of the NGV tip seal which was described in section 5.3). The profile of the vane is symmetric about its span-chord plane - thereby providing no turning to the mainstream flow. One side of the vane is equipped with four rows of cylindrical film-cooling holes: Two rows at the leading edge, and two rows further downstream - mimicking the FACTOR NGV. The IR camera views the film-cooled surface of the vane, through the IR window, at an angle to the surface normal of the vane. This angle is shown in fig. 6.4 as 65° - the view angle, however, can be adjusted by tilting the IR camera, to range between 55° and 75° , in 5° increments.

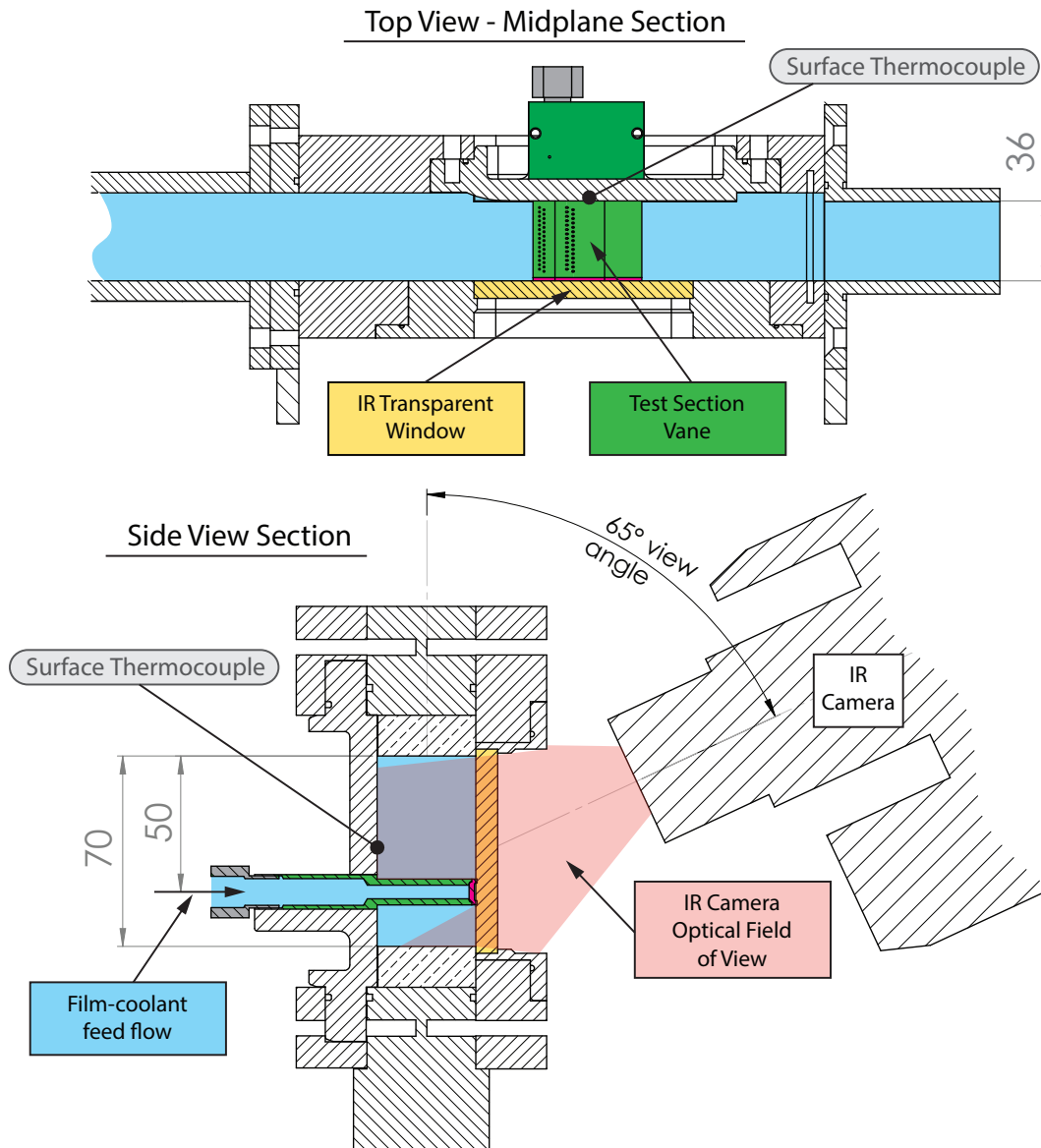


Fig. 6.4 3D vane rig test section (dimensions in mm)

Test Section Vanes

Four test-section vanes were made for use in the 3D vane rig. Each vane is briefly described below:

1. Torlon 4203 (unfilled) - **without** film-cooling holes

This vane was constructed out of unfilled Torlon (no glass fibre or carbon fibre additives, as with Torlon 5030 and 7130). With an unfilled grade of Torlon, the material is

assumed to be isotropic and homogeneous in its thermal conductivity and heat capacity. In addition, Torlon 4203 has a significantly lower thermal conductivity than Torlon 5030 and 7130. This vane was used for the baseline heat transfer measurement, against which measurements on other vanes were compared.

2. Torlon 5030 - **without** film-cooling holes

This vane was constructed out of the same material which has been used to construct the FACTOR NGV and LP vane. Film-cooling holes are omitted from this vane, such that the substrate would be representative of the FACTOR LP vane.

3. Torlon 5030 - **with** film-cooling holes

With the addition of film-cooling holes, this vane closely represented the measurement arrangement which will exist for the film-cooled FACTOR NGVs.

4. Torlon 7130 and Titanium 6,4 composite - **without** film-cooling holes

A composite vane was constructed, matching the material specification and fabrication process of the composite FACTOR turbine blade described in section 5.2. This vane enabled measurements to be taken which are representative of the measurement conditions which will exist for the FACTOR rotor.

Each vane had its gas-washes surfaces coated with a thin layer of black-paint, to increase its emissivity.

Two of the test vane geometries are shown in figure 6.5 - The film-cooled geometry and the Torlon 7130/Titanium 6,4 composite geometry. (The un-cooled geometry of the Torlon 5030 vane is identical to the cooled geometry, with the removal of the film-cooling holes and the coolant feeding cavity).

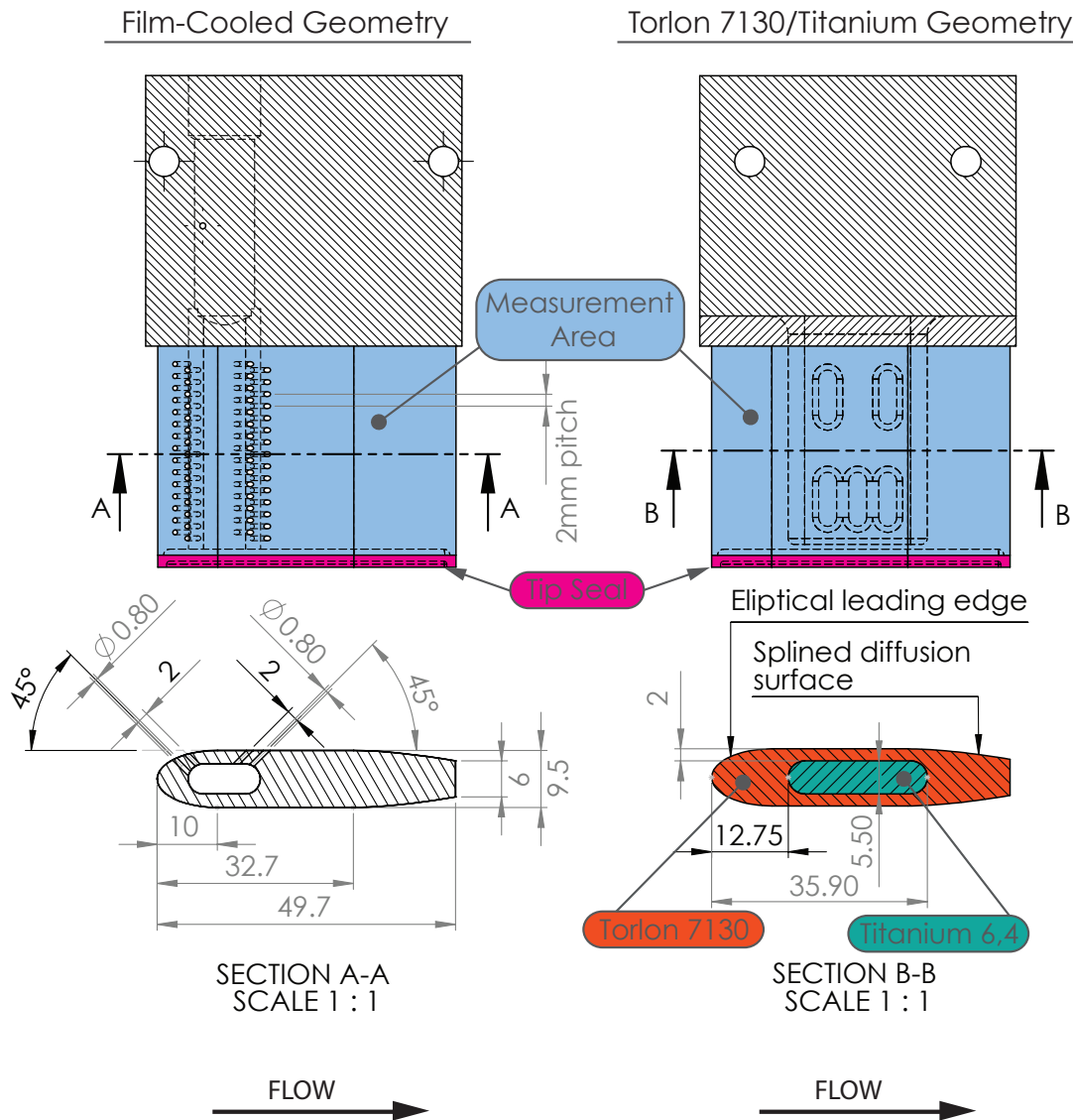


Fig. 6.5 Film-cooled and composite 3D vane geometry (dimensions in mm)

Instrumentation Locations

With the exception of the in-situ thermocouple, the instrumentation locations on the 3D vane rig are the same as with the Flat Plate rig described in section 6.2.1, and are not repeated here.

- An **In-situ thermocouple** was located on the end-wall of test section, at the gas-washed surface, as indicated in figure 6.4, and was used for in-situ IR camera calibration. The

thermocouple was not located on the 3D vane itself, such that a single thermocouple could be used for all 3D vanes.

Aerodynamic Conditions

Table 6.2 summarises the aerodynamic conditions 20mm upstream of the leading edge of the 3D vane, at the nominal rig operating conditions. The conditions for the case with zero heating power and maximum heating power from the heater-mesh are shown. (The turbulence measurements were provided by D'Ammaro [2016]).

Table 6.2 Baseline 3D vane rig operating conditions

	Heater-mesh Power	
	0 [kW]	15 [kW]
Mach number [-]	0.38	0.38
Mainstream velocity [m.s ⁻¹]	129.6	137.3
Mainstream total temperature [K]	298	334
Mainstream static temperature [K]	289.6	324.6
Density [kg.m ⁻³]	1.10	0.98
Dynamic viscosity [N.s.m ⁻²]	1.80x10 ⁻⁵	1.96x10 ⁻⁵
Mass flow [kg.s ⁻¹]	0.36	0.34
Re (based on vane chord - 49.7mm) [-]	389,000	341,000
Turbulence intensity[%] (Approximate)	1.3	-
Turbulence length scale [mm] (Approximate)	17	-

6.3 Infra-Red Thermography

In Chapter 3 it was shown that uncertainty in the transient heat transfer measurements can be strongly impacted by the non-dimensional surface temperature measurement uncertainty $U_{\Theta_{\text{wall}}}$. In this section, the method by which low uncertainty surface temperature measurements were enabled with IR thermography is described.

Determining the surface temperature of a measured object from the raw signal output of an IR camera, requires a calibration. The calibration method used, consisted of three distinct stages: 1) an IR Detector Calibration, 2) an Optical Path Calibration and 3) an Emissivity Calibration. These calibration procedures are described separately, in section 6.3.3, 6.3.4 and 6.3.5, respectively.

The principle behind the selection of an appropriate IR camera, and lens, are described in section 6.3.1 and 6.3.2 respectively.

6.3.1 Camera selection

With regards to selection of an appropriate IR camera for a particular measurement application, there are four key parameters which must be met:

1. The **single point measurement uncertainty** must be low enough to yield a low value of $U_{\Theta_{\text{wall}}}$. Evaluation of the single point measurement uncertainty of the camera chosen, and its impact on the heat transfer measurement uncertainty was performed in Chapter 4.
2. The **acquisition rate** must be high enough to resolve the transient response of the surface. Evaluation of the acquisition frequency of the camera chosen, and its impact on the heat transfer measurement uncertainty was performed in Chapter 4.
3. The **integration time** (exposure time), must be low enough to avoid motion blur when taking measurements on rotating turbine blades. A maximum motion blur equivalent to the imaging width of a single pixel ($\sim 0.8\text{mm}$) was specified. This equates to $\sim 2.5\%$ of rotor pitch. With a FACTOR blade tip speed of 250m/s , this results in an integration time of $\sim 3\mu\text{s}$.
4. The **resolution** of the camera should be high enough to image the entire blade surface, with a surface resolution capable of resolving the film-cooling flows. (i.e. the imaging width of a single pixel should be approximately equal to or less than the film-cooling hole diameter).

The camera selected for this research was selected based on its suitability for measurements on the FACTOR rig. By far the most challenging of the measurements on the FACTOR rig, in terms of maintaining a low value of $U_{\Theta_{\text{wall}}}$, is the measurements on the rotor. The high tip speed of the rotor requires a low integration time, which leads to an increase in the single point measurement uncertainty - giving a low SNR. Consequently, the camera was chosen to suit the turbine blade measurements.

The FACTOR rig will operate with a mean turbine blade surface temperature of approximately 400K. The black body spectral radiance, as a function of wavelength, at 400K is shown in figure 6.6, and was calculated with Plank's law.

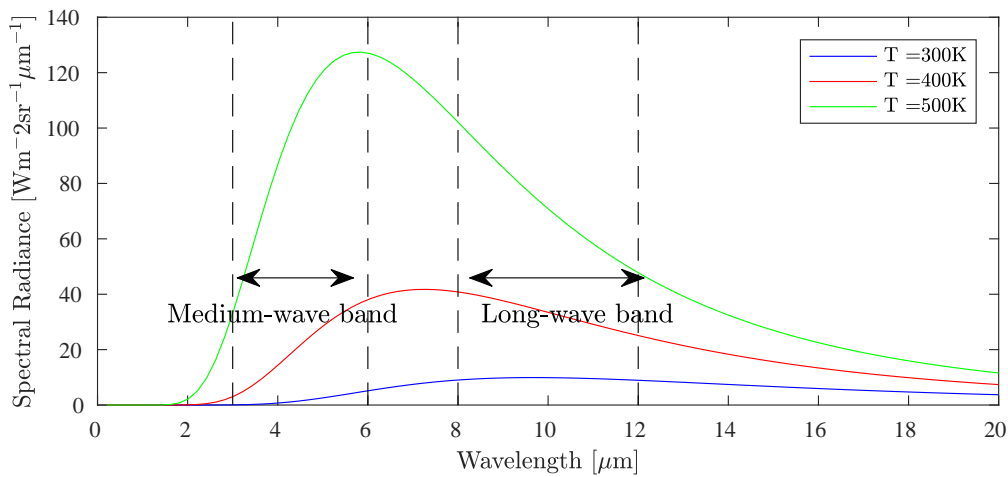


Fig. 6.6 Spectral radiance of a black body at FACTOR rotor blade temperature

IR cameras tend to be sensitive in either the long, medium or short wave IR band. From figure 2.9 it can be seen that the highest radiance will be available to a long-wave IR camera, at FACTOR operating temperatures.

A long-wave, high SNR IR camera was selected for the FACTOR heat transfer measurements. Details of the camera, provided by the manufacturer, are given in the table 6.3.

Table 6.3 IR camera technical specification

Manufacturer	FLIR
Model	SC7000LW
Detector Type	Mercury Cadmium Telluride (MCT)
Spectral Range	7.7 – 9.3 μ m
Resolution	320 x 256
Full frame sample rate	220 frames/s
Detector pitch	30 μ m
Noise Equivalent Temperature (NET)	< 25mK
Detector Cooling	Internal Sterling
Detector Temperature	77K

The Noise Equivalent Temperature (NET), is the value of a signal temperature variation which would match the noise of the camera. Typically one value of NET is quoted by the manufacturer, without reference to the measurement condition. The NET will be strongly dependant on the integration time of the camera, and the absolute temperature of the radiating body. A measurement of NET was performed with the camera, at known values of integration time and radiating body temperature. The results are shown in table 6.4.

Table 6.4 IR camera NET at FACTOR conditions

	Integration time	
	3 μ s	55 μ s
Radiating black body temperature	400K	400K
Detector saturation	6%	80%
NET	0.3K	0.068K

The left hand column of figure 6.4 shows a measurement of NET taken at conditions which closely match those of the FACTOR turbine blade measurements. The integration time is short, such that motion blur is avoided. This results in a low detector saturation, which leads to a high NET. (Note that these measured values of NET were used to define the input uncertainty in the uncertainty modelling in Chapter 4 - the impact of these uncertainty values are therefore validated by the results of the uncertainty model).

On the FACTOR turbine rig, transient surface temperature measurements of the same turbine blade can only be taken at a maximum of one sample per turbine revolution (assuming only one camera is used). The rotational speed of the FACTOR turbine is 8500 RPM. Consequently, an IR camera sample rate of at least 141 frames/second is required to capture one frame per revolution (Note that the camera selected can acquire at 200 frames/s). In figure 6.7 an analytical solution is shown for the theoretical non-dimensional surface temperature rise, over time, for the FACTOR turbine blade. A high h value of $2000 \text{ [Wm}^{-2}\text{K}^{-1}\text{]}$ is assumed, such that the solution represents the upper limit of rate of surface temperature rise which can be expected. The location of the discrete samples which would be acquired at a sample rate of 141 frames/s is shown.

It can be seen from figure 6.7 that the analytical solution appears to be well resolved in time by the discrete measurements - implying that one IR camera, with a sample rate >141 frames/s is sufficient for the measurements. Indeed this conclusion is confirmed by the Monte-Carlo modelling results in Chapter 4.

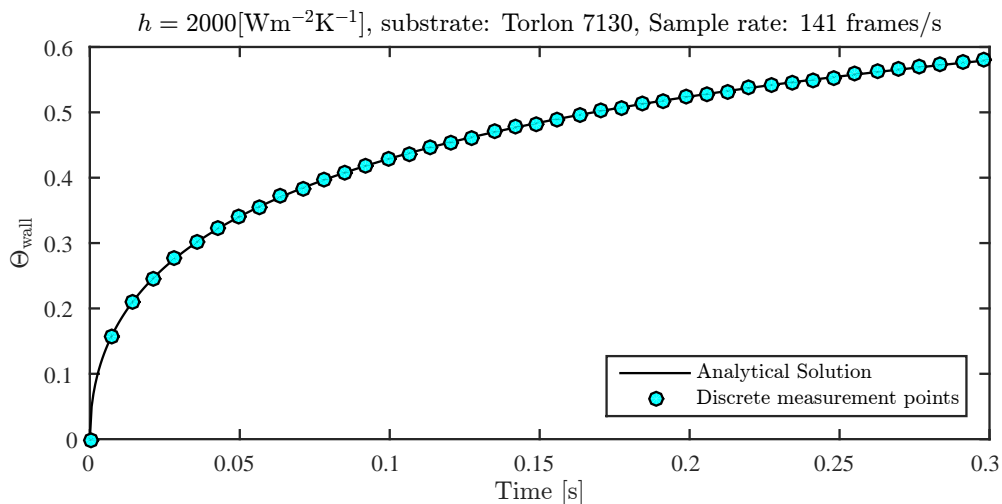


Fig. 6.7 An estimate of the temporal resolution of the transient surface temperature temperature on the FACTOR rotor - limited to one sample per revolution

6.3.2 Lens selection

The choice of lens used with the IR camera, defines entirely, or partially, the depth of field, the NET, the spatial measurement resolution (surface mm/pixel), and the field of view. There are three important trade-offs which need to be balanced for this specific application, which can be affected by three optical parameters: The F-number, the Focal distance and the Focal length.

1. **F-number** - Trading depth of field vs. NET

The F-number is the ratio of the focal length of the lens, to the diameter of the aperture. For a given focal distance (see definition below), an increase in the F-number will yield an increase in the depth of field, at the cost of a reduction in the signal strength or NET.

If measurements are being taken on a surface which is not perpendicular to the optical axis, then a reduction in the depth of field may result in portions of the image becoming out of focus. Multiple measurements at multiple focuses may be required to fully capture the surface.

2. **Focal distance** - Trading depth of field vs. surface resolution

The focal distance is the distance between the objective lens and the measurement surface. For an optical system with a given focal length (see definition below), an increase in the focal distance will yield an increase in the depth of field and a reduction in the surface resolution.

3. **Focal length** - Trading surface resolution vs. field of view

The focal length, is the distance over which parallel rays of light will be focused by the optical system. For a given focal distance, an increase in the focal length will yield a higher surface measurement resolution, but a reduced field of view.

There are two important limits to these trade-offs, in this application. Firstly, there is limited advantage in having a surface resolution (i.e. mm/pixel) which is significantly smaller than the heat penetration depth in the substrate. As was shown in section 3.6, the surface temperature gradients at a length scale less than the heat penetration depth may be dominated by lateral conduction effects. Therefore, if one-dimensional heat flux processing methods are used, this additional information offers little advantage. If three-dimensional heat flux processing methods are used, however, some increase in measurement resolution can be gained.

A second limitation is that the field of view should only be sufficiently large to capture an image of the whole blade - and no more - since a wider field of view would not provide useful information.

These trade-offs need to be balance to arrive at an optimum optical system.

Optical cone clearance

In addition to the trade-offs described above, there is a geometric constraint which must be considered. If the focal distance is short, and the objective lens diameter is large, then the

solid angle of the captured radiation will be large. It is critical, with quantitative radiance measurements, that the optical paths within the light cone are not partially obstructed by any rig components. A partial obstruction will result in a spatial variation of the proportion of the light cone which is captured by the lens - which cannot easily be calibrated out. This principle is illustrated in figure 6.8, and is representative of an attempt to measure in the passage of, say, an NGV.

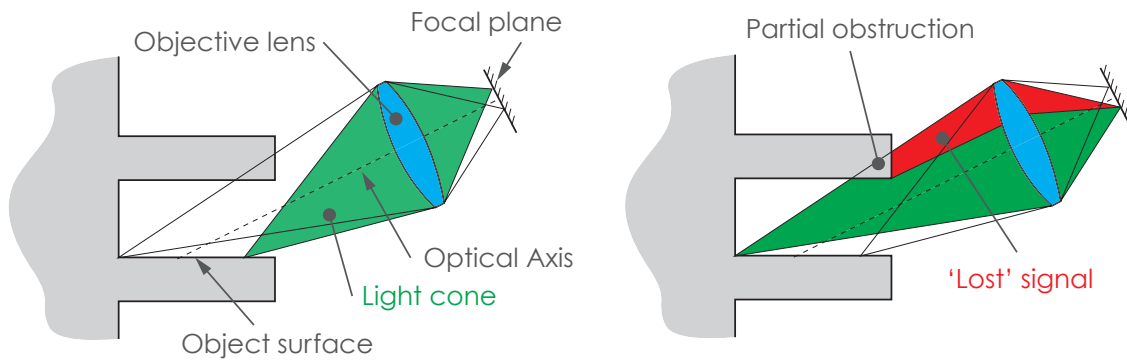


Fig. 6.8 Illustration of 'lost signal' by optical cone obstruction

Lens comparison

The IR camera described in section 6.3.1, is sold along side a range of compatible lenses. Table 6.5 shows the depth of field and surface resolution which can be achieved, as a function of lens model and focal distance. (The F-number, and the focal length, are fixed properties of the lens).

The FACTOR turbine vanes and blades have a span of approximately 40mm. It is consequently desirable to have an optical system with a depth of field of 40mm - and no more. This will permit IR measurements of the full blade span, with the whole blade in focus, whilst not unnecessarily sacrificing surface resolution or NET.

The IR camera will need to be positioned at an angle from the surface normal of the vanes and blades, in order to maintain optical cone clearance. For the FACTOR rig, this will be $\sim 60^\circ$ from the surface normal. The consequence of this, is that there will be an effective geometric reduction in the surface resolution, given by $\cos(60^\circ) = 0.5$. Consequently, a surface resolution of at least 0.5 times the heat penetration depth should be achieved by the optical system, in order to compensate for this. This leads to a target surface resolution of a maximum of $\sim 1\text{mm/pixel}$.

Table 6.5 Optical performance of candidate lenses

Lens Model		L0306	L0324	L0302	L0201		
Focal Length		12	25	50	100		
Horizontal Field of view (Deg)		44	22	11	5.5		
F-number		f/2.0	f/2.0	f/2.0	f/2.0		
Minimum focal distance (mm)		50	500	1000	2800		
Focal Distance	50mm	Image width (mm)	40.4	Too close to focus	Too close to focus	Too close to focus	
		Surface Resolution (mm/pixel)	0.13				
		Depth of Field (mm)	0				
	160mm	Image width (mm)	129.2				
		Surface Resolution (mm/pixel)	0.40				
		Depth of Field (mm)	10				
	250mm	Image width (mm)	201.9				
		Surface Resolution (mm/pixel)	0.63				
		Depth of Field (mm)	50.00				
	500mm	Image width (mm)	403.8				194.3
		Surface Resolution (mm/pixel)	1.25				0.60
		Depth of Field (mm)	210				50
1000mm	Image width (mm)	807.6	388.6	192.5			
	Surface Resolution (mm/pixel)	2.50	1.2	0.6			
	Depth of Field (mm)	999	190	50			

In table 6.5, areas highlighted in red indicate an issue which makes that optical arrangement inadequate. Areas highlighted in green, indicate that all criterion at satisfied. Lens L0324 and L0302 can both provide an adequate optical arrangement, with a depth of field > 50mm, and a surface resolution <1mm. However, they both do so at the limit of their focal distance. Lens L0306 can also provide an adequate optical arrangement, with the benefit of not being at the limit of its focal distance. Lens L0306 was selected for the measurements, based on its greater flexibility in its set up.

6.3.3 IR detector calibration

The IR detector calibration gives the relationship between incident radiance entering the lens of the camera, from a black body, to the temperature output signal from the camera. The calibration accounts for the effects of the following:

1. Incident radiation reflections off the camera lens (gain term)
2. Attenuation of radiation through the lens (gain term)
3. Grey body emission from the lens and from within the camera (offset term)

4. The characteristics of the detector within the camera; in terms of:
 - Incident radiation to output signal
 - Pixel-wise gain and offset characteristics (i.e inconsistencies between pixel responses)

The calibration was performed in three sequential steps: 1) A pixel-wise gain normalisation of all pixels, 2) A pixel-wise offset correction of all pixels, and 3) a characterisation of the relationship between an observed black body temperature and the mean output signal from a group of pixels.

1. Pixel-wise gain normalisation

The spatial gain normalisation was performed by sequentially presenting a grey body at two different temperatures, with a high emissivity, and a uniform temperature distribution in front of the IR camera, and acquiring two separate images. The grey body was constructed from a thick copper disk, ensuring high temperature uniformity. In the first instance, the grey body was at ambient temperature, and in the second instance, it was heated to approximately 50°C. The surface of the copper body was coated with a black paint, increasing its emissivity to ~ 0.95 . This reduced the influence of spatially varying reflection terms.

The mean signal from all pixels was calculated from each image. A mean signal difference between the two images could then be determined. The pixel-wise signal difference between each image was then calculated and divided by the mean signal difference - producing a mean value normalised pixel-wise gain variation data set. An example of this output is given in figure 6.9, where a normalised gain variation of approximately $\pm 2\%$ was observed.

An individual pixel-wise gain normalisation was performed for each integration time setting used on the IR camera.

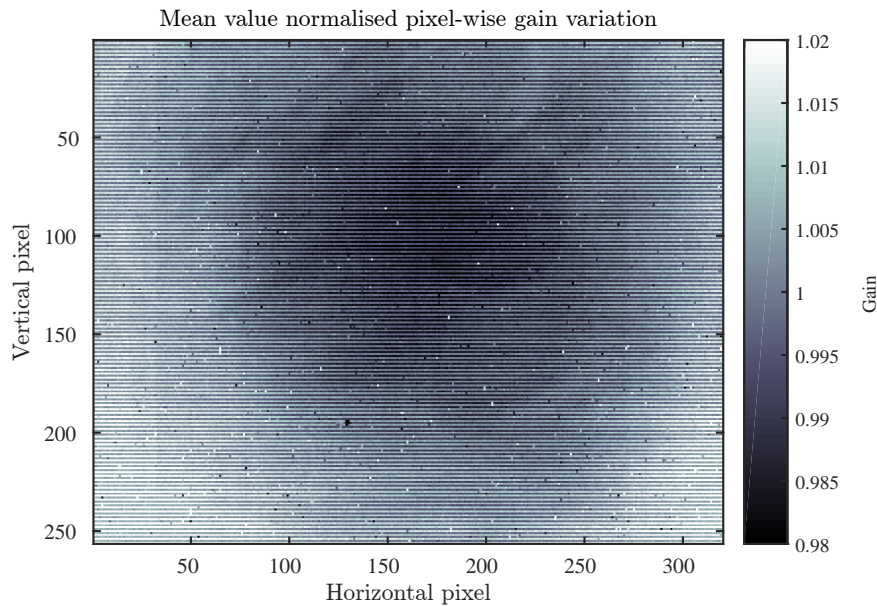


Fig. 6.9 Measurement of pixel-wise gain, normalised by the mean value - some spatial non-uniformity is observed - both inter-line and large scale. Note that only a $\pm 2\%$ variation in gain is measured.

2. Pixel-wise offset correction

A pixel-wise offset correction was performed in a similar manor to the pixel-wise gain variation correction. The same uniform temperature grey-body was placed in-front of the IR camera, and an image was acquired. The variation of each pixel from the mean value of the whole image was calculated - providing an offset correction. When doing the offset correction, the temperature of the grey-body was set at a value approximately equal to the temperature of the substrate within the test-rig. This was done to minimise the extrapolation of any residual errors in the pixel wise gain correction.

3. Characterisation of detector

Characterisation of the detector was performed by recording the mean signal output from a group of 6 pixels (3x2), as a function of the temperature of a virtual black body, which was in the field of view of the camera.

The virtual black body was created by drilling a high aspect ratio hole (length/diameter ratio = 5), into a circular disk of temperature controlled copper. The inside surfaces of the hole were coated with a black paint, with an emissivity of 0.95. Incident rays of light entering the hole undergoing multiple internal reflections before leaving again, (due to the high aspect ratio), resulting in almost total signal absorption. (For example

- if only three internal reflections occur, an effective emissivity of the hole of 0.9998 will be achieved)

The copper disk was heated with a distributed circular electrical adhesive heater on its back face. A Platinum Resistance Thermometer (PRT), with a measurement uncertainty of $< 0.02\text{K}$ was installed in the centre of the disk, to monitor its temperature (*Fluke 5608*). Temperature control of the copper disk was achieved with a custom tuned PID controller, which was able to maintain the copper disk at the set temperature, $\pm 0.02\text{K}$. The optical axis of the camera was positioned normal to the front face of the copper disk. A radiation shield, with black walls, maintained at constant temperature, was then placed over the virtual black body and the camera, in order to shield the assembly from time varying signals, which could be caused by temperature fluctuation in the ambient environment.

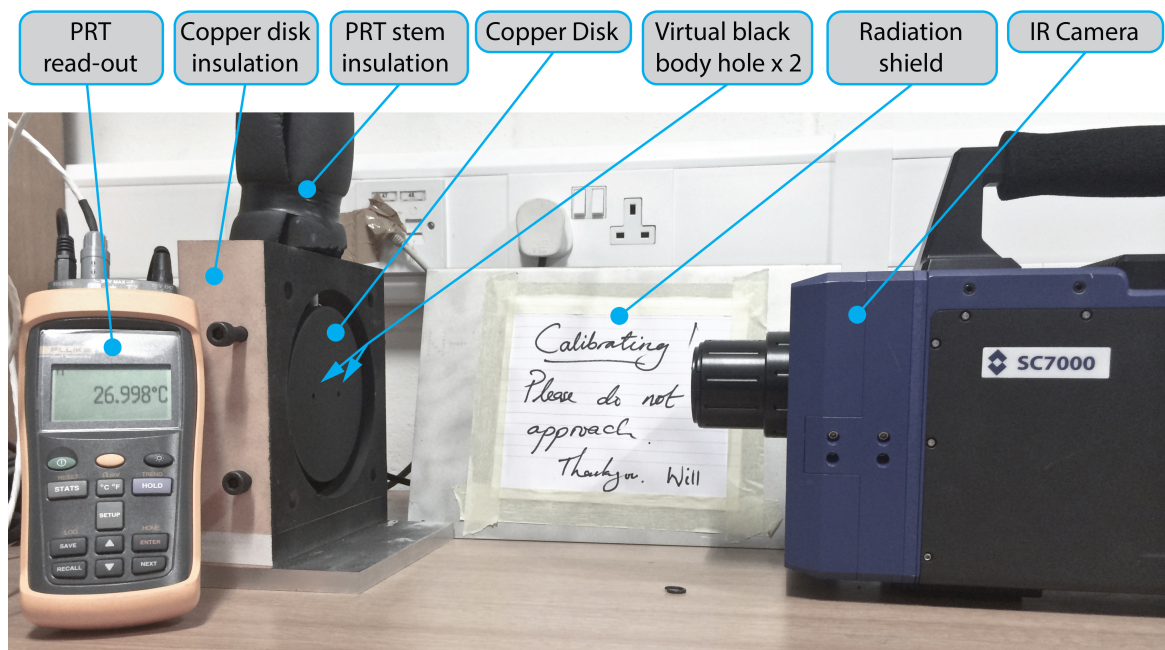


Fig. 6.10 Photograph of detector characterisation calibration assembly

The virtual black body was set to a range of temperatures. Ten images were taken with the IR camera at each temperature - the average value was taken for the calibration point. Three calibrations are shown in figure 6.11a and 6.11b, at three different Integration Times (IT).

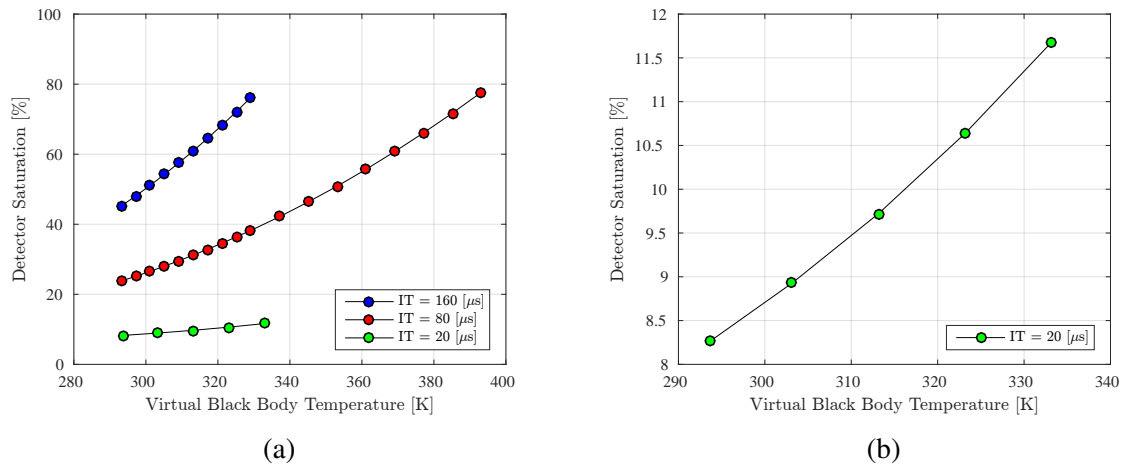


Fig. 6.11 IR detector output vs. Virtual black body temperature for three different integration times. (b) is a zoom in of the 20 μs data from (a)

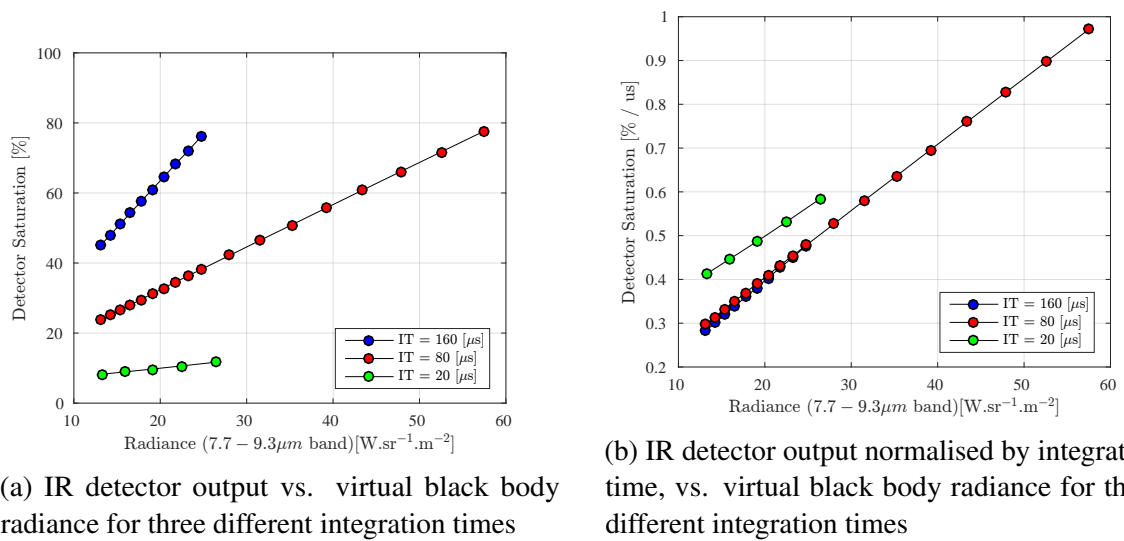


Fig. 6.12

From figure 6.12b it can be seen the the rate of detector saturation is approximately linearly proportional to incident radiance, and largely independent of integration time. A polynomial function was fitted to the data in figure 6.12b for each integration time, providing a continuous calibration function. The radiance values of the virtual black body were calculated using Plank's law (equation 2.4).

With the three IR detector calibration elements performed, they were then applied to the acquired raw IR camera digital level data from the heat transfer measurements, in the

sequence illustrated in figure 6.13, where the ‘first frame’ refers to the first IR image (in digital levels), in the video sequence.

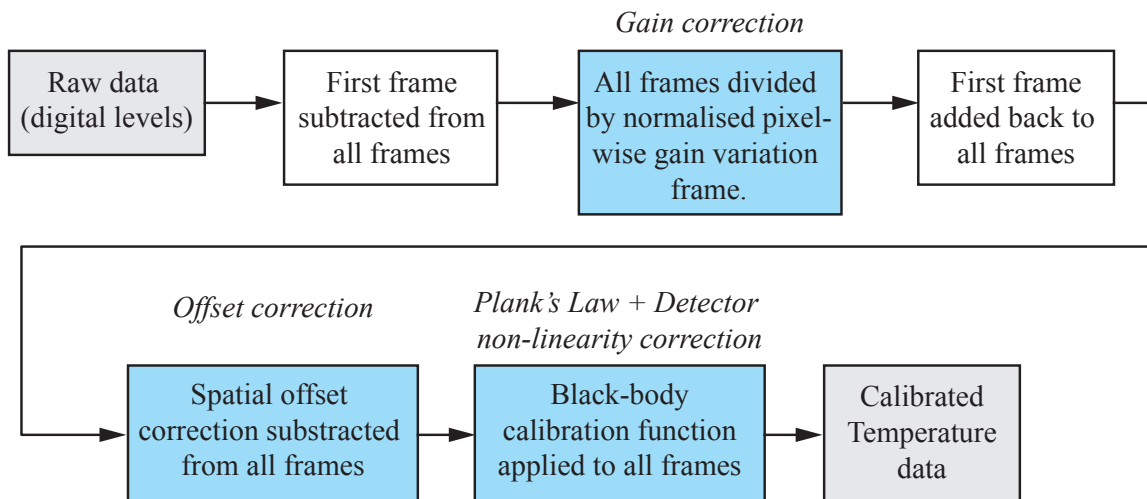


Fig. 6.13 IR Detector calibration algorithm

6.3.4 Optical path calibration

The next step in the calibration process is to perform an optical path calibration. The optical path calibration accounts for the difference in radiance from the emitting object of interest, and the entrance to the lens of the IR camera. The radiance will be corrupted by a combination of reflected, attenuated and emitted radiation, which can either add to, or subtract from the signal measured by the IR camera. The atmosphere, near-by bodies, IR windows, as well as the IR camera itself will all act as source terms of radiation, whose contribution to the measured radiance may need to be removed in order to accurately determine that from the object. Furthermore, the magnitude of these error terms will vary in space, as well as time (as the temperature of the rig will not be stable during the transient measurement). The dominant signal terms are illustrated in figure 6.14.

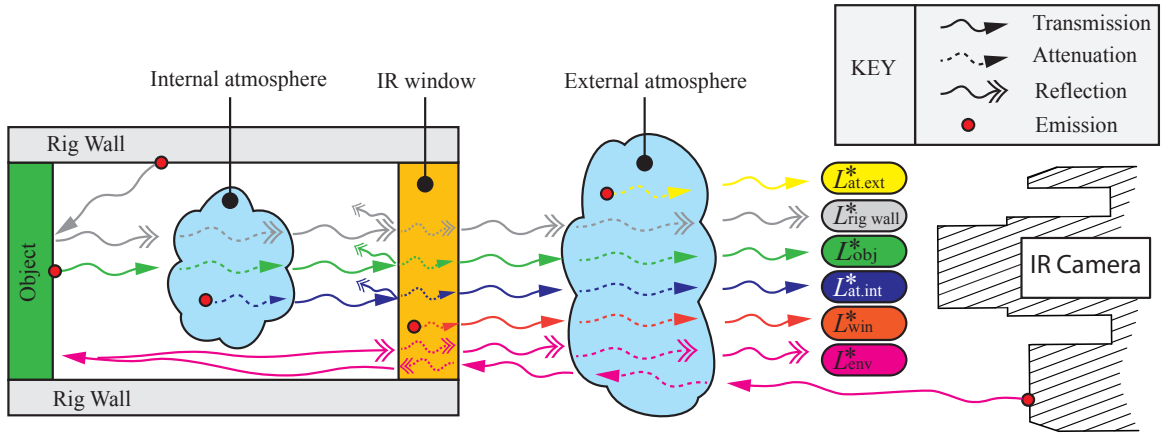


Fig. 6.14 Illustration of the dominant optical path signal terms

The intensity of the emission from each source will be governed by the source surface emissivity (ϵ) and absolute temperature. The attenuation through the internal atmosphere, IR window and external atmosphere, will be governed by the transmissivity (τ) of each medium - which may be a function of its temperature and the wavelength of radiation. The intensity of reflected radiation, will be a function of the incident radiation and the reflectivity (R) of the surface, which may also be a function of wavelength and direction. The total incident radiance arriving at the IR camera lens, L_{cam}^* , is given by equation 6.6. ($L_{bb}(\lambda, T)$ is the spectral radiance of a black body at temperature T , and has the units [$W \cdot sr^{-1} m^{-3}$]).

$$L_{obj}^* = L_{bb}(\lambda, T_{obj}) \cdot \epsilon_{obj} \cdot \tau_{at.int} \cdot \tau_{win} \cdot \tau_{at.ext} \quad (6.1)$$

$$L_{rig.wall}^* = L_{bb}(\lambda, T_{rig.wall}) \cdot \epsilon_{rig.wall} \cdot R_{obj} \cdot \tau_{at.int} \cdot \tau_{win} \cdot \tau_{at.ext} \quad (6.2)$$

$$L_{at.int}^* = L_{bb}(\lambda, T_{at.int}) \cdot \epsilon_{at.int} \cdot \tau_{win} \cdot \tau_{at.ext} \quad (6.3)$$

$$L_{win}^* = L_{bb}(\lambda, T_{win}) \cdot \epsilon_{win} \cdot \tau_{at.ext} \quad (6.4)$$

$$L_{env}^* = L_{bb}(\lambda, T_{env}) \cdot \epsilon_{env} \cdot R_{win} \cdot 2\tau_{at.ext} + L_{bb}(\lambda, T_{env}) \cdot \epsilon_{env} \cdot R_{obj} \cdot 2\tau_{win} \cdot 2\tau_{at.ext} \cdot 2\tau_{at.int} \quad (6.5)$$

$$L_{cam}^* = L_{obj}^* + L_{rig.wall}^* + L_{at.int}^* + L_{win}^* + L_{env}^* \quad (6.6)$$

(Note that the superscript * is an indicator of an *transmitted* signal)

IR Window material selection

Ochs et al. [2009] determined that the transmissivity of the transparent mediums ($\tau_{\text{at.int}}$, $\tau_{\text{at.ext}}$ and τ_{win}), within the sensitive spectral bandwidth of the IR camera, may depend on the temperature of the transparent medium, and on the wavelength of the incident radiation. Three cases were identified:

- **Case 1:** $\tau_{\text{medium}} = \text{Constant}$

This is the simplest case, in which the transmissivity of the medium is constant with temperature and wavelength, across the sensitive spectral bandwidth of the IR camera.

- **Case 2:** $\tau_{\text{medium}} = f(T)$

In this case, the transmissivity of the medium is dependant on temperature, but not on wavelength across the sensitive spectral bandwidth of the IR camera. A calibration of the transmissivity of the medium as a function of medium temperature is required.

- **Case 3:** $\tau_{\text{medium}} = f(T, \lambda)$

In the third case, the transmissivity of the medium is dependant on the temperature of the medium, and on the wavelengths within the sensitive spectral bandwidth of the IR camera. A calibration of the transmissivity of the medium as a function of medium temperature and incident radiation wavelength is required.

The relative intensities of radiation emitted by the object, within the sensitive spectral bandwidth of the IR camera, are a function of object temperature. The consequence of these two statements, is that there will be a unique medium transmissivity, for all object temperatures and all medium temperatures. This represents a challenging calibration task.

In addition to the observations by [Ochs et al., 2009], there is an further complication in the present transient heat transfer rig: The temperature of the IR window and internal atmosphere will vary in time, as a result of the mainstream temperature step. If the transmissivity of the IR window falls under either Case 2 or 3, then the calibration will also need to be time varying. It is consequently desirable to select an IR window material which exhibits a low transmissivity sensitivity to both temperature and wavelength.

The three most common and commercially available LWIR transparent window materials are: Germanium, Zinc Selenide and Zinc Sulphide. Germanium is a tough durable material, which can be relatively easily machined into complex shapes (making it ideal for the complex window geometry required for the FACTOR rig). The transmissivity of Germanium, however, exhibits a strong dependence with both temperature and wavelength at FACTOR operating

temperatures, (within the sensitive spectral bandwidth of the IR camera (7.7 - 9.3 μm)) - putting it in **Case 3**.

Zinc Selenide is a soft material, which can damage easily without careful handling. The transmissivity of Zinc Selenide, however, is independent of temperature and wavelength, within the relevant wavelength range - putting it in **Case 1**. This makes it a highly suitable candidate for window material choice.

Zinc Sulphide is somewhat harder and tougher than Zinc Selenide, and can withstand moderate handling without damage. The transmissivity of Zinc Sulphide, is also independent of temperature and wavelength, within the relevant range. Of all three window materials, Zinc Sulphide is the most appropriate for use in the FACTOR rig and falls under **Case 1**.

The spectral transmission through a 4mm thick sample of each of the three materials, as a function of temperature, is shown in figure 6.15. (Note that the majority of the loss of signal in this data is due to reflection at the surface of the window (as it is uncoated), rather than absorption. The fact that the FACTOR windows have variable thickness, has a negligible effect on the variation of the transmissivity at different locations).

It is important to note that the best choice of window material will depend on the IR camera used (or vice-versa), and the temperature at which the window is operated.

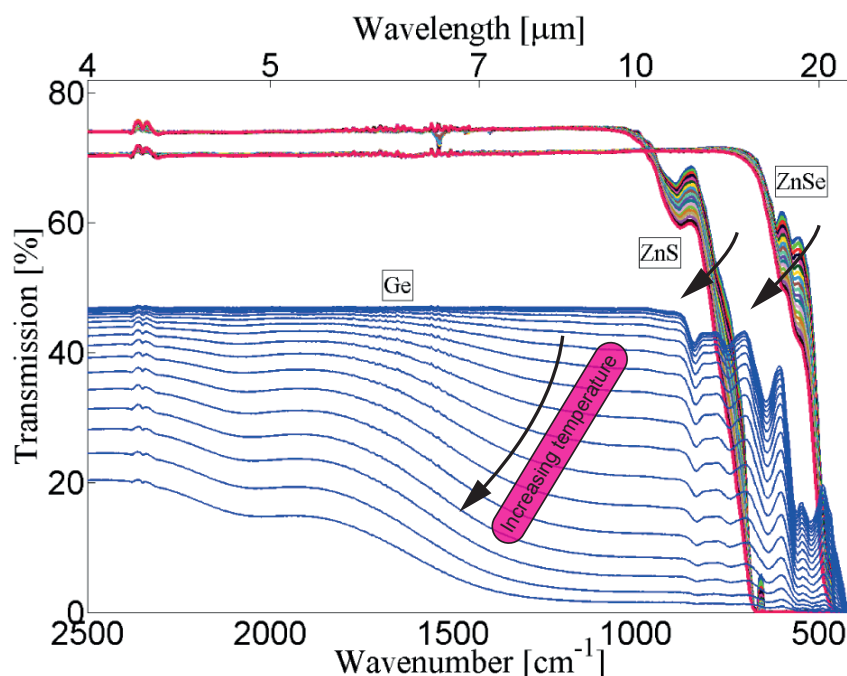


Fig. 6.15 From 20°C to 200°C in 20°C increments - 4mm thick - uncoated [Stolberg-Rohr et al., 2015]

Two-stage in-situ calibration

With the transmissivity characteristics of the window determined from figure 6.15 (i.e temperature dependant, wavelength dependant, or both, or neither), equations 6.1 to 6.5 can be qualified with their appropriate dependence on temperature and wavelength. During the transient heat transfer measurement, the object, rig walls and IR window will vary in temperature, and hence their temperature is expressed as a function of time. (We can generally assume that the environment temperature remains sufficiently stable for L_{env}^* to be considered constant in time).

$$L_{obj}^*(T(t)) = L_{obj}(T(t)) \cdot \tau_{at.int} \cdot \tau_{win} \cdot \tau_{at.ext} \quad (6.7)$$

$$L_{rig.wall}^*(T(t)) = L_{rig.wall}(T(t)) \cdot R_{obj} \cdot \tau_{at.int} \cdot \tau_{win} \cdot \tau_{at.ext} \quad (6.8)$$

$$L_{at.int}^*(T(t)) = L_{at.int}(T(t)) \cdot \tau_{win} \cdot \tau_{at.ext} \quad (6.9)$$

$$L_{win}^*(T(t)) = L_{win}(T(t)) \cdot \tau_{at.ext} \quad (6.10)$$

$$L_{env}^* = L_{env} \cdot R_{win} \cdot \tau_{at.ext} \quad (6.11)$$

$$L_{cam}^*(T(t)) = L_{obj}^*(T(t)) + L_{rig.wall}^*(T(t)) + L_{at.int}^*(T(t)) + L_{win}^*(T(t)) + L_{env}^*(T) \quad (6.12)$$

We can consider the time dependent spectral radiance error terms, $L_{rig.wall}^*(T(t))$, $L_{at.int}^*(T(t))$ and $L_{win}^*(T(t))$ to consist of a steady error component, $\bar{L}^*(T)$, and a unsteady error component, $\tilde{L}^*(T(t))$.

The sum of the steady components, $\bar{L}_{error}^*(T)$, being the spectral radiance error at steady rig operating temperature (with the heater mesh off), given in equation 6.13. The sum of the unsteady components, $\tilde{L}_{error}^*(T(t))$, being the change in spectral radiance which occurs as a result of the rig increasing in temperature during the rig transient, given in equation 6.14.

$$\bar{L}_{error}^*(T_{initial}) = \bar{L}_{rig.wall}^*(T_{initial}) + \bar{L}_{at.int}^*(T_{initial}) + \bar{L}_{win}^*(T_{initial}) + \bar{L}_{env}^*(T_{env.}) \quad (6.13)$$

$$\tilde{L}_{error}^*(T(t)) = \tilde{L}_{rig.wall}^*(T(t)) + \tilde{L}_{at.int}^*(T(t)) + \tilde{L}_{win}^*(T(t)) \quad (6.14)$$

The radiance received at the IR camera lens can be expressed as the summation of the object signal, plus the steady and unsteady error terms.

$$L_{\text{cam}}^*(T(t)) = L_{\text{obj}}^*(T(t)) + \bar{L}_{\text{error}}^*(T_{\text{initial}}) + \tilde{L}_{\text{error}}^*(T(t)) \quad (6.15)$$

The two error terms, $\bar{L}_{\text{error}}^*(T(t))$ and $\tilde{L}_{\text{error}}^*(T)$, are then quantified independently, such that the value of L_{obj}^* (the signal of interest), could be determined from the value of L_{cam}^* . The method by which the steady and unsteady radiance error terms are quantified is described in the following two subsections.

Steady spectral intensity error measurement

The steady radiance error component, $\bar{L}_{\text{error}}^*(T)$, can be quantified in-situ by comparing the measured object temperature from a thermocouple installed at the surface of the object, with the temperature measured from the IR camera, while the rig is at steady operating conditions, with the heater-mesh turned off.

The magnitude of radiance which would be required to produce the apparent temperature difference between the in-situ TC and the IR camera reading is given by an integral of Planks law, equation 6.16, and is equal to $\bar{L}_{\text{error}}^*(T)$. This calibration step corrects for all time-steady offset terms.

$$\bar{L}_{\text{error}}^* = 2hc^2 \left(\int_{\lambda_{\text{min}}}^{\lambda_{\text{max}}} \frac{1}{\lambda^5 (\exp(\frac{hc}{\lambda k T_{\text{IR}}}) - 1)} d\lambda - \int_{\lambda_{\text{min}}}^{\lambda_{\text{max}}} \frac{1}{\lambda^5 (\exp(\frac{hc}{\lambda k T_{\text{TC}}}) - 1)} d\lambda \right) \quad (6.16)$$

Where;

- T_{IR} is the temperature reading from the IR camera,
(i.e. The temperature reading which is given for the incident radiance L_{cam}^*
- T_{TC} is the temperature reading from the surface mounted thermocouple
- $\lambda_{\text{max}}, \lambda_{\text{min}}$ is the upper and lower wavelength limit of the sensitive spectral bandwidth of the IR camera

Unsteady radiance error measurement

The unsteady component of the two-stage in-situ calibration was measured experimentally, using a virtual black-body, embedded within the flat plate test-rig. The virtual black body was located in place of the test-section-plate, in the flat-plate rig, described in section 6.2.1. The virtual black body was maintained at constant temperature, and the apparent radiance

emitted from it was measured with the IR camera, during a rig-transient. If the unsteady component of the error terms is zero - then zero change in radiance will be measured by the IR camera during a transient. Conversely, any change in radiance measured, must only be due to unsteady error terms. The general arrangement of the unsteady in-situ calibration set-up is shown in figure 6.16.

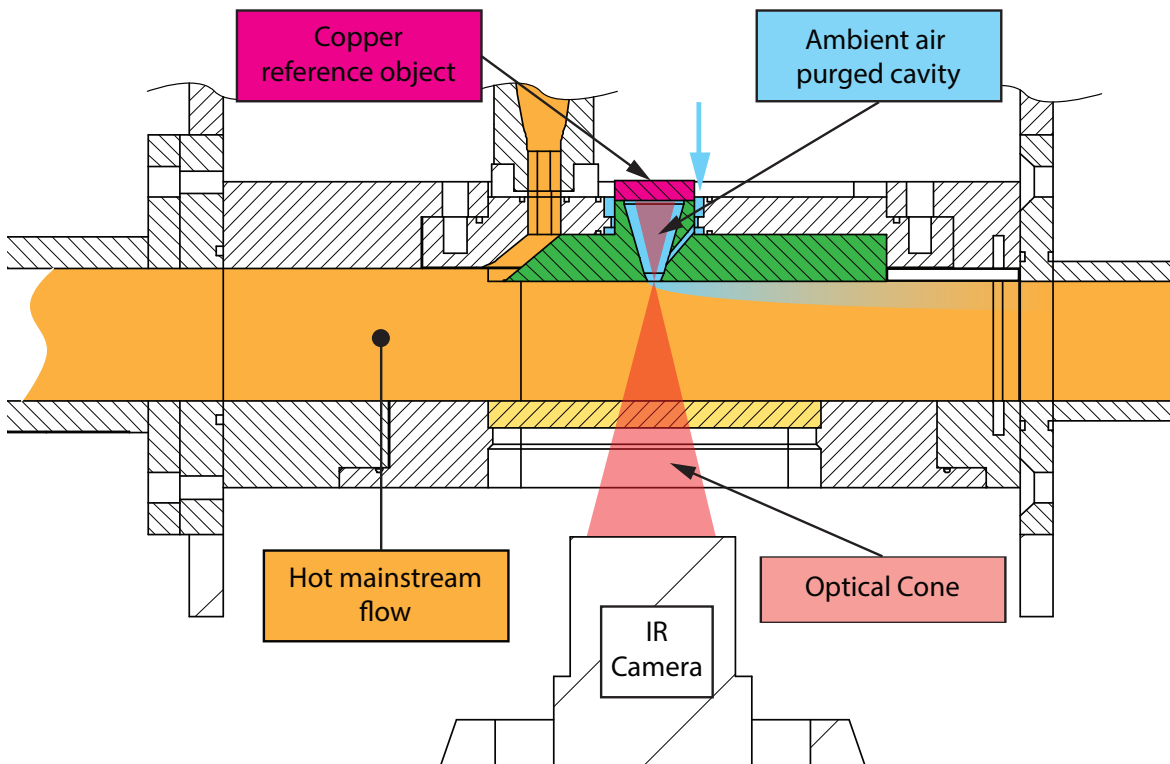


Fig. 6.16 Illustration of the unsteady radiance calibration test rig

The virtual black body was formed from a conical cavity, with black walls. A copper reference object at the end of the cavity provided an emitting object with uniform, and importantly, constant temperature. The temperature of the copper reference object was maintained at a constant value, (ambient temperature), by means of an ambient air purge flow. The purge flow provided a small quantity of air, at a constant temperature, through the cavity and into the mainstream flow. This ensured no hot mainstream gas could enter the cavity and alter the temperature of the copper reference object. The small aperture of the cavity into the mainstream, and the conical shape of the cavity and the black walls, all ensured that a negligible amount of incident radiation into the cavity could be reflected back out. The body forming the conical walls of the cavity was constructed out of a plastic, with low thermal diffusivity, ensuring that negligible heat transfer would occur, by conduction, from the gas

washes surface to the conical walls. The copper reference object was also painted with black internal walls.

The unsteady radiance, $\tilde{L}_{\text{error}}^*(T(t))$, was defined by equation 6.17.

$$\tilde{L}_{\text{error}}^*(T) = 2h^*c^{*2} \left(\int_{\lambda_{\min}}^{\lambda_{\max}} \frac{1}{\lambda^5 (\exp(\frac{h^*c^*}{\lambda k T_{\text{IR}}(t)}) - 1)} d\lambda - \int_{\lambda_{\min}}^{\lambda_{\max}} \frac{1}{\lambda^5 (\exp(\frac{h^*c^*}{\lambda k T_{\text{IR}}(t(0))}) - 1)} d\lambda \right) \quad (6.17)$$

Where $T_{\text{IR}}(t)$ is the temperature reading from the IR camera over time and $T_{\text{IR}}(0)$ is the initial temperature reading from the IR camera, at $t(0)$, prior to the transient.

An example measurement of $\tilde{L}_{\text{error}}^*(T(t))$ is shown in figure 6.17a, which is non-dimensionalised by L_{obj}^* in figure 6.17b. It can be seen that the transient radiance error term $\tilde{L}_{\text{error}}^*(T(t))$, which varies in time, acts to provide an almost time steady fractional error in the measured radiance change of $\sim 5\%$. (Note that the shape of the transient signal in 6.17a correlates well with the shape that would be expected from a semi-infinite transient surface temperature rise caused by heating by forced convection).

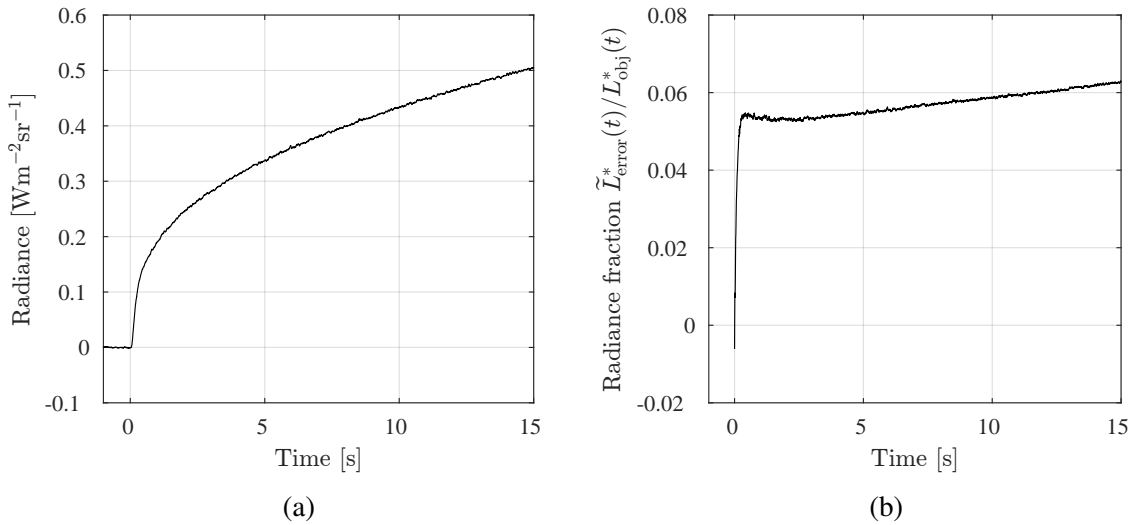


Fig. 6.17 Example measurement of transient offset error $\tilde{L}_{\text{error}}^*(T(t))$

Note that because the virtual black body has a reflectivity of approximately zero, the unsteady error term $\tilde{L}_{\text{rig.wall}}^*(T(t))$ is absorbed, and consequently not measured by the IR camera. The unsteady radiance error measurement primarily accounts for the unsteady window emission term $\tilde{L}_{\text{win}}^*(T(t))$. In this research, no method of experimentally measuring $\tilde{L}_{\text{rig.wall}}^*(T(t))$ was used. Instead, a high emissivity coating was used to reduce its magnitude.

Data correction procedure

With both the unsteady and steady radiance error terms quantified, their values need to be used to appropriately modify the IR camera temperature measurements. The radiance error terms need to be subtracted from the observed radiance measurements from the IR camera. It is essential that this subtraction takes place in units of $[\text{W}\cdot\text{sr}^{-1}\cdot\text{m}^{-2}]$, and not directly as temperature or IR camera sensor value, so as to satisfy conservation of energy.

The process was conducted as follows:

1. Convert the IR camera temperature measurements, into measured radiance values, by integration of Planks law. (The correct spectral bandwidth of the IR camera must be used to perform the integration)
2. Subtract the measured steady and unsteady radiance error terms, \bar{L}^*_{error} and $\tilde{L}^*_{\text{error}}(t)$
3. Divide the radiance terms by the combined optical path transmissivity, $\tau_{\text{win}} \cdot \tau_{\text{at.int}} \cdot \tau_{\text{at.ext}}$.
4. Convert the corrected radiance data set back into units of temperature, with Planks law in reverse.

6.3.5 Emissivity calibration

The remaining step in the calibration process is to determine the difference between the ideal black body spectral radiance, and the actual spectral radiance of the black paint used on the object surface: This relationship is governed by the emissivity, ϵ , which can be a function of wavelength, object temperature, and view angle from surface normal (θ).

$$L_{\text{obj}}(\lambda, T_{\text{obj}}, \theta) = L_{\text{bb}}(T_{\text{obj}}) \cdot \epsilon_{\text{obj}}(\lambda, T_{\text{obj}}, \theta) \quad (6.18)$$

The emissivity of the black paint, which was used on all object surfaces, was determined by comparing the measured radiance intensity from a virtual black body to that from the black painted surface, where both were at the same temperature, and viewed from the same angle (normal to the surface). The radiance from the virtual black body (subscript: vbb) and from the surface of the black paint (subscript: bp) can then be expressed as follows, (where R_{bp} is the reflectivity of the black paint):

$$L_{\text{vbb}}(T_{\text{obj}}) = L_{\text{bb}}(T_{\text{obj}}) \cdot \epsilon_{\text{vbb}} \quad (6.19)$$

$$L_{bp}(T_{obj}) = L_{bb}(T_{obj}) \cdot \epsilon_{bp} + L_{bb}(T_{amb}) \cdot R_{bp} \quad (6.20)$$

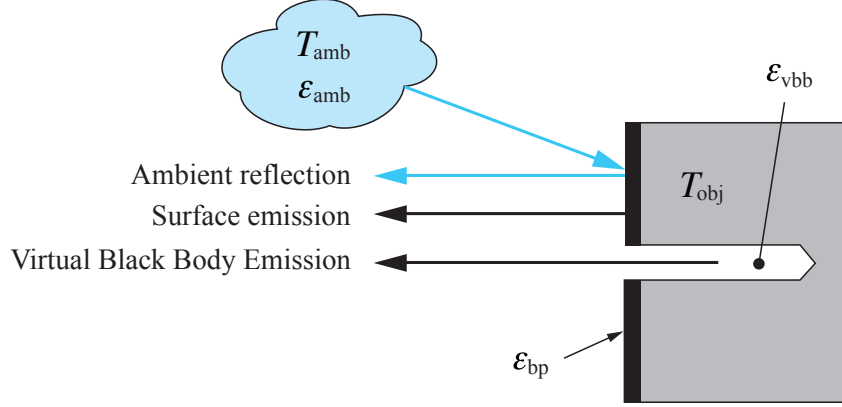


Fig. 6.18 Illustration of emissivity calibration parameters

If we assume that the emissivity of the virtual black body is equal to one, and that the ambient temperature remains constant, then equation 6.19 and 6.20 simplify to:

$$L_{vbb}(T_{obj}) = L_{bb}(T_{obj}) \quad (6.21)$$

$$L_{bp}(T_{obj}) = L_{bb}(T_{obj}) \cdot \epsilon_{bp} + \text{constant} \quad (6.22)$$

Substituting equation 6.21 into equation 6.22:

$$L_{bp}(T_{obj}) = L_{vbb}(T_{obj}) \cdot \epsilon_{bp} + \text{constant} \quad (6.23)$$

The linear equation 6.23 has two unknowns, ϵ_{bp} and a constant - assuming we can measure $L_{vbb}(T_{obj})$ and $L_{bp}(T_{obj})$ with an IR camera. Hence two linear simultaneous equations will define a solution. Two equations can be defined by setting the object temperature to two different values; T_1 and T_2 . Doing so, and rearranging yields the following equation for the emissivity.

$$\epsilon_{bp} = \frac{L_{bp}(T_2) - L_{bp}(T_1)}{L_{vbb}(T_2) - L_{vbb}(T_1)} \quad (6.24)$$

The virtual black body rig, described in section 6.3.3, and the IR camera, were used to perform this measurement. The temperature T_1 , was set to ambient temperature ~ 294 K. The temperature T_2 was set to a range of temperatures, between ~ 294 and 329 K -

providing multiple solutions to ϵ_{bp} as a function of T_{obj} . The measured solutions to equations 6.24 are shown in the graph in figure 6.19.

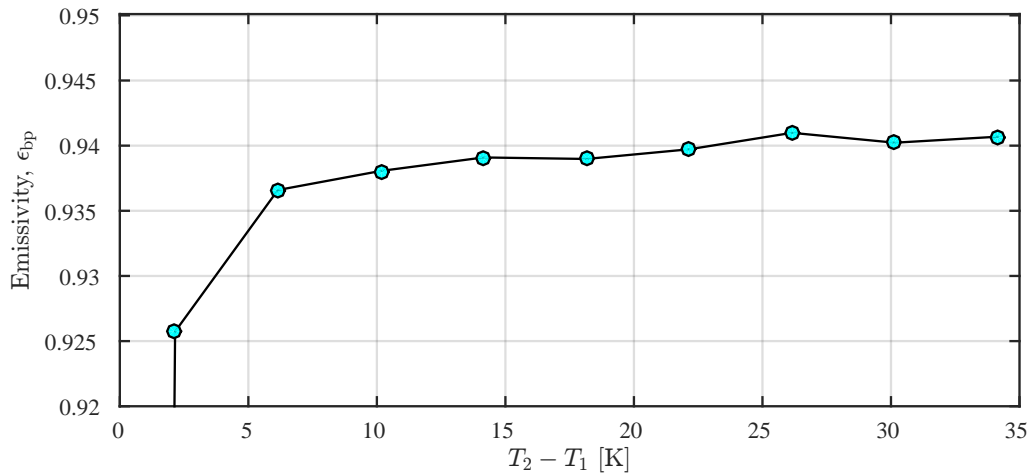


Fig. 6.19 Black paint emissivity measurement results (Paint: Electrolube PNM400)

At low values of $T_2 - T_1$, the measurement is ill-conditioned, as the signal to noise levels become low. This can be seen by the large change in the measured value of ϵ_{bp} as $T_2 - T_1$ approaches zero. At higher values of $T_2 - T_1$, the emissivity value stabilises to approximately 0.94, and appears to be reasonably insensitive to object temperature - which is highly desirable.

Measurements were also performed off-axis - which showed an approximately constant emissivity between 0 and 70°.

It should be noted that this emissivity measurement is only valid for the narrow spectral band of the IR camera which was used to conduct the measurements - 7.7 μm - 9.3 μm .

An uncertainty analysis was performed to estimate the bias uncertainty in the emissivity measurement. It was assumed that natural convection occurred at the front face of the black body, with a heat transfer coefficient of 50 [$\text{Wm}^{-2}\text{K}^{-1}$], causing a difference in temperature between the black paint surface and the platinum resistance thermometer. This difference in temperature was estimated to cause a maximum of a $\sim 2\%$ error in the evaluation of emissivity.

6.4 Thermal Effusivity Calibration

6.4.1 Measurement requirements

In Chapter 3, it was shown that uncertainty in the thermal effusivity of the substrate will have a direct linear influence on the uncertainty in the heat transfer coefficient measurement. Consequently it is important that the thermal effusivity of the substrate is known to a low uncertainty.

In Chapter 5 the substrate materials selected for the FACTOR turbine rig components were specified as Torlon 5030 and Torlon 7130. The thermal effusivity of these substrate materials, according to the manufactures data sheet, are shown in figure 6.20 (Torlon 4203, the unfilled grade, is also shown). The data-sheet values indicate that there is a variation in thermal effusivity of all three materials with temperature, where there is a $\sim 1\%$ change in thermal effusivity for every 10K increment in temperature.

The FACTOR NGV will have large temperature gradients on its surface, due to the high levels of film-cooling. NGV surface temperatures can be expected to be between 300 and 500K - yielding a spatial thermal effusivity variation of $\sim \pm 10\%$. It is therefore important that temperature dependant material properties are used in the evaluation of heat flux in the FACTOR rig measurements.

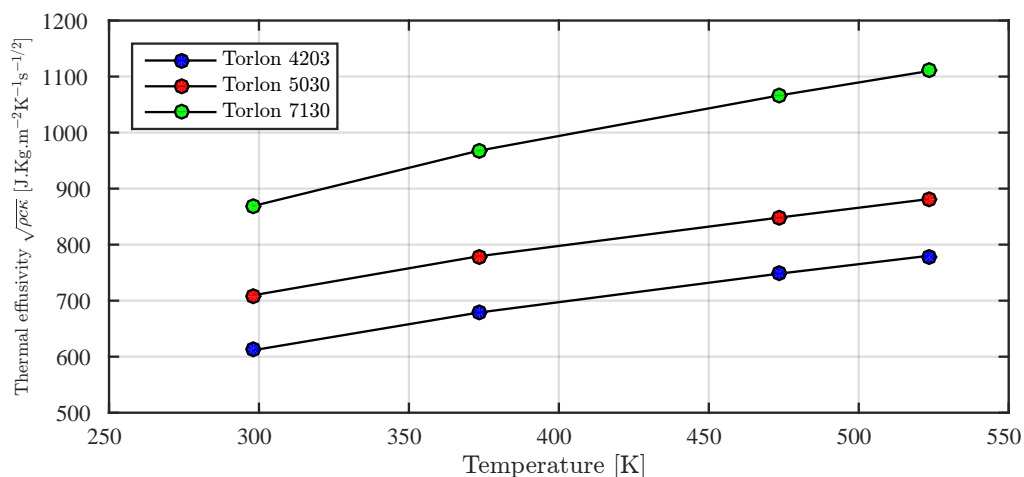


Fig. 6.20 Thermal effusivity of Torlon polymers as a function of temperature [Solvay, 2014]

The surface temperature variations in the two rigs described in this research (Flat plate rig and 3D vane rig), will be lower - with a maximum variation of $\sim 32\text{K}$. This will yield a thermal effusivity variation of $\sim \pm 1.6\%$. Due to this value being small, temperature

dependant material properties were not used in the data analysis for these rigs. The value of the thermal effusivity at near ambient temperature, for the three grades of Torlon substrate were measured experimentally, for the purpose of data-sheet value verification.

6.4.2 Measurement method

A new method of thermal effusivity measurement was developed, which enabled high spatial resolution measurements of thermal effusivity directly, and non-destructively, on the test section plates. The method can also be applied directly to the FACTOR vanes and blades. The method consists of exposing a sample material to a step change in surface heat flux, provided by a series of high power halogen lamps, and measuring the transient surface temperature response of the substrate surface with an IR camera. With the transient surface temperature response and knowledge of the surface heat flux provided by the lamps, the thermal effusivity can be deduced. The measurement method employs some of the principles described by Schultz and Jones [1973] and Maulard [1969], who both used lumped mass copper bodies as reference heat flux gauges. The measurement technique consisted of three discrete steps, which are described below:

Step 1 - Area average radiant heat flux calibration

In the first step, an area average radiant heat flux absorbed by a body exposed to the lamps is measured. A copper disk with heat capacity ρcV , frontal area exposed to the illumination A , and surface emissivity ε , rises in temperature over time when exposed to a step increase in heat flux from the lamps. (A step increase is achieved using a large guillotine, which rapidly exposes the copper disk to the radiation). After an exposure period, t_{exposure} , the lamps are turned off and the copper mass cools down back to room temperature. On account of the high thermal conductivity of the copper, the mass is treated as a lumped thermal mass. The time resolved temperature of the copper body is measured with a high accuracy platinum resistance thermometer embedded within the body.

While the copper body is at a temperature greater than ambient temperature (i.e while it is heating up and cooling down), it loses heat to its surroundings. The rate of heat loss from the copper body to the surrounds is small in comparison to the rate of heat addition by the lamps - nevertheless a correction was required for ambient heat loss. A time averaged cool-down time constant, $\tau_{\text{nat.convection}}$, was determined by fitting an exponential decay function to the measured cool-down temperature history. The rate of copper body cooling could then be expressed as a function of the temperature difference between the copper body and the ambient temperature, as shown by equation 6.25, following Newtons law of cooling.

$$\frac{dT_{\text{copper}}}{dt} = (T_{\text{ambient}} - T_{\text{copper}}) / \tau_{\text{nat.convection}} \quad (6.25)$$

A cumulative ‘temperature loss’, $\Delta T_{\text{copper}}(t)$, could then be defined, by an integration over time, given by equation 6.26.

$$\Delta T_{\text{copper}}(t) = \int_0^t \frac{T_{\text{ambient}} - T_{\text{copper}}}{\tau_{\text{nat.convection}}} dt \quad (6.26)$$

Finally, a ‘heat loss corrected’ temperature history was defined as the measured temperature history plus $\Delta T_{\text{copper}}(t)$. The measured temperature and heat loss corrected temperature are shown in figure 6.21 (left), where the lamps are turned on at $t = 0[s]$ and turned off at $t = 540[s]$. It can be seen that the ‘heat loss corrected’ temperature at $t > 540[s]$ remains largely constant over time, indicating that the heat loss correction function is performing well.

(Note that there will be a time-lag in the PRT temperature measurement - however, since the temperature of the copper disk rises uniformly in time, the time-lag has no effect (after a short period of time) on the measurement of the rate of change of the temperature of the copper disk).

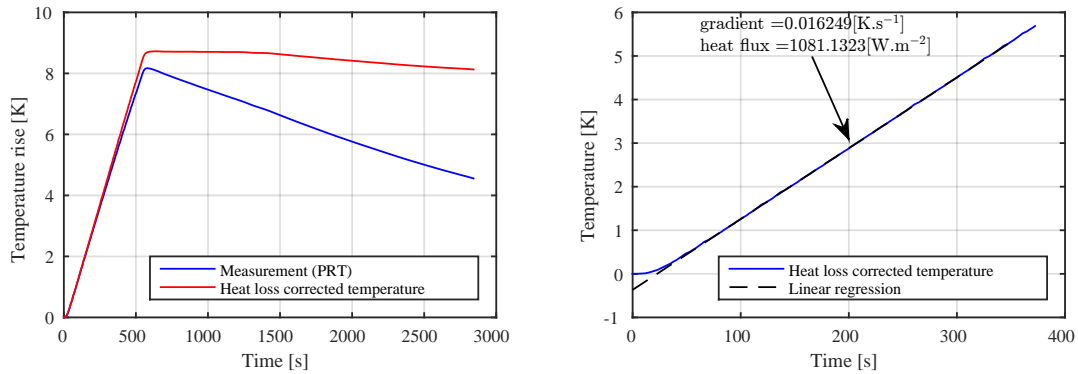


Fig. 6.21 Thermal effusivity of Torlon polymers as a function of temperature [Solvay, 2014]

In figure 6.21 (right) a linear regression function is fitted to the ‘heat loss corrected’ temperature data over the heating-up phase - where the gradient provides a time averaged rate of temperature increase of 0.0162 [K/s]. The time average heat flux into the copper body was then defined according to equation 6.27.

$$\dot{q} = \frac{\frac{dT}{dt} \cdot \rho \cdot c \cdot V}{A} \quad (6.27)$$

The disk is made of unalloyed copper - and hence the ρ and c are known to a high accuracy. The area of the disk is measured to an uncertainty of $\pm 0.2\%$, and the volume to an uncertainty of $\pm 0.8\%$.

Step 2 - A spatial calibration of the illumination field is performed

In the second step, the calibrated area average heat flux determined in Step 1 is converted to a spatially resolved heat flux field, (this is necessary since the lamps will not provide spatially uniform heating). The copper body from Step 1 is replaced with a thick plate of acrylic plastic, such that the illuminated face of the acrylic lies on the same plane that copper was in. The acrylic is also painted with the same black paint, such that the emissivities can be assumed to be the same. The acrylic is then exposed to a step change in heat flux, again, provided by the halogen lamps and guillotine. The surface temperature response of the acrylic is measured with the same IR camera. An illustration of the arrangement is shown in figure 6.22.

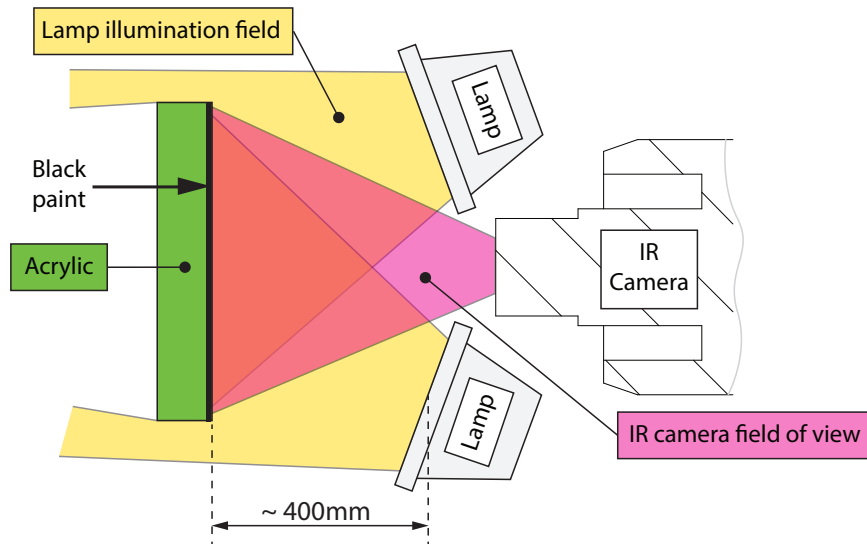


Fig. 6.22 Illustration of the optical arrangement for Step 2 of the effusivity calibration method

As the Acrylic absorbs the radiation from the lamps, it increases in temperature, and heat conducts through the plate, in a direction parallel to its surface normal. While the heat has not significantly conducted through the full thickness of the acrylic, it behaves as a semi-infinite solid. The analytical solution to the heat equation, for a semi-infinite solid, with a constant heat flux boundary condition, and uniform initial temperature, is given by equation 6.28.

$$T(0,t) - T_i = \frac{2q_0}{\sqrt{\pi}} \cdot \frac{\sqrt{t}}{e} \quad (6.28)$$

Where;

$T(0,t)$ is the surface temperature of the acrylic over time [K]

T_i is the initial temperature of the Acrylic (which must be uniform in space) [K]

\dot{q}_0 is the heat flux received by the surface, from the lamps [Wm^{-2}]

e is the thermal effusivity $\sqrt{\rho c \kappa}$ [$\text{Wm}^{-2}\text{K}^{-1}\text{s}^{0.5}$]

t is the elapsed time from the start of illumination [s]

Equation 6.28 can be re-arranged into the following:

$$e = \frac{\sqrt{\pi}(T(0,t) - T_i)}{2\dot{q}_0\sqrt{t}} \quad (6.29)$$

Hence an area average value of e for the acrylic, where the area corresponds to the same illumination area circumscribed by the copper body from Step 1, can be calculated, if the value of \dot{q}_0 is defined as that which was determined in Step 1, and if an area average value of $T(0,t) - T_i$ is used. Assuming the acrylic to have homogeneous material properties, then the area average value of e is equal to the spatially resolved value of e .

Finally, the spatially resolved heat flux field can be defined as follows;

$$\dot{q}_0(m,n) = \frac{\sqrt{\pi}e(T(m,n,t) - T_i)}{2\sqrt{t}} \quad (6.30)$$

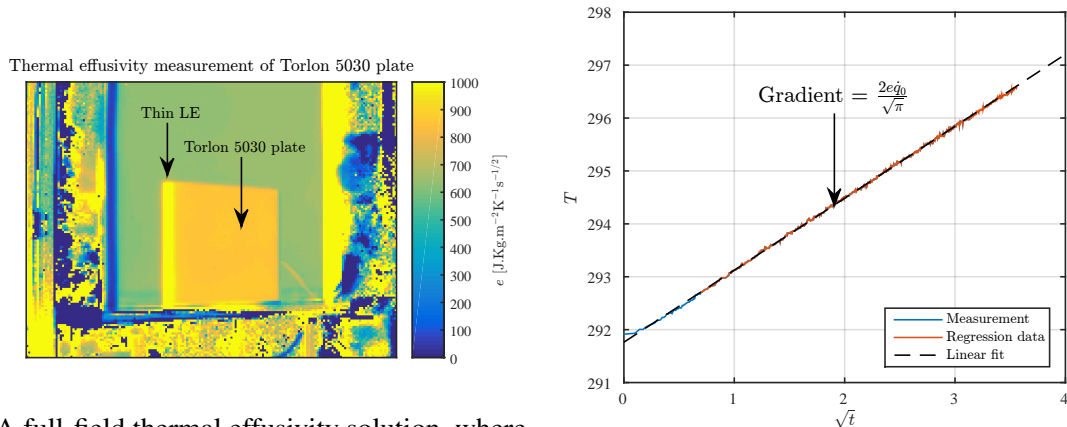
where $T(m,n,t) - T_i$ are spatially resolved measurements from the entire surface of the acrylic, and e is the effusivity of the acrylic determined previously.

Step 3 - Spatially resolved effusivity measurements of the samples are made

In the final step, the acrylic is replaced with the samples which require measurement of their thermal effusivity. The lamps and guillotine are used provide a step change in the surface heat flux, and an IR camera is used to measure the surface temperature response, in a similar manor to step 2. The thermal effusivity of the samples are then determined using equation 6.29, where \dot{q}_0 is the spatially resolved heat flux field determined in Step 2.

A solution to the spatially resolved thermal effusivity of the Torlon 5030 flat plate (from section 6.2.1), is shown in figure 6.23a. Accurate measurement of the thermal effusivity requires a finite substrate thickness, and hence there is a local error at the sharp leading edge of the Torlon plate, which is highlighted in the figure. Within the thick section of the plate, the mean value of the thermal effusivity is $859.7 \text{ [J.Kg.m}^{-2}\text{K}^{-1}\text{s}^{1/2}]$, and the standard deviation is 0.12%. The thermal effusivity values obtained for Torlon 7130 and 4203 were 983.7 and 607.8 [$\text{J.Kg.m}^{-2}\text{K}^{-1}\text{s}^{1/2}$] respectively. (Note that there is significant deviation (upto $\sim 20\%$)

in these values from the data sheet values provided in figure 6.20). In figure 6.23b a single pixel measurement is shown for the Torlon 5030 plate, where a linear regression is performed to find the value of e .



(a) A full-field thermal effusivity solution, where the Torlon 5030 flat plate can be seen, at an angle, in the centre of the image

(b) A linear regression is performed on the measurements from each pixel to determine e

Fig. 6.23

In the table 6.6, an estimate of the uncertainty in the effusivity measurement is provided, where a root-mean-square summation is used to determine the total measurement uncertainty.

Table 6.6 Estimate of the thermal effusivity measurement technique uncertainty

Source	Uncertainty	Comment
Area of copper disk	0.2%	Linear measurement uncertainty
Volume of copper disk	0.8%	Linear measurement uncertainty
Heat loss correction error	2%	i.e. $\sim 80\%$ of total error is corrected
Lamp power drift	4%	Estimate
Acrylic effusively non-uniformity	2%	Estimate
Temperature rise measurement error	1.5%	Based on emissivity bias error
RMS total uncertainty	5.2%	

6.5 Heat Flux Modelling

Two heat flux modelling approaches were used in the experimental work in this research to determine heat flux from the transient surface temperature measurements from the substrate surface: A one-dimensional analytical method, and a 3-dimensional numerical method. The advantages and disadvantage of each modelling approach were described in section 2.4.2.

[Oldfield, 2008] developed a computationally efficient method of one-dimensional transient heat flux modelling, referred to as the ‘Impulse Response’ method. The method was described in detail the literature review (section 2.4.2). The ‘Impulse Response’ method was used for all one-dimensional heat flux modelling.

A finite difference numerical model was developed for the three-dimensional heat flux modelling. As with the one-dimensional modelling, the three-dimensional model made use of the semi-infinite assumption, such that an adiabatic back-face boundary condition could be assumed. The model also assumed that the substrate surface is flat. The three-dimensional model allows for the resolution of lateral heat flux terms within a flat semi-infinite substrate, which are induced by non-uniform convective boundary conditions on the substrate surface (as described in section 3.6.4). This will permit greater heat flux measurement resolution at length scales less than the heat penetration depth. Note that the numerical model is a prototype for the FACTOR measurements - its purpose was primarily to allow the benefits of 3D heat flux modelling to be explored, and is not necessarily the most computationally efficient method of modelling the 3D heat flux.

The numerical scheme, boundary conditions and model resolution parameters are described in the following subsections, as well as the results from a model validation procedure.

6.5.1 Numerical scheme

A three-dimensional explicit finite difference computational model was created to solve the heat equation, equation 6.31. This model determined the full 3D temperature distribution within the substrate, over time. The time resolved temperature measurements, from the IR camera, were applied as one of the boundary conditions to the model.

$$\frac{\partial T_{(t,x,y,z)}}{\partial t} = \alpha \left(\frac{\partial^2 T_{(t,x,y,z)}}{\partial x^2} + \frac{\partial^2 T_{(t,x,y,z)}}{\partial y^2} + \frac{\partial^2 T_{(t,x,y,z)}}{\partial z^2} \right) \quad (6.31)$$

Time resolved heat flux, at the surface of the substrate, was extracted from the 3D temperature field solution by determining the temperature gradient at the gas-washed wall of

the substrate, over time. An expression for the surface heat flux is given by equation 6.32, where z is a normal vector to the gas washed surface.

$$\dot{q}_{(t,x,y,0)} = \kappa \cdot \frac{\partial T_{(t,x,y,0)}}{\partial z} \quad (6.32)$$

A second order in space central differencing scheme and a first order in time Euler forward differencing scheme was used to approximate equation 6.31. The scheme is shown in equation 6.33 to 6.36.

$$\frac{\partial^2 T_{(t,x,y,z)}}{\partial x^2} = \delta_x^2 [T](x) + O(x^2) = \frac{T_{t,x-1,y,z} - 2T_{(t,x,y,z)} + T_{(t,x+1,y,z)}}{\Delta x^2} + O(\Delta x^2) \quad (6.33)$$

$$\frac{\partial^2 T_{(t,x,y,z)}}{\partial y^2} = \delta_y^2 [T](y) + O(y^2) = \frac{T_{(t,x,y-1,z)} - 2T_{(t,x,y,z)} + T_{(t,x,y+1,z)}}{\Delta y^2} + O(\Delta y^2) \quad (6.34)$$

$$\frac{\partial^2 T_{(t,x,y,z)}}{\partial z^2} = \delta_z^2 [T](z) + O(z^2) = \frac{T_{(t,x,y,z+1)} - 2T_{(t,x,y,z)} + T_{(t,x,y,z-1)}}{\Delta z^2} + O(\Delta z^2) \quad (6.35)$$

$$\frac{T_{(t+1,x,y,z)} - T_{(t,x,y,z)}}{\Delta t} = \alpha \cdot \left(\delta_x^2 [T](x) + \delta_y^2 [T](y) + \delta_z^2 [T](z) \right) + O(\Delta t) \quad (6.36)$$

As will be described shortly, the computational mesh used for the analysis had a high and low resolution region, where the spatial step in the z direction changes between the two regions. At this region interface, an adapted version of the central differencing scheme was used. This accounted for the unequal neighbouring node distance either side of the interface, in the z -direction. The scheme is given in equation 6.37, where ‘int.’ refers to the interface node number in the z direction. (The scheme was determined by manipulation of the Taylor series expansion). (The subscripts HR and LR refer to the High Resolution and Low Resolution regions of the mesh respectively)

$$\frac{\partial^2 T_{(t,x,y,int.)}}{\partial z_{LR}^2} = \delta_z^2[T](z) + O(z^2) = \frac{\Delta z_{LR} \cdot T_{(t,x,y,int.+1)} - (\Delta z_{LR} + \Delta z_{HR}) \cdot T_{(t,x,y,int.)} + \Delta z_{HR} \cdot T_{(t,x,y,int.-1)}}{0.5 \cdot (\Delta z_{HR} - \Delta z_{LR}) \cdot \Delta z_{LR} \cdot \Delta z_{HR}} \quad (6.37)$$

A third order forward difference scheme, equation 6.38, was used to approximate the heat flux at the wall. The scheme is shown in equation 6.32.

$$\dot{q}_{(t,x,y,0)} = \kappa \cdot \frac{\partial T_{(t,x,y,0)}}{\partial z} \approx \kappa \cdot \frac{-3T_{(t,x,y,0)} + 4T_{(t,x,y,1)} - T_{(t,x,y,2)}}{2\Delta z} + O(\Delta z^3) \quad (6.38)$$

The numerical model was written and executed in ‘Matlab’.

6.5.2 Structured mesh & boundary conditions

An illustration of the structured mesh is shown in figure 6.24. The mesh had uniform node density in the x and y directions. There were 320 nodes in the x direction, and 256 nodes in the y direction, which matched the resolution of the IR camera. Time resolved temperature measurements from the IR camera could then be directly linked to the values of the nodes on the front-face, with no interpolation required.

The node density in the z direction (normal to the substrate surface) was non-uniform. A high resolution layer, 30 nodes deep, was used at the front face. The remainder of the domain, in the z direction, had a resolution 20 times lower. A high z -direction spatial resolution was required close to the substrate surface, in order to resolve the high curvature in the temperature distribution in this region which occurs for a short duration immediately after the mainstream temperature step.

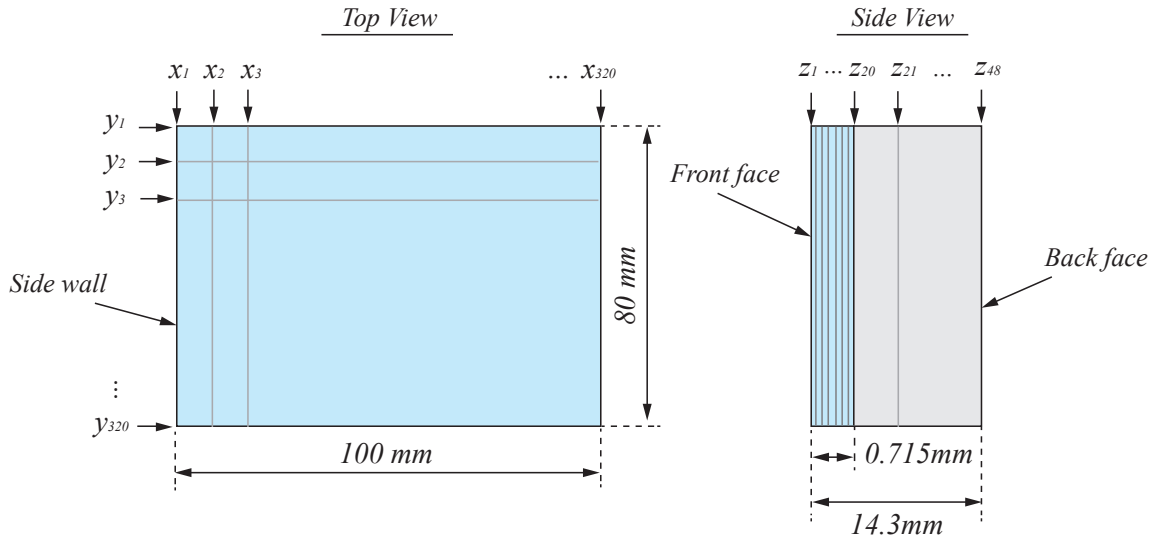


Fig. 6.24 Graphical representation of structure mesh

Two categories of boundary conditions were applied:

1. **Front face** - Dirichlet boundary condition - Fixed value

The values of the nodes on the front-face of the mesh, were defined to match the time-resolved temperature measurements from the IR camera. The resolution of the mesh, in x and y , were set to match the resolution of the IR camera images - as such no interpolation was required.

$$T_{(t,x,y,0)} = T_{\text{IR}(t,x,y)} \quad (6.39)$$

2. **Side walls and Back face** - Neumann boundary condition - Fixed gradient

The values of the nodes on the side walls and back face of the mesh were defined to produce a temperature gradient of zero at the boundaries. This enforced an adiabatic condition on these faces. It is important to note, that only a negligible temperature rise will occur on the back face, as the thickness of the substrate is sufficiently thick to remain semi-infinite through the simulation.

$$T_{(t,0,y,z)} = T_{(t,1,y,z)} \quad (6.40)$$

$$T_{(t,320,y,z)} = T_{(t,319,y,z)} \quad (6.41)$$

$$T_{(t,x,0,z)} = T_{(t,x,1,z)} \quad (6.42)$$

$$T_{(t,x,256,z)} = T_{(t,x,255,z)} \quad (6.43)$$

$$T_{(t,x,y,48)} = T_{(t,x,y,47)} \quad (6.44)$$

6.5.3 Model resolution

In figure 6.25 the mesh node locations are shown on an idealised semi-infinite transient response to a constant convective boundary condition, with an h of $400 \text{ [Wm}^{-2}\text{K}^{-1}\text{]}$. The substrate material has the properties of Torlon 5030. This represented a probable set of measurement data. It can be seen that the high resolution layer enables good resolution of the temperature field at all relevant time scales.

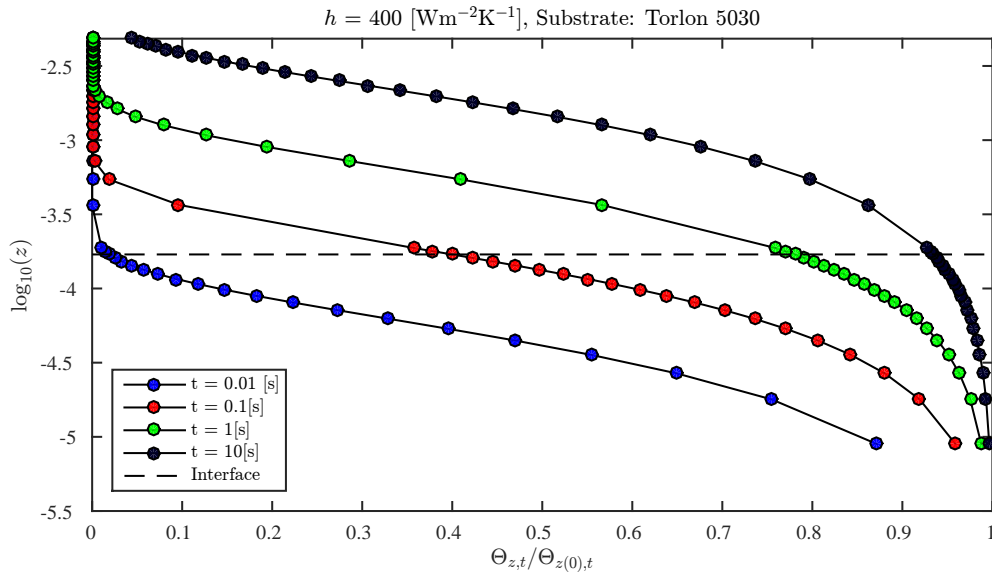


Fig. 6.25 The mesh resolution was evaluated using a probable temperature distribution, determined using a one-dimensional analytical solution.

The temporal resolution was defined by setting the temporal step size, Δt , such that a Peclet number of 2.5 was achieved (the Peclet number is a non-dimensional value, which characterises the numerical stability - and is given in equation 6.45). A Peclet number greater than 2 is required for numerical stability, when modelling a linear diffusion equation, which is forward explicit in time, and central difference in space. The time step, Δt , is defined in equation 6.45, as a function of Peclet number, thermal diffusivity, α , and grid spacing Δz .

$$\Delta t = \frac{\Delta z^2}{\text{Pe} \cdot \alpha} \quad (6.45)$$

The grid spacing in the x and y direction is larger than in the z direction, hence numerical stability will be achieved in the x and y direction.

The high resolution layer and the low resolution layer of the mesh have two different grid spacing values Δz . Consequently, the two regions of the mesh required different time steps. In order to avoid interpolation in the time-domain between the two regions of the mesh, the temporal step of the low resolution region, Δt_{LR} , was rounded to the closest integer number of high resolution time steps Δt_{HR} . This ensured that all low resolution region evaluation instances, coincided with a high resolution region evaluation instance - avoiding interpolation.

6.5.4 Model validation

Validation of the 3D-heat-flux model was performed in two stages: Firstly, by determining the ability of the model to accurately calculate wall heat flux in a one dimensional, semi-infinite, constant convective boundary condition case. The model solution was compared to the exact analytical solution to determine the models errors, as a function of spatial and temporal discretisation step sizes.

Secondly, a solution to the three dimensional heat equation with non-uniform convective boundary conditions was generated by means of a high resolution finite difference model. The two dimensional time resolved surface temperature from this model was then used as an input for the 3D-heat-flux model. The ability of the 3D-heat-flux model to determine the original boundary conditions was compared with that of the one dimensional 'Impulse Response' heat flux processing method. This served to determine the impact of resolving lateral heat flux in computation of the convective boundary conditions.

These two model validation steps are described in the following subsections.

1D Validation

A uniform convective boundary condition was applied to the 3D-heat-flux model, with a heat transfer coefficient of $400 \text{ [Wm}^{-2}\text{K}^{-1}]$ and an adiabatic wall temperature rise defined by an exponential of the form given in equation 6.46, where the temperature rise time constant τ was set to 0.1s. The substrate material properties were set to those of Torlon 5030. This provided boundary conditions representative of those which can be expected in the present heat transfer rigs.

$$\frac{T_{\infty}(t)}{T_{\infty}(t \rightarrow \infty) - T_{\infty}(t(0))} = 1 - \exp(-t/\tau) \quad (6.46)$$

The exact analytical solution and the model solution, for non-dimensional heat flux at the wall are shown in figure 6.26. The model was run with a Peclet number of 2.5 and a Δz scaling factor of 1. (i.e Δz matched the definition given in figure 6.24)

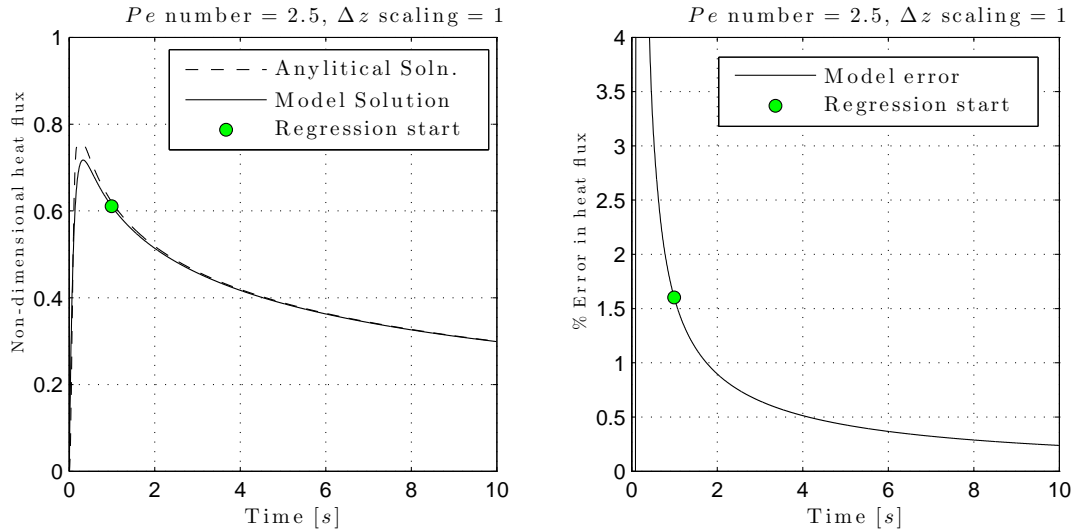


Fig. 6.26 A comparison of an analytical solution and numerical solution to heat flux, for a representative set of boundary conditions

The influence of truncation errors can be seen to affect the model solution significantly at low values of time, where the second derivative of temperature in space is large. As the model progresses in time, these errors diminish. The under-estimate of heat flux at low values of time, represents a loss of total heat in the model domain. By conservation of energy, this error is then diffused through the domain. Accurately capturing the heat flux at low values of time requires high spatial and temporal model resolution. The number of computations scales with $1/\Delta z^3$, whereas the truncation errors scale with $1/\Delta z$.

The sensitivity of the model error to the discretisation step size Δz and Δt (Pe number), are shown in figure 6.27. The graph on the left, shows the sensitivity of the model error to Pe number, where the Pe number varies between 2.5 and 3.5. The graph on the right, shows the sensitivity to the Δz step size, where the step size was varied between 0.5 and 2 times the nominal step size.

Pe numbers less than 2.1 resulted in unstable solutions. The sensitivity of the solution to $Pe > 2.5$ is low. This indicates that the first order error in the time stepping scheme, equation 6.36, is low, and higher order methods are not required. A nominal Pe number of 2.5 was chosen for all subsequent modelling.

The model error showed an approximately linear relationship to the step size Δz - where halving the spatial step size resulted in a halving the error. This agrees with expectations, as although the spatial central differencing numerical scheme is second order in space, the heat flux is only first order in space, as shown by equation 6.47 and 6.48.

$$\dot{q}_{(t,x,y,0)} \propto \frac{\partial T_{t,x,y,0}}{\partial z} = \frac{f(\delta_z^2[T](z)) + O(\Delta z^2) + O(\Delta t)}{\Delta z} + O(\Delta z^3) \quad (6.47)$$

$$\dot{q}_{(t,x,y,0)} \propto \frac{\partial T_{t,x,y,0}}{\partial z} = \frac{f(\delta_z^2[T](z))}{\Delta z} + O(\Delta z) + O\left(\frac{\Delta t}{\Delta z}\right) + O(\Delta z^3) \quad (6.48)$$

A nominal Δz scaling factor of 1, was used for all subsequent modelling.

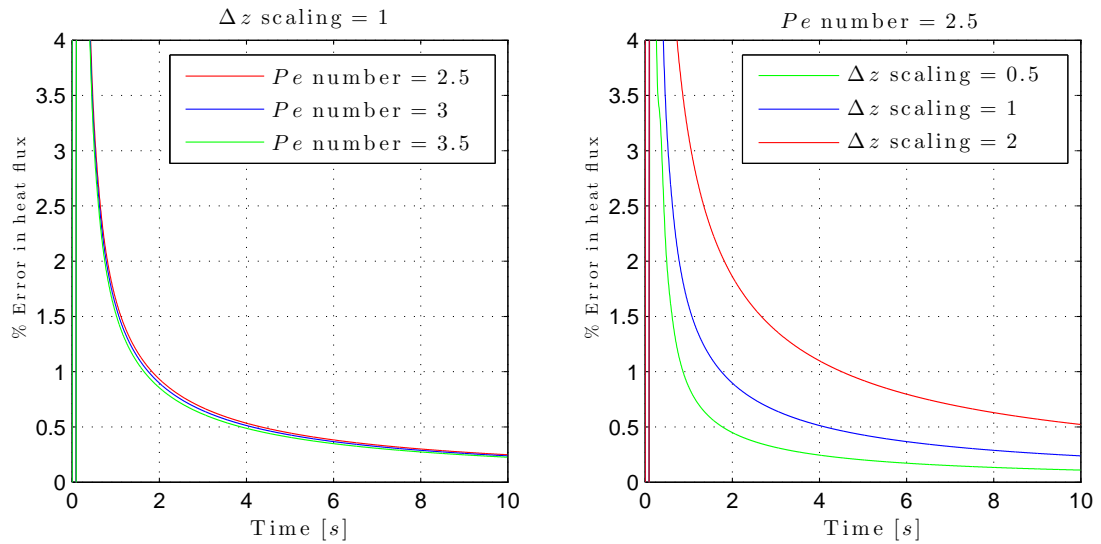


Fig. 6.27 3D heat flux model errors, as a function of temporal and spatial mesh resolution

3D Validation

A solution to the three-dimensional heat equation, in a cuboid domain (18 x 18 x 4mm (X,Y,Z)), was generated by means of a finite difference model. In doing so, an idealised set of hypothetical surface temperature measurement data was generated. Spatially non-uniform convective boundary conditions were applied to the top surface of the domain, which are given in figure 6.28. Adiabatic boundary conditions were applied to the remaining 5 faces of the cuboid. The boundary conditions were constant over time. The initial condition was set to a uniform initial temperature, T_i . The model was run for a duration of 10 [s], with substrate material properties set to those of Torlon 5030. A snap-shot of the top surface temperature, at $t=10[s]$, is shown in figure 6.29.

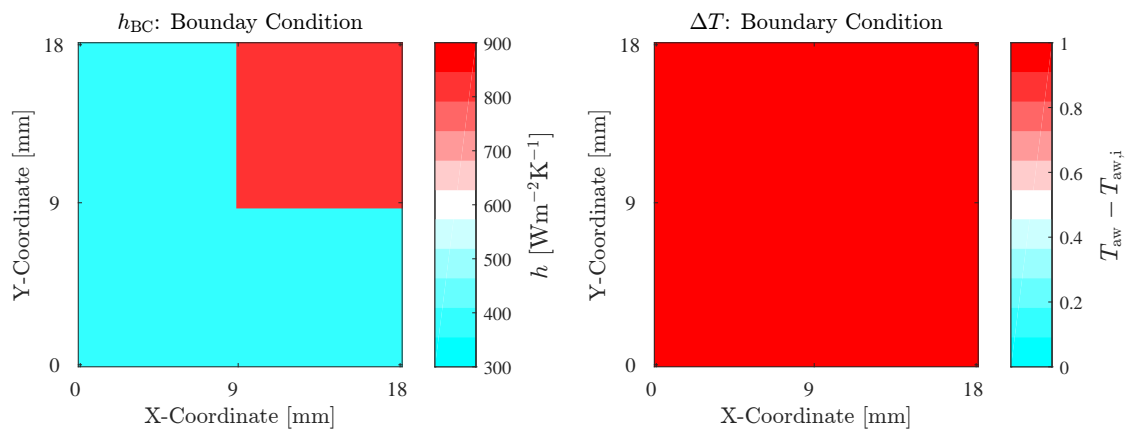


Fig. 6.28 Exact convective boundary conditions used to generate surface temperature distribution

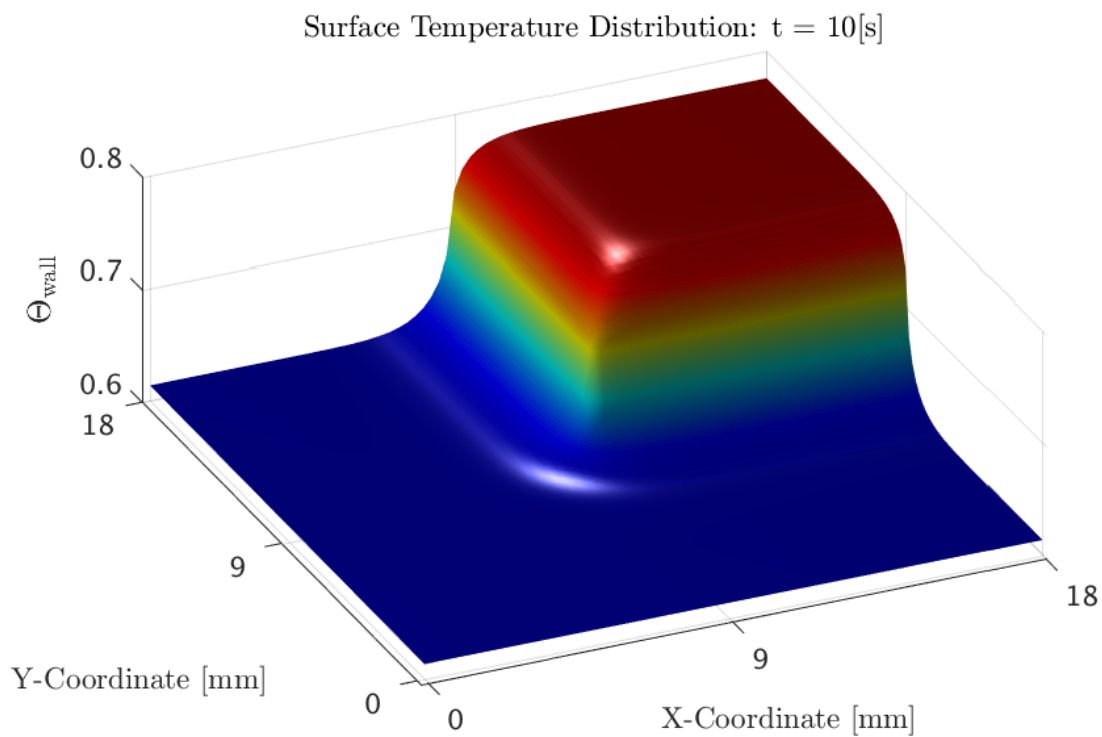


Fig. 6.29 A snap shot of the numerically generated idealised measurement data

The time resolved temperature of the top surface was extracted from the numerical solution, and used as an input boundary condition for both the 3D-heat-flux model

and the 1D Impulse response model. The ability of each model to reconstruct the initial boundary conditions was assessed. The reconstructed boundary conditions from the 3D and 1D modelling approach are shown in figure 6.30 and 6.31, respectively. Note that the reconstructed boundary conditions have been non-dimensionalised by the exact original boundary conditions.

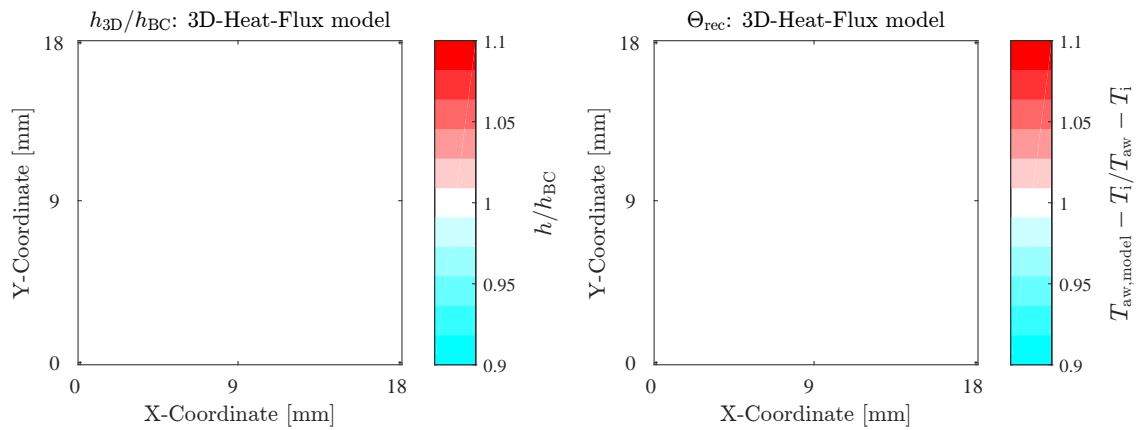


Fig. 6.30 3D-Heat Flux model reconstructed BCs - normalised by exact BCs

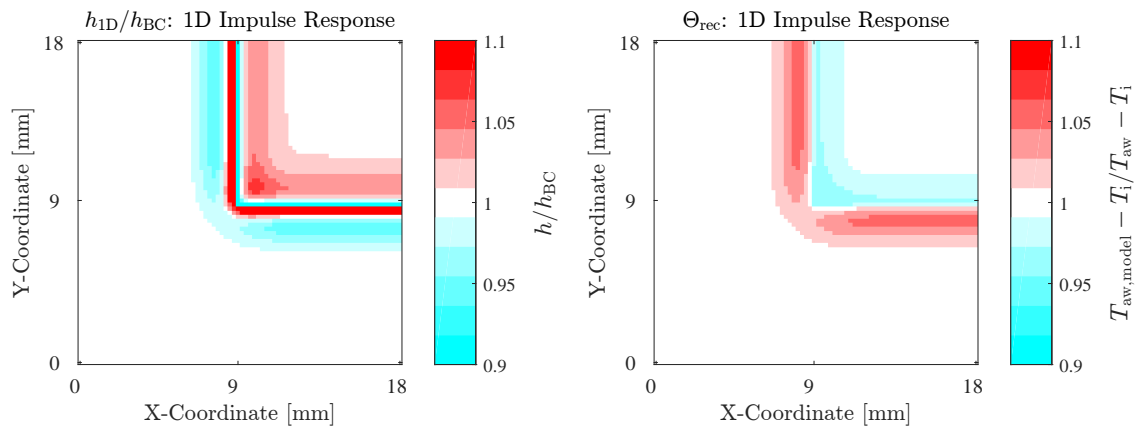


Fig. 6.31 1D Impulse response model reconstructed BCs - normalised by exact BCs

It can be seen from figure 6.31, that in regions where the convective boundary conditions have high gradients in space, the ability of the 1D model to accurately reconstruct the boundary conditions is diminished. Errors of the order of $\pm 10\%$ are present. This is due to

the influence of unresolved lateral heat-flux terms. The heat penetration depth in this data set was ~ 3.7 mm. The length scale of the '3D affected region' is approximately 7mm - which, as expected, corresponds closely to twice the heat penetration depth.

From this, it can be drawn that boundary condition features with length scales less than two times the heat penetration depth may be inaccurately determined by 1D dimensional heat flux modelling methods. The 3D-heat flux model was able to reconstruct the original boundary conditions with a greater accuracy, in the *3D affected region*. Errors of the order of $\pm 0.5\%$ are present, which are due to truncation errors in the numerical model.

The area averaged value of the reconstructed BCs, for both the 1D and 3D modelling approach, both accurately match that of the original BCs.

Chapter 7

Heat Transfer Measurement Results and Discussion

In section 6.1, the experimental objectives were outlined. The objectives fell into two categories: Firstly, to verify the principles behind performing well conditioned heat transfer measurements, which were established in Chapter 3, and secondly, to test and validate the measurement system which will be used for the FACTOR rig heat transfer measurements.

The first objective is dealt with in section 7.2 through to 7.4 where the three key measurement conditioning parameters, U_{Θ} , U_{Q^*} and Θ_R , are varied in isolation. A baseline measurement is provided in section 7.1. The sensitivity of the heat transfer measurement result to these parameters will be established experimentally. The flat-plate rig was used to conduct the measurements, so that established heat transfer correlations could be used to validate the measurement results.

The second experimental objective is dealt with in section 7.5 and 7.6, where heat transfer measurements were performed at conditions closely representing those of the FACTOR rig NGV, rotor, and LP vane.

7.1 Flat Plate Rig Experiments - Baseline Measurement

A baseline heat transfer measurement is required as a control - against which measurements performed at different conditions can be compared. The measurement conditions, and the measurement result for this baseline measurements are described in this section.

7.1.1 Baseline measurement conditions

The baseline measurement was performed on the flat plate rig, with the rig running at the conditions described in table 6.1. The values of the rig, data acquisition, and data processing variables which were used to perform the measurement are given in table 7.1 below.

Table 7.1 Variables for the baseline measurement

Parameter	Setting
Mainstream conditions	
Mainstream temperature step - $\Delta T_{0,\infty}$	36 [K]
Temperature step time constant - τ	0.07 [s]
Substrate	
Substrate material	Torlon 5030
Substrate initial condition, T_i	Steady-state
IR camera	
IR camera integration time	160 [μ s]
IR camera acquisition rate	200 [frames/s]
Optical resolution	0.305 [mm/pixel]
Flat plate length in field of view	92 [mm]
Data processing	
Heat flux processing method	1D Impulse Response
Linear regression delay period	6τ
Heat penetration depth limit	7 [mm]
Semi-infinite criterion	$1/\sqrt{Fo_{limit}} = 3.5$

The measurement conditions for the baseline were set to provide the minimum value of U_{Θ} that is achievable with the test rig. This was achieved by setting the mainstream temperature step to the maximum value achievable with the rig, and setting the IR camera

integration time to provide an $\sim 80\%$ saturation of the detector, maximising the SNR of the radiance measurements.

It is important that the measurement conditions for the IR camera on the Flat Plate Rig are closely representative of the measurement conditions on the FACTOR rig. Most importantly, the change in IR camera detector digital level, as a result of the temperature step needs to be matched. In table 7.2 the black body radiance level, for the heater-mesh ‘On’ and ‘Off’ condition are shown for the FACTOR NGV and the Flat Plate Rig. Three different temperature steps are shown for the Flat Plate Rig; 36, 18 and 9K. It can be seen that on the FACTOR rig (at the NGV location), the temperature step will result in a $\sim 24\%$ increase in the detector level output. A 36K mainstream temperature step on the Flat Plate rig will result in a 47% change in the detector level output, and a 28% and 15% change will result from a mainstream temperature step of 18 and 9K respectively. An 18K temperature step on the Flat plate rig can then be considered to be closely representative of the FACTOR NGV condition.

Table 7.2 Radiance level changes as a result of mainstream temperature step for the FACTOR rig and the Flat Plate Rig for a range of mainstream temperature steps

	$\Delta T_{0,\infty}$ [K]	$T_{0,\infty}$ [K]		Black Body Radiance [Wm ⁻² Sr ⁻¹ m ⁻¹]		$\frac{L_{BB.On}-L_{BB.Off}}{L_{BB.On}}$
		HM Off	HM On	HM Off	HM On	
				($L_{BB.Off}$)	($L_{BB.On}$)	
FACTOR NGV	30	420	450	48.2	63.6	0.24
	36	295	331	8.55	16.0	0.47
Flat plate rig	18	295	313	8.55	11.9	0.28
	9	295	304	8.55	10.1	0.15

The heater-mesh time constant was set to the minimum value achievable, and a large heat penetration depth of 7mm was defined. This will result in a large value of Θ_R , resulting in a well conditioned linear regression. A conservative $1/\sqrt{Fo_{limit}}$ of 3.5 was chosen, to ensure good accuracy in the semi-infinite modelling assumption. Due to the relatively large heat penetration depth, the length scale of lateral conduction affects will be large. As a result aerodynamic boundary conditions features with length scales less than ~ 7 [mm] will not be accurately resolved. Since the flat plate is relatively featureless, this is acceptable.

7.1.2 Results

In figure 7.1, the full field solution to the heat transfer coefficient is shown. The stream-wise coordinate 0 and 1 correspond to the leading edge and a 92mm distance from the leading edge respectively. The span-wise coordinates 0 and 1 correspond to the bottom and top of the test section plate, spanning 70mm. The flow direction is from left to right.

The value of h can be seen to decrease with stream-wise distance from the leading edge. At low and high span-wise coordinates, a reduced value of h can be seen, which is caused by low velocity fluid from the ingested boundary layer on the top and bottom walls of the wind tunnel. A region of '2D flow' is identified between the span-wise coordinate 0.3 and 0.7. The 2D flow region is assumed to be unaffected by the low velocity fluid regions.

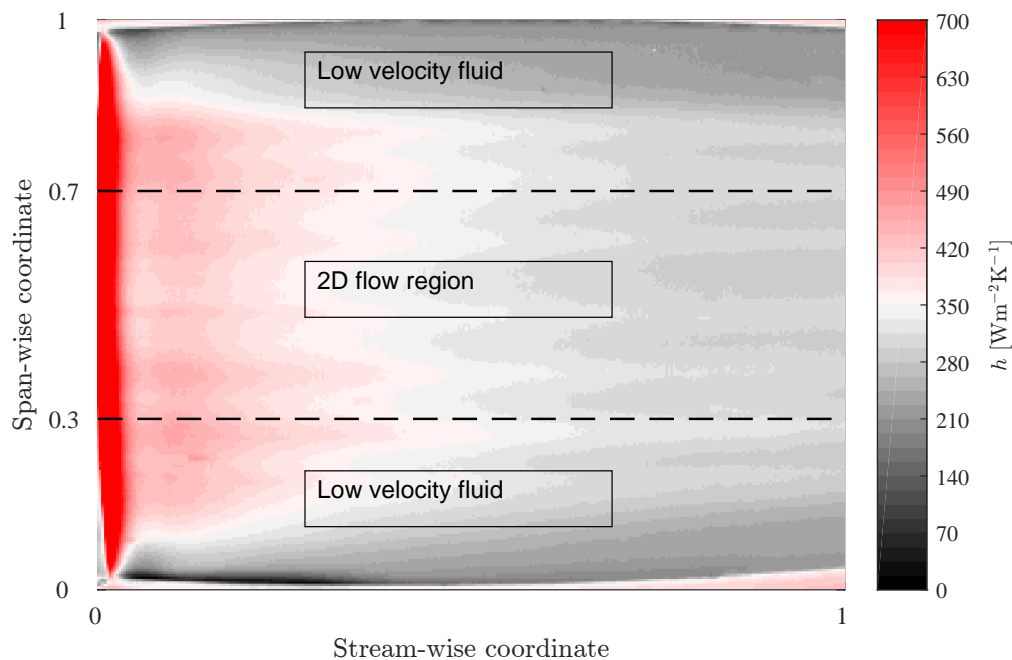


Fig. 7.1 Baseline flat plate heat transfer coefficient measurement

The flat plate on which these measurements were taken, has a sharp leading edge (see figure 6.2). Consequently, during the transient measurement, the leading edge region of the flat plate has a heat flux initiated on both sides. As a result, the transient conduction within a small region of the leading edge is not one-dimensional, and is not semi-infinite. In this region, one-dimensional semi-infinite heat flux models are not accurate. Figure 7.2 illustrates the geometric condition, where an approximate semi-infinite (SI) cut-off location can be defined, based on a heat penetration depth, and leading edge angle. The flat plate can be

considered one-dimensional and semi-infinite downstream of the ‘SI cut-off’ location. (Note that an $1/\sqrt{Fo_{\text{limit}}}$ number of 2 was used to calculate δ)

$$L_{\text{error}} = \delta / \sin(\theta/2) = \delta / \sin(20^\circ) \approx 2.92\delta \quad (7.1)$$

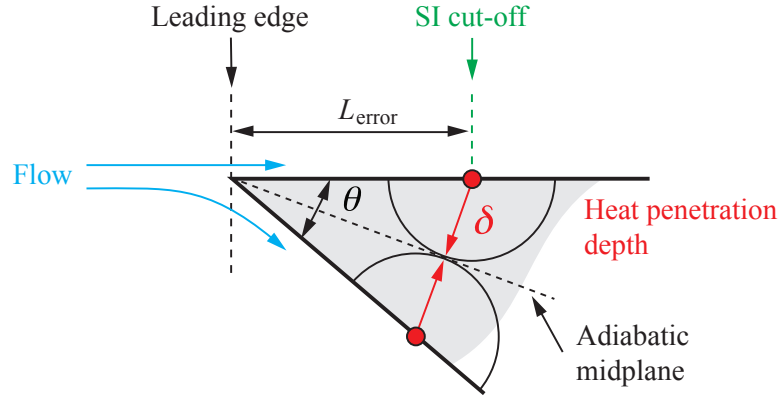


Fig. 7.2 Illustration of SI cut-off location on sharp leading edge of the flat plate

In figure 7.3 span-wise averaged values of h and Θ_{rec} are shown for the baseline measurement. Span-wise averaging was performed over the 2D flow region highlighted in figure 7.1. The SI cut-off location is indicated. No laminar flow is observed over the flat plate, which is proposed to be caused by the vary sharp leading edge of the flat plate.

The Chilton-Colburn turbulent heat transfer correlation for turbulent flow over a flat plate [Incropera et al., 2006], is given in equation 7.2. The solution to the correlation, at the baseline measurement conditions, is shown on the left hand plot in figure 7.3 for comparison to the measurement.

$$h_x = 0.0296 \frac{\kappa}{x} \text{Re}_x^{4/5} \text{Pr}^{1/3} \quad (7.2)$$

Where:

- κ = Thermal conductivity of gas [$\text{Wm}^{-1}\text{K}^{-1}$];
- x = The stream-wise distance from the leading edge [m];
- Re_x = Local Reynolds number based on stream-wise distance from leading edge;
- Pr = Prandtl number.

In section 3.5.2 it was identified that the mainstream fluid temperature would be related to the adiabatic wall temperature, where the relationship is a function of Ma and recovery

factor \hat{r} , as given by equation 7.3. (The relationship constant is evaluated as 1.0271 for the flat plate test rig conditions, assuming a recovery factor of 0.89 [Schlichting, 1979]).

$$T_{aw} = T_{\infty} \left(1 + \hat{r} \frac{\gamma - 1}{2} \text{Ma}_{\infty}^2\right) = T_{\infty} \times 1.0271 \quad (7.3)$$

The change in the adiabatic wall temperature can then be related to the change in the mainstream temperature as follows;

$$\Delta T_{aw} = \Delta T_{\infty} \times 1.0271 \quad (7.4)$$

Recalling the expression for Θ_{rec} ,

$$\Theta_{rec} = \frac{\Delta T_{aw}}{\Delta T_{\infty}} \quad (7.5)$$

Now substituting equation 7.4 into 7.5, we have;

$$\Theta_{rec} = \frac{\Delta T_{\infty} \times 1.0271}{\Delta T_{\infty}} = 1.0271 \quad (7.6)$$

From equation 7.6 we can see that the empirical solution to Θ_{rec} is 1.0271, and it is the value we would expect to measure for Θ_{rec} on the flat plate rig heat transfer measurement.

This empirical solution to Θ_{rec} will now be called Θ_{emp} , so as to distinguish it from the actual measurements of Θ_{rec} . In figure 7.3, the value of Θ_{emp} is shown for comparison to the measurement.

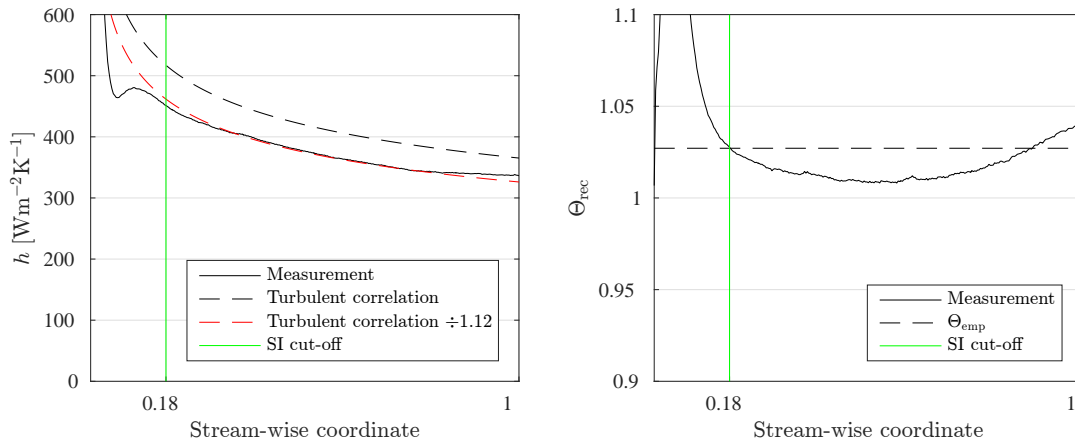


Fig. 7.3 Spanwise averaged baseline measurements

From figure 7.3, the following can be observed:

- The measured value of h follows the trend of the turbulent correlation closely. A difference in magnitude between measurement and correlation of approximately 12% can be observed. (A correlation scaled by 12% is shown). This is within the accuracy which can reasonably be expected from this correlation.
- The measured value of h declines with stream-wise coordinate at a slightly reduced rate, in comparison to the correlation. This is likely to be due to the slight increase in wind-tunnel blockage with stream-wise coordinate, caused by an increasing boundary layer thickness. The increase in blockage will slightly increase the mainstream flow velocity, increasing h .
- Upstream of the SI cut-off location, the measured value of h and Θ_{rec} , deviate significantly from the correlation and from Θ_{emp} , which is expected, since the semi-infinite assumption is invalid in this region.
- The average value of $\Theta_{\text{rec}}/\Theta_{\text{emp}}$ is 0.990, which suggests there is a -1% average measurement error.

An example of the time varying values of Θ_{wall} and heat flux, \dot{q} , on which the linear regression was performed, is shown in figure 7.4. The data was taken from the location corresponding to a stream-wise and span-wise location of 0.5. The data limits, ‘LR start point’ and ‘LR end point’ are highlighted. The linear regression was performed on the measurement data within these limits. The fitted linear function is shown, as well as the value of Θ_{rec} found by extrapolation of the function. It is apparent from the figure that the data between the regression limits is highly linear, and has low noise, and appears well conditioned.

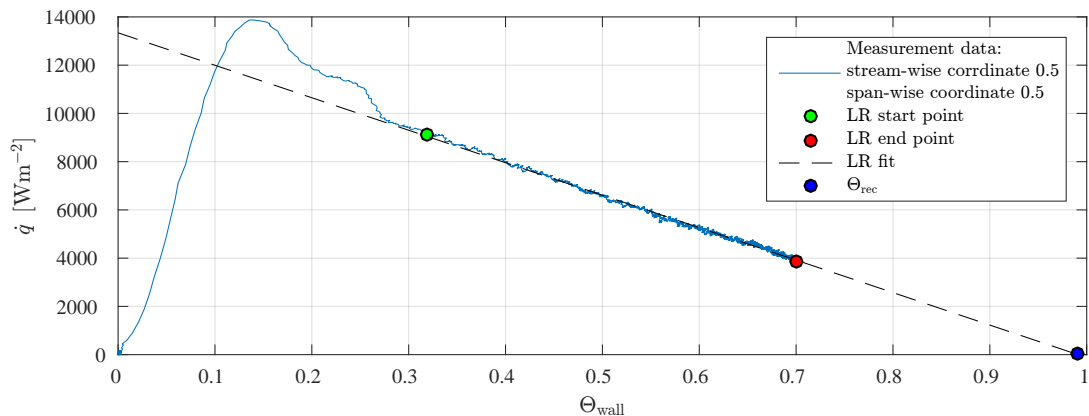


Fig. 7.4 Linear regression for a single pixel - baseline measurement

The temporal location of the data limit ‘LR start point’ is given by the linear regression delay period, provided in table 7.1, as 6τ , which is equal to 0.42 seconds.

The temporal location of the data limit ‘LR end point’, is given by equation 3.51, where FO_{limit} , and the substrate material properties are also given in table 7.1. The calculated value is 17.2 seconds.

From figure 7.4, we can observe that the value of $\tilde{\Theta}$ and Θ_{limit} are ~ 0.32 and 0.70 respectively - making Θ_R equal to ~ 0.38 . These values are now compared to the output of the analytical expressions for $\tilde{\Theta}$ and Θ_{limit} which were given in section 3.7.

Recalling equation 3.46, and evaluating it with the measured value of h , of 370.1 $[\text{W}/\text{m}^2\text{K}]$. (where the value of h was extracted from the solution at a span-wise and stream-wise location of 0.5).

$$\tilde{\Theta} \approx 1 - \exp\left(\frac{6h^2\tau}{e^2}\right) \text{erfc}\left(\frac{h\sqrt{6\tau}}{e}\right) = 0.25 \quad (7.7)$$

Recalling equation 3.49, and evaluating,

$$\Theta_{\text{limit}} \approx 1 - \exp\left(\frac{\text{Bi}^2}{FO_{\text{limit}}}\right) \text{erfc}\left(\frac{\text{Bi}}{\sqrt{FO_{\text{limit}}}}\right) = 0.69 \quad (7.8)$$

From these solutions, it can be seen that the values of $\tilde{\Theta}$ and Θ_{limit} can be estimated reasonably well by equation 7.7 and 7.8, which provides confidence in the uncertainty modelling in chapter 4 which is based on these equations.

7.2 Flat Plate Rig Experiments - Varying $U_{\Theta_{\text{wall}}}$

In this section, experimental results are shown, where the value of $U_{\Theta_{\text{wall}}}$ has been altered from the baseline case. Three experiments were performed.

In the first experiment, the magnitude of the mainstream temperature step is altered - changing the magnitude of the surface temperature rise. In doing so, the wall temperature SNR is altered.

The second experiment is the same as the first, except that the film-cooled flat-plate is used. Areas of high film-cooling effectiveness lead to a yet further increase in $U_{\Theta_{\text{wall}}}$.

In the third experiment, the influence of the in-situ IR calibration is determined, by performing the data analysis with and without various elements of the calibration - leading to the inclusion of bias errors in the wall temperature.

7.2.1 Varying the mainstream temperature step - un-cooled flat plate

Measurements were performed on the flat plate rig, under the same conditions as the base line case - with the exception of the magnitude of the mainstream temperature step. Measurements were performed at three different temperature step magnitudes; 36K, 18K and 9K. The measured value of h is shown in figure 7.5. Measurement data upstream of the SI cut-off location have been excluded.

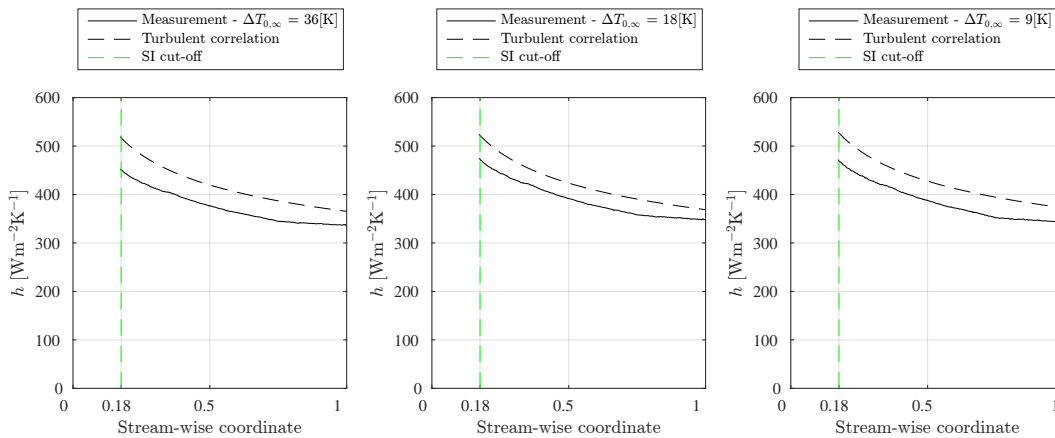


Fig. 7.5 Measured values of h as a function of mainstream temperature rise

Due to the differing mainstream conditions in each measurements, the local Reynolds number in each measurement differs. As a result, there is an individual solution to the turbulent correlation for each measurement. The solutions therefore cannot be collapsed with Nusselt number. By non-dimensionalising h into the Stanton number however, (equation 7.9), the correlation collapses onto one solution. The measurement solutions are shown in terms of Stanton number in the left hand plot in figure 7.6.

$$\text{St} = \frac{\text{Nu}_L}{\text{Re}_L \text{Pr}} \quad (7.9)$$

Where;

$\text{Nu}_L =$ Nusselt number (hL/κ)

$L =$ The stream-wise extent of the plate [m]

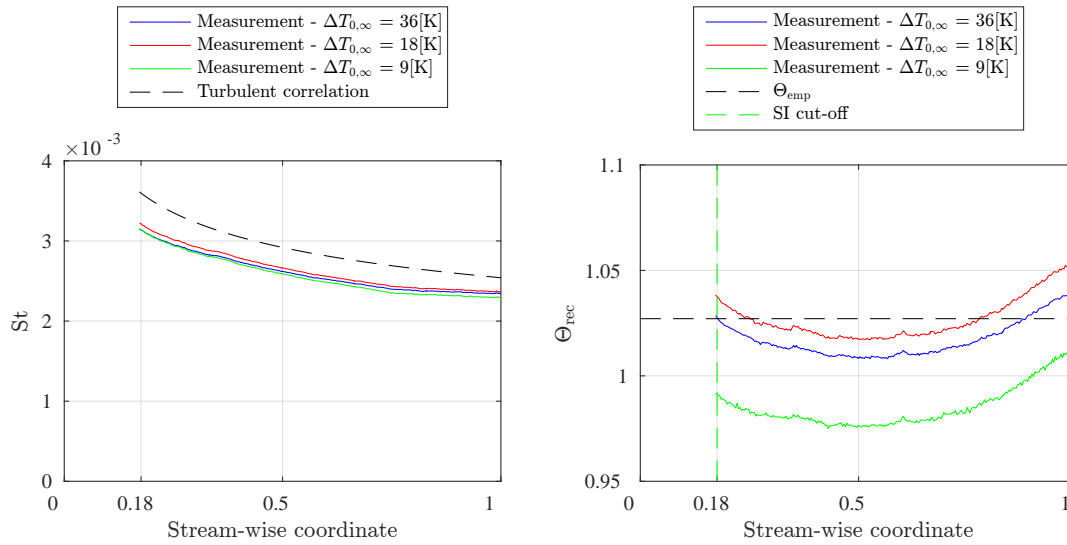


Fig. 7.6 Measured values of St and Θ_{rec} as a function of mainstream temperature rise

From figure 7.6 it can be seen that the solution to the Stanton number appears to be largely independent of mainstream temperature step, between 36 and 9K. The mean stream-wise deviation of the solution from the baseline case at 36K, is 1.6%, and -1.3% for the 18K and 9K solution respectively.

In the right hand plot of figure 7.6, the solution to Θ_{rec} is shown. The following can be observed:

1. The trend in the solution is highly consistent between each measurement. Variations between the solutions appear to be dominated by a spatially uniform offset component.
2. The level of high frequency noise can be seen to grow slightly, as temperature step magnitude is decreased.
3. The mean deviation of Θ_{rec} from Θ_{emp} is -1.0%, 0.0% and -4.1% for the 36, 18 and 9K measurements. The deviation does not appear to be correlated with mainstream temperature step.

7.2.2 Varying the mainstream temperature step - film-cooled flat plate

On the FACTOR turbine rig, a mainstream heater mesh will provide the temperature step, initiating the transient measurement. The NGV of the FACTOR rig is film-cooled. Regions of the NGV with a high film-cooling effectiveness will be isolated, to some degree, from

changes in the mainstream fluid temperature. Consequently, film-cooled regions of the NGV will see a reduced temperature step, increasing the magnitude of $U_{\Theta_{\text{rec}}}$.

A series of measurement experiments were performed on the film-cooled flat plate described in section 6.2.1, at three mainstream temperature steps; 36, 18 and 9K. The film-cooling hole geometry and film-coolant blowing ratio was set to match that of the FACTOR NGV, and consequently, appropriate levels of film-cooling effectiveness can be expected.

In order to achieve an appropriate film-cooling hole length/diameter ratio, the film-coolant air feeding plenum, within the film-cooled plate, was situated 2.55[mm] beneath the gas washed surface of the plate. Consequently, a 7[mm] heat penetration depth could not be used for this geometry, as with the base-line case, as the semi-infinite assumption would not hold true. A limit to the heat penetration depth of 2.55[mm] was applied, with an $1/\sqrt{Fo_{\text{limit}}}$ of 2. The consequence of this, is that a lower non-dimensional surface temperature rise was achieved, further ill-conditioning the measurement with respect to the baseline.

The measured solution to h and Θ_{rec} for the three mainstream temperature steps are shown in figure 7.7. The one-dimensional semi-infinite heat flux modelling assumption does not hold true in close proximity to the film-cooling holes - this is due to the un-modelled absence of mass introduced by the holes. A data exclusion region is highlighted by two dashed green lines, which extend one heat penetration depth upstream and downstream of the holes. The solutions in figure 7.7 have been trimmed to the region of interest.

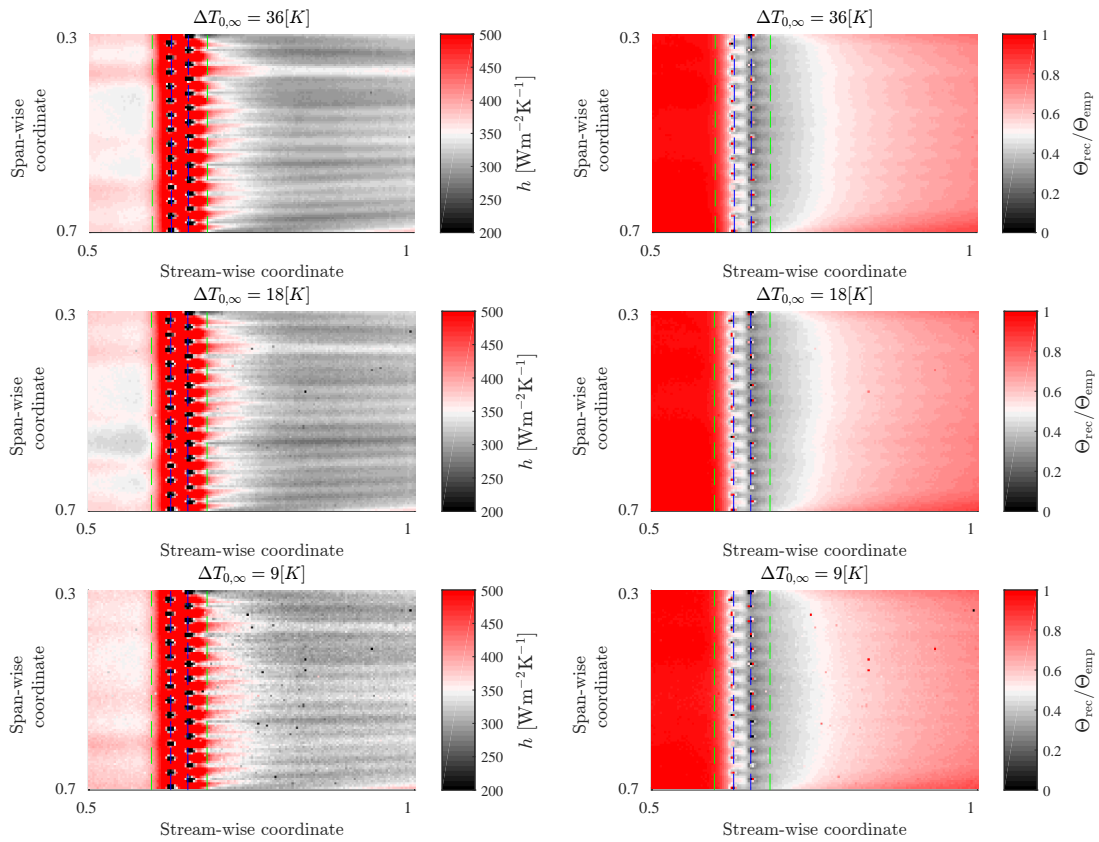


Fig. 7.7 Measured values of h and Θ_{rec} on the film-cooled flat plate for different mainstream temperature rise magnitudes

It can be seen in figure 7.7 that SNR levels for both h and Θ_{rec} decrease with decreasing mainstream temperature step magnitude - shown by the increase in noise in the image. The regions with high film-cooling effectiveness (i.e. low Θ_{rec}), do not appear to have significantly lower SNR levels, than regions with low film-cooling effectiveness.

In figure 7.8 a span-wise mean solution to St and Θ_{rec} is shown. The heat transfer coefficient has been non-dimensionalised into Stanton number, due to the differing mainstream conditions in each measurement. Span-wise average was performed between the span-wise coordinates 0.3 and 0.7.

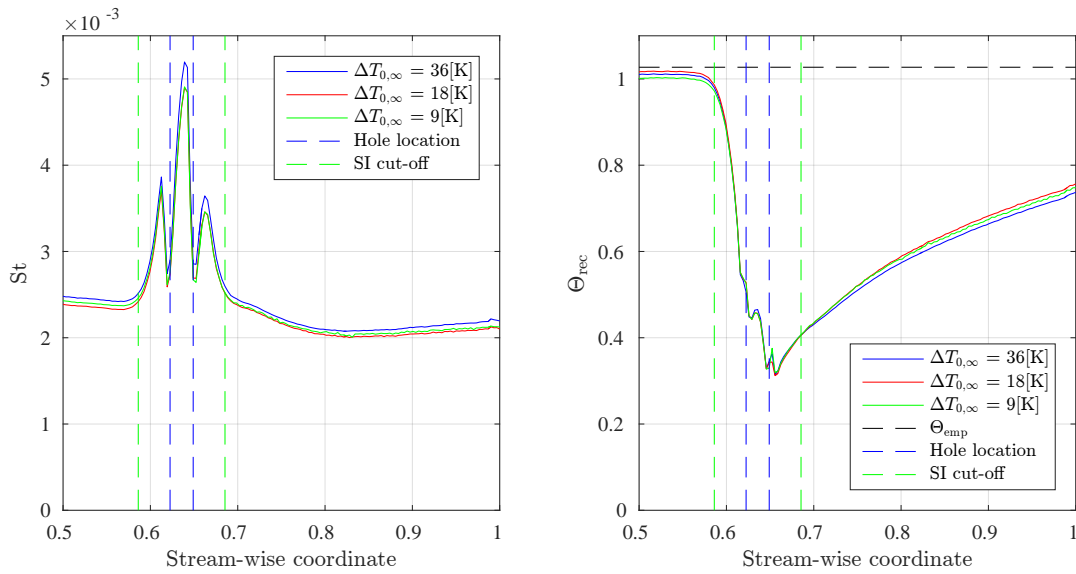


Fig. 7.8 Spanwise averaged measurements of Stanton number and Θ_{rec} for the film cooled flat plate for different mainstream temperature rise magnitudes

In figure 7.8 the stream-wise locations of the two rows of film-cooling holes is shown, as are the data cut-off limits - ‘SI cut-off’. Measurement data between the two ‘SI cut-off’ limits are assumed to be invalid. The following can be observed from figure 7.8:

1. The Stanton number and Θ_{rec} solutions appear to be largely independent of mainstream temperature step and do not show increased noise levels in regions of high film-cooling effectiveness.
2. The trend and magnitude of the Stanton number and Θ_{rec} solutions is highly consistent in each measurement.
3. The value of Θ_{rec} upstream of the film-cooling holes is close to Θ_{emp} in each measurement. A maximum deviation from Θ_{emp} of $\sim -3\%$ is observed.

7.2.3 In-situ IR calibration effect

In section 6.3.4, the procedure by which the optical path is calibrated was described. The optical path calibration corrects for alterations in the radiance received by the IR camera, as a result of various sources of attenuation, reflection and emission from the test rig. It was shown that both a steady and an unsteady signal offset correction would be required to accurately calibrate the optical path.

The steady offset component is evaluated in-situ - where the IR camera temperature reading is corrected, based on the reading from a single thermocouple located on the surface of the test plate. This calibration procedure makes the assumption that the steady signal offset which is to be corrected, is uniform in space. Note that this is a reasonable assumption to make, as slight spatial non-uniformities in the steady offset component will have a very small affect on the measurement. (The effect of a steady radiance offset error is to cause the IR camera to be calibrated on the wrong portion of the calibration curve, leading to a gain error. Since the calibration curve is approximately linear over short sections, the effect of small radiance offsets becomes negligible).

The unsteady offset component is also evaluated in-situ - where the unsteady radiance emission is measured by means of an embedded black-body with in the test rig. The unsteady emission is primarily caused by the variation in emission from the IR window as it heats during the transient measurement.

Due to the impracticality of taking a high spatial resolution in-situ off-set correction measurements, it was considered important to understand the magnitude of the impact that the offset corrections have on the solution to h and Θ_{rec} . A data analysis experiment was performed, where the baseline experimental data was calibrated in three different ways. The three calibration methods are described below:

1. **Steady & Unsteady** - Both the steady and the unsteady off-set correction are applied to the experimental data. This is the base-line measurement.
2. **Steady only** - The unsteady component of the offset correction is disabled. The steady component remains.
3. **No cal** - Neither the steady nor the unsteady offset corrections are applied.

The solutions to h and Θ_{rec} for each calibration procedure are shown in figure 7.9. It can be seen that the solution to h is largely unaffected by the calibration procedure. The stream-wise mean value for the ‘Steady only’ and ‘No cal’ case deviate from the baseline case by +0.7% and -2.2% respectively. The influence of the calibration procedure is seen more evidently, however, in the solution to Θ_{rec} , which varies from from Θ_{emp} by 0.5% (Steady & unsteady), 3.4% (Steady only) and 8.2% (No cal.).

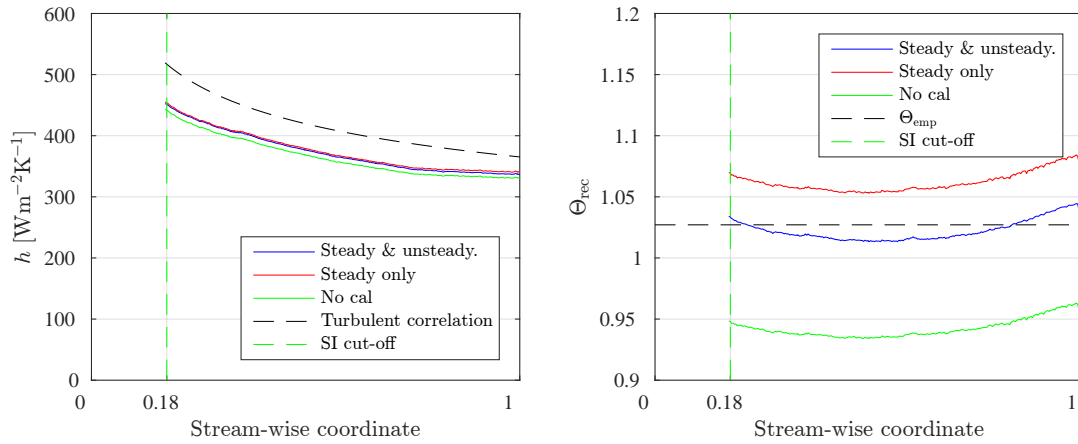


Fig. 7.9 Measured values of h and Θ_{rec} as a function of offset correction method

Figure 7.10 shows the non-dimensional surface temperature and non-dimensional heat flux over time, for the three calibration cases, at a stream-wise and span-wise coordinate of 0.5. The influence of the steady and unsteady calibration can be seen to affect the non-dimensional wall temperature over time. The steady component of the offset calibration applies a constant radiance offset to the measured radiance. Because radiance and wall temperature are not linearly proportional, a time-constant offset applied in radiance, results in a time-varying offset in temperature. The offset corrected wall temperature, result in an altered non-dimensional heat-flux evaluation, as shown in the right hand plot in figure 7.10.

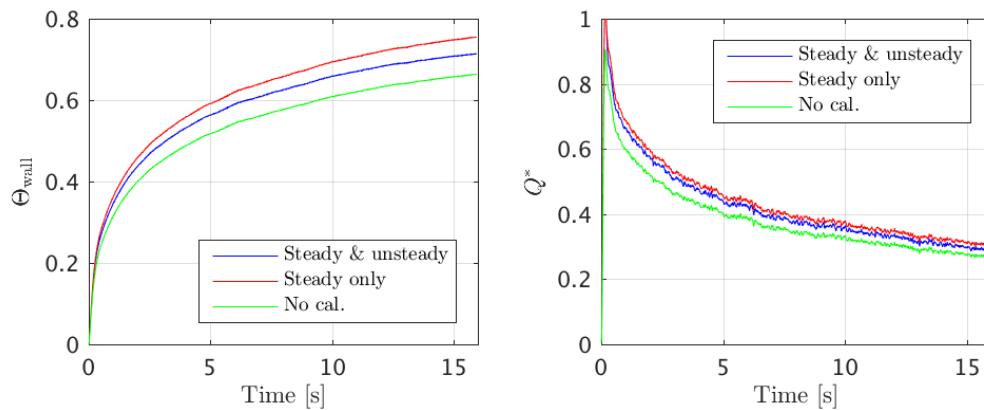


Fig. 7.10 $Q^*(t)$ and $\Theta_{\text{wall}}(t)$ as a function of offset correction method

Figure 7.11 shows the absolute value of non-dimensional wall temperature contribution from the steady and unsteady offset correction. The magnitude of the affect of the steady calibration is approximately twice that of the unsteady calibration. It is expected that the

magnitude of the steady calibration will vary significantly between different measurement arrangements, as its magnitude is largely determined by the relative magnitude of ambient radiance reflections.

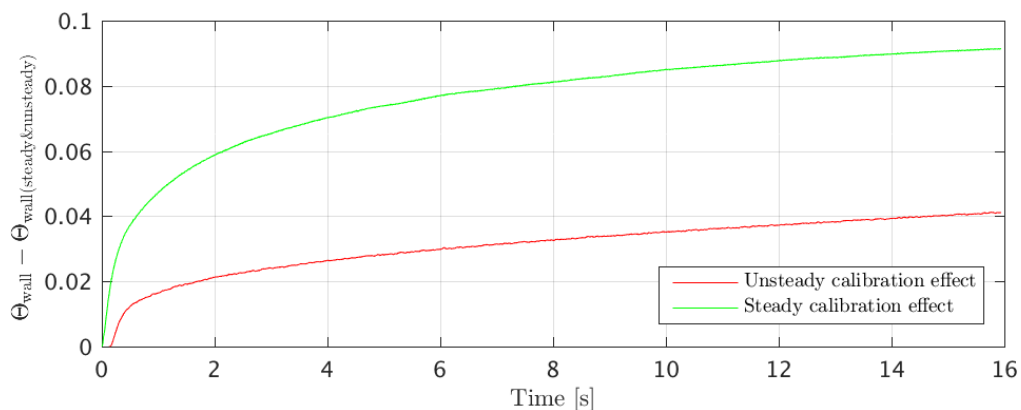


Fig. 7.11 Non-dimensional surface temperature measurement errors caused by the absence of either the steady or unsteady offset calibration

Figure 7.10 shows the non-dimensional surface temperature plotted against the non-dimensional heat flux, for the three calibration cases. The influence of the off-set corrections have remarkably little affect on the gradient of the regression function, and act predominantly to alter the value of Θ_{rec} .

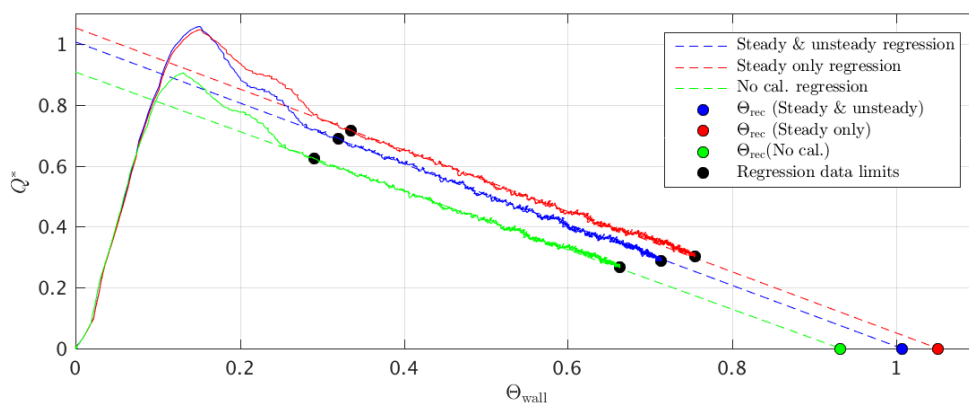


Fig. 7.12 The linear regression data fitting for the three offset calibration methods

7.2.4 Key observations

- A reduction in the mainstream temperature step magnitude leads to an increase in the precision errors in Θ . Precision errors in h and Θ_{rec} are consequently increased, but bias errors remain largely unaffected.
- The affect of the in-situ IR calibration is to remove bias errors in the measurement of Θ_{wall} . Under the measurement conditions tested, the solution to h is largely unaffected by the presence or absence of these bias errors, whereas the bias errors in Θ_{wall} are approximately linear proportional to the bias errors in Θ_{rec} .

7.3 Flat Plate Rig Experiments - Varying U_{Q^*}

In this section, experimental results are shown, where the value of U_{Q^*} has been altered from the baseline case. The influence of U_{Q^*} on the measured value of h and Θ_{rec} is shown.

In section 3.6 the key mechanisms by which uncertainty can be introduced into the derived value of Q^* from an assumed perfect set of wall temperature measurements was identified. They are listed again, below, for convenience:

- **Uncertainty in substrate material properties**

An understanding of the influence of uncertainty in substrate material properties was developed in Chapter 3. The material property calibration methods adopted, and measurement results, were shown in section 6.3.5.

- **Numerical errors**

The magnitude and impact of the numerical errors from both the impulse response and 3D finite difference heat flux processing methods have been investigated in section 6.5.4. An experimental comparison of the solution to h and Θ_{rec} for each processing method will be given.

- **Uncertainty in substrate initial conditions**

In Chapter 3, it was established that steady-state initial conditions within the substrate must be established prior to a measurement.

- **Invalid modelling assumptions**

In Chapter 3, it was described how the 1D semi-infinite substrate modelling assumption, which is commonly made, can be invalidated by the following:

- Finite substrate thickness

In order to achieve the maximum non-dimensional semi-infinite surface temperature rise during the transient measurement, all available substrate thickness should be utilised - up to the limit of the validity of the semi-infinite modelling assumption. Consequently, the impact of uncertainties introduced in Q^* by a substrate with finite thickness must be closely balanced against the benefits of achieving an increased value of Θ_R . An experimental study of the influence of a finite substrate thickness is shown alongside the study of maximising Θ_R , in section 7.4.2.

- Spatial variations in boundary conditions

It was shown in section 3.6.4, that if the length scale of the boundary conditions features is approximately equal to or less than the heat penetration depth, then heat flux within the substrate, during the transient measurement will be significantly three-dimensional. The results of an experiential study are provided, where benefits of 3D heat flux modelling over 1D heat flux modelling, under these conditions is shown.

- 3D geometry effects

It was described in section 3.6.3 how three-dimensional geometric features can locally invalidate the 1D semi-infinite modelling assumption. The sharp leading edge of the flat plate, on the flat plate rig provides such a feature. The results of an experimental study are provided, where the extent of the invalid data region in proximity to the sharp leading edge is investigated.

7.3.1 Spatial variation in boundary conditions

In order for boundary condition induced lateral heat flux terms to be significant in magnitude, the length scale of the boundary condition features must be approximately equal to or less than the heat penetration depth. The film-cooled flat plate in the flat plate rig has film-cooling holes with a diameter of 0.8mm, and hence boundary condition features with length scale of this order can be expected. Analysis of the transient heat flux within the film-cooled flat plate was performed with both the 1D impulse response and the 3D finite difference heat flux processing method, where the heat penetration depth was set to 4.5mm (based on an $1/\sqrt{Fo_{limit}}$ number of 3.5).

In order to provide an appropriate control measurement, and also to validate the output from the 3D finite difference heat flux model, analysis was first performed on the base line

case, with the 1D and 3D method. The un-cooled baseline case boundary condition length scales significantly greater than the heat penetration depth, and hence lateral heat flux terms are expected to be negligible. 1D and 3D heat flux modelling should consequently produce a similar result.

Figure 7.13 shows the solutions to h and Θ_{rec} for the baseline case, where heat flux has been computed with the 1D Impulse Response and 3D finite difference model. A high degree of consistency in the results, from each of the modelling methods can be seen. In the measurements of h in figure 7.13, stream-wise artefacts can be seen, which are consistent between the 1D and 3D model - these are understood to be real variations in the mainstream flow conditions. In the measurements of Θ_{rec} in figure 7.13 variations of the order of $\pm 5\%$ can be seen, which are predominantly bias errors in the measurement.

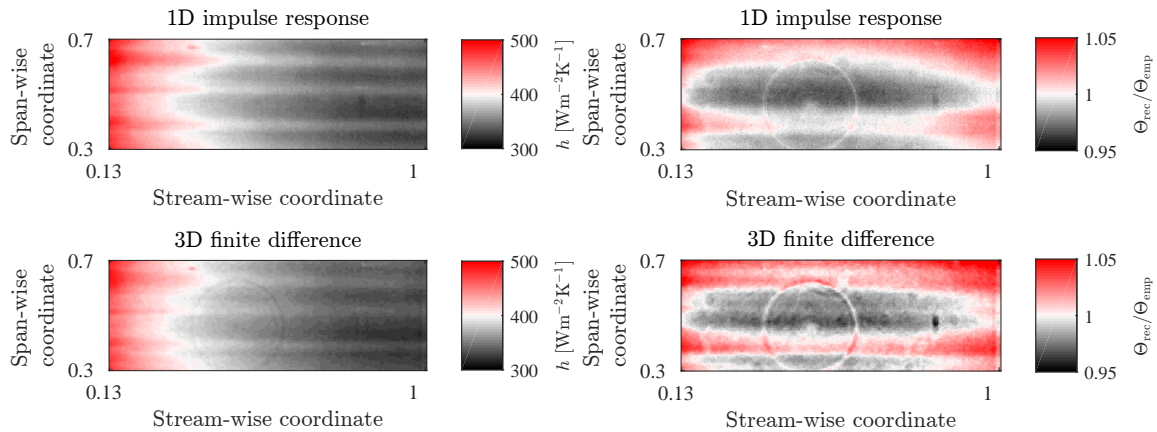


Fig. 7.13 Flat plate measurements of h and Θ_{rec} comparing 1D and 3D heat flux modelling solutions

In figure 7.14 the span wise averaged solutions to h and Θ_{rec} are shown for the two modelling methods. Span-wise averaging was performed between the span-wise coordinates 0.3 and 0.7.

The 3D heat flux model under evaluates the heat transfer coefficient, with respect to the 1D model by 0.9% - which is consistent with the magnitude of the predicted errors, due to truncation errors, described in section 6.5.4. Θ_{rec} is over evaluated by 0.3%. (It was shown in section 6.5.3, that increasing the mesh resolution in the finite difference model can reduce these errors)

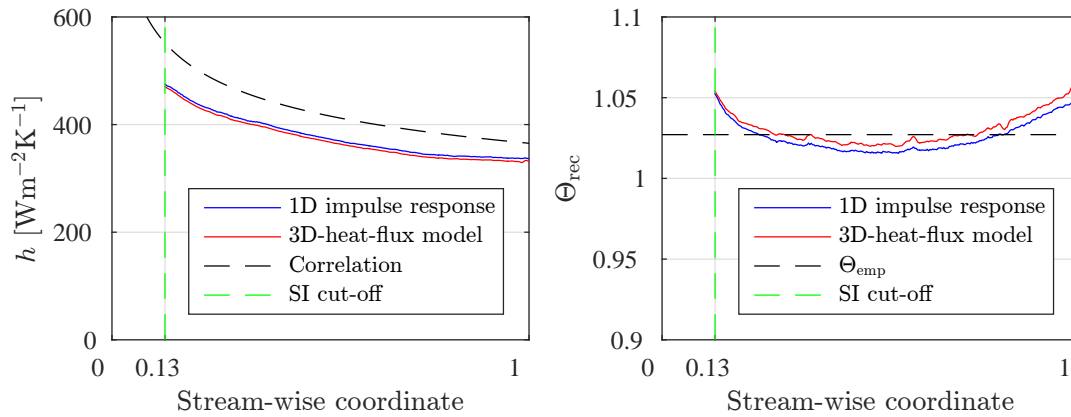


Fig. 7.14 Span-wise average values of flat plate measurements of h and Θ_{rec} comparing 1D and 3D heat flux modelling solutions

Data analysis was subsequently performed on the film-cooled plate. The computed solution to h and $\Theta_{\text{rec}}/\Theta_{\text{emp}}$ for each modelling method are shown in figure 7.15. Data in close proximity to the film-cooling holes is affected by the absence of thermal mass caused by the holes, and should be considered invalid. This region of data is highlighted by the black boxes, where the borders of the box are extended by one heat penetration distance away from the holes on all four sides.

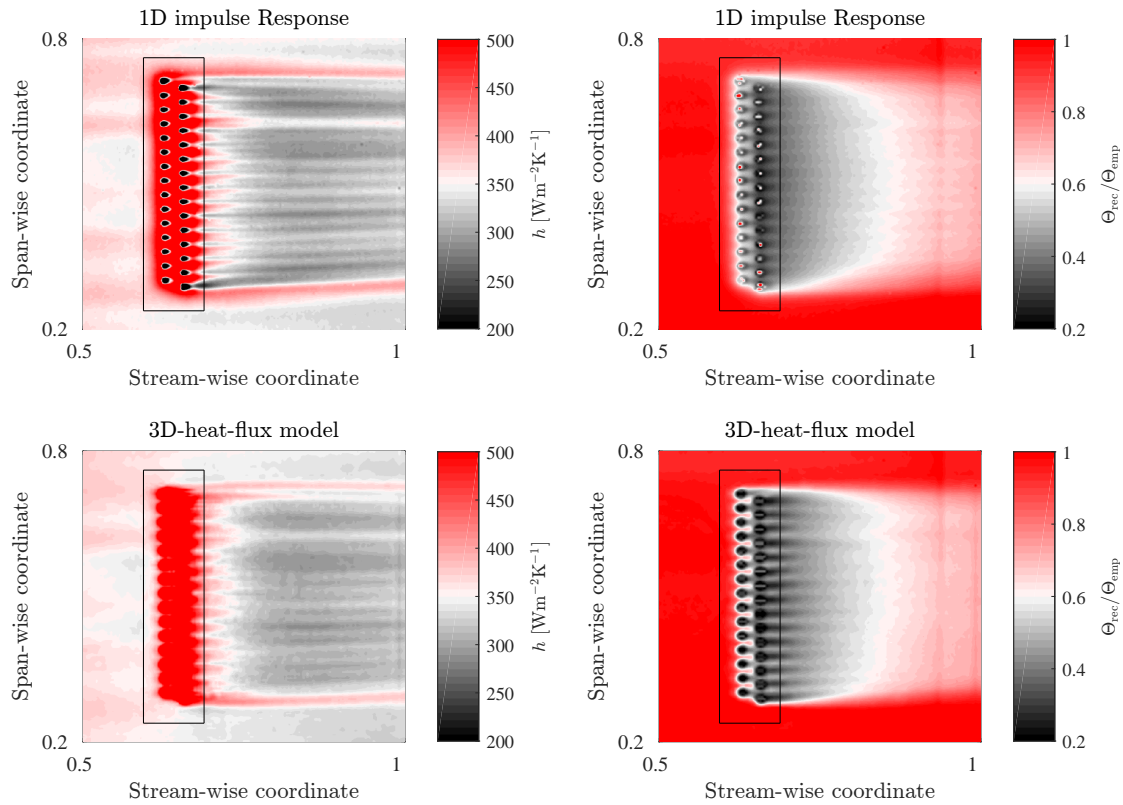


Fig. 7.15 Film-cooled flat plate measurements of h and Θ_{rec} comparing 1D and 3D heat flux modelling solutions

The following can be observed from figure 7.15:

- The solutions for the 1D and 3D model match closely, upstream of the film-cooling holes (less than 1% difference).
- Downstream of the film-cooling holes:
 - The 1D model evaluates h to have a greater span-wise variation than the 3D model - the traces from individual cooling jets are more distinguishable with the 1D model.
 - The 1D model evaluates Θ_{rec} to have a lower span-wise variation than the 3D model - the traces from individual cooling jets are more distinguishable with the 3D model.
- Downstream of the two film-cooling hole rows, in the highest and lowest span-wise location, the spatial gradient of Θ_{rec} , in the span-wise direction, is larger in the 3D

model, compared to the 1D model. i.e. The interface between the film-cooled region and the un-cooled region is sharper with the 3D model.

In figure 7.16 the normalised difference between the output from the two models is shown.

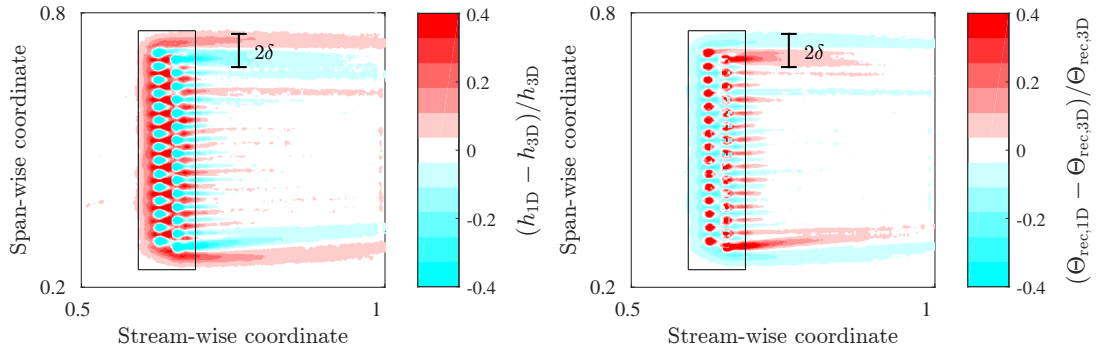


Fig. 7.16 Normalised error in the measurement of h and Θ_{rec} caused by non-1D conduction field

The following can be observed from figure 7.16:

- The normalised differences between the output of the two models are as high as 40% in small localised regions near the holes. Larger regions, which extend more than 30 holes diameters down stream, have differences of $\sim 5 - 10\%$.
- The greatest difference between the output of the models can be seen where large lateral temperature gradients exist. These regions exist between ~ 1.5 and 3 hole diameters down stream of the film-cooling holes, and at the streamwise interface between the film-cooled and un-cooled region.
- The normalised difference in output for h and Θ_{rec} are approximately equal in magnitude and opposite in sign. i.e. overestimates in h are coupled to underestimates in Θ_{rec} .
- The area averaged mean value for the normalised differences in h and Θ_{rec} are equal to 0.6 and -0.8% respectively - which is approximately equal to zero. This shows that the 3D model provides only an increase in local accuracy, and that both models evaluate the same area averaged heat transfer rates.
- The length scale of the region significantly affected by 3D heat flux, is approximately equal to two times the heat penetration depth - as indicated on the plot by 2δ .

In figure 7.17 the transient non-dimensional wall temperature is plotted against the computed heat flux, at two locations on the film-cooled plate. Solutions for both the 1D and 3D model are shown. The two locations, indicated by *Pixel A* and *Pixel B* are in a region of high lateral temperature gradient, where lateral heat flux terms are significant. The linear regression function for each measurement, and the locations of Θ_{rec} are also shown on the horizontal axis intercept.

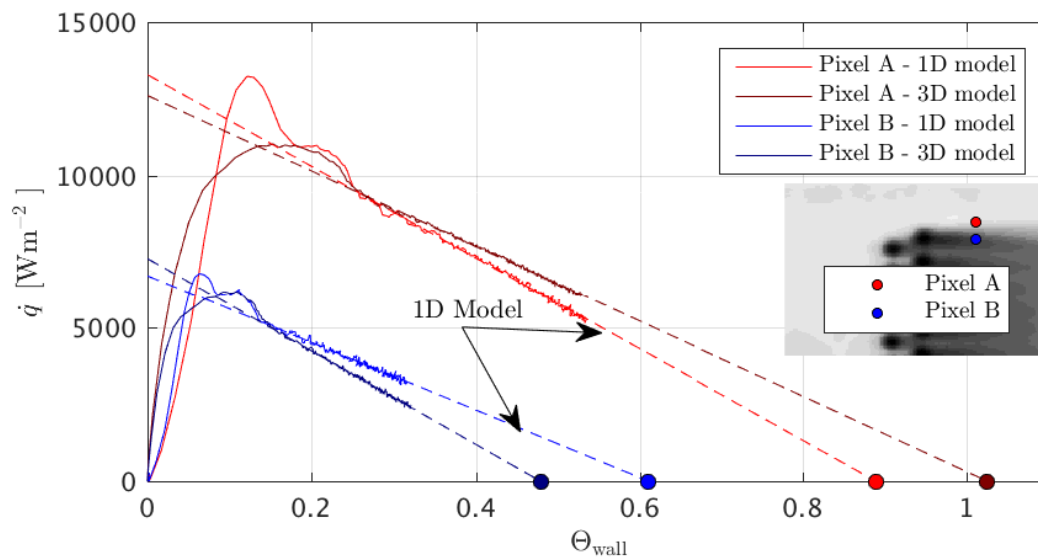


Fig. 7.17 Example linear regression showing the presence of large errors in 1D modelling methods in regions of high lateral heat flux

The following can be observed from figure 7.17;

- The heat flux values from the two models differ significantly at the very beginning of the transient measurement - where Θ is less than ~ 0.25 and 0.15 for Pixel A and B respectively. This is caused by initial truncation errors in the 3D model. Beyond this point, truncation errors are negligible.
- As the measurement proceeds in time, an increasing quantity of heat is transfer by lateral diffusion from the location at Pixel A to the location at pixel B. This causes Pixel A to increase in temperature at a reduced rate, and Pixel B to increase temperature at an increased rate - when compared to a case with no lateral diffusion. This causes the 1D model to under and over predict the heat flux for pixel A and B respectively.
- The deviation in heat flux between the two models is approximately equal in magnitude but opposite in sign, for the two pixels.

- The data within the valid regression region Θ_R , for both the 1D and 3D model are both relatively linear - this could lead you to the incorrect conclusion that the 1D model data is accurate. It is therefore important to determine whether lateral heat-flux terms are significant or not, before assuming a set of linear data is correct.

7.3.2 3D geometry effects

The sharp leading edge of the flat plate provides a geometric feature which locally invalidates the the 1D semi-infinite heat flux modelling assumption. In figure 7.2, the geometric condition which leads to the invalid modelling assumption was illustrated. The extent of the leading edge region which is significantly affected by three dimensional heat diffusion is assumed to be approximately linearly proportional to the heat penetration depth, and also to be a function of the geometric shape.

A series of experiments were performed on the flat plate rig, where the heat penetration depth was varied over a range of values. The solution to h and Θ_{rec} in the leading edge region are shown in figure 7.18. In figure 7.18, the solution to h has been non-dimensionalised by the turbulent heat transfer correlation (equation 7.2). (Note that there is an uncertainty in the heat transfer correlation of $\sim 15\%$).

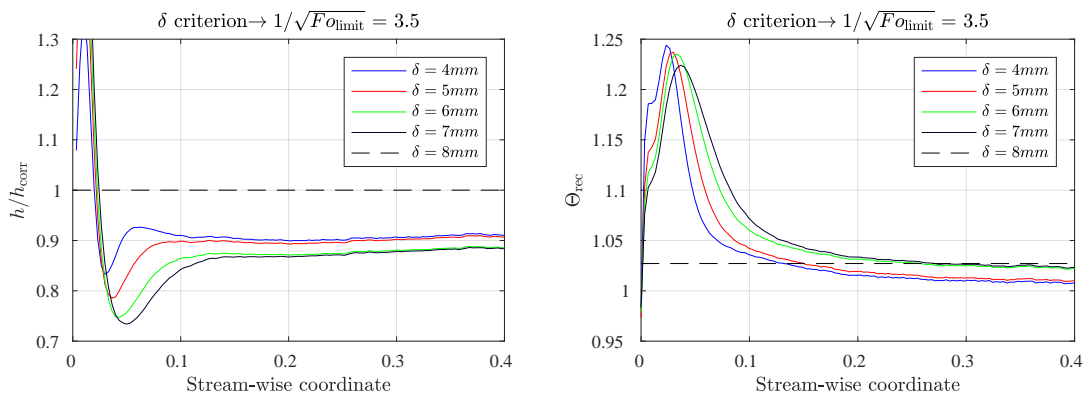


Fig. 7.18 The streamwise extent of the non-1D behavior of the leading edge of the flat plate, as a function of heat penetration depth

It can be seen from figure 7.18 that:

- The solution to h and Θ_{rec} deviate significantly from unity and Θ_{emp} at small distances from the leading edge.
- Increasing the heat penetration depth leads to an increase in the stream-wise extent of the affected region.

In figure 7.19 the solution to h and Θ_{rec} is shown as a function of stream-wise distance, non-dimensionalised by heat penetration depth. The solutions show a high degree of correlation with one-another, where peak error in h and Θ_{rec} consistently occurs at 0.7δ and 0.5δ , respectively. The solutions to h and Θ_{rec} appear to be unaffected where the stream-wise distance is greater than 1.5δ . This corresponds closely to the first order prediction given in equation 7.1, where a value of 1.56δ is estimated.

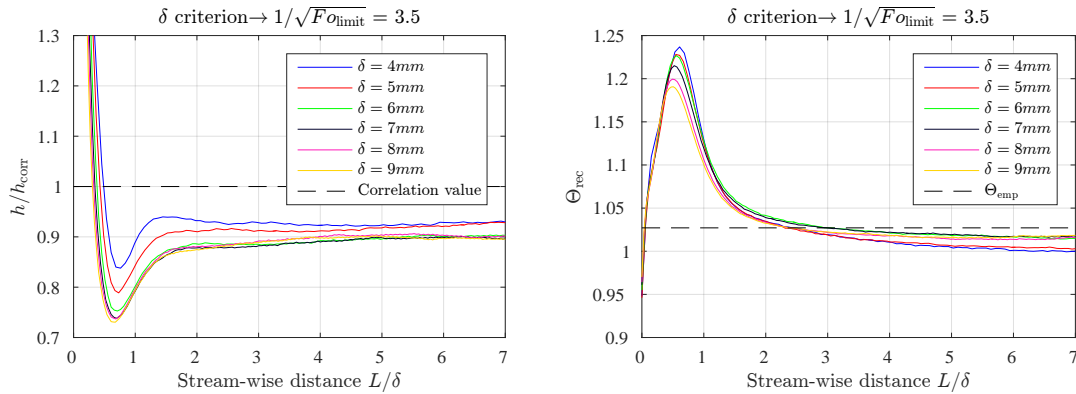


Fig. 7.19 The streamwise extent of the non-1D behavior of the leading edge of the flat plate, as a function of heat penetration depth

7.3.3 Key observations

- With one-dimensional heat flux modelling approaches, significant errors in the derived heat flux are found:
 - when large variations in surface boundary conditions exist over a surface distance equal to approximately one heat penetration depth (where $1/\sqrt{Fo_{\text{limit}}} = 3.5$). Significant errors in the surface heat flux extend up to one heat penetration depth, in the positive and negative direction of the boundary condition gradient. The area average value of heat flux, however, remains constant. This is consistent with the theory established in section 3.6.4.
 - when the distance between the point of observation and a 3D geometric feature is equal to or less than approximately one heat penetration depth.
- Three-dimensional heat flux modelling methods can be used to resolve lateral heat flux terms, introduced by non-uniform boundary conditions - leading to reduced local errors in h and Θ_{rec} .

7.4 Flat Plate Rig Experiments - Varying Θ_R

In this section, experimental results are shown, where the value of Θ_R has been altered from the base line case. The experiments are separated into two sections: In the first section, the extent of the loss of initial linear data, $\tilde{\Theta}$, is varied; in the second section, the extent of the loss of end data, Θ_E , is varied.

The influence of varying $\tilde{\Theta}$ and Θ_E on the measured value of h and Θ_{rec} is shown.

7.4.1 Experiments varying $\tilde{\Theta}$

Recalling equation 3.46 from section 3.7.1, the approximate expression for $\tilde{\Theta}$ is given as follows.

$$\tilde{\Theta} \approx 1 - \exp\left(\frac{6h^2\tau}{e^2}\right) \operatorname{erfc}\left(\frac{h\sqrt{6\tau}}{e}\right) \quad (7.10)$$

The value of $\tilde{\Theta}$ is wholly governed by the term $h^2\tau/e^2$, and so the value of $\tilde{\Theta}$ can be controlled by the varying τ .

Heater mesh time constant

The left hand graph in figure 7.20 shows mainstream temperature change measurements, from the free-stream thermocouple in the flat plate rig. The heater mesh power supply was controlled to supply power to the mesh according to an exponential decay function, given by equation 7.11, with time constants; 0, 0.25, 0.5, 1 and 2 seconds.

$$\frac{\Delta T_\infty(t)}{\Delta T_\infty(t \rightarrow \infty)} = 1 - \exp(-t/\tau) \quad (7.11)$$

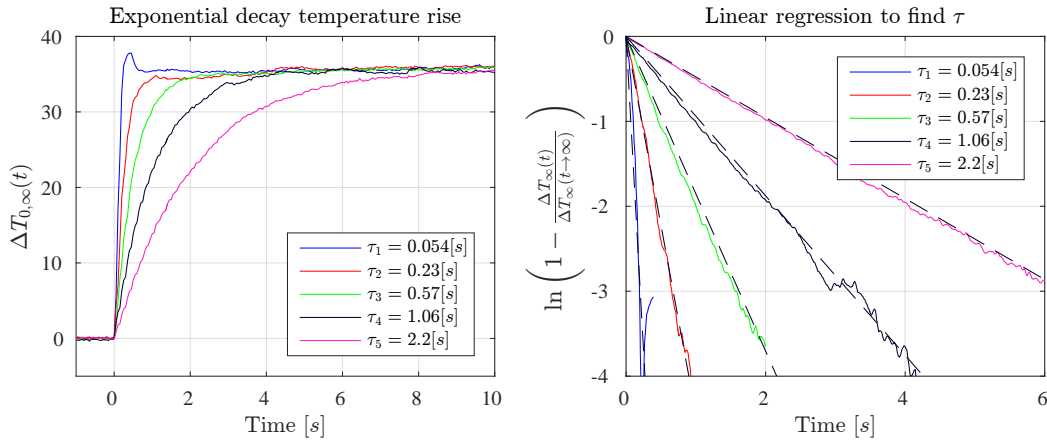


Fig. 7.20 Measurements of the mainstream temperature rise exponential exponent

Equation 7.11 can be re-arranged in order to give an expression for τ , and is shown by equation 7.12. The time constants of the measured mainstream temperature rise functions were evaluated.

$$-\frac{1}{\tau} = \frac{d}{dt} \ln \left(1 - \frac{\Delta T_{\infty}(t)}{\Delta T_{\infty}(t \rightarrow \infty)} \right) \quad (7.12)$$

Differentiation to find τ was performed by a least squares linear regression method. The linear regression functions are shown in the right hand graph in figure 7.20. The measured values of τ are indicated on the graphs, and their values matched the requested values to an average of 11% (excluding the $\tau = 0$ case).

The solutions to h and Θ_{rec} obtained for each heater mesh time constant are shown in figure 7.21. The linear regression delay period was defined as 6τ , matching the baseline case.

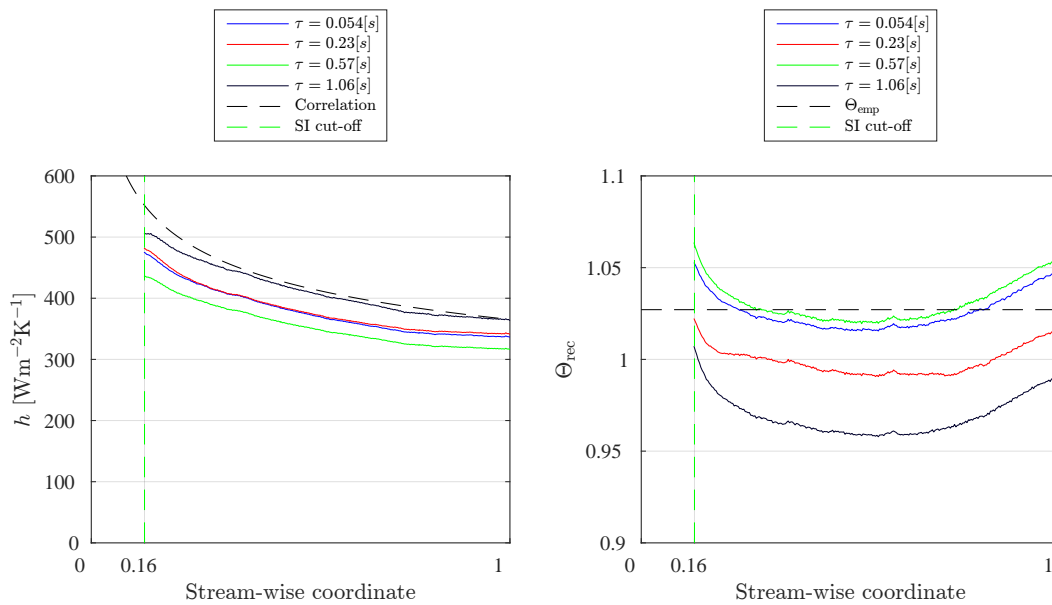


Fig. 7.21 Flate plate measurements of h and Θ_{rec} as a function of mainstream temperature rise time constant

The solutions in figure 7.21 show a significant variation with time constant, where the solutions to h and Θ_{rec} vary in stream-wise mean magnitude by -5 and +7% from the baseline case. The stream wise trends in each measurement, however, are highly correlated.

In an attempt to identify the source of this variation, some additional investigation into the characteristics of each of the mainstream temperature rise functions was undertaken. In figure 7.22 each of the four measured mainstream temperature rise functions are shown, and the temporal location at which the linear regression of Θ_{wall} and Q^* starts and ends is indicated. It can be seen that between the linear regression limits, there is a varying degree of mainstream temperature stability, and critically, an apparent non-zero mean linear gradient.

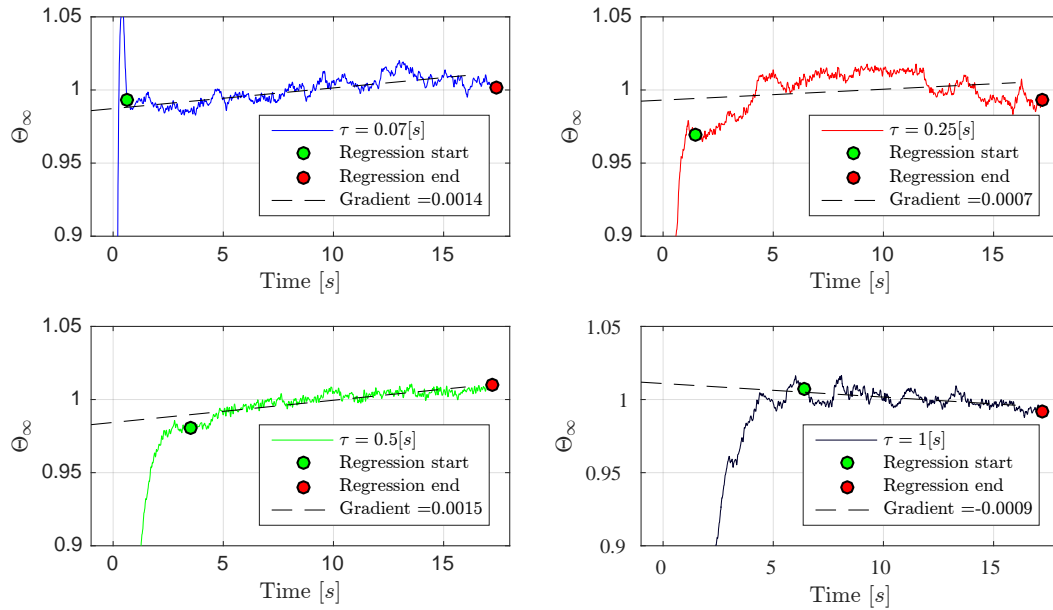


Fig. 7.22 Measurements of mainstream temperature step, where the linear component of the variation, between the regression limits, is highlighted

A linear regression function was fitted to the mainstream temperature measurement data for each time constant, between the regression limits. The linear function is shown in figure 7.22 and the gradient of the function is indicated. The validity of the method by which a linear regression of Θ and Q^* is used to find h and Θ_{rec} , depends on the mainstream temperature rise function being constant with time, during the regression period.

The time varying mainstream temperatures between the regression limits indicated in figure 7.22 will introduce measurement errors in h and Θ_{rec} .

Floating linear regression

Given measurements of the mainstream temperature fluctuations, it is possible to redefine the expression for the non-dimensional wall temperature, to take account of this additional information. With exact mainstream fluid temperature measurements, it would be possible to fully account for their influence on h and Θ_{rec} . An expression for the non-dimensional wall temperature is given in equation 7.13, where the denominator, $\Delta T_{0,\infty}(t)$, is a function of time. The method of using knowledge of the mainstream temperature fluctuations to improve the linear regression, was described by Collins et al. [2015].

$$\Theta_{\text{wall}}(t) = \frac{\Delta T_{\text{wall}}(t)}{\Delta T_{\text{aw}}(t)} \approx \frac{\Delta T_{\text{wall}}(t)}{\Delta T_{\infty}(t)(1 + \hat{r} \frac{\gamma-1}{2} \text{Ma}_{\infty}^2)} \quad (7.13)$$

Equation 7.13 is evaluated at a Mach number of 0.39 below.

$$\Theta_{\text{wall}}(t) = \frac{\Delta T_{\text{wall}}(t)}{1.027 \times \Delta T_{\infty}(t)} \quad (7.14)$$

The data presented in figure 7.21 was re-processed, where a linear regression was performed against Q^* and Θ_{wall} , where Θ_{wall} was defined by equation 7.13. The solutions to h and Θ_{rec} are shown in figure 7.23.

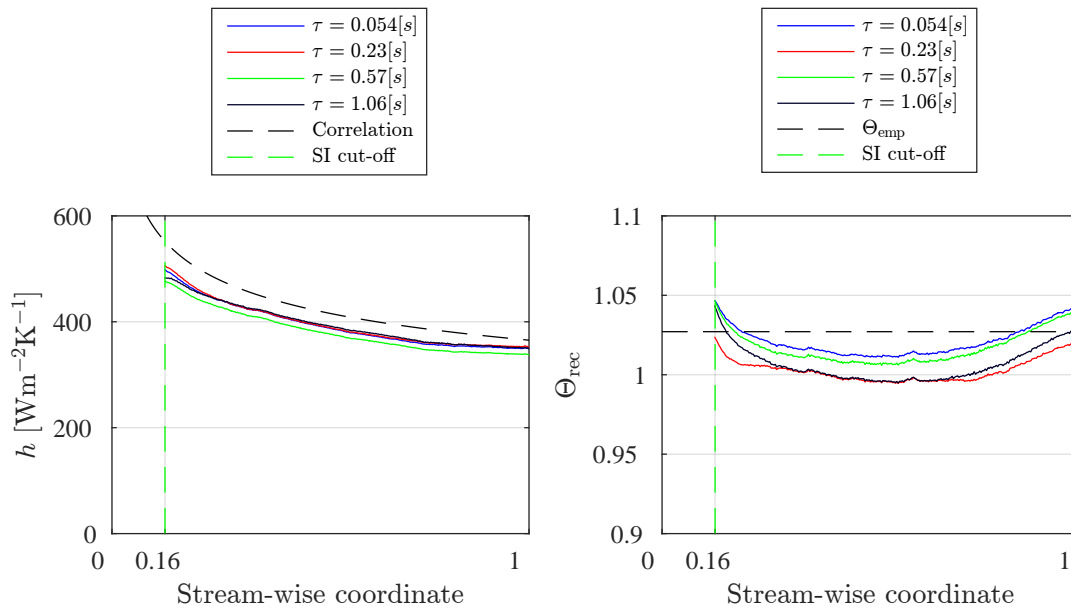


Fig. 7.23 Flat plate measurements of h and Θ_{rec} as a function of mainstream temperature rise time constant - with floating linear regression

The measurements in figure 7.23 show a significant improvement in the repeatability of the measurements, as a function of time constant, when compared to the results in figure 7.21.

The stream-wise values of h vary from the baseline case by 0.6% ($\tau = 0.23$), -3.0% ($\tau = 0.57$) and 0.5% ($\tau = 1.06$).

The stream-wise values of Θ_{rec} vary from the baseline case by -1.8% ($\tau = 0.23$), -0.4% ($\tau = 0.57$) and -1.4% ($\tau = 1.06$).

The variations in non-dimensional mainstream fluid temperature, shown in figure 7.22, are not greater than $\pm 3\%$ from unity, during the regression period. However, the influence

of this unsteadiness has an amplified affect on the solutions to h and Θ_{rec} , as can be seen by the reduction in the spread of solutions to h , from +5% and -7% to +0.6%, -3%.

This illustrates that the unsteadiness in the mainstream fluid temperature, shown in figure 7.22, was having a significant influence on the solutions in figure 7.21. Consequently, it can be said that the non-dimensional mainstream temperature must either be steady, or measured to an accuracy greater than the required accuracy of the heat transfer measurements.

7.4.2 Experiments varying Θ_{limit}

Recalling equation 3.49 from section 3.7.2, the approximate expression for Θ_{limit} was given as follows.

$$\Theta_{limit}(0,t) = 1 - \exp(\text{Bi}^2 \text{Fo}_{limit}) \text{erfc}(\text{Bi} \sqrt{\text{Fo}_{limit}}) \quad (7.15)$$

The value of Θ_{limit} is wholly a function of $\text{Bi} \sqrt{\text{Fo}_{limit}}$, where a large value of $\text{Bi} \sqrt{\text{Fo}_{limit}}$ results in a large value of Θ_{limit} . Experiments were conducted, where the value of Bi and Fo_{limit} were varied in isolation - the results are shown in the following subsections.

Experiments varying Biot number

Recalling equation 3.10, the Biot number is given as follows:

$$\text{Bi} = \frac{hx}{\kappa} \quad (7.16)$$

A series of experiments were performed on the flat plate rig, using the baseline uncooled geometry. The heat penetration depth, δ , was limited to a range of values between 1.5 and 6mm, which were chosen to approximately represent the full range of substrate thicknesses. An $1/\sqrt{\text{Fo}_{limit}}$ value of 3.5 was used to define the duration of the transient measurement, where the measurement duration is given as a function of Fo_{limit} and x , in equation 3.51. The measurements of h and Θ_{rec} are shown in figure 7.24. Note that a floating linear regression method, described in section 7.4.1, was used in the data analysis. Span-wise averaging was performed over the span-wise limits 0.3 and 0.7.

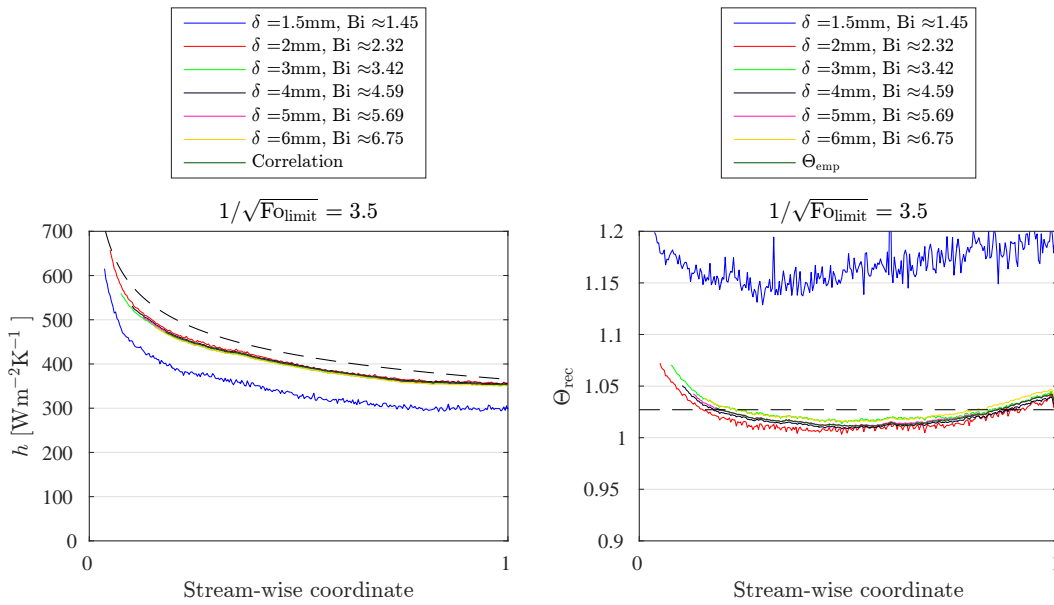


Fig. 7.24 Measurements of h and Θ_{rec} as a function of Biot number

The following can be observed from figure 7.24:

- At Biot numbers greater than or equal to ~ 2.3 , the solutions to h and Θ_{rec} are highly repeatable, with a maximum stream-wise mean deviation of 1.9% and -1.4% respectively.
- At a Biot number of 1.45, the solution deviates significantly. This is due to the small value of Θ_{R} , caused by a low value of Θ_{limit} . This ‘sudden’ increase in uncertainty was predicted in figure 4.7c from the uncertainty modelling, which is shown again below, for convenience. (Note that the measurement conditions do not match the uncertainty modelling conditions exactly, which is the reason for the slight difference on the value of δ at the ‘cliff edge’).

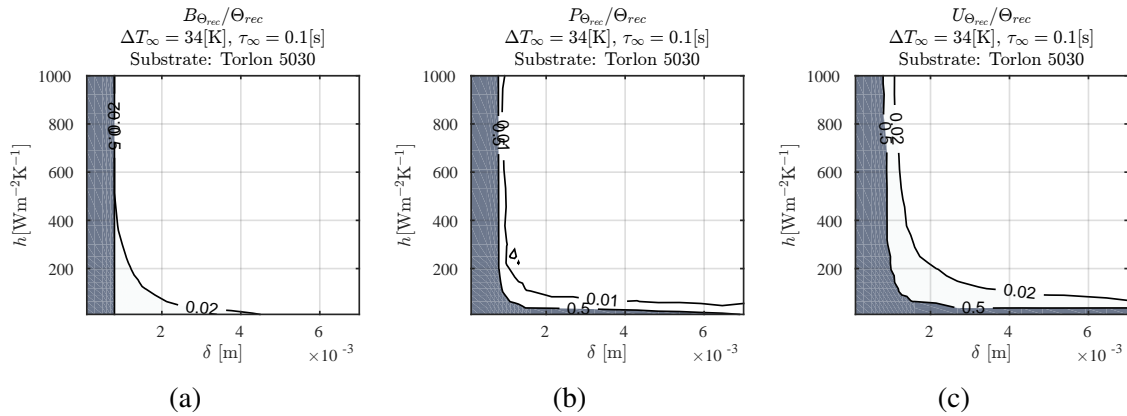


Fig. 7.25 Uncertainty in Θ_{rec} measurements on the FACTOR NGV, as a function of h and δ

- The stream-wise extent of the leading edge region affected by 3D conduction is reduced as δ is reduced, allowing measurements closer to the leading edge. This also results in a negligible increase in measurement error. Once δ is reduced below 1.5mm however, the measurement uncertainty in all locations rapidly rises. This indicates that in order to reduce the influence of 3D conduction errors, the measurement should be undertaken as close to the ‘cliff edge’ as possible, without significantly increasing measurement error.

Experiments varying Fo_{limit}

In section 3.7.2, it was shown that the Fourier number can be considered as a control parameter which balances the uncertainty contributions, in h and Θ_{rec} , from two sources: From uncertainty in the linear regression of Q^* and Θ_{wall} , and from uncertainty in the values of Q^* . A low $1/\sqrt{Fo_{limit}}$ will permit the transient measurement to run for a longer period of time, increasing the value of Θ_R , which will reduce the uncertainty in the linear regression of Q^* and Θ_{wall} . However, for a finite thickness substrate, the validity of the semi-infinite assumption decreases with reducing $1/\sqrt{Fo_{limit}}$, increasing uncertainty in Q^* .

In figure 7.26, solutions to h and Θ_{rec} are shown, for the same experimental data presented in figure 7.24. In this instance, $1/\sqrt{Fo_{limit}}$ number of 2, rather than 3.5 was specified. (Note an optimum $1/\sqrt{Fo_{limit}}$ number of 2 was deduced in section 3.7.2). It can be seen that with the modified definition of $1/\sqrt{Fo_{limit}}$, the heat penetration depth at which the error in h grows rapidly, is ~ 0.75 [mm]. This compares to a value of ~ 1.5 [mm] with the original definition of $1/\sqrt{Fo_{limit}}$ from figure 7.24. At low stream-wise coordinates (less than ~ 0.1), the value of Θ_{rec} begins to deviate significantly from the value of Θ_{emp} . One explanation for this is that there are high gradients in h at this location, which may be giving rise to significant

lateral conduction, in the stream-wise direction. Since the data processing is 1D, this will be leading to increased measurement errors.

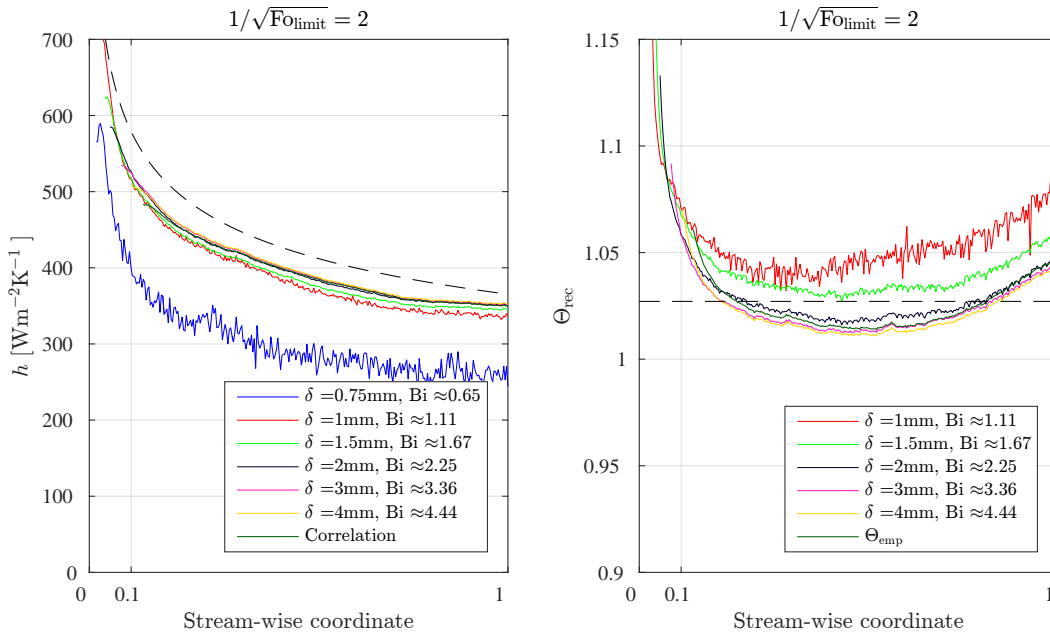


Fig. 7.26 Flate plate measurements of h and Θ_{rec} as a function of Biot number

In order to experimentally validate the optimum value of $1/\sqrt{Fo_{limit}}$, a series of experiments were performed of the film-cooled flat plate, described in section 6.3. The film-cooled flat plate has an internal film-coolant feeding plenum, which is situated 2.55mm beneath the gas washed surface, and upstream of the film-cooling holes. This region of low substrate thickness was used to determine how low the $1/\sqrt{Fo_{limit}}$ can be specified, before significant errors in the semi-infinite assumption introduce significant errors in h and Θ_{rec} .

Data analysis was performed at a range of Fo_{limit} numbers. The solutions to h and Θ_{rec} were span-wise averaged between the span wise limits of 0.3 and 0.6. The mean stream-wise value of h was non-dimensionalised by the turbulent heat transfer correlation, and the mean stream-wise value of Θ_{rec} , was normalised by Θ_{emp} . The stream-wise averaging was performed over the stream-wise limits of 0.34 and 0.53. These coordinate limits correspond to the location of the film-coolant feeding plenum. The solutions are shown in figure 7.27, where a qualitative representation of the uncertainty in the linear regression (using the average Coefficient of Determination - R^2 , from the linear regression fitting), is shown on the plot.

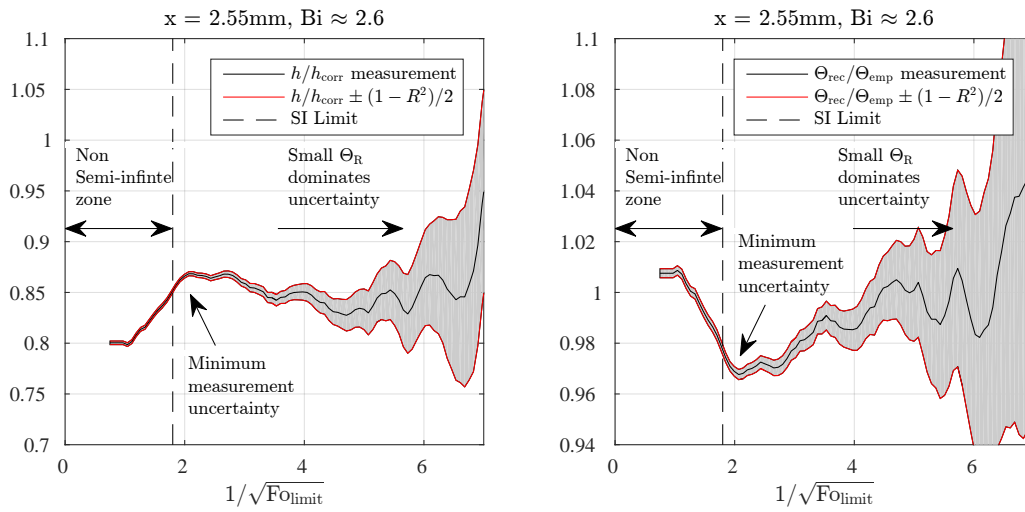


Fig. 7.27 Normalised spanwise averaged values of h and Θ_{rec} as a function of Fo_{limit}

From figure 7.27, the following can be observed:

- As $1/\sqrt{Fo_{\text{limit}}}$ numbers increases from ~ 2 , the solution to h/h_{corr} and $\Theta_{\text{rec}}/\Theta_{\text{emp}}$ becomes increasingly uncertain, indicated by the increasing value of $(1 - R^2)/2$. The high value of $1/\sqrt{Fo_{\text{limit}}}$, limits the duration of the transient measurement, such that value of Θ_R is reduced, and the uncertainty in the linear regression of Q^* and Θ_{wall} is increased. It is important to note, that the $1/\sqrt{Fo_{\text{limit}}}$ number at which this rapid increase in uncertainty occurs, is also a function of Biot number.
- At $1/\sqrt{Fo_{\text{limit}}}$ numbers less than ~ 1.8 , the solution to h/h_{corr} and $\Theta_{\text{rec}}/\Theta_{\text{emp}}$ deviate increasingly, with reducing Fo_{limit} number. The low value of $1/\sqrt{Fo_{\text{limit}}}$ allows the transient measurement to extend for a longer period of time, such that significant heat penetration occurs through the whole thickness of the substrate. As a result, the validity of the semi-infinite assumption is weakened, and errors in the derived value of Q^* are introduced. The errors result in an underestimate of h and an overestimate of Θ_{rec} , which is what would be expected for an adiabatic back face boundary conditions, as described in section 3.7.2.
- At a $1/\sqrt{Fo_{\text{limit}}}$ number between ~ 1.8 and 2.5, there appears to be a region of minimum measurement uncertainty. This is deduced by the value of h/h_{corr} and $\Theta_{\text{rec}}/\Theta_{\text{emp}}$ appearing to stabilise at a fixed value. It is worth noting that the theoretical optimum value of $1/\sqrt{Fo_{\text{limit}}}$, deduced in section 3.7.2, was equal to ~ 2 .

-
- The value of h/h_{corr} is not equal to one at the suggested minimum measurement uncertainty location. This is understood to be the result of uncertainty in the heat transfer correlation, which is $\sim 15\%$ [Incropera et al., 2006].

7.4.3 Key observations

- Unsteadiness in the mainstream temperature can cause significant errors in the evaluation of h and Θ_{rec} , if a floating linear regression is not used. This effect is most significant when there is a linear trend to the mainstream fluid temperature, with non zero mean gradient, over the linear regression period.
- In the case where there is variation in the mainstream fluid temperature, during the linear regression period, floating linear regression methods can be effective in maintaining low measurement uncertainties. However, this method relies on accurate free-stream temperature measurements, which are highly resolved in time.
- Uncertainties in h and Θ_{rec} are a non-linear function of $\text{Bi}\sqrt{\text{Fo}_{\text{limit}}}$. Under the measurement conditions tested, errors can increase by more than two orders of magnitude, over a $\sim 20\%$ reduction in $\text{Bi}\sqrt{\text{Fo}}$.
- Experiments suggest that with measurements on a substrate with finite thickness, an $1/\sqrt{\text{Fo}_{\text{limit}}}$ of ~ 2 yields the lowest overall uncertainty in h and Θ_{rec} , which corresponds closely with the theory in section 3.7.2. This effectively permits heat transfer measurements of substrates with lower thickness's than is suggested possible in the literature [Schultz and Jones, 1973].
- By using an $1/\sqrt{\text{Fo}_{\text{limit}}}$ of 2, rather than 3.16 [Schultz and Jones, 1973], it is also possible to measure in regions with lower values of h , before the measurement becomes ill-conditioned. (Note that this advantage is only apparent when measurements are constrained to be taken on materials with suboptimal material properties, and small heat penetration depths).

7.5 3D Vane Rig Experiments: Without film-cooling

In this section, the experimental results from the 3D vane rig, with the un-cooled vane are presented. The objectives of the 3D vane rig experiments were outlined in section 6.1.

The 3D vane rig applies the following additional measurement constraints, with respect to the flat plate rig experiments:

1. U_{Θ} matched to FACTOR

On the FACTOR rig, the values of $U_{\Theta_{\text{wall}}}$ will vary between different measurement locations. Most notably, there will be a relatively high value of $U_{\Theta_{\text{wall}}}$ for all measurements on the rotor. This is because very low IR camera integration times must be used in order to avoid motion blur in the IR images, which result in increased noise levels in the IR temperature measurements. Experimental results are shown, where $U_{\Theta_{\text{wall}}}$ levels match those of the FACTOR rig.

2. Biot number matched to FACTOR

As has been shown in section 7.4.2, the Biot number has a critical influence on the uncertainty in h and Θ_{rec} . Experiments in this section have been conducted at Biot numbers similar to those expected in the FACTOR rig.

3. Surface curvature matched to FACTOR

In section 3.6.3, the theoretical impact of surface curvature on the measurement uncertainty in h and Θ_{rec} , when making use of 1D semi-infinite modelling assumptions, was quantified. The 3D vane test geometry in this section, has geometric features with surface curvature approximately matching that of the FACTOR rig blades and vanes. The ability to determine h and Θ_{rec} in regions of high surface curvature will be examined.

4. Viewing angles matched to FACTOR

In the flat plate rig experiments, all IR radiation measurements were taken approximately parallel to the plate surface normal. In the FACTOR rig, IR radiation measurements will need to be taken from angles deviating significantly from the surface normal. Experimental measurements are taken at a 60° angle from the surface normal.

5. Substrate material matched to FACTOR

In the FACTOR rig, the NGV and LP vane have been produced from Torlon 5030. The rotor has been produced from a Torlon 7130 & Titanium 6/4, in a composite

construction. Experimental results are shown for the same substrate materials, which were fabricated using the same manufacturing processes as those of the FACTOR vanes and blades - i.e. injection moulding for the Torlon 7130.

7.5.1 3D vane coordinate system mapping

As indicated in figure 6.4, the optical axis of the IR camera was at an angle of 60° to the surface normal of the 3D vane. As a result, the IR images were acquired in a distorted coordinate system, where image remapping techniques were required to return to a span-wise/stream-wise coordinate system.

Measurement data was mapped on to a span-wise/stream-wise coordinate system, using a combination of the 'Matlab' functions 'fitgeotrans' and 'imwarp'. A series of control points were manually defined in the original, unmapped solutions (figure 7.28, left), which were related to known locations in the span-wise/stream-wise coordinate system (figure 7.28, right). The functions 'fitgeotrans' and 'imwarp' were used to apply a piecewise linear 2D geometric transformation of the image - mapping the image from the distorted coordinate system to the stream-wise/span-wise coordinate system.

A cut-away iso-metric view of the 3D vane rig is provided in figure 7.29, to aid the reader in orientating themselves with respect to the images in figure 7.28.

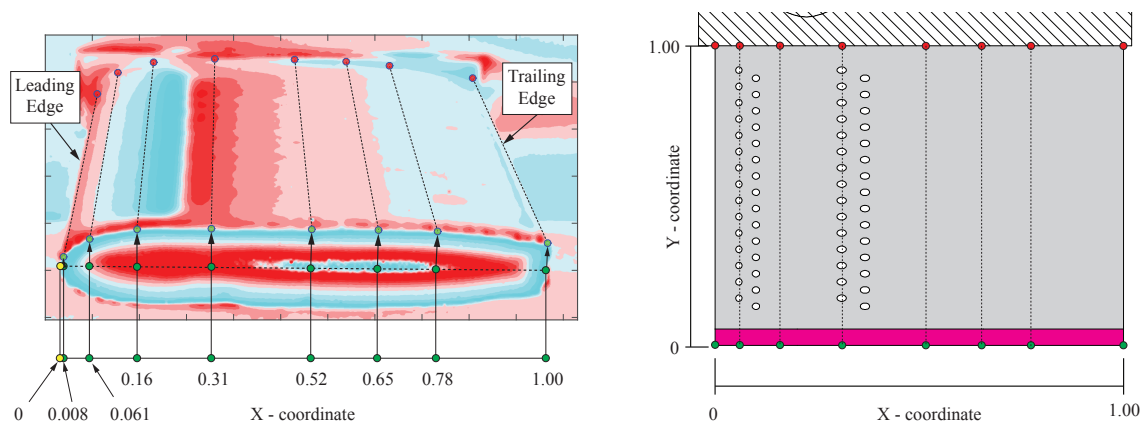


Fig. 7.28 Measurement coordinate system (left) and span-wise/stream-wise coordinate system (right). The control points used to linear map data between each coordinate system are shown.

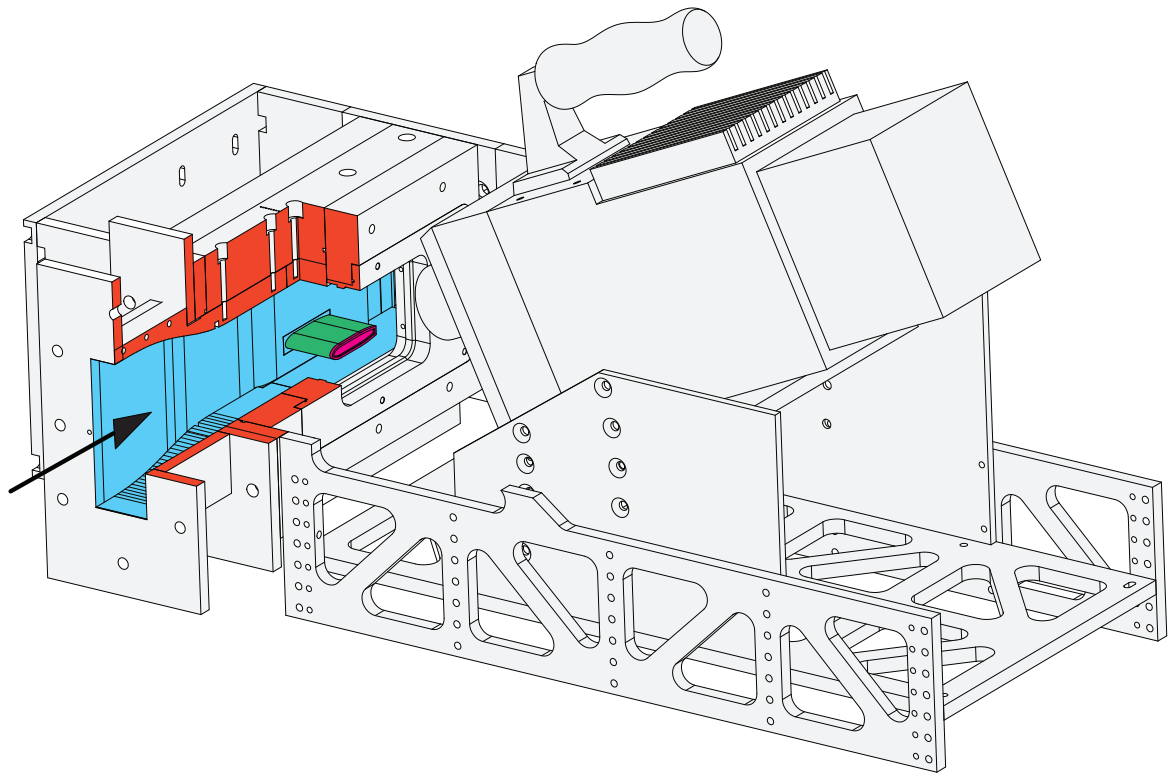


Fig. 7.29 A cut-away iso-metric view of the 3D vane rig

In figure 7.30 an example of the mapping process is given, where; the original image is shown on the left, the mapped image output is shown in the middle, and the mapped image output, trimmed to the span-wise and stream-wise coordinates limits of zero and one is shown on the right.

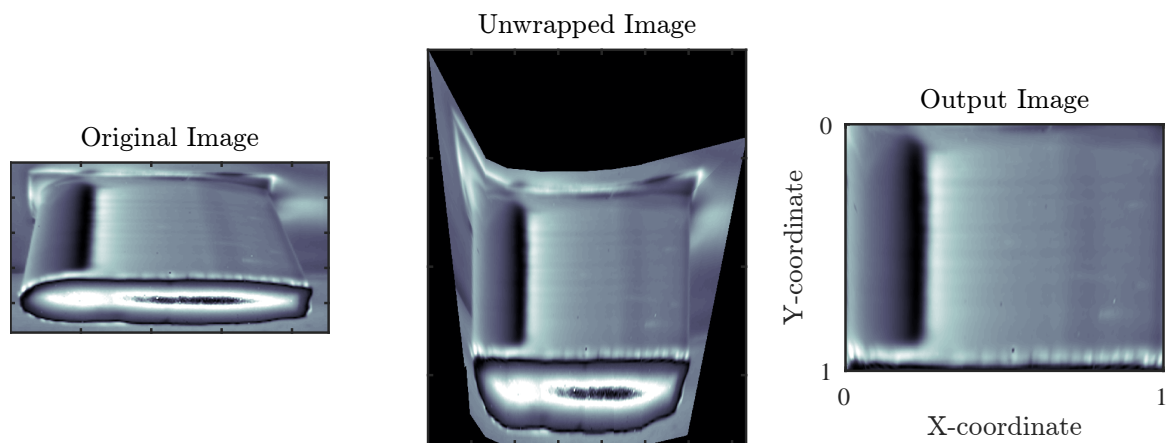


Fig. 7.30 An example of the image mapping process

7.5.2 Integration time specification for SNR levels matching FACTOR

Measurements on the 3D vane were performed at two IR camera integration times; $160\mu\text{s}$ and $20\mu\text{s}$, such that IR camera SNR levels matches the SNR levels expected in the FACTOR NGV and Rotor measurements respectively.

On the FACTOR rig, IR measurements on the static components, the NGV and the LP vane, can be taken at relatively large integration times, as there is no requirement to avoid motion blur. Under these conditions, it is desirable to define the integration time of the camera to result in IR measurements with an optimal detector saturation level, which is $\sim 80\%$.

On the FACTOR rotor however, the optimum integration time is governed by a trade-off between the requirement to avoid motion blur and the requirement to maintain sufficient SNR levels. An integration time of $6\mu\text{s}$ will relate to a FACTOR rotor tip circumferential displacement of ~ 1.4 mm, during one imaging period. This is equivalent to $\sim 5\%$ or Rotor pitch, and also equates to the imaging width of 2 pixels. A detector saturation level of $\sim 10\%$ will be reached.

The 3D vane rig operates at a lower absolute temperature than the FACTOR rig, and hence radiance levels are reduced. In order to obtain equivalent detector saturation levels, such that SNR levels are matched, between the FACTOR and 3D vane rig, the IT values in the 3D vane measurements were increased. Table 7.3 shows the integration times for the FACTOR rig, and the equivalent integration times for the 3D vane rig.

Table 7.3 Table showing the integration times required to achieve either 80% or 10% detector saturation in each rig location

Rig	Relative total temperature	Black body radiance (7.7 - 9.3 μm band)	Integration time	
			80% Saturation	10% Saturation
FACTOR NGV	450 [K]	102 [$\text{Wm}^{-2}\text{Sr}^{-1}$]	46 μs	-
FACTOR Rotor	425 [K]	81.0 [$\text{Wm}^{-2}\text{Sr}^{-1}$]	-	6 μs
FACTOR LP Vane	359 [K]	23.0 [$\text{Wm}^{-2}\text{Sr}^{-1}$]	162 μs	-
3D Vane rig	331[K]	25.7 [$\text{Wm}^{-2}\text{Sr}^{-1}$]	160 μs	17 μs

In addition to matching the absolute radiance levels between the two rigs, it is also important to match the radiance change which occurs as a result of the mainstream heater-

mesh (HM) temperature step. By matching the radiance change, the change in IR camera detector output will be matched. The radiance change levels for the FACTOR and 3D vane rig are shown in table 7.4. The maximum mainstream temperature step which could be achieved on the 3D vane rig was 36K, which results in a radiance change of $12.0[\text{Wm}^{-2}\text{Sr}^{-1}]$, which is 100% lower than the FACTOR NGV and 40% higher than the FACTOR LP vane.

Table 7.4 Table of radiance change as a result of mainstream temperature step in each rig location

Rig	Relative total temperature HM off	Relative total temperature HM on	$\Delta T_{0,\infty}$	Radiance change
FACTOR NGV	420 [K]	450 [K]	30 [K]	24.5 [$\text{Wm}^{-2}\text{Sr}^{-1}$]
FACTOR Rotor	397 [K]	425 [K]	28 [K]	20.2 [$\text{Wm}^{-2}\text{Sr}^{-1}$]
FACTOR LP Vane	302 [K]	324 [K]	22 [K]	7.3 [$\text{Wm}^{-2}\text{Sr}^{-1}$]
3D Vane rig	295 [K]	331 [K]	36 [K]	12.0 [$\text{Wm}^{-2}\text{Sr}^{-1}$]

7.5.3 Un-cooled vane measurement conditions

The values of the rig, data acquisition, and data processing variables which were used to perform the measurements on the uncooled vane, are given in table 7.5. Note that the heat penetration depth limit has been set to 2mm, which corresponds to the limit on the FACTOR NGV and Rotor. The 3D heat-flux modelling method was used throughout the 3D vane data processing.

Table 7.5 Uncooled 3D vane measurement conditions

Parameter	Setting
Mainstream conditions	
Mainstream temperature step - $\Delta T_{0,\infty}$	36 [K]
Temperature step time constant - τ	0.07 [s]
Substrate	
Substrate material	Torlon 4203, 5030 & 7130
Substrate initial condition, T_i	Steady-state
IR camera	
IR camera integration time	160 & 20 [μ s]
IR camera acquisition rate	200 [frames/s]
Span-wise optical resolution	~ 0.305 [mm/pixel]
Stream-wise optical resolution	~ 0.49 [mm/pixel]
3D vane stream-wise length	49.7 [mm]
Optical axis angle from surface normal	60°
Data processing	
Heat flux processing method	3D finite difference
Linear regression delay period	6 τ
Floating linear regression	Applied
Heat penetration depth limit	2 [mm]
Semi-infinite criterion	$1/\sqrt{Fo_{\text{limit}}} = 2$

7.5.4 Valid data region

In figure 7.31 the measurement of h on the uncooled vane is shown. At the trailing edge, and at the two extreme span-wise locations on the 3D vane, measurement data must be excluded, due to 3D geometry effects which invalidate the semi-infinite assumption. The measurement data is assumed to be valid if it is taken from a region at least two heat penetration depths away from the end-walls and trailing edge. The data exclusion region at low span-wise coordinates is slightly increased, due to the presence of the tip seal cavity.

The data exclusion region at the leading edge, is specified such that the IR camera optical axis does not exceed a value greater than 60 Degrees from the surface normal.

The data outside of the dashed black box is given as invalid.

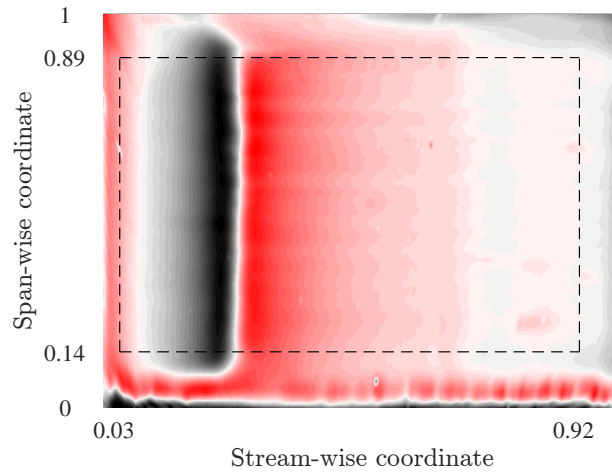


Fig. 7.31 Specification of valid and invalid regions of measurement data on the uncooled vane

7.5.5 Preliminary result evaluation

In figure 7.32, the solution to h and Θ_{rec} is shown for the Torlon 4203 vane, at an integration time of $160\mu\text{s}$. The blade profile section is also shown above the plot.

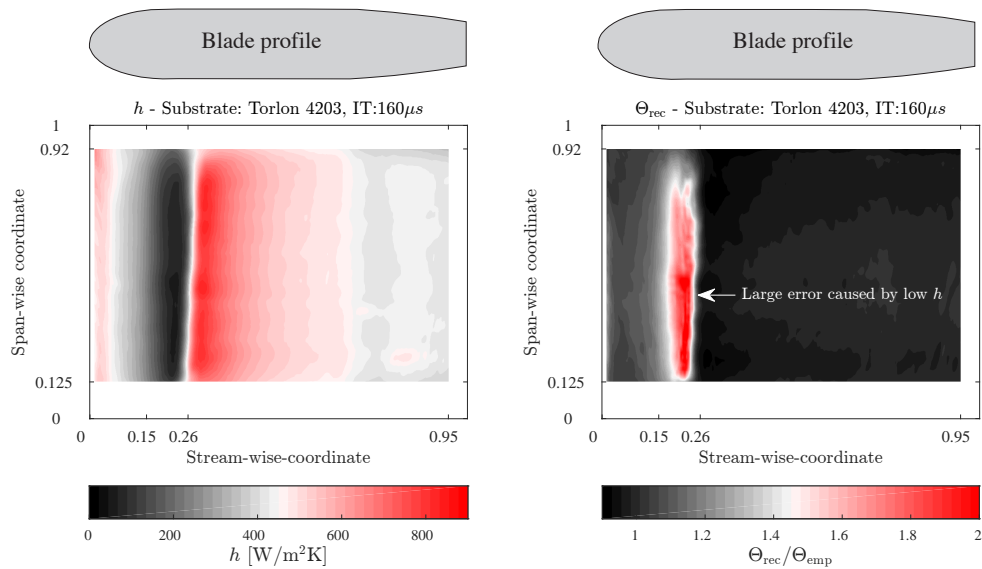


Fig. 7.32 Measurement of h and Θ_{rec} on the uncooled 3D vane

The following can be observed from figure 7.32:

-
- The heat transfer coefficient diminishes with stream-wise distance from the leading edge, until a stream-wise coordinate of ~ 0.2 , where it reaches a value of \sim zero. At a stream-wise coordinate of ~ 0.26 , there is a sudden large increase in h , which then gradually diminishes to trailing edge of the vane.
 - The heat transfer coefficient is highly uniform in value across the span of the vane.
 - The value of $\Theta_{\text{rec}}/\Theta_{\text{emp}}$ is ~ 1.05 at the leading edge. Its value then rises to ~ 1.7 at a stream-wise coordinate of 0.2. At stream-wise coordinates between 0.26 and 0.95, the value of $\Theta_{\text{rec}}/\Theta_{\text{emp}}$ is relatively uniform, with standard deviation of 0.13% and area average mean value of 0.983.

It is evident that the measurement of Θ_{rec} , and possibly h , between the span wise coordinate of zero and 0.26 are invalid. It is believed that there are two reasons for this error:

1. The presence of a laminar separation bubble

The low values of h between the stream-wise coordinates 0.15 and 0.26, followed by the rapid rise between 0.26 and 0.3, is indicative of the presence of a laminar separation bubble, followed by a turbulent reattachment. The transition of the vane body profile, from its elliptical leading edge, to its parallel wall section, occurs at a stream-wise coordinate of 0.18. At this location, there is a step change in the curvature of the surface of the vane, which is a geometric feature well known to often trigger boundary layer separation in compressor blade leading edges [Goodhand and Miller, 2009].

Low flow velocities in a separation bubble, caused by two stagnation lines on the surface, result in low shear stress, leading to low heat transfer coefficients. As a result, the Biot number is reduced to near zero. A limited surface temperature rise then occurs in this region, during the transient heat transfer measurement, leading to a low value of Θ_{R} , and a poorly conditioned linear regression of Q^* and Θ_{wall} . Additionally, the large variation in h over a relatively small surface distance, may cause significant boundary condition induced lateral heat flux terms.

Figure 7.33 shows the skin friction coefficient and boundary layer shape factor solution for the 3D vane, from a 2D CFD model. The program '*Xfoil*', (released under the GNU General Public Licence), was used to perform the calculation. It can be seen from figure 7.33, that a region of negative skin friction coefficient occurs at a stream-wise location of ~ 0.2 , indicating a small region of reverse flow - i.e. the presence of a recirculating bubble. It can also be seen that the shape factor of the boundary layer,

between the stream wise coordinate zero and ~ 0.15 , is approximately 2.5, which is typical of a laminar boundary layer. At stream-wise coordinates greater than ~ 0.25 , the shape factor is ~ 1.4 , which is characteristic of a turbulent boundary layer. This indicates that the boundary layer is laminar, when it separates.

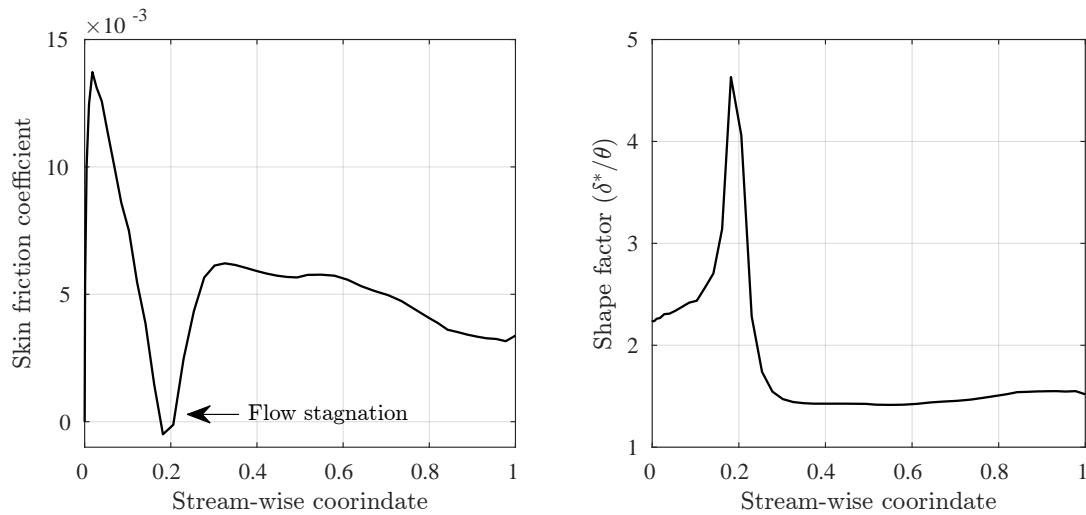


Fig. 7.33 2D CFD solution to ‘Skin friction coefficient’ and boundary layer ‘Shape factor’ for the uncooled 3D vane. The solutions indicate the presence of a laminar flow separation.

2. Surface curvature induced errors at the leading edge

In section 3.6.3 the theoretical influence of surface curvature on the solutions to h and Θ_{rec} was described. The Biot number, based on the radius of curvature, Bi_r , was identified as a measure by which the influence of surface curvature can be evaluated. It was shown that Bi_r greater than ~ 40 are required for curvature induced errors to be less than $\sim 1\%$.

In figure 7.34, the Bi_r number for the 3D vane is shown. The measured values of h were used to determine the value of Bi_r , and hence the values are subject to the uncertainties in h . Note that the value of Bi_r is infinite between the stream-wise coordinates 0.18 and 0.52, and 0.8 and 1, as the radius of curvature of the surface is infinite.

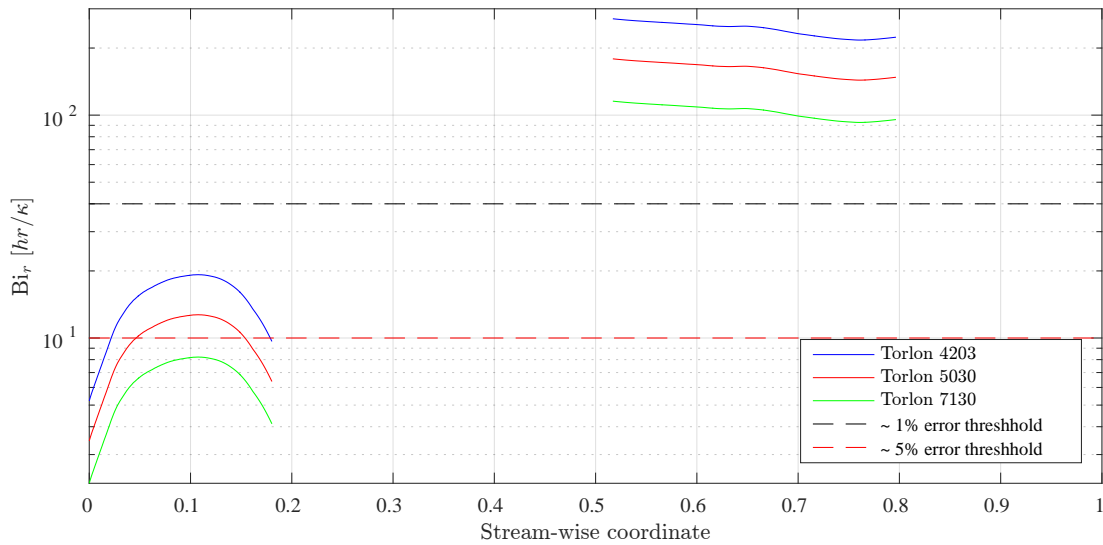


Fig. 7.34 Bi_r numbers for the uncooled 3D vane, derived from the measurements of h

The following can be observed from figure 7.34:

- An increase in the Bi_r number occurs with span-wise coordinate, between the stream-wise locations zero and 0.1. This is caused by the decreasing surface curvature.
- A decrease in the Bi_r number occurs with span-wise coordinate, between the span-wise locations 0.1 and 0.18. This is caused by the decreasing heat transfer coefficient.
- The mean value of Bi_r in the leading edge region is ~ 15 , for Torlon 4203. The theory suggests that there should be consequential error in h and Θ_{rec} of approximately -4 and +4% respectively.
- The Bi_r number, for all three materials, between the span-wise locations 0.52 and 0.8 is greater than 90. Consequently, curvature induced errors are expected to be significantly lower than 1% in this region.
- The flat sections of the 3D vane (span-wise coordinates 0.18 to 0.52 and 0.8 to 1), have infinite radius, and consequently have an infinite Bi_r number.

The error in Θ_{rec} , on the elliptical LE section, predicted by the surface curvature error model (+4%), does not match closely with the apparent measured error. The area average mean value of the Θ_{rec} measurement, between the span-wise coordinates zero and 0.15 is equal to 1.18 - suggesting an +18% error.

It is suggested that the reason for this larger error is due to a lateral conduction effects, which are exacerbated by the low Biot number in these region, which serve to make the measurement ill conditioned. Since the heat flux in this region is low, small errors in the heat flux modelling represent a large proportion of the total heat flux, resulting in large gradient errors in the linear regression.

7.5.6 Un-cooled vane results

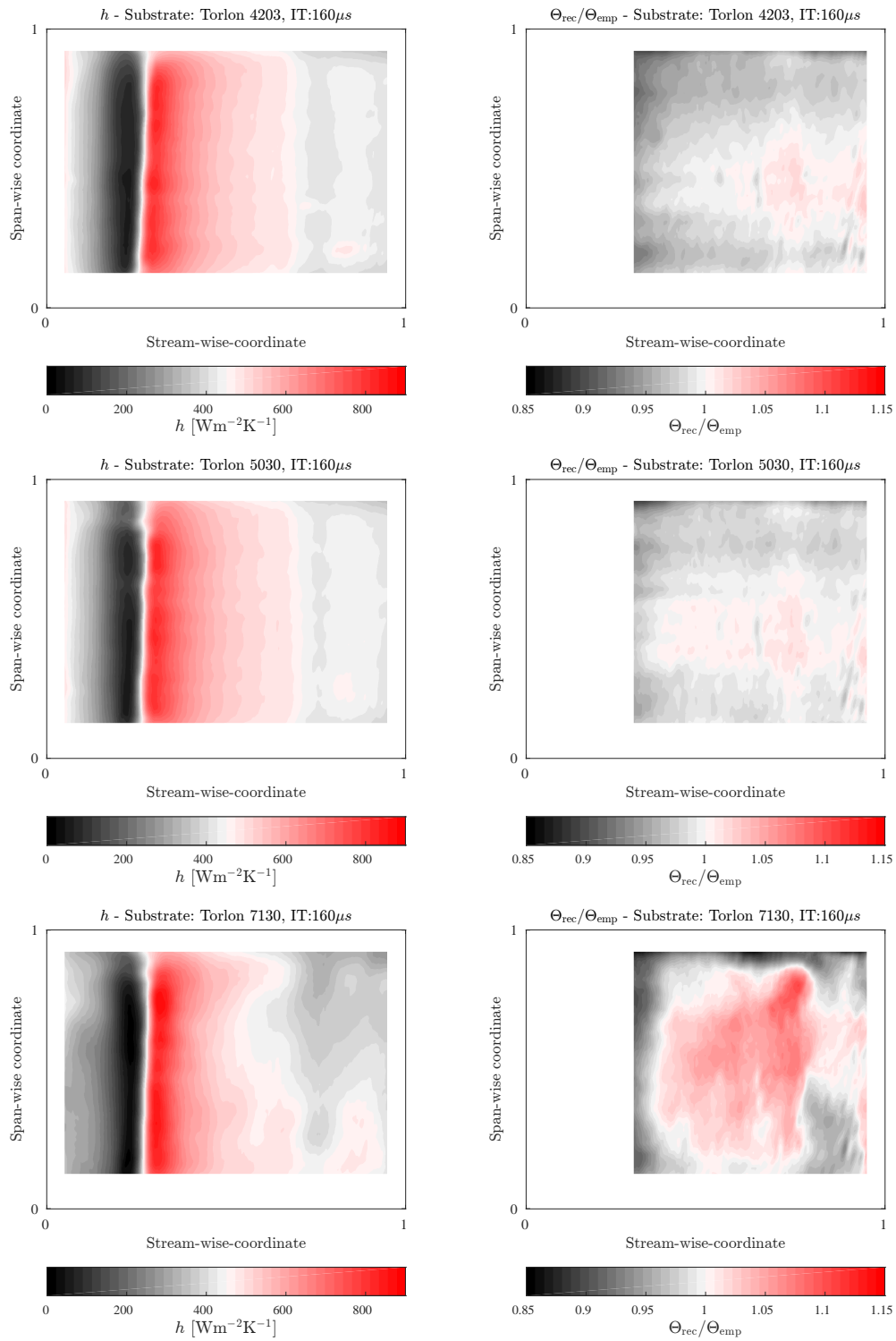


Fig. 7.35 Measurements of h and Θ_{rec} on the uncooled vane with 160 μ s integration time

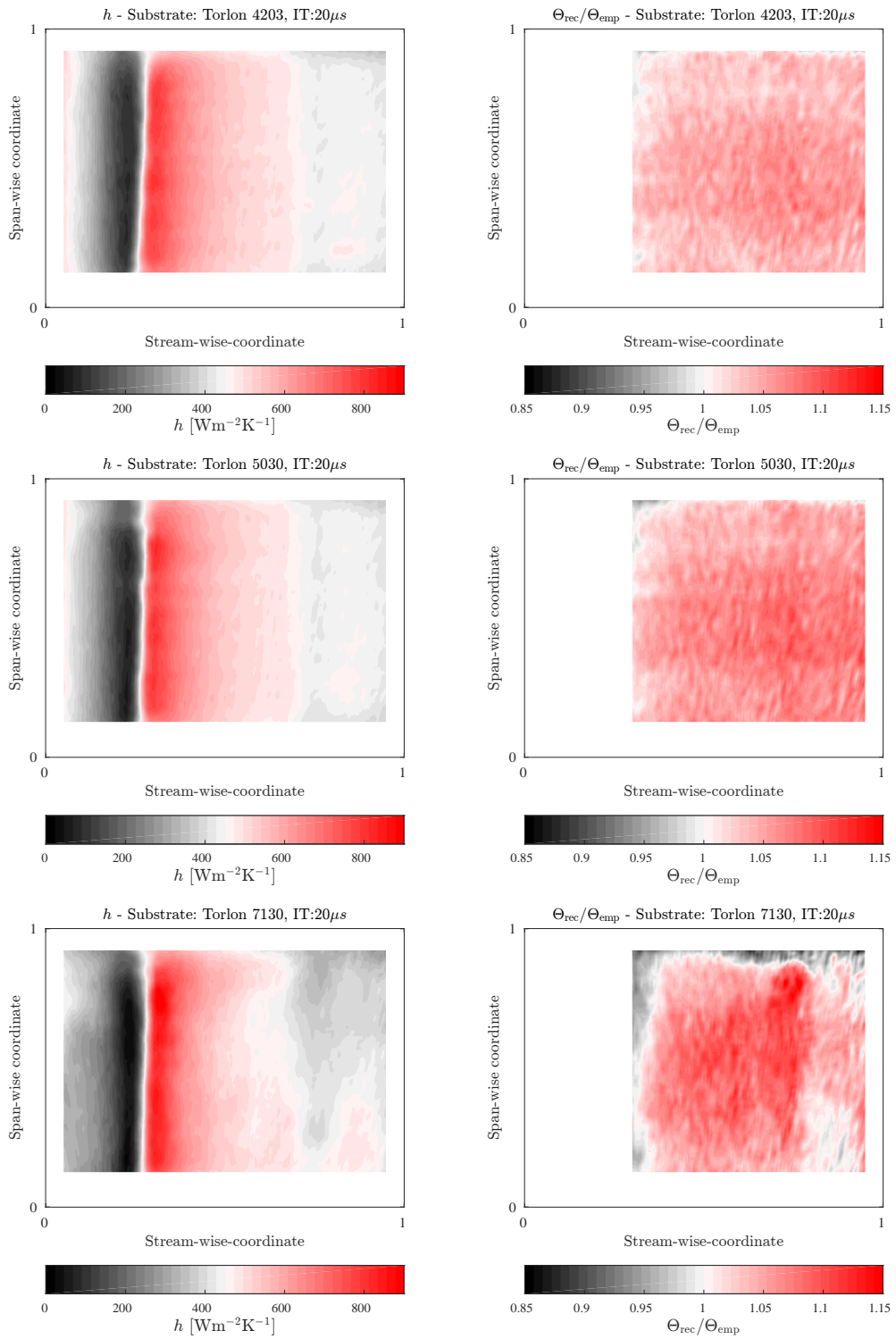


Fig. 7.36 Measurements of h and Θ_{rec} on the uncooled vane with $20\mu\text{s}$ integration time

Figure 7.35 and 7.36 show the solution to h and Θ_{rec} , for each of the three substrate materials, with integration times 160 and 20 μs respectively. Table 7.6 provides a numerical summary of the solutions. The solutions to $\Theta_{\text{rec}}/\Theta_{\text{emp}}$ between the stream-wise coordinates 0 and 0.26 are excluded. The following observations are made from figure 7.35 and 7.36:

- The solutions to h for Torlon 4203 and 5030, and at each integration time are highly correlated, showing a similar trend and limited span-wise variation in value. The increased noise level is clearly visible at the low integration time. The solution to h for the Torlon 7130 vane, shows a similar distribution, but with a noticeable span-wise variation in its value. The span-wise variation pattern seen in the Torlon 7130 vane is consistently visible in the 160 and 20 μs case. It is believed that this variation is caused by spatial variation in the thermal effusivity of the substrate, introduced in the injection moulding process of the composite.
- A similar pattern is seen in the solutions to $\Theta_{\text{rec}}/\Theta_{\text{emp}}$, where the solutions from the Torlon 4203 and 5030 vanes are similar in spatial distribution and in average value. The solution for the 7130 vane shown significantly more spatial variation in its value, again believed to be caused by variations in material properties. The area average value, however, matched that of the Torlon vane 5030 exactly. The solutions to Θ_{rec} at 20 μs , are all at least 5% higher than those at 160 μs . It is believed that this is caused by a reduced black-body calibration accuracy at the lower integration time.

Table 7.6 Summary of uncooled vane measurement values

Test case	Area average value		Span-wise variation	
	h [$\text{Wm}^{-2}\text{K}^{-1}$]	$\Theta_{\text{rec}}/\Theta_{\text{emp}}$	$(\sigma/x)_h$	$(\sigma/x)_{\Theta_{\text{rec}}}$
Torlon 4203, IT 160 μs	452.3	1.006	4.1%	1.5%
Torlon 5030, IT 160 μs	458.3	1.015	3.7%	1.2%
Torlon 7130, IT 160 μs	429.1	1.027	7.6%	2.8%
Torlon 4203, IT 20 μs	462.9	1.067	4.2%	1.3%
Torlon 5030, IT 20 μs	457.7	1.081	3.7%	1.5%
Torlon 7130, IT 20 μs	439.7	1.071	7.3%	2.9%

In figure 7.37 and 7.38, the stream-wise variations in h and Θ_{rec} , averaged across the span, are shown.

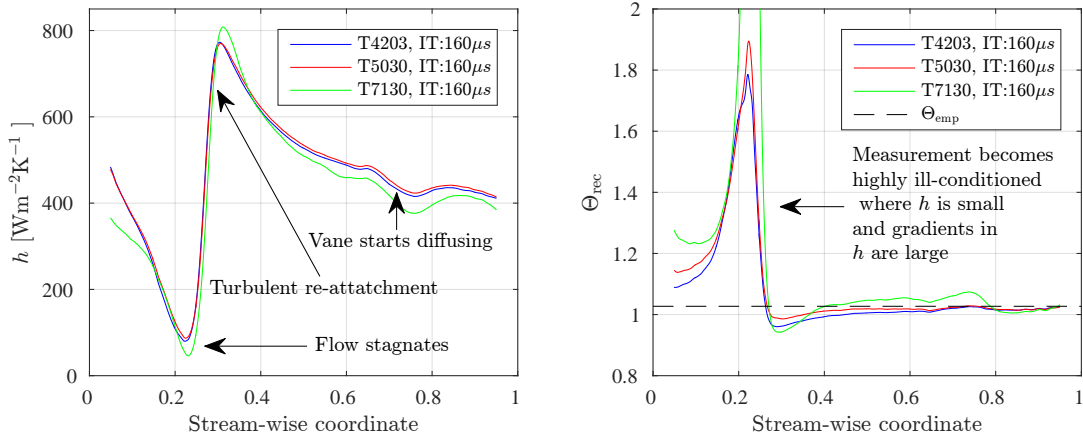


Fig. 7.37 Span-wise average measurements of h and Θ_{rec} for the uncooled vane at $160\mu\text{s}$

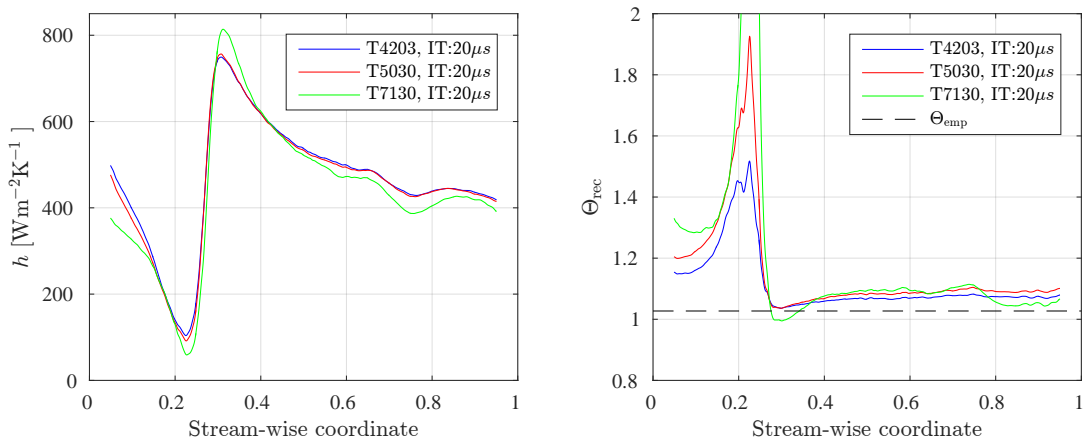


Fig. 7.38 Span-wise average measurements of h and Θ_{rec} for the uncooled vane at $20\mu\text{s}$

7.5.7 Key observations

- Large measurement errors in Θ_{rec} were observed at the leading edge of the un-cooled 3D vane, of approximately 20%. This was caused by a complex interaction of three mechanisms: 1) Surface curvature introduced errors in the 1D semi-infinite modelling assumption, introducing errors in the derived heat flux, 2) Significant lateral heat flux terms, induced by high gradients in surface boundary conditions, 3) Low Biot numbers in the laminar separation bubble region resulted in low surface heat flux. This caused

the measurements in this region to be highly sensitive to lateral heat flux terms caused by the non-uniform boundary conditions upstream - resulting in large measurement errors in Θ_{rec} - which is consistent with the principles established in Chapter 3.

- Heat transfer measurements were performed on three vanes, from differing substrate materials: two of them were fabricated from billet material, (Torlon 4203 and 5030), and the third was fabricated by injection moulding of Torlon 7130 on a titanium root section (Matching the FACTOR fabrication process). The billet materials produced highly consistent results in the measurements of h (1.2% average difference) and $\Theta_{\text{rec}}/\Theta_{\text{emp}}$ (1.1 % average difference), with a high degree of uniformity across the span. The injection moulded vane, however, produced measurements with clearly distinguishable and repeatable a-symmetry across the span. It is proposed that this is caused by non-uniform substrate material properties introduced by the injection moulding process, owing to the repeatability of the spatial pattern. The span-wise standard deviation in the measured solutions to h and $\Theta_{\text{rec}}/\Theta_{\text{emp}}$ were approximately twice as high with the injection moulded vane, compared to the billet vanes, with a 2σ variation of $\sim 14.8\%$ and 5.7% respectively.

7.6 3D Vane Rig Experiments: With film-cooling

In this section, heat transfer measurements performed on the cooled 3D vane, described in section 6.2.2, are presented. Measurements were performed over a range of non-dimensional film-coolant mass flow rates, which ranged from zero flow, to values larger than that which is commonly found in gas turbine engines. On the FACTOR rig, only the NGV is film-cooled, hence measurements were only performed on a Torlon 5030 substrate, and at an integration time of $160\mu\text{s}$, matching the FACTOR parameters.

7.6.1 Cooled vane measurement conditions

The values of the rig, data acquisition, and data processing variables which were used to perform the measurements on the cooled vane, are given in table 7.7. The film-coolant mass flow rates, velocity ratio, blowing ratio and momentum flux ratio, for each measurement, are given in table 7.8.

Table 7.7 Cooled 3D vane measurement conditions

Parameter	Setting
Mainstream conditions	
Mainstream temperature step - ΔT_∞	36 [K]
Temperature step time constant - τ	0.07 [s]
Substrate	
Substrate material	Torlon 5030
Substrate initial condition, T_i	Steady-state
IR camera	
IR camera integration time	160 [μ s]
IR camera acquisition rate	200 [frames/s]
Span-wise optical resolution	~ 0.305 [mm/pixel]
Stream-wise optical resolution	~ 0.49 [mm/pixel]
3D vane stream-wise length	49.7 [mm]
Optical axis angle from surface normal	60°
Data processing	
Heat flux processing method	3D Finite difference
Linear regression delay period	6 τ
Floating linear regression	Applied
Heat penetration depth limit	2 [mm]
Semi-infinite criterion	$1/\sqrt{Fo_{\text{limit}}} = 2$

Table 7.8 List of coolant flow rates and key non-dimensional values

Mass flow [kg/s]	Velocity ratio $v_{\text{coolant}}/v_{\infty}$	Blowing ratio $M = \frac{(\rho v)_{\text{coolant}}}{(\rho v)_{\infty}}$	Momentum flux ratio $I = \frac{(\rho v^2)_{\text{coolant}}}{(\rho v^2)_{\infty}}$
0	0.00	0.00	0.00
2.0×10^{-3}	0.49	0.55	0.27
3.0×10^{-3}	0.75	0.84	0.63
4.2×10^{-3}	1.03	1.15	1.19
5.0×10^{-3}	1.25	1.4	1.74
6.1×10^{-3}	1.50	1.69	2.55

7.6.2 Valid data region

In figure 7.39, the region of valid measurement data on the cooled 3D vane, is highlighted by two dashed boxes.

In addition to the data exclusion region specified in section 7.5.4, data is also excluded where it coincides with the location of a film-cooling hole array. The absence of thermal mass in these regions causes by the holes, invalidates the semi-infinite assumption. A data exclusion region, extending 1.5δ in all directions from the film-cooling hole array is applied.

Note that due to the high levels of turbulence introduced by the first array of film-cooling holes, near the leading edge, a laminar separation bubble at stream-wise coordinate 0.2 is not present, as was found on the un-cooled vane. Consequently, measurements are well conditioned throughout the valid data region.

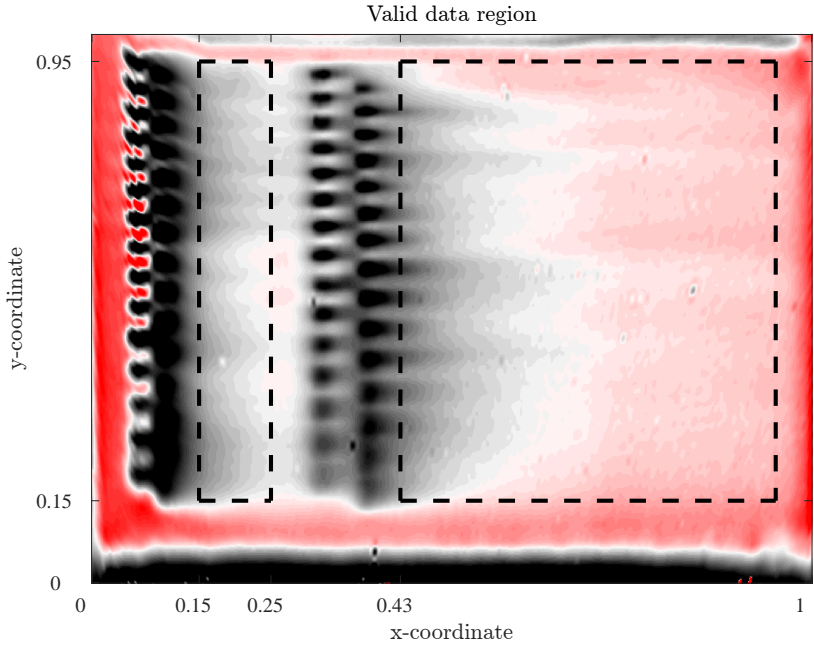


Fig. 7.39 Specification of valid and invalid regions of measurement data on the cooled vane

7.6.3 Film-cooled vane results

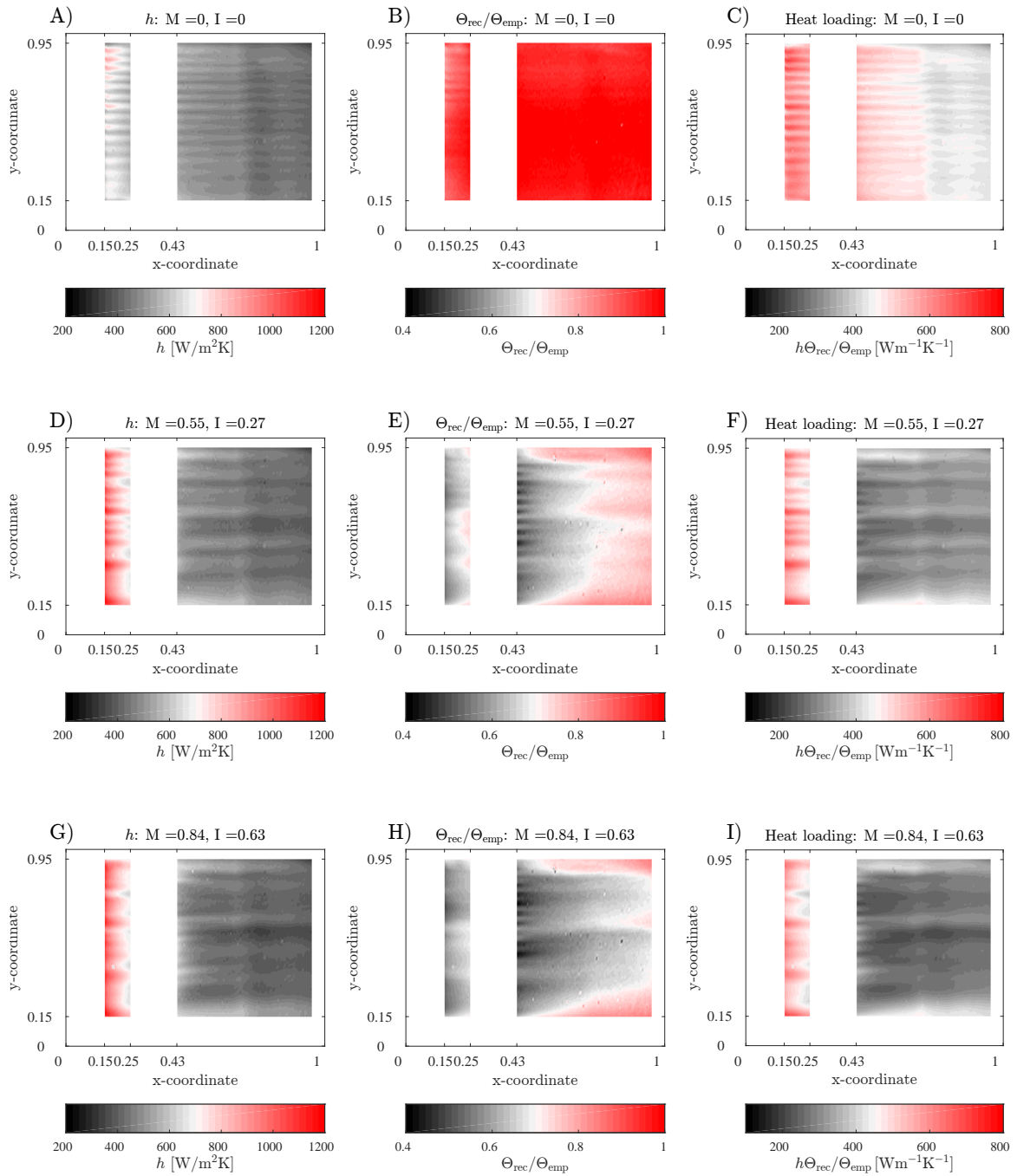


Fig. 7.40 Measurements of h and Θ_{rec} and Heat loading on the cooled vane, at three different film-coolant flow rates

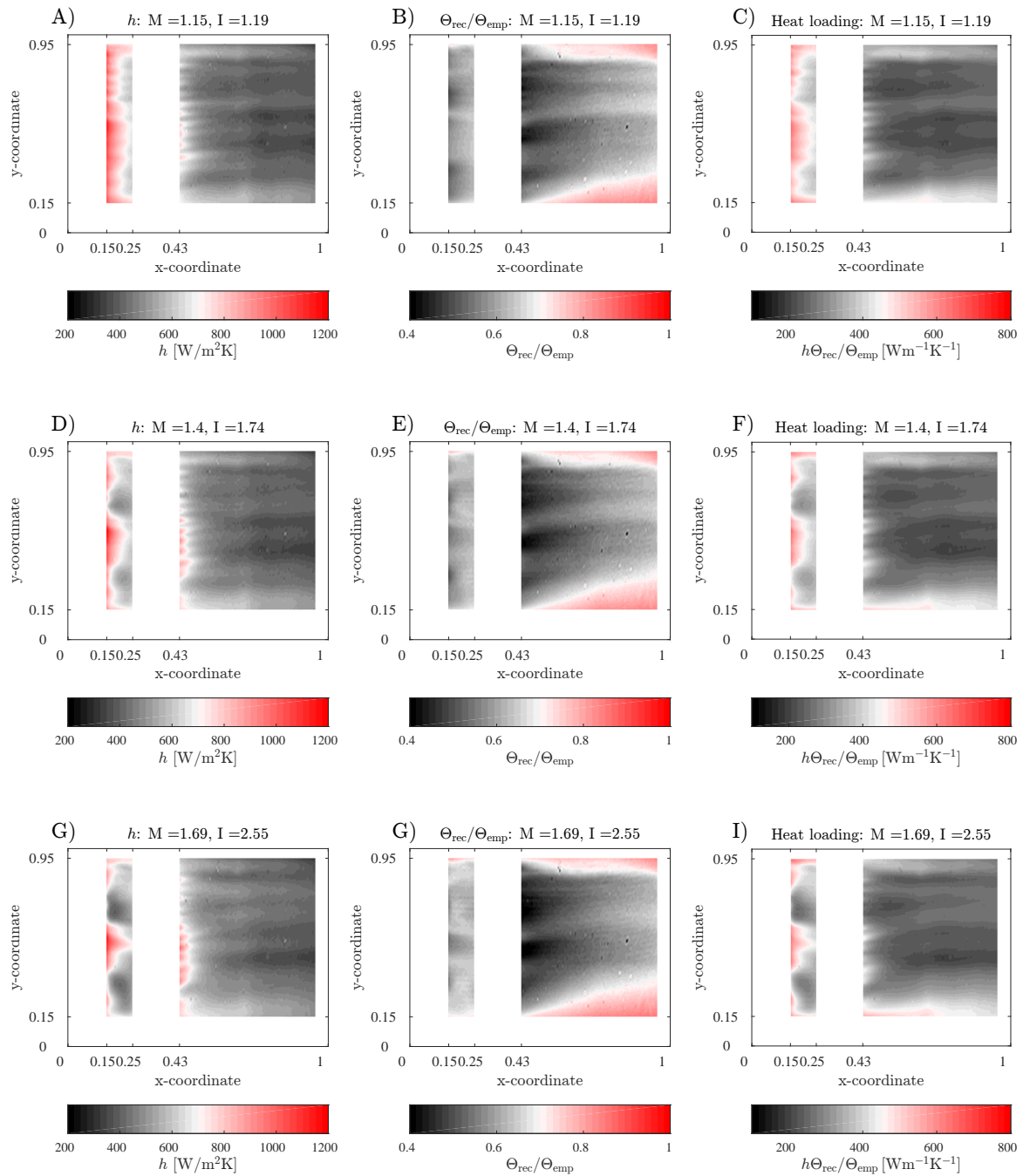


Fig. 7.41 Measurements of h and Θ_{rec} and Heat loading on the cooled vane, at three different film-coolant flow rates

In figure 7.40 and 7.41, the solutions to h and $\Theta_{\text{rec}}/\Theta_{\text{emp}}$ are shown for each film-coolant flow rate. A ‘Heat Loading’ value is also shown, which is given as $h\Theta_{\text{rec}}/\Theta_{\text{emp}}$, and represents the heat flux per unit non-dimensional temperature difference between the wall

temperature and mainstream temperature. It therefore provides a measure of the local heat absorption rate which would be established at steady state conditions.

Observations and analysis are now made from the measurements in figure 7.40 and 7.41.

- For no coolant flow measurement ($M=0$), the measurements of h and $\Theta_{\text{rec}}/\Theta_{\text{emp}}$ have a distribution which is relatively uniform across the span. A slightly reduced value of $\Theta_{\text{rec}}/\Theta_{\text{emp}}$ can be seen between the stream-wise coordinates 0.15 and 0.25. It is believed that this is caused by a recirculating flow between the first pair of rows and second pair of rows of film-cooling holes. The static pressure, at the exit of the first pair of rows is expected to be lower than that of the second pair of rows, due to the higher mainstream stream velocities at the leading edge. The pressure difference drives a small quantity of mainstream flow into the film-coolant cavity, via the second pair of rows, and subsequently out of the first pair of rows. In transit through the cooling holes and coolant cavity, the temperature of the flow is reduced by heat exchange. On exit from the first pair of rows, the cooled fluid results in a decreased value of $\Theta_{\text{rec}}/\Theta_{\text{emp}}$, downstream of the holes.
- As M is increased from zero to 0.55, a significant increase in h at the leading edge is seen. Some evidence of inconsistent coolant jet behaviour can be seen by the non-periodic stream-wise pattern in h and $\Theta_{\text{rec}}/\Theta_{\text{emp}}$. This appears to be caused by a small number of jets separating from the gas washed surface. The value of Θ_{rec} is at a minimum immediately downstream of each pair of film-cooling hole rows, and can be seen to rise in value with increasing stream-wise distance.
- As M is increased further, from 0.55 to 1.69, the following trends are visible:
 - The value of h , between the stream-wise coordinates 0.15 and 0.2, decreases with increasing M , and an increasing non-uniform distribution across the span is visible. Between the stream-wise coordinates 0.43 and 0.95, the value of h does not appear to vary significantly with M , however span-wise non-uniformity is increased.
 - As M is increased, the area average value of $\Theta_{\text{rec}}/\Theta_{\text{emp}}$ increases. The value of $\Theta_{\text{rec}}/\Theta_{\text{emp}}$ is significantly lower immediately downstream of the second pair pair of film-cooling hole rows, in comparison to the first pair, under all M . As M is increased, the evidence of two poorly cooled regions, at high and low span-wise locations becomes increasingly apparent. The regions increase in span-wise extent with increasing stream-wise distance. This is likely caused

two counter-rotating horse-shoe vortices entraining high temperature mainstream fluid.

In figure 7.42, the span-wise averaged solutions to h are shown. Span wise averaging was performed between the span-wise coordinates 0.15 and 0.95.

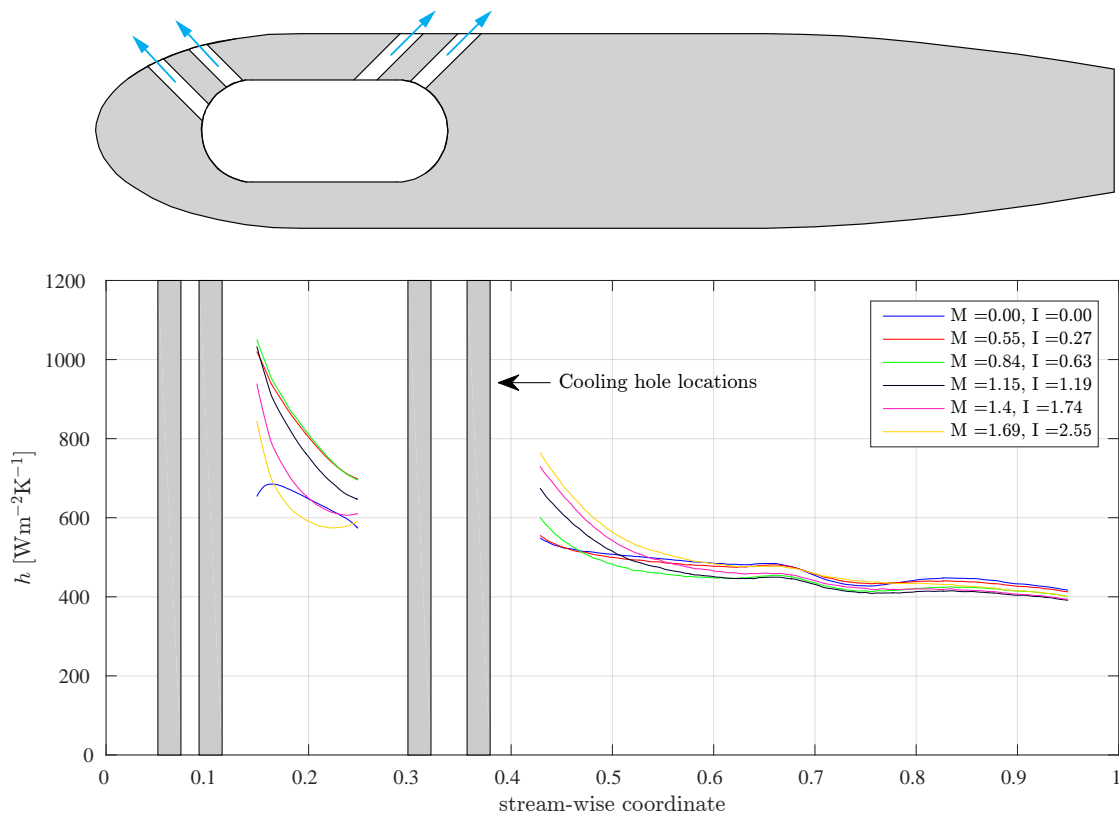


Fig. 7.42 Span-wise average measurements of h for each of the coolant flow rates

From figure 7.42, the following observations and analysis are made:

- As M is increased from zero to 0.55, a significant increase in h is seen between the span-wise coordinates 0.15 and 0.25. However, between the coordinates 0.43 and 0.95, a slight decrease is seen. The hole axis of first pair of film-cooling hole rows, are oriented approximately perpendicular to the blade surface - it is expected that the film-coolant jets will consequently introduce significant turbulence into the flow field - which is consistent with the large increase in h observed immediately downstream. The hole axis of the second pair of film-cooling hole rows, however, are oriented at 45 degrees to the blades surface, such the film-coolant jets have a significant proportion of their momentum in the mainstream flow direction, and consequently will introduce

a lower level of turbulence. A greater proportion of the coolant mass flow will also exit from the first pair of film-cooling hole rows, due to the greater pressure difference between the coolant plenum and mainstream pressure, exacerbating this effect.

- As M is increased from 0.55 to 1.69, the value of h decreases between the coordinates 0.15 and 0.25, and increases downstream of the second pair of film-cooling hole rows. It is believed that the decrease in h , downstream of the first pair of rows, is caused by a decreasing shear stress in the boundary layer, caused by the addition of film-coolant with significant momentum in a direction opposed to the mainstream flow, reducing the overall momentum in the boundary layer. The converse is true with the second pair of film-cooling hole rows, where the film-cooling flow serves to increase the momentum in the boundary layer - increasing shear stress and h . With increasing stream-wise distance, the variation between the solutions subsides, which is consistent with the mixing out of the high momentum film-cooling jets.
- At high stream-wise coordinates ($\sim 0.85 - 0.95$) a reversal of the trend is seen, where a high M leads to a slight reduction in h . It is suggested that this is partly caused by the reduction in the thermal conductivity of air, with decreasing temperature. The adiabatic temperature difference, at stream-wise coordinate 0.95, between the $M = 0$ and $M = 1.54$ case, is equal to $\Delta T_{\infty}(\Theta_{\text{rec},M(0)} - \Theta_{\text{rec},M(1.54)}) \approx 12.6K$. This relates to a decrease in thermal conductivity, and consequently a decrease in h , of $\sim 3\%$,

In figure 7.43, the span-wise averaged solutions to η (i.e. $1 - \Theta_{\text{rec}}$) are shown. Span wise averaging was performed between the span-wise coordinates 0.15 and 0.95.

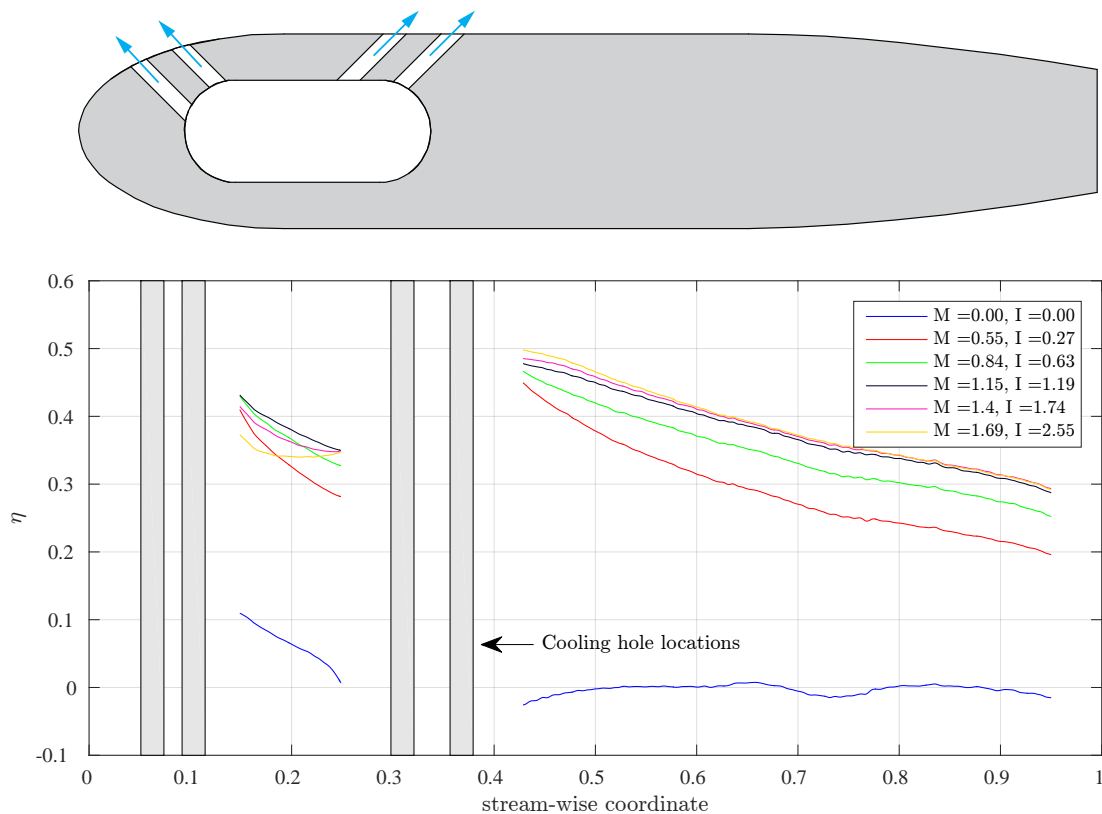


Fig. 7.43 Span-wise average measurements of Θ_{rec} for each of the coolant flow rates

From figure 7.43, the following observations and analysis are made:

- For the zero M case, a η value of 0.12 is measured at a stream-wise coordinate of 0.15. This is thought to be caused by the recirculating cooling effect described earlier. The value then reduces to ~ 0 at a stream-wise coordinate of 0.25, which is consistent with the coolant jets mixing out. Between the stream-wise coordinates 0.43 and 0.95, the stream-wise mean value of η is 0.03.
- For the M equals 0.55 case, between the stream-wise coordinates 0.15 and 0.25, the value of η decreases with increasing stream-wise distance. This is consistent with the mixing out of the film-cooling jets. As M is increased, the rate of decline of η with stream-wise distance decreases, and even reverses for the M equals 1.69 case. It is thought that this trend is caused by the increasing dominance of inertial effects: The large momentum introduced by the film-cooling flow, approximately perpendicular to the blade surface, and partially in a direction opposed to the free stream momentum, causes a highly non-uniform, three dimensional flow field. This is indicated by the

solutions to h in figures 7.40 and 7.41, where large variations across the span, and a significant reduction in the average value is seen.

- Between the stream-wise coordinates 0.43 and 0.95, an approximately uniform stream-wise increase in η is seen with increasing M . The value of η decreases with stream-wise distance, which is consistent with the mixing out the coolant film.

7.6.4 Key observations

- Measurements were performed on the film-cooled 3D vane, at conditions closely representative of the FACTOR NGV conditions. The cooled vane measurements were significantly better conditioned than that of the uncooled vane, despite the lower value of $\Delta T_{0,\infty}$. The reason for the improvement in the measurements was due to the increased level of turbulence, leading to a suppression of the laminar separation bubble, which lead to an increase in the Biot number.
- The trends in the measured solutions to h and Θ_{rec} , as a function of blowing ratio, correlated well with fluid dynamic theory.

Chapter 8

Conclusions & Future Work

8.1 Conclusions

- In the Literature Review it was found that a large body of work exists on heat transfer measurement techniques that can be used to measure heat transfer coefficients and adiabatic wall temperatures. It was found that most of these techniques were applied to turbine test rigs which did not have the full complexity of engine-scale turbine rigs. Features such as film-cooling flows, high temperatures mainstream flows with matched Mach and Reynolds numbers, high-speed rotating components and engine representative combustor inlet profiles were rarely found.
- In the Theory section, it was shown that the addition of some of these engine-representative rig features could lead to significant heat transfer measurement errors if some of the techniques and instrumentation described in the literature were used. The three most influential rig features are described below, along with the solutions developed in this work to address them:

1. Small scale vanes and blades

Small scale vanes and blades tend to lead to a more 3D transient conduction field, rather than a 1D field, during the transient measurement. Engine-scale turbine rigs will typically have engine length scale geometry. This relatively small scale gives rise to a number of problems in transient heat transfer measurement techniques. Most notably, the need to achieve a large transient surface temperature response, whilst being able to make valid modelling assumptions about the three-dimensional heat conduction within the blade. It was shown that under some circumstances, a reduction in the geometric length scale of the test geometry by 20%, could lead to an increase in

the measurement error by two orders of magnitude. To address this problem, a new definition of the semi-infinite measurement period over which a transient measurement should be performed was determined. This new definition better balanced the error contributions from competing mechanisms, and permitted measurements on geometry half the geometric length scale, for a given measurement uncertainty.

2.Non-adiabatic initial conditions

Many of the transient measurement techniques in the literature depend on the assumption that initial conditions on the measurement surface are adiabatic. This will likely not be the case on engine-scale turbine rigs, and indeed is not the case on the FACTOR rig. A new method which enabled a meaningful non-dimensional adiabatic wall temperature to be defined, in the presence of non-adiabatic initial conditions, was determined and presented.

2.High mechanical stresses and temperatures

On account of the high temperatures and high rotor tip speeds (leading to high mechanical stresses), a number of otherwise ideal measurement instruments and substrate materials cannot be used. This can lead to increases in measurement uncertainty. To alleviate this affect, a new kind of composite rotor blade construction was developed and tested in this project for use in the FACTOR rig, which combined high mechanical integrity with the appropriate substrate material properties required to enable low uncertainty heat transfer measurements. New advanced materials and manufacturing processes were used.

- In the Theory section, it was found that an optimum substrate material thermal conductivity exists for all transient measurement techniques, which minimised measurement uncertainty. It was shown that an analytical calculation can be used to determine the optimum, as a function of the measurement condition. Substrate materials were selected to match this optimum as closely as possible, whilst satisfying other constrains.
- In both the Theory and Uncertainty Modelling sections, relationships between measurement variables and overall measurement uncertainty were established. It was found that overall measurement uncertainty can be highly sensitive, and non-linearly dependant, on a number of rig specific variables. It was found that a Monte-Carlo approach to modelling the non-linear sensitivities was an effective means of predicting measurement uncertainty, which served as a useful tool in the rig design process.

- In the Methods chapter a range of tools and techniques were developed and presented. A new time-dependant calibration method was developed for use with IR thermography, which reduced adiabatic wall temperature measurement uncertainty by $\sim 5\%$. A time-resolved three-dimensional heat flux modelling tool was also developed, which enabled an increase in the heat transfer measurement resolution, when compared to one-dimensional methods, allowing surface boundary condition features with length scales lower than the heat penetration depth to be resolved. It was shown that this could lead to a reduction in local measurement error, when compared to one-dimensional methods, by as much as 40%. A new method of thermal effusivity measurement was also developed, tested and used on the FACTOR vanes and blades. The method was able to provide non-destructive spatially resolved measurements of effusivity on the FACTOR test blades and vanes.
- In the Results chapter a series of experiments were performed, designed to test and verify the principles established in the Theory and Uncertainty modelling chapters. The key conclusions are as follows:
 1. It was shown that small-scale film-cooling flows, with engine scale geometry could be resolved in detail. The benefits of using 3D heat-flux modelling to resolve these fine details was shown to be significant when when the length scale of the boundary condition features were comparable to, or less than, the heat penetration depth.
 2. It was found that in some circumstances, the measurement uncertainty could grow to a very large value. This was found in regions with low shear stress (for example; around the stagnation lines of laminar separation bubbles), and in regions of high surface curvature, where the Biot number based on radius of curvature was below 40. It was also found that regions with low heat transfer coefficients became highly sensitive to heat flux modelling errors caused by 3D geometric features, such as the high curvature of the leading edge of a vane.
 3. It was found that the Monte-Carlo uncertainty model in Chapter 4 was able to accurately predict these errors.

8.2 Future Work

In this section further research tasks are identified which are required, or are otherwise beneficial for using the heat transfer measurement technique developed in this thesis, on the FACTOR rig.

8.2.1 Transient radiance corrections on the FACTOR rig

In the heat transfer measurements results presented in Chapter 7, a time-resolve radiance offset calibration procedure was used to correct the IR camera readings. The method was described in section 6.3.4. The method depended on measuring the time varying radiance signal, emitted by the IR window, and subtracting it from the total IR camera radiance measurement, so as to remove the transient influence of the window. The measurement of this signal was enabled by the inclusion of an embedded black-body within the test section wind-tunnel. It was shown in section 7.2.3 that omitting the transient component of the calibration would have a negligible effect on the measurement of h , but $\sim 5\%$ effect on the measurement of Θ_{rec} .

On the FACTOR rig, there is no embedded black-body calibrator, and as such this measurement cannot be performed. Instead, a different method of transient radiance calibration must be performed. An altered method is proposed here, but was not tested experimentally:

It was shown in section 7.2.3 that the transient component of the radiance correction lead to the removal of a measurement error in Θ_{wall} with an asymptote value of approximately 5% (see figure 7.11). It was found that the subsequent measurement error in Θ_{rec} was correspondingly equal to appropriately 5% - which stands to reason. It is expected that this 5% value is strongly correlated to a combination of the thermal effusivity and absorptivity of the IR window - which will be unchanging.

A different method of accounting for the transient radiance error could then be as follows:

1. Radiance measurements are taken of the test surface through the window at two steady state rig conditions; one with the heater mesh on, and one with it off.
2. The steady state radiance error at each steady state condition is then calculated, by comparing the measured radiance against the ideal black-body radiance based on the in-situ thermocouple readings, which are embedded in the test surface.
3. The difference between these two steady state radiance errors is then equal to the total transient error component.

4. ΔL_{CAM}^* measurements can then be modified accordingly (i.e. a subtraction) with this time-constant correction.

Despite no longer being time-resolved, this method of calibration has an additional benefit, when compared to the embedded black-body method, in that the transient component of diffuse reflections will also be accounted for in the process. As was stated in section 6.3.4, these error sources were not measured and removed in the measurements in this thesis - although their magnitude was expected to be small.

8.2.2 Specular transient reflection errors on the FACTOR rig

It was identified in section 6.3.4 that the in-situ calibration method which has been developed in this thesis, does not correct for the *transient* component for radiance sources which are reflected off the measurement surface. For example, when measuring on the blade surface of the FACTOR rig NGV, a component of the transient radiance signal will come from, for instance, the hub. The magnitude of this transient reflection will scale with $1 - \varepsilon$ (where ε is the emissivity of the black paint on the NGVs). No method was proposed for correcting for this error source.

It has just been described in section 8.2.1 that a transient radiance correction method can be used on the FACTOR rig, which will account for both the transient effect of the window, and also the transient effect of *diffuse* reflections. (Only diffuse reflections are accounted for, as the surface mounted thermocouples will not be sufficient in number to provide meaningful spatial resolution). Specular reflections, which will vary in space, are still not accounted for.

In figure 8.1 an analytical evaluation of the expected magnitude of the specular reflection error source is provided, in order to bound the magnitude of the error. In figure 8.1 (top left), an analytical solution to the transient wall temperature of two surfaces are provided; the NGV and the Hub. It is assumed that the film-cooling effectiveness of the NGV and Hub are 0.6 and 0 respectively - representing a likely worst case scenario, with the greatest relative magnitude of the transient reflection signal.

The radiance emitted from each surface, as a function of the surface temperature over time is then calculated, using Plank's Law, and shown in figure 8.1 (top right). The absolute temperatures of the FACTOR mainstream, film-cooling air and mainstream temperature step are used in the calculation. The signal which the IR camera would record from the surface of the NGV is shown as L_{CAM} - whose signal comprises a component of both the NGV and hub radiance. An emissivity of 0.94 specified, which matches that of the paint used in the FACTOR rig.

In figure 8.1 (bottom left), the transient wall temperature, based on L_{CAM} is shown, alongside the actual transient wall temperature of the NGV. It can be seen that Θ_{CAM} over predicts the wall temperature.

Finally, in figure 8.1 (bottom right), the error in the measurement of transient wall temperature is shown, which is equal to $\Theta_{CAM} - \Theta_{NGV}$. The magnitude of the error is shown as a function of the local film-cooling effectiveness on the NGV. It is expected that the highest level of film-cooling effectiveness will be ~ 0.6 , which leads to a Θ_{wall} error of $\sim 5\%$. At lower film-cooling effectivenesses, which is representative of the majority of the NGV surface, the error is lower.

It is suggested that a method to remove this error sources could be developed in future work - perhaps through a different calibration procedure, or through the use of surface coatings with higher emissivity.

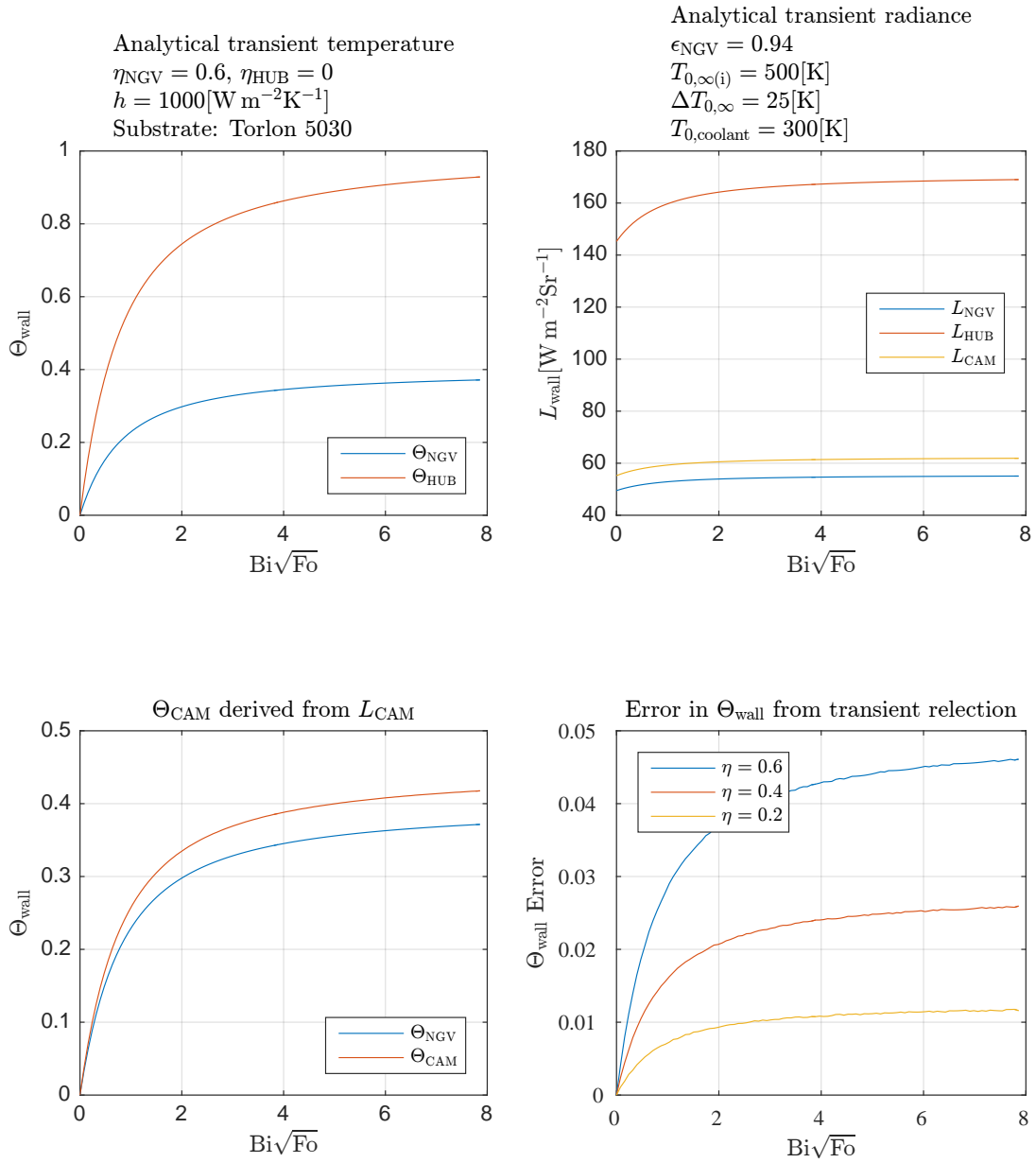


Fig. 8.1 Analytical thought experiment - illustrating the magnitude of Θ_{wall} measurement errors as a function of η and ϵ

8.2.3 FACTOR IR window lensing effects

In all of the heat transfer measurement performed in this work, a flat IR window was used. In the FACTOR rig, the window is plano-concave, and consequently behave as a lens. This will lead to two effects: Firstly, a spatial distortion will occur in the image as a result, secondly, and more problematically, the radiance intensity received at the IR camera detector will be modified. If unaccounted for, this will lead errors in the temperature measurement.

The IR camera lens which is to be used in the FACTOR project has a focal length of 12 [mm]. The the HP window on the FACTOR project will have a focal length of -205 [mm], as shown by equation 8.1, where \hat{f} is the focal length, r_1 and r_2 are the radius of curvature of the first and second lens surfaces, n is the refractive index of the lens material and d is the thickness of the lens.

$$\frac{1}{\hat{f}} = (n - 1) \left(\frac{1}{r_1} - \frac{1}{r_2} + \frac{(n - 1)d}{nr_1r_2} \right) \quad (8.1)$$

For the FACTOR rig, R_2 is infinite, and thus the equation simplifies to the following, where the focal length is negative on account of the concave curvature of the first surface (the refractive index of Zinc Sulphide is specified as 2.22):

$$\hat{f} = \frac{r_1}{n - 1} = \frac{0.25}{2.22 - 1} = -0.205\text{m} \quad (8.2)$$

The focal length of the combined optical system is then given as follows;

$$\frac{1}{\hat{f}_{\text{CAM+WIN}}} = \frac{1}{\hat{f}_{\text{CAM}}} + \frac{1}{\hat{f}_{\text{WIN}}} = \frac{1}{0.0127[\text{m}]} \quad (8.3)$$

$$\frac{1}{\hat{f}} = \frac{1}{u} + \frac{1}{v} \quad (8.4)$$

Using the expression in equation 8.4, (where u is the distance from the object to the lens, (i.e. the focal distance), and v is the distance from the lens to the detector) it can then be deduced that the focal distance of the combined optical system is increased by 6.2% (equivalent to ‘zooming out’ by 6.2%). Note that this change in focal distance only occurs in one optical plane, as the IR window is not rotationally symmetric. It can be shown that this will lead to a 6.2% reduction in radiance received at the IR camera.

The transmissivity of the FACTOR IR window, which is effectively a ‘gain’ value, slightly below 1, will need to be measured using the method described in section 6.3.4. The gain

introduced by the lensing effect will be 1.062. These two gain values can be measured together as one combined gain value.

Since the FACTOR IR windows are still in manufacture at the time of writing, this calibration could not be performed.

8.2.4 Heat transfer measurements on vane and blade leading edges

In section 3.6.3, it was shown that errors in heat-flux modelling methods which neglect to model surface curvature will be kept below 1% provided the Biot number based on the radius of curvature is kept above 40. This will be the case for majority of the surfaces on the FACTOR vanes and blades, but will not be the case at the leading edge of the NGV, Rotor blade and LP vane. In order to accurately measure heat transfer in these regions, the curvature must be accounted for in the heat-flux modelling. Development of a surface curvature corrected heat-flux model was considered beyond the scope of this project, but is recommended by the author as a valuable development of the method.

Nomenclature

Roman Symbols

\dot{q}	Heat flux [W m^{-2}]
\hat{f}	Focal length [m]
\hat{r}	Recover factor
Bi_r	Biot number number (based on radius of curvature)
A	Area [m^2]
B	Bias uncertainty
c	Specific heat capacity [$\text{J kg}^{-1}\text{K}^{-1}$]
c^*	The speed of light in a vacuum [m s^{-1}]
e	Thermal effusivity [$\text{J m}^{-2}\text{K}^{-1}\text{s}^{-1/2}$]
f	Frequency [s^{-1}]
h	Heat transfer coefficient [$\text{W m}^{-2}\text{K}^{-1}$]
h^*	Plank's constant [$\text{m}^2 \text{kg s}^{-1}$]
I	Momentum flux ratio
k	Boltzmann constant [$\text{m}^2 \text{kg s}^{-2}\text{K}^{-1}$]
L	Emitted spectral radiance [$\text{W Sr}^{-1}\text{m}^{-2}$]
L^*	Transmitted spectral radiance [$\text{W Sr}^{-1}\text{m}^{-2}$]
M	Blowing ratio

P Precision uncertainty ($\pm 2\sigma$)

Q^* Non-dimensional Heat flux

R Reflectivity

r Radius [m]

T Temperature [K]

t Time [s]

U Uncertainty

V Volume [m³]

x Distance [m]

Bi Biot number

Fo Fourier number

Ma Mach number

Nu Nusselt number

Pe Peclet number

Pr Prandtl number

Re Reynolds number

St Stanton number

Greek Symbols

α Thermal diffusivity [m²s⁻¹]

β Non-dimensional transient conduction term ($\beta = Bi\sqrt{Fo}$)

δ Heat penetration depth [m]

ε Emissivity

η Film-cooling effectiveness

γ	Heat capacity ratio
κ	Thermal conductivity [$\text{W m}^{-1}\text{K}^{-1}$]
λ	Wavelength [m]
π	3.14159...
ρ	Mass density [kg m^{-3}]
σ	Standard deviation
τ	Transmissivity
τ_{∞}	Mainstream temperature rise time constant [s]
Θ	Non-dimensional transient temperature
θ	Angle from surface normal [degrees]
Θ_{limit}	Non-dimensional wall temperature at the semi-infinite limit
Θ_{rec}	Non-dimensional recovery temperature
Θ_{R}	Non-dimensional wall temperature change over linear regression period
$\tilde{\Theta}$	Non-dimensional wall temperature change - during unsteady mainstream temperature period

Subscripts

∞	Conditions in the mainstream
0	Stagnation condition
amb	Ambient
at.ext	External atmosphere
at.int	Internal atmosphere
aw	Adiabatic wall
bb	Black body

bp Black paint

CAM IR camera

conv Convection

coolant Film-coolant conditions

emp Empirical

end At infinite time

HM Heater mesh

i Initial

IR Infra-red

limit At the semi-infinite limit

obj Object

rec Recovery

steady Steady state component

TC Thermocouple

transient Component which varies in time

vbb Virtual black body

wall Wall

win IR Window

Acronyms / Abbreviations

CFD Computational fluid dynamics

CLTE Coefficient of linear thermal expansion

DLR Deutsches Zentrum für Luft- und Raumfahrt (The German Aerospace Center)

DNS Direct Numerical simulation

erfc	Complimentary error function
exp	Exponential
FEA	Finite element analysis
HP	High pressure
HTC	Heat transfer coefficient
IR	Infra-red
LES	Large eddie simulation
LP	Low pressure
LWIR	Long wave infra-red
LWIR	Long-wave Infra-red
MC	Monte-Carlo
MWIR	Medium wave infra-red
NET	Noise Equivalent Temperature
NGV	Nozzle guide vane
NGVs	Nozzle Guide Vanes
PRT	Platinum Resistance Thermometer
RANS	Reynolds average Navier-Stokes
RPM	Revolutions per minute
SFC	Specific Fuel Consumption [$\text{g s}^{-1}\text{kN}^{-1}$]
TET	Turbine entry temperature
TFG	Thin-film gauge
TLCs	Thermo-chromic liquid crystals
TRL	Technology Readiness Level

URANS Unsteady Reynolds average Navier-Stokes

VKI The Von Karman Institute

References

- Baldauf, S., Schulz, A., and Wittig, S. (1999). High-resolution measurements of local effectiveness from discrete hole film cooling. *Journal of Turbomachinery*, 123(4):758–765.
- Bertolazzi, E., Battisti, L., and Trivellato, F. (2012). Numerical processing of thin-film thermometer data for determining transient heat fluxes. *Applied Mathematical Modelling*, 36(8):3645 – 3662.
- Boyle, R. J., Spuckler, C. M., Lucci, B. L., and Camperchioli, W. P. (2000). Infrared low temperature turbine vane rough surface heat transfer measurements. *Proceedings of ASME Turbo Expo*.
- Buttsworth, D. R. and Jones, T. V. (1997). Radial conduction effects in transient heat transfer experiments. *The Aeronautical Journal*, pages 209–212.
- Camci, C. and Arts, T. (1985). Experimental heat transfer investigation around the film-cooled leading edge of a high-pressure gas turbine rotor blade. *Journal of Engineering for Gas Turbines and Power*, 107(4):1016–1021.
- CES (2017). Granta ces selector. <https://www.grantadesign.com/products/ces/>.
- Chen, W., Jiang, H., and Zhang, Q. (2014). A simple corener correction technique for transient thermal measurement. *Proceedings of ASME Turbo Expo*.
- Clifford, R., Jones, T. V., and Dunne, S. (1980). Techniques for obtaining detailed heat transfer coefficient measurements within gas turbine blade and vane cooling passages. *ASME paper 83-GT-58*.
- Collins, M., Chana, K., and Povey, T. (2015). Improved methodologies for time resolved heat transfer measurements, demonstrated on an unshrouded transonic turbine casing. *Proceedings of ASME Turbo Expo 2015*.
- Cook, W. and Felderman, E. (1966). Reduction of data from thin film heat transfer gauges: a concise numerical technique. *AIAA J.*, 4:561–562.
- D’Ammaro, A. (2016). *Cooling hole geometry and turbulence effects on the early suction side surface of a turbine vane*. PhD thesis, The University of Cambridge, Department of Engineering.
- Didier, F., Dénos, R., and Arts, T. (2002). Unsteady rotor heat transfer in a transonic turbine stage. *Journal of Turbomachinery*, 124(4):614–622.

-
- Doorly, J. and Oldfield, M. L. (1987). The theory of advanced multi-layer thin film heat transfer gauges. *Int. J. Heat Mass Transfer*, 30(6):1159–1168.
- Doorly, J. E. and Oldfield, M. L. G. (1986). New heat transfer gages for use on multilayered substrates. *Journal of Turbomachinery*, 108(1):153–160.
- Du, H., Han, J. C., and Ekkad, S. V. (1998). Effect of unsteady wake on detailed heat transfer coefficient and film effectiveness distributions for a gas turbine blade. *Journal of Turbomachinery*, 120(4):808–817.
- Ekkad, S., Ou, S., and Rivir, R. (2004). A transient infrared thermography method for simultaneous film cooling effectiveness and heat transfer coefficient measurements from a single test. *Journal of Turbomachinery*, 126:597–603.
- Epstein, A., Guenette, G., Norton, R., and Yuzhang, C. (1986). High-frequency response heat-flux gauge. *Review of Scientific Instruments*, 57(5):639–649.
- Giel, P. W., Boyle, R. J., and Bunker, R. S. (2004). Measurements and predictions of heat transfer on rotor blades in a transonic turbine cascade. *Journal of Turbomachinery*, 126(1):110–121.
- Gillespie, D. (1996). *Intricate internal cooling systems for gas turbine blading*. PhD thesis, The University of Oxford.
- Goodhand, M, N. and Miller, R, J. (2009). Compressor leading edge spikes: A new performance criterion. *ASME Journal of Turbomachinery*, (GT2009-59205).
- GUM (2008). *Evaluation of measurement data - Guide to the expression of uncertainty in measurement*. Joint Committee for Guides in Metrology.
- Guo, S. M., Lai, C. C., Jones, T. V., Oldfield, M. L. G., Lock, G. D., and Rawlinson, A. J. (2000). Influence of surface roughness on heat transfer and effectiveness for a fully film cooled nozzle guide vane measured by wide band liquid crystals and direct heat flux gages. *Journal of Turbomachinery*, 122(4):709–716.
- Han, J.-C., Dutta, S., and Ekkad, S. (2012). *Gas Turbine Heat Transfer and Cooling Technology*. Taylor & Francis.
- Iliopoulou, V., Dénos, R., Billiard, N., and Arts, T. (2004). Time-averaged and time-resolved heat flux measurements on a turbine stator blade using two-layered thin-film gauges. *Journal of Turbomachinery*, 126(4):570–577.
- Incropera, F., Dewitt, D., Bergman, T., and Lavine, A. (2006). *Fundamentals of Heat and Mass Transfer*. John Wiley and Sons, 6th edition.
- Ireland, P. and Jones, T. (1987). The response time of a surface thermometer employing encapsulated thermochromic liquid crystals. *Journal of Physics E: Scientific Instruments*, 20(10):1195.
- Ireland, P. and Jones, T. V. (2000). Liquid crystal measurements of heat transfer and surface shear stress. *Measurement Science and Technology*, 11(7):969.

- Ireland, P., Neely, A., Gillespie, R., and A.J., R. (1999). Turbulent heat transfer measurements using liquid crystals. *International journal of heat and fluid flow*, 4(20):355–367.
- Laveau, B., Abhari, R. S., Crawford, M., and Lutum, E. (2012). High resolution heat transfer measurement on flat and contoured endwalls in a linear cascade. *Proceedings of ASME Turbo Expo 2012*.
- Laveau, B., Abhari, R. S., Crawford, M., and Lutum, E. (2015). High resolution heat transfer measurement technique on contoured endwall with non-uniform thermal resistance. *ASME. Turbo Expo: Power for Land, Sea, and Air*, 5B(GT2015-43639).
- Luque, S., Kanjirakkad, V., Aslanidou, I., Lubbock, R., Rosic, B., and Uchida, S. (2015). A new experimental facility to investigate combustor–turbine interactions in gas turbines with multiple can combustors. *Journal of Engineering for Gas Turbines and Power*, 137(5):051503–051503.
- Luque, S. and Povey, T. (2010). A novel technique for assessing turbine cooling system performance. *Journal of Turbomachinery*, 133(3):031013–031013.
- Ma, H., Wang, Z., Wang, L., Zhang, Q., Yang, Z., and Bao, Y. (2015). Ramp heating in high-speed transient thermal measurement with reduced uncertainty. *Proceedings of ASME Turbo Expo 2015*.
- Martini, P., Schulz, A., and Bauer, H. J. (2005). Film cooling effectiveness and heat transfer on the trailing edge cutback of gas turbine airfoils with various internal cooling designs. *Journal of Turbomachinery*, 128(1):196–205.
- Martiny, M., Schiele, R., Gritsch, M., Schultz, A., and Wittig, M. (1997). In situ calibration for quantitative infrared thermography. *QIRT 96 - Eurotherm Series 50*.
- Maulard, J. (1969). Calibration method used at onera for hotshot and shock tube heat transfer transducers. *Proc. 3rd Int/ Congr. Instr. Aerosp. Simul. Fascilities, iEEE/G-AES*, page 96.
- Metzger, D. E., Bunker, R. S., and Bosch, G. (1991). Transient liquid crystal measurement of local heat transfer on a rotating disk with jet impingement. *Journal of Turbomachinery*, 113(1):52–59.
- Najafabadi, H. N., Karlsson, M., Kinell, M., and Utriainen, E. (2015). Film-cooling performance of a turbine vane suction side: The showerhead effect on film-cooling hole placement for cylindrical and fan-shaped holes. *Journal of Turbomachinery*, 137(9):091005–091005.
- Ochs, M., Horbach, T., Schulz, A., Koch, R., and Bauer, H. (2009). A novel calibration method for an infrared thermography system applied to heat transfer experiments. *Measurement Science and Technology*, 20(7):075103.
- O’Dowd, D. O., Zhang, Q., He, L., Ligrani, P. M., and Friedrichs, S. (2010). Comparison of heat transfer measurement techniques on a transonic turbine blade tip. *Journal of Turbomachinery*, 133(2):021028–021028.

-
- Oldfield, M. L. (2008). Impulse response processing of transient heat transfer gauge signals. *Journal of Turbomachinery*, 130(2):021023–021023.
- Piccini, E., Guo, S., and Jones, T. (2000). The development of a new direct-heat-flux gauge for heat-transfer facilities. *Measurement Science and Technology*, 11(4):342.
- Plaut, R. L., Herrera, C., Escriba, D. M., Rios, P. R., and Padilha, A. F. (2007). A Short review on wrought austenitic stainless steels at high temperatures: processing, microstructure, properties and performance. *Materials Research*, 10:453 – 460.
- Schlichting, H. (1979). *Boundary layer theory*. McGraw-Hill, seventh edition.
- Schultz, A. (2000). Infrared thermography as applied to film cooling of gas turbine components. *Measurement Science and Technology*, 11(7):948.
- Schultz, D. and Jones, T. V. (1973). Heat transfer measurement in short duration hypersonic facilities. *Paper No. AGARD AG-165*.
- Solidworks (2017). Dassault systems. <http://www.solidworks.co.uk>.
- Solvay (2014). Torlon pai design guide. Technical report, Solvey Inc.
- Stolberg-Rohr, T., Gary, J., and Hawkins, D. (2015). Spectral design of temperature-invariant narrow bandpass filters for the mid-infrared. *Opt. Express*, 23:580–596.
- Sweeney, P. C. and Rhodes, J. F. (1999). An infrared technique for evaluating turbine airfoil cooling designs. *ASME*, (99-GT-142).
- Terzis, A., Wolfersdorfm, J., Weigand, B., and Ott, P. (2012). Thermocouple thermal inertia effects on impingement heat transfer experiments using the transient liquid crystal technique. *Measurement Science and Technology*, 23(11):115303.
- Thorpe, S., Yoshino, S., Ainsworth, R., and Harvey, N. (2004a). An investigation of the heat transfer and static pressure on the over-tip casing wall of an axial turbine operating at engine representative flow conditions. (i). time-mean results. *International Journal of Heat and Fluid Flow*, 25(6):933–944.
- Thorpe, S., Yoshino, S., Ainsworth, R., and Harvey, N. (2004b). An investigation of the heat transfer and static pressure on the over-tip casing wall of an axial turbine operating at engine representative flow conditions. (ii). time-resolved results. *International Journal of Heat and Fluid Flow*, 25(6):945–960.
- Thorpe, S., Yoshino, S., Thomas, G. A., Ainsworth, R., and Harvey, N. W. (2005). Blade-tip heat transfer in a transonic turbine. *Proc. IMechE: J. Power and Energy*, 219(Part A):421–430.
- Yan, Y. and Owen, J. (2002). Uncertainties in transient heat transfer measurements with liquid crystal. *International Journal of Heat and Fluid Flow*, 23(1):29–35.

Appendix A

FACTOR

A.1 Photographs of Vanes and Blades

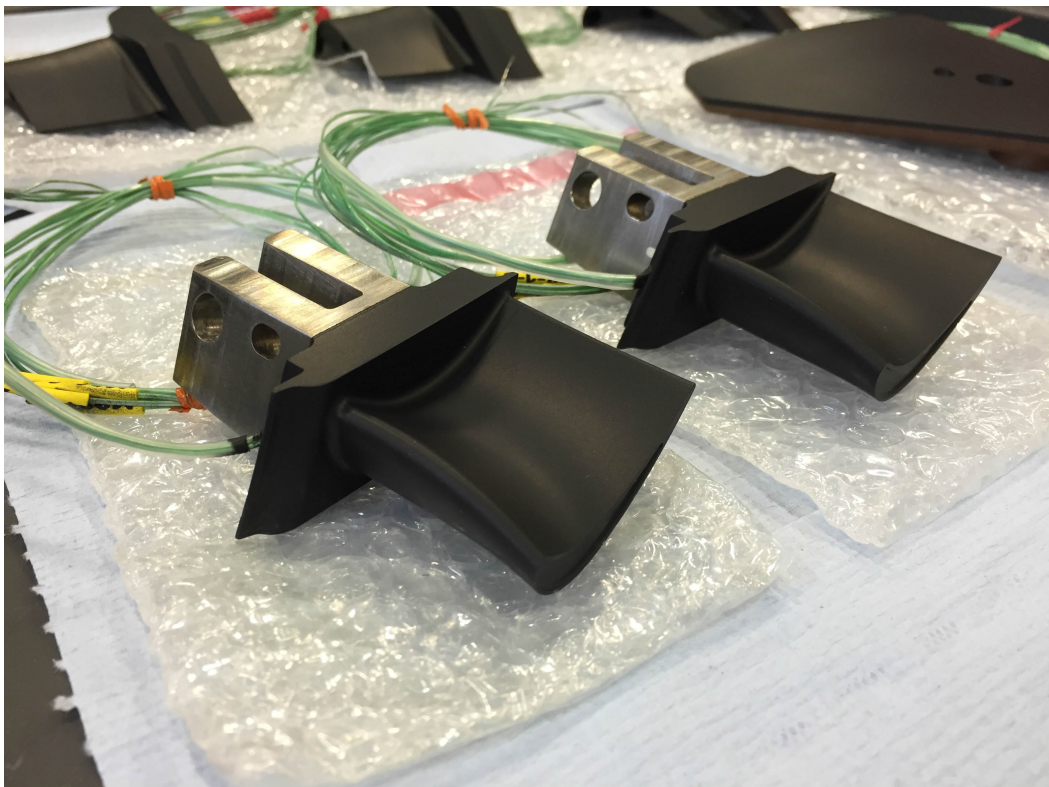


Fig. A.1 Photograph of the manufactured Torlon 7130 - Titanium 6/4 composite rotor blades. The surface mounted thermocouples were installed by VKI. The high emissivity black coating has been applied.

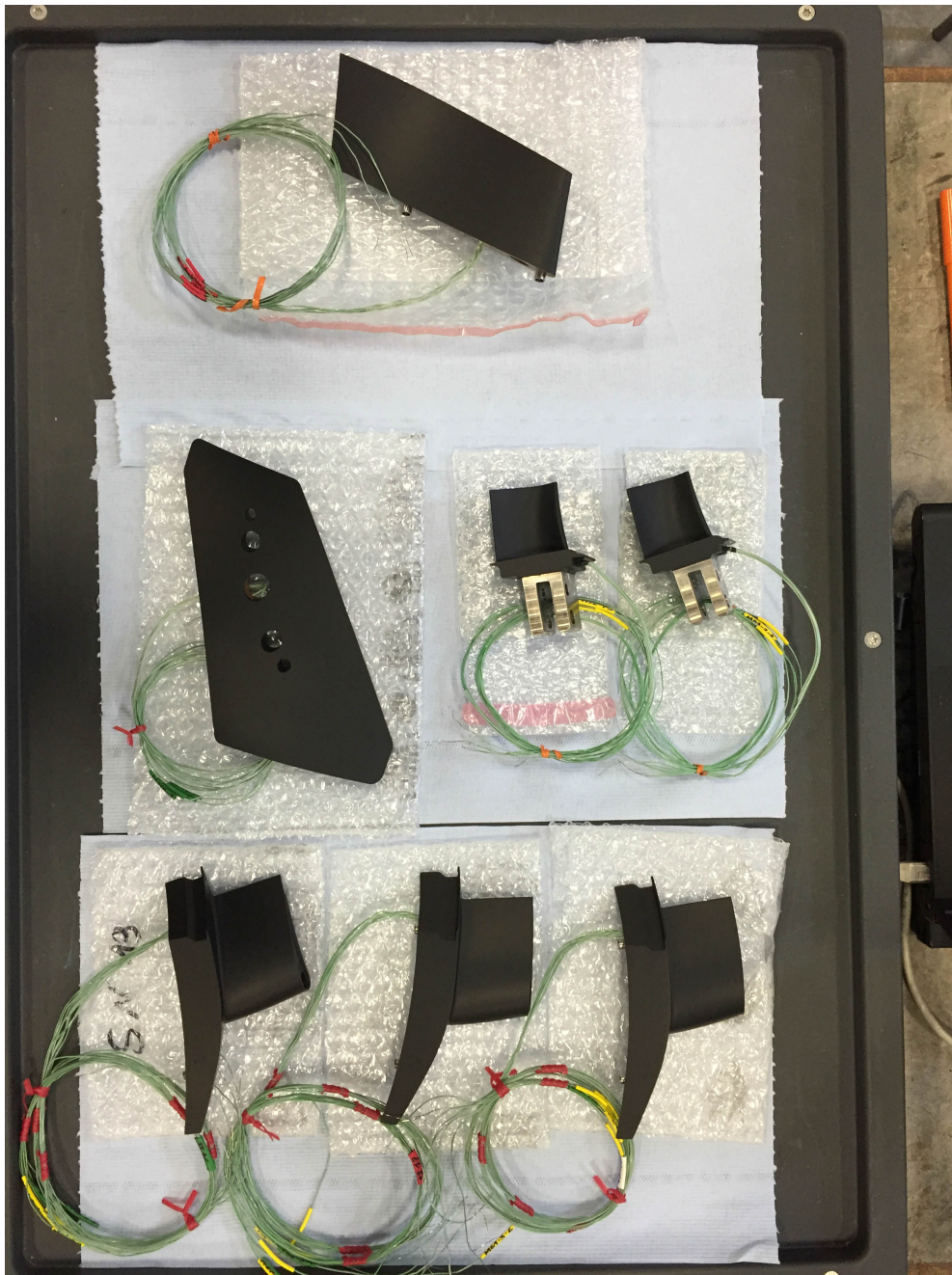


Fig. A.2 Photograph of the FACTOR Torlon 5030 NGVs (bottom), Torlon 7130 Rotor blades (Middle right), Torlon 5030 LP Vane (Top) and Torlon 5030 LP Vane hub section (Middle left)

A.2 Photographs of FACTOR Rig

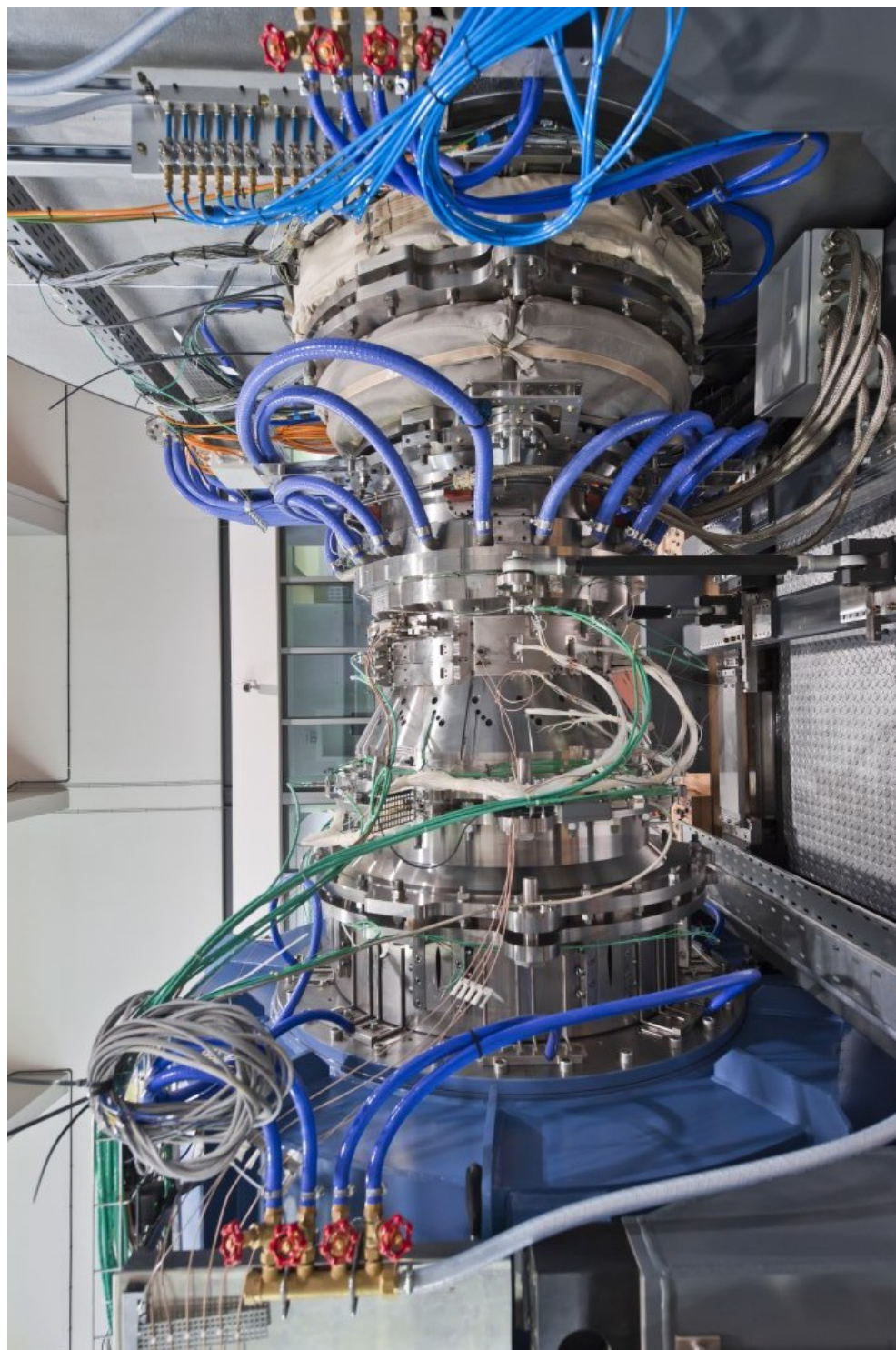


Fig. A.3 The assembled FACTOR rig during commissioning (August 2017)

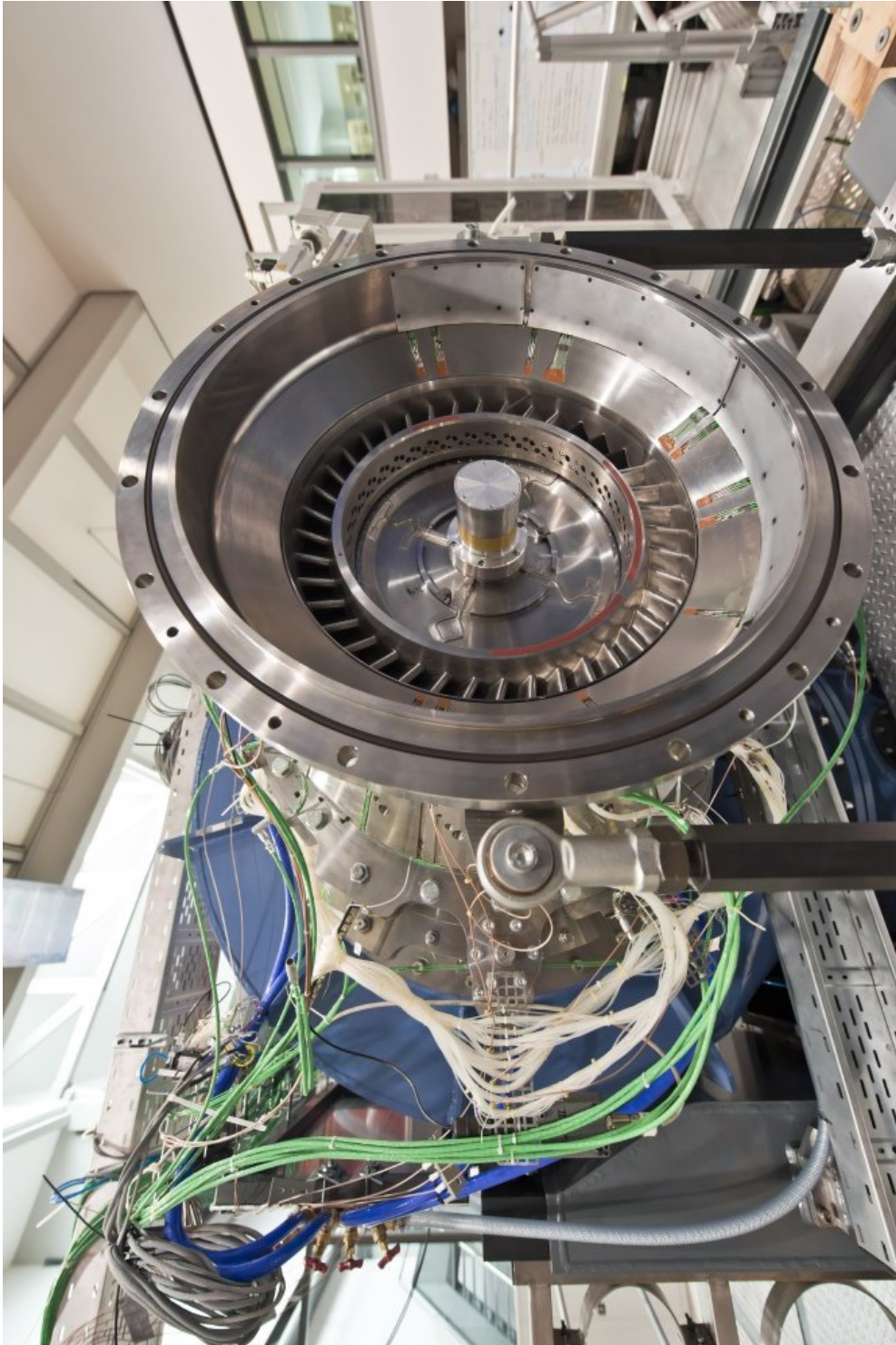


Fig. A.4 The assembled FACTOR rig during commissioning (August 2017)

A.3 Photographs of FACTOR IR Windows



Fig. A.5 Photograph of HP IR window

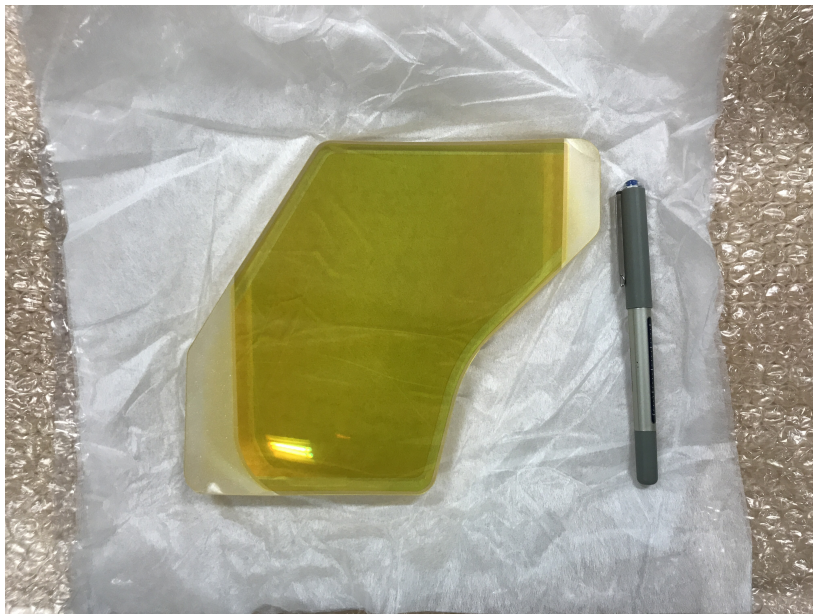


Fig. A.6 Photograph of LP IR window

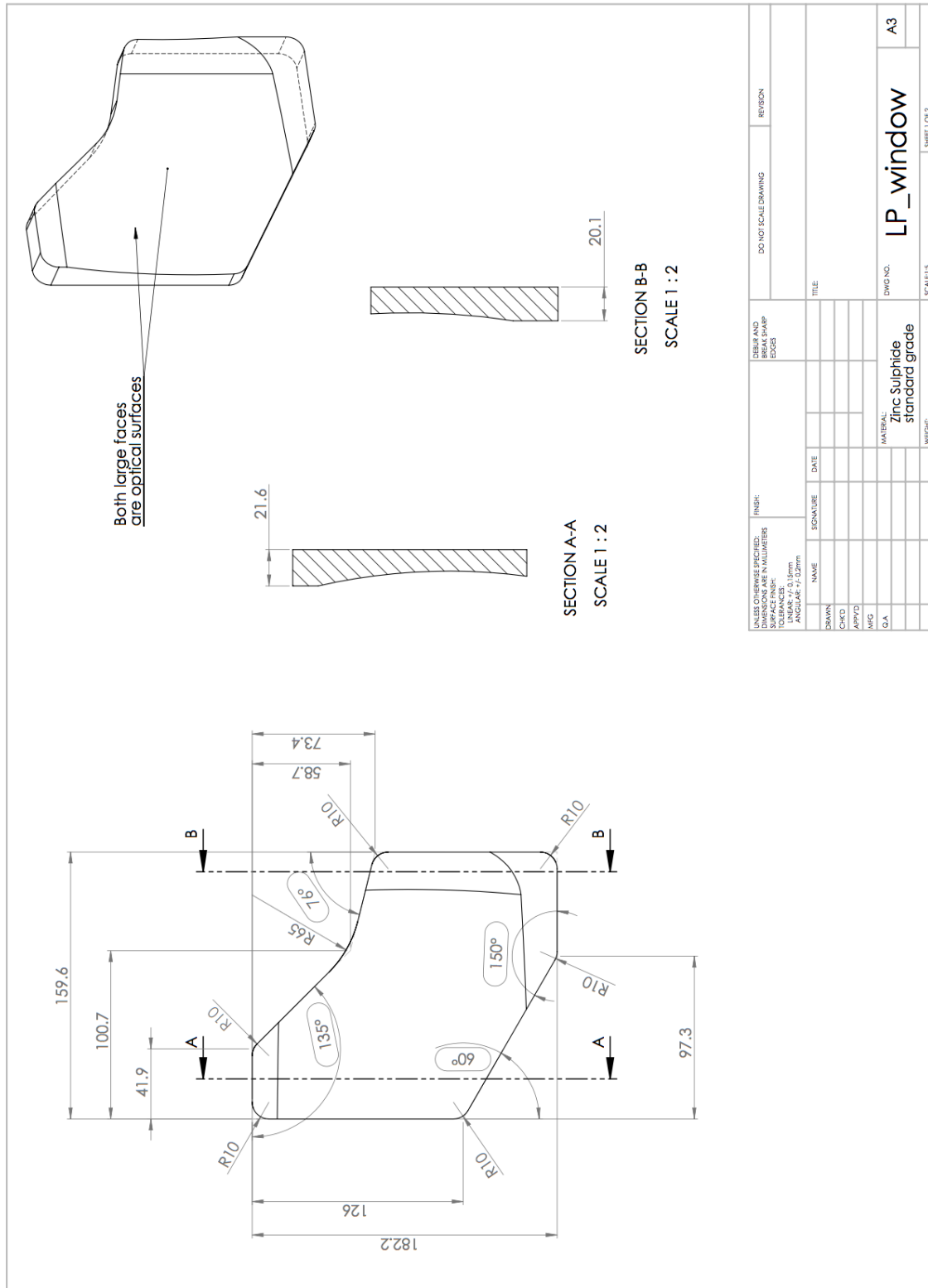


Fig. A.8 Drawing of the LP IR window from the FACTOR rig